Estimation of Raindrop Size Distribution from Spaceborne Radar Measurement(Dissertation_全文)

AUTHOR(S):

Kozu, Toshiaki

ESTIMATION OF RAINDROP SIZE DISTRIBUTION FROM SPACEBORNE RADAR MEASUREMENT

Toshiaki Kozu

Submitted to the Graduate School of Engineering
in partial fulfillment of the requirements
for the degree of Doctor of Engineering at Kyoto University

August 1991

ESTIMATION OF RAINDROP SIZE DISTRIBUTION FROM SPACEBORNE RADAR MEASUREMENT

August 1991

Toshiaki Kozu

ABSTRACT

The growing importance of global climate change monitoring has given rise in recent years to the development of rainfall measuring systems from space. Microwave sensors should play an important role for such systems. Radars are particularly important since they work regardless of background (land/ocean) and provide the information on vertical storm structures. For "quantitative" measurements, however, more studies need to be done to reduce measurement errors. The purpose of this study is to develop a method for spaceborne radars to estimate parameters of raindrop size distribution (DSD) and thereby to reduce the error due to the uncertainty in DSD that is known as a major non-instrumental error source in radar rainfall measurements. Estimating the DSD parameters should lead not only to a better estimate of a meteorological quantity of interest but to a deeper understanding of precipitation processes.

It is well known that dual-parameter (DP) radar measurements can reduce the rain rate estimation error significantly. This is because the DP measurement can provide two independent DSD parameters in contrast with single-parameter (SP) measurements providing only one DSD parameter. The dual-polarization (Z_{DR}) technique is a promising method to make a "complete" (i.e. for each range gate basis) DP measurement for ground-based radars. For spaceborne radars, however, it is difficult to perform such complete DP measurements because of the reduced Z_{DR} measurement sensitivity (due to the down-looking observation geometry) and limitations in mass, size and electric power. In this study, therefore, the combination of a radar reflectivity profile and a path-integrated attenuation derived from surface return or microwave radiometers, which will be available from most spaceborne systems, is employed for the DSD estimation. To discuss this type of DP measurement generally, a new concept, "semi-dual-parameter" (SDP) measurement is proposed together with a "two-scale" DSD model the parameters of which can be estimated from an SDP measurement. An algorithm is proposed for the SDP measurement to estimate the DSD parameters and then to derive rainfall rate.

In order to test the performance of various radar rain rate estimation methods, a large amount of DSD data measured on the ground by a disdrometer are employed after examining the accuracy and the validity of the disdrometer data for radar rainfall remote sensing studies. The test result indicates that the SDP measurement has an accuracy in rain rate estimation from 2 to 4 times better than the SP measurement depending on the range resolution in the attenuation measurement.

The performance of the SDP measurement is also tested using the data obtained from a dual-frequency airborne radar experiment. The SDP measurement is constructed by the combination of an X-band radar reflectivity profile and either X- or Ka-band path attenuation obtained from sea-surface echo. The validity of the estimated DSD parameter and of the derived rain rate is confirmed by a consistency check using the measured Ka-band radar reflectivities.

Based upon the results obtained in this study, a consideration is given of general strategies for processing spaceborne radar data to generate accurate and useful rainfall parameters. Discussion is also made on the usefulness of the DSD estimation method developed in this study to improve a wide range of radar rainfall measurements from space.

CONTENTS

LIST OF TABLES

LIST OF FIGURES

List of Acronyms

APR	Average Probability Ratio
BEST	Bilan Energetique du Systeme Tropical
BSE	Broadcasting Satellite for Experimental purposes
CRL	Communications Research Laboratory
CS	Communication Satellite
DM	Disdrometer
DP measurement	Dual-Parameter measurement
DSD	(Rain) Drop Size Distribution
DSRT	Dual-wavelength Surface Reference Target method
DWT	Dual Wavelengths Technique
EOF	Empirical Orthogonal Function
FOV	Field-of-View
GEWEX	Global Energy and Water Cycle Experiment
GSFC	Goddard Space Flight Center
H-B solution	Hitschfeld-Bordan solution
HPBW	Half-Power Beam Width
IRP	Integral Rain Parameters
J-D distribution	Joss-Drizzle distribution
JEM	Japanese Experimental Module
J-T distribution	Joss-Thunderstorm distribution
J-W distribution	Joss-Wide spread distribution
LDR	Linear Depolarization Ratio
LWC	Liquid Water Content
MARS	Microwave Airborne Rain Scatterometer/radiometer
MLE	Maximum Likelihood Estimation
M-N model	Modified Nishitsuji model
MoM	Method of Moment
MP distribution	Marshall-Palmer distribution
NASA	National Aeronautics and Space Administration
N/N model	Noncoalescence/Nonbreakup model
NUBF	Non-uniform Beam Filling
pdf	Probability density function
P-P	Pruppacher-Pitter (raindrop shape)
SDP measurement	Semi-Dual-Parameter measurement
SP measurement	Single-Parameter measurement
SRT method	Surface Reference Target method
TMI	TRMM Microwave Imager
TOGA	Tropical Ocean and Global Atmosphere
TP measurement	Triple-Parameter Measurement
TRAMAR	Tropical Rain Mapping Radar
TRMM	Tropical Rainfall Measuring Mission
WCRP	World Climate Research Program
WFF	Wallops Flight Facility

CHAPTER 1. BACKGROUND AND OUTLINE OF THIS STUDY

1.1 Importance of Global Rain Mapping and Necessity of Rain Measurement from Space

Rainfall, the major water flow from atmosphere to land and to ocean, is a life-giving resource for Earth biosphere. It sometimes exhibits dangerous anomalies (flood/drought), and appears as destructive storms, however. Rainfall distribution is also one of the most important and least-known parameters related to the global hydrological cycle, which is associated with energy fluxes between atmosphere and land/ocean and therefore couples various components of the global climate system[1-7]. Knowledge of the variation of global rainfall distribution is therefore crucial to understand and to predict the global climate change and weather anomalies.

At present, reliable rainfall data are available only from limited developed countries mainly located around mid-latitudes. In particular, little is known about the rainfall over vast ocean areas where no rain gage or weather radar exists. Therefore, satellite remote sensing is recognized as the most effective and probably the only way to measure global rainfall. However, the rainfall is also recognized as one of the hydrological and meteorological parameters most difficult to measure mainly because of its high spatial and temporal variabilities. Although spaceborne visible and infrared sensors have sufficiently high spatial resolutions, they can not penetrate cloud. Although microwave sensors can directly "see" the rain below cloud cover, spaceborne sensors that have been flown to date (i.e., all radiometers) have had only very crude spatial resolutions. The lack of adequate spatial resolution makes the quantitative measurement difficult [1,3].

Yet, because of its important role in global hydrological cycle and climate, a number of studies of rainfall measurement from space have been attempted using visible/infrared and microwave radiometers onboard several remote sensing satellites. In spite of the problem of spatial nonuniformity of rain within their field-of-view (FOV), microwave radiometers operating at 10 to 20 GHz have been recognized as promising tools for estimating vertically integrated rain rate over the oceans[8]. Microwave absorption by raindrops causes an increase in brightness temperature from the cold ocean background. Higher frequency ($\gtrsim$ 37 GHz) radiometers are also useful to estimate the upper structure of rain storms since the brightness temperature is sensitive to scattering by ice particles aloft[8]. Algorithms combining multi-frequency radiometers ranging from 18 to 90 GHz have also been proposed[9]. Such

combination may also provide a crude rainfall profile. Clearly, there are several weak points in the microwave/millimeter wave passive sensors; there is no range resolution capability except for the crude profiles obtained from the multi-frequency inversion technique, and there is difficulty in estimating rain rate over land. In this sense, the radar is an excellent instrument complement to the radiometers.

The capability and the usefulness of radar to observe precipitation were recognized more than 40 years ago [10]. Since its inception, numerous studies have been performed to extend its ability to discriminate particle type, to improve rain rate estimation accuracy and to measure various atmospheric processes. As a result, weather radars are now widely used throughout the world for weather forecasting, warning, and meteorological and climatological studies. However, use of the weather radar has been limited to ground-based usage except for some special-purpose applications of airborne and shipborne radars.

As mentioned above, radars will play a very important role in space-based rainfall measurements. Potential benefits expected from the radar measurements are:

(1) Unlike the passive microwave sensors, the radar can provide rainfall estimates independent of the microwave emission properties of the background (land or ocean). The radar measurement is, therefore, especially important over land where the radiometers do not work so well.

(2) The radar has range profiling capability. Data on the vertical storm structure is important for developing accurate passive microwave rainfall retrieval algorithms, for estimating latent heat release profile, and for other fundamental atmospheric science studies.

(3) By utilizing the surface return as a tool to estimate path-averaged rain rate, the radar can extend the rain rate measurement dynamic range toward the higher rain rates.

(4) The storm structure and rainfall characteristics that are inferred from the radar observation could be utilized to improve the passive microwave rainfall retrieval accuracy not only for the rainfall within the radar swath but to outside the radar swath.

(5) The radar data could be combined with the passive microwave data to provide more accurate rain rate estimates and to infer raindrop size distribution (DSD). The latter can then be used to estimate the relationships between radar reflectivity and rain rate, and between other rain-parameters for each observation or each storm bases, which may further improve the accuracy of radar algorithms.

Complementarity of the radar and other passive sensors has been well documented in the literature[1,3,5,8] and is summarized in Table 1-1[5].

Table 1-1. Complementarity between sensors for rainfall measurement [5].

	Microwave Radiometer	Radar	VIS/IR Radiometer
Advantages	• Quantitative measure of rain • Wide swath	• Quantitative measure of rain • Better spatial resolution • Vertical profile of rain • Can provide layer thickness	• Best spatial resolution • Distinguish between convective and stratiform precipitation • Transfer standard to geosynchronous and polar orbiters
Limitations	• Less quantitative over land for low rainfall • Moderate spatial resolution	• Narrow swath • Largely untested in space	• Less quantitative measure • Obscuration by cirrus shields

Table 1-2. Accuracy and temporal/spatial resolution requirements of rainfall data [1].

Application	*Accuracy*	*Resolution*	
		Horizontal (km)	*Temporal*
1. Global climate			
Global	10–25%	200–500	1 week–1 month
Continent	10	25	1 day
2. Global weather	10	100	1 day
3. Synoptic weather forecast	10	100	6–12 hr
4. GCM	0.5–2 mm/day	100	1 day
5. Tropical cyclone (over water)	10–30%	2–20	0.5–6 hr
6. Thunderstorm-flash flood	10–30%	1–10	10–30 min
7. Mesoscale modeling	10–25%	25–100	15–60 min
8. Crop-yield modeling	10–30%	50	1 day
9. Soil-moisture evaluation	20%	20–100	1 day
10. Water-supply forecast	10%	10	1 day
11. Hydrological structure design	50%	10	1 week

1.2 Problems in Quantitative Rainfall Remote Measurements

The rainfall retrieval algorithms are closely related to the resolution requirements. Table 1-2 lists the accuracy and resolution requirements of rain products addressed in the workshop report of the precipitation measurement from space[1]. The temporal and spatial resolution requirements range from one month to a half hour and from 500 km to 1 km, depending on the application. If only monthly averaged rainfall is required, one can utilize statistical properties of rainfall to improve the estimate. On the other hand, one has to rely on instantaneous data if a quantitative "snap shot" of rainfall is required (e.g. applications to short-term weather forecast). Although the instantaneous rainfall map may not directly be required to achieve a main

goal of a space mission, such high temporal and spatial resolution data are required to determine the statistical properties of rainfall, and therefore important also to develop statistical rain-retrieval algorithms. In this study, therefore, we focus our attention on the problem of estimating the high resolution rainfall parameters; rainfall profile or path-averaged quantities.

As described later in this thesis, the quantity that can be measured by rain radar is the receiver video output voltage, which is digitized and stored on a storage device. By means of internal and external calibrations, it can be related to the receiver input power and then to a radar reflectivity factor of rain (called Z or Z-factor; later in this thesis, a more general definition of Z-factor, Ze will also be used) or a surface scattering cross section (σ^0). Z-factors and in some cases σ^0 are then used to estimate various rainfall parameters such as rain rate and liquid water content. The term "quantitative" rainfall remote-sensing is defined as quantitative estimation of those rainfall parameters required for Earth sciences such as hydrology, climatology and meteorology, and for microwave or millimeter wave communication engineering.

There are various error sources in the rain parameter estimation:

(1) Absolute radar calibration is required to determine quantitatively the Z-factor and σ^0 from the raw radar data.

(2) Relative radar calibration is required to obtain differences in power between two received signals from which rain attenuation and other rain parameters can be deduced.

(3) Statistical fluctuations in the radar received power cause an error in the estimation of mean received power. To reduce these fluctuations, a large number of independent samples should be averaged.

(4) Noise and interference mask rain echoes and cause bias (usually positive) errors. To diminish this bias error, the noise or interference signal level should be estimated and be subtracted from the total (signal plus noise or interference) level.

(5) Rain attenuation of the radar signal during propagation between the radar and a radar scattering volume can cause a negative bias error if a radar equation neglecting the attenuation is used to estimate the Z-factor. Correction for the attenuation tends to be very unstable and results in highly erroneous Z-factor estimates.

(6) Partial beam filling or nonuniformity of rain within a scattering volume may cause bias errors due to the non-linear relationships between Z-factor and other rain parameters.

(7) Variation in raindrop size distribution is a major cause of error in rain parameter estimation

from the Z-factor.

(8) Uncertainty in the phase of hydrometeors is another cause of error because the scattering properties and falling velocities are largely affected by the phase state.

Roughly speaking, the above error sources are aligned in such order that the smaller item numbers are more affected by the radar system performance in engineering sense (i.e. sensitivity and accuracy in Z-factor measurement), and that larger item numbers are more affected by natural precipitation properties. For example, the errors described in items (7) and (8) cannot be eliminated only by improvements in the radar system performance and, therefore, must be solved by improved rainfall retrieval techniques.

1.3 Survey of the Studies and System Development for Rainfall Remote Measurement from Space

1.3.1 Spaceborne radar systems [11]

Pioneering results on the design of spaceborne rain radar were reported by Eckerman[12], Skolnik[13], Okamoto et al.[14] in the mid to late 1970's. Although their studies have never proceeded beyond the conceptual design stage (at present, their designs still seem to be ambitious), their study results and design approach have been followed in more recent studies during the 1980's [15-23]. Although most of the design studies have focused on rain measurements in the tropics, some millimeter wave radars for measuring global precipitation including snow and cloud have also been proposed [25-27].

Among those studies, the Tropical Rainfall Measuring Mission (TRMM), which has been studied jointly by the US and Japan [4,5], is expected to be the first satellite carrying a rain radar. The TRMM satellite, which has a low orbital altitude (≈ 350 km) and low inclination angle (35°), is dedicated to measuring tropical rain and is scheduled to be launched in 1996. Following the TRMM, several proposed projects such as BEST *(Bilan Energetique du Systeme Tropical)* project by France[21], a rain radar on Japanese Experimental Module (JEM) [22] and TRAMAR *(Tropical Rain Mapping Radar)*[20], would enable continuous measurement of tropical rainfall. Observations of precipitation at higher latitudes may be performed by some satellites having larger orbital inclination angles [7].

The major parameters of TRMM radar is listed in Table 1-3 [24]. Although in the original design, a dual-frequency radar (14 and 24 GHz) was pursued, cost, weight and power consumption limitations have forced final implementation to include only a single frequency

Table 1-3. Major parameters of proposed TRMM radar.

Item	Specification	Note
Frequency	13.8 GHz*1	*1 Two-channel frequency agility (13.796, 13.802 GHz)
Antenna		
Type	Planar array	128-element waveguides
Gain	47.7 dB	
Beam width	0.71° x 0.71°	
Aperture	2.2 m x 2.2 m	
Sidelobe level	< -30 dB	
Scan angle	± 17°	Cross track scan
Transmitter		
Type	SSPA's (x128)	Solid State Power Amplifiers
Peak power	578 W	
Pulse width	1.67 μs x 2 ch.*1	Total 3.34 μsec
PRF	2778 Hz	Fixed PRF
Receiver		
Noise figure	2.3 dB	
IF frequency	156 MHz, 162 MHz	
Band width	0.78 MHz x 2 ch.*1	
Dynamic range	> 70 dB	
Others		
Total system loss	2.0 dB	
N_{samp}*2	64	*2 Number of independent samples
Data rate	85 kbps	
Power consumption	224 W	
Mass	347 kg	

radar. In down-looking spaceborne radar measurements, most dual-polarization techniques are not applicable, and, therefore, dual-frequency radars are very attractive. The dual-frequency radar, however, will not appear until TRAMAR.

1.3.2 Rain parameter estimation methods

Apart from system dependent errors, the most significant error source in the radar estimates of rainfall parameters should be fluctuations in DSD. The effect of DSD fluctuations depends on the combination of rain parameters to be measured and estimated. For example, estimating rain rate from microwave rain attenuation measurement is relatively insensitive to DSD fluctuations, but estimating rain rate from Z-factor is very sensitive to DSD fluctuations and subject to large estimation errors unless DSD is estimated by some means[28,29].

Among the various rainfall parameters, rain rate (R) is required to be estimated most frequently from scientists. Therefore, most of the estimation methods proposed to date aimed at the estimation of R. The conventional method that has been used with ground-based operational radars is to use an empirical Z-R relation, for estimating R from Z. Although this

method has advantages of high range resolution and large dynamic range, as mentioned above, variations in the DSD can cause large errors. In order to reduce the error from this source, a large number of studies have been performed.

Adjusting the Z-R relationship based on rainfall type, seasonal and regional dependences has been found to reduce the error to some extent [30]. Utilizing the insensitivity of the relation between rain attenuation coefficient (k) and R (k-R relation) to DSD variation, measurements of rain attenuation instead of the radar reflectivity has also been proposed[31]. However, the attenuation measurement on the ground usually needs a receiver or a reflector away from the radar site unless a dual-frequency radar is employed[32], and it is difficult to achieve high range resolution. In recent years, it has been proposed to use the difference in the phases between horizontally and vertically polarized rain backscattered signals, which is related to the differential phase shift (k_{DP}) caused by the rain along the two-way propagation path, to estimate rain rate[33,34]. The k_{DP} has the advantage similar to the attenuation coefficient that k_{DP}-R relation is almost linear and insensitive to the DSD variation. As in the attenuation measurement, however, k_{DP} is difficult to be measured with high range resolution particularly in light rain and requires a coherent, dual-polarization radar.

In addition to these "single-parameter" approaches, measurements of multiple rain parameters (in most cases two parameters) have been studied extensively [28,29]. They include dual-frequency and dual-polarization radars to measure Z and k, and Z and Z_{DR}, respectively. These dual-parameter rainfall measurements have the ability to provide other rain parameter estimates better than those obtainable from the single-parameter measurements. The larger the number of measurable parameters is, the better the estimates would be. In practice, however, the difficulty in making multiparameter measurements increases rapidly with the increase in the number of rain parameters to be measured. It is anticipated that the error due to other sources dominate the total error and little improvement is obtained even though a sophisticated multi-parameter measurement is conducted. At present, the consensus is that even a dual-parameter measurement with a modest implementation has several difficulties such as calibration and errors caused by statistical signal fluctuation, but that, if an error-free measurement is performed, the dual-parameter measurement can provide a sufficient accuracy. In other words, although the natural variation in DSD can be large, estimating two DSD parameters is significant to reduce the error due to the DSD variation to an acceptable level.

1.3.3 Aircraft experiment

Rainfall retrieval methods should be tested using data obtained from actual measurements. Aircraft experiments are therefore essential to test the spaceborne radar algorithms. Communications Research Laboratory (CRL) has been conducting a series of aircraft experiments using a Microwave Airborne Rain-Scatterometer/radiometer (MARS) since 1979 [35]. Although there are several airborne radars for weather observation in several countries, at present, the MARS appears to be the only instrument dedicated to acquiring data for the development of algorithms for spaceborne rain radars. The MARS consists of X-band (10 GHz) and Ka-band (34.5 GHz) radars and radiometers with matched-beam antennas. In this study, data from a MARS experiment will be used for developing and testing a method proposed in this study. The major results obtained from the MARS rain observation experiments are outlined below:

• 1979 ~ 1981: Radar experiments using a Cessna 404 aircraft were conducted around Japan. A flight to make simultaneous observations with a C-band ground-based radar was also conducted to evaluate the feasibility of measuring rain from aircraft. A dual-frequency algorithm to estimate rain rate profile was proposed and tested [36]. Sea surface return and X-band brightness temperature over the ocean were analyzed and the feasibility of estimating path-integrated rain rate from these data were suggested [36,37].

• 1985 ~ 1986: A joint experiment was started between NASA/GSFC and CRL using a NASA P3-A aircraft. With the data obtained from this experiment, several rain rate estimation methods have been tested and compared[38-41]. The methods include a conventional Z-R method, Surface Reference Technique (SRT; estimating path-integrated attenuation from the surface return), Dual-Wavelength Technique (DWT; estimating an integrated attenuation from the differential radar reflectivities between two frequencies, different from the Fujita's dual-frequency algorithm [36]), and mirror image methods. Intercomparisons of the results from those methods suggest that the Z-R, SRT and DWT methods are feasible from space. It was also found that each method has its own advantages and drawbacks. For example, the SRT method does not work well for light rain because of the small path attenuation in comparison to the fluctuation in surface scattering cross section. On the other hand, the Z-R method under-estimates the rain rate when the radar wave attenuation up to the radar scattering volume becomes significant.

• 1988 ~ 1989: The Cessna 404 and the P3-A experiments had a limitation that the maximum

flight altitude was not high enough to fly over convective storms. In order to make a better simulation of spaceborne measurements, a jet airplane that can fly high is desirable. For this reason, the NASA T-39 jet plane which can fly up to about 12 km was employed, and various types of storms, including both stratiform and convective, were observed around the Wallops Flight Facility (WFF) of NASA, VA[42]. The data from this experiment have not yet been completely analyzed; however, similar conclusions have been obtained from the same type of analyses as those for the P3-A experiment [43].

• 1990: The X-band radar was modified to measure the cross polarized component of return signals as well as the original co-polarized component. The NASA/CRL joint experiment team participated in the Tropical Cyclone Motion experiment (TCM-90) [44]. The MARS system was installed on the NASA DC-8 aircraft together with several NASA microwave radiometers and measured several typhoons in the western North Pacific. The data from this experiment is now under processing, and preliminary results indicate that the LDR (Linear Depolarization Ratio; the ratio of cross-polarized to co-polarized components) is a good measure to identify hydrometeor phase [45].

1.4 Purpose and Outline of This Study

As described above, there have been three types of approaches in the development of radar rainfall retrieval algorithms applicable to spaceborne radars: (1) The conventional single-parameter method, i.e., using empirical Z-R relations, (2) attenuation methods using surface reflection or differential radar reflectivity factors between two different frequencies, and (3) the combination of (1) and (2) to take advantage of both methods; i.e., a high range resolution and an insensitivity to DSD variations. There are also other approaches to make dual-parameter (DP) measurements as described in a series of papers by Ulbrich and Atlas[28,29,46-48], a dual-wavelength method[49,50], and a number of works for the dual-polarization radar measurements[29]. This approach is to use the two kinds of integral rain parameters that are measured for estimating two DSD parameters which in turn can be used to estimate other rainfall parameters. This type of approach has the advantage that the most fundamental rainfall parameter, DSD, is incorporated into the estimation process and, therefore, the DSD estimation method would clearly be related to physical processes and can have a wider applicability of the estimation result to a variety of scientific studies and rainfall remote sensing.

However, because of the difficulty in making a complete DP measurement for each

range resolution cell of the order of a few hundred meters[49,50], the DSD estimation methods have never proceeded beyond the analytical and simulation studies except for the standard dual-polarization measurement (Z and Z_{DR} combination). Since Z_{DR} is close to unity in down-looking radar observations (i.e., there is little difference between H- and V-polarized back-scattered signals), such dual-polarization measurements do not work as DP measurements. As a result, the estimation of DSD has never been tried for airborne or spaceborne radar rainfall retrieval algorithms.

The major purpose of this study is to develop a method to estimate DSD parameters from either the single- or dual-frequency spaceborne radar measurements. Because the complete DP measurement is difficult to perform for each resolution cell, we pursue methods to use "semi" DP (SDP) measurements in which the first measurement, Z-factor, has a fine range resolution but the second measurement is obtained only with a much coarser resolution. To make the DSD estimation possible from the SDP measurement, we propose the concept of "two-scale" DSD model. A method to estimate the parameters of a two-scale model is proposed and tested by means of a simulation with a large amount of DSD data measured on the ground. Moreover, the method is tested using the data obtained from the CRL/NASA joint aircraft experiment. Finally, consideration is given to the strategy and issues in developing overall algorithms for single frequency spaceborne radars like the TRMM radar.

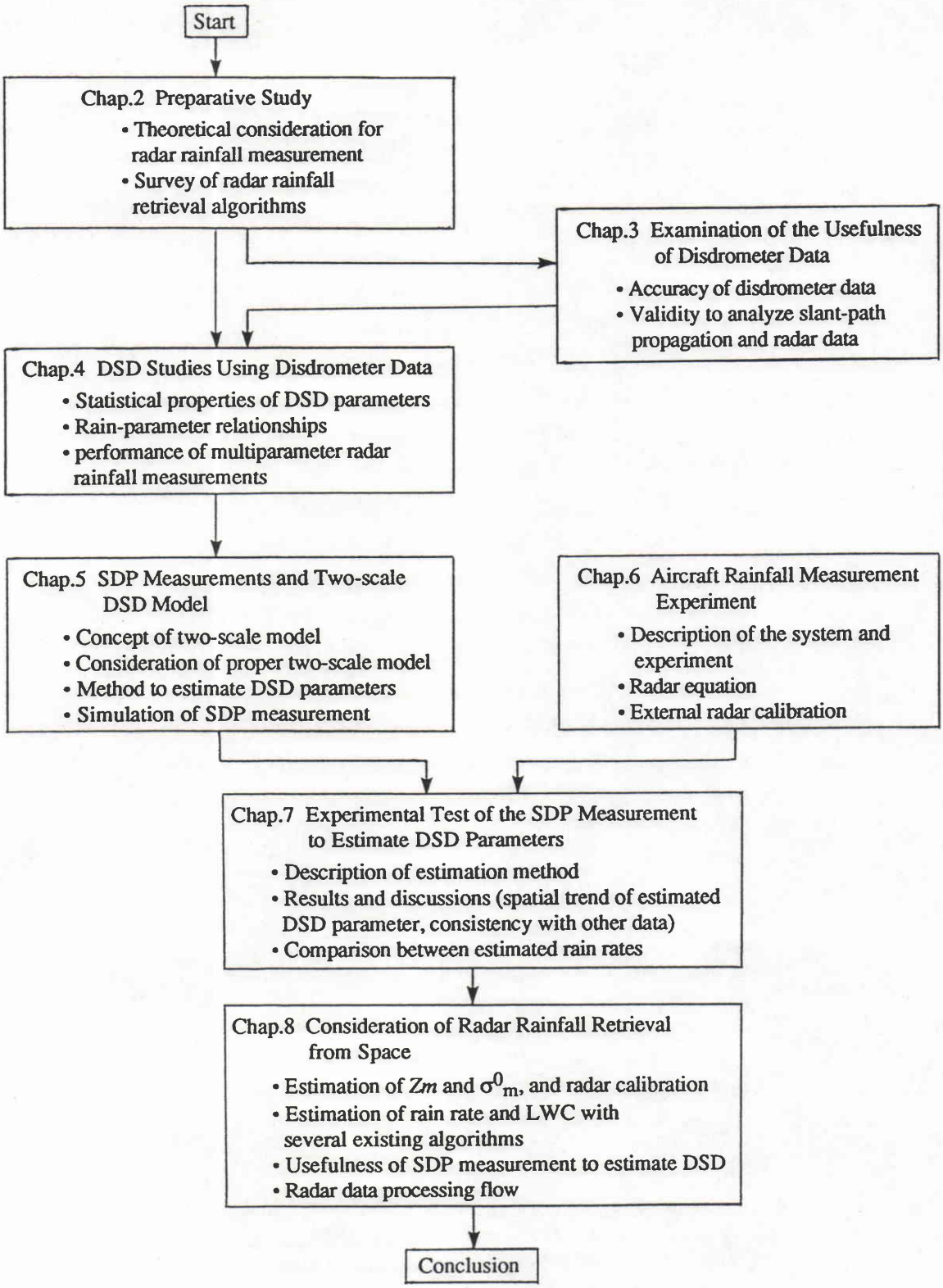

Figure 1-1. Flowchart of this thesis

Figure 1-1 shows a flowchart of this thesis organized by the following chapters:

Chapter 2: Fundamental meteorological and radar quantities are summarized, basic theory of radar rainfall measurement is outlined, and the radar equations relevant to this study are described.

Chapter 3: We consider the DSD measurement by a disdrometer for the study of radar remote sensing. Followed by an introductory explanation of the disdrometer, consideration is given to possible errors in disdrometer measurement. Two experimental data analyses which justify the use of disdrometer data for the study of radar rainfall measurement are described: (1) an analysis of slant-path rain attenuation properties, and (2) the external calibration of a Ku-band FM-CW radar.

Chapter 4: Based on the experimental validation of the disdrometer data, we perform statistical analyses of parameters of DSD modeled by gamma and lognormal models, including rain rate and Z-factor dependences of the DSD parameters, and relations between integral rain parameters of interest such as Z-R, k-R and k-Z relations as well. In this chapter, the validity of using the gamma and lognormal models, both three-parameter and two-parameter models, is tested in terms of the accuracy in rain rate estimation. From the test, we find that the dual-parameter (DP) rainfall measurement combining Z and attenuation measurements has sufficient accuracy in rain rate estimation.

Chapter 5: Based on the results obtained in the preceding chapters, we propose a "semi" dual-parameter (SDP) rainfall measurement combining a Z-factor profile and path-integrated attenuation for estimating DSD parameters. To do this, we introduce the concept of "two-scale" DSD model and propose some two-scale models adequate for describing short-term (or small spatial scale) DSD variations. Rain rate profiling accuracy of the SDP measurement is evaluated through a simulation employing the disdrometer dataset. The result shows that the SDP measurement has an ability to estimate the rain rate profile reasonably well; 2 to 4 times better than the single-parameter (SP) measurement using a Z-R relation, depending on the temporal or spatial resolution of the attenuation measurement and depending on the two-scale model assumed.

Chapter 6: The DSD estimation method proposed in Chapter 5 is tested using the data obtained in the CRL/NASA joint aircraft experiment. For this experiment, the MARS system was upgraded and installed on the NASA T-39 aircraft. In this chapter, descriptions are given of the experiment conducted in the fall 1988, the modified MARS system, and the method and

result of external radar calibration.

Chapter 7: Experimental tests of the DSD estimation method are performed using the data obtained from the T-39 experiment. The method proposed in Chapter 5 is modified to some extent so as to allow use of more general IRP relationships and to accommodate the attenuated *Z*-factor profile. The validity of estimated DSD parameter is confirmed by means of a consistency check with the Ka-band *Z*-factor profile that is independent of the DSD estimation process. The test result is found to be very encouraging. It is also suggested that the non-uniform beam filling and the attenuation due to hydrometeors aloft such as bright band particles can cause non-negligible errors in the estimated DSD and in the final product (rain rate and LWC).

Chapter 8: Based on the results obtained in the preceding chapters together with those obtained from previous studies, we consider general strategies for processing a spaceborne radar data to generate accurate and useful rainfall parameters. A discussion is made on the usefulness of the method proposed in this thesis to improve the overall radar rainfall retrieval. The proposed DSD estimation method may not always be applicable mainly because of the effect of non-uniform beam filling and the unavailability of path-integrated attenuation; however its unique feature to provide the most fundamental rainfall parameter, DSD, will be very useful to improve rainfall retrieval accuracies for a wide range of rainfall measurements.

References

(1) Atlas, D. and O.W. Thiele, eds., 1981: Precipitation measurements from space. Workshop report, NASA/Goddard Space Flight Center, Greenbelt, MD.

(2) NASA, 1984: Earth Observing System Working Group Report Vol. I. NASA TM-86129.

(3) Thiele, O.W., ed., 1987: On the requirements for a satellite mission to measure tropical rainfall. NASA RP-1183.

(4) Simpson, J., R.F. Adler, G.R. North, 1988: A proposed tropical rainfall measuring mission. *Bull. Amer. Meteor. Soc.*, **69**, 278-295.

(5) Simpson, J., ed., 1988: A satellite mission to measure tropical rainfall. Report of the Science Steering Group. NASA/Goddard Space Flight Center.

(6) WCRP, 1990: Scientific plan for the TOGA coupled ocean-atmosphere response experiment. WCRP Publ. Ser. No.3 Addendum, Int'l TOGA Project Office, WMO, Geneva.

(7) Schiffer, R.A., 1988: Global energy and water cycle experiment (GEWEX). *Tropical Rainfall Measurements*, J.S. Theon and N. Fugono, eds. A. Deepak Publ., Hampton, VA, 21-25.

(8) Wilheit, T.T., 1986: Some comments on passive microwave measurement of rain. *Bull. Amer. Meteor. Soc.*, **67**, 1226-1232.

(9) Kummerow, C., R.A. Mack, and I.M. Hakkarinen, 1989: A self-consistency approach to improve microwave rainfall rate estimation from space. *J. Appl. Meteorol.*, **28**, 869-884.

(10) Atlas, D., ed., 1990: *Radar in meteorology*. Amer. Meteor. Soc., Boston, 806pp.

(11) Meneghini, R. and T. Kozu, 1990: *Spaceborne Weather Radar*, Artech House, Norwood, MA, 199pp.

(12) Eckerman, J., 1975: Meteorological radar facility for the space shuttle. *IEEE National Telecomm. Conf.*, New Orleans, IEE Publ. 75 CH1015 CSCB, 37-6 - 37-17.

(13) Skolnik, M.I., 1974: The application of satellite radar for the detection of precipitation. NRL Report 2896, October.

(14) Okamoto, K., S. Miyazaki, and T. Ishida, 1979: Remote sensing of precipitation by a satellite-borne microwave remote sensor, *Acta Astronautica*, **6**, 1043-1060.

(15) _____, T. Ojima, S. Yoshikado, H. Masuko, H. Inomata, and N. Fugono, 1982: System design and examination of spaceborne microwave rain-scatterometer. *Acta Astronautica*, **9**, 713-721.

(16) Goldhirsh, J. and E.J. Walsh, 1982: Rain measurements from space using a modified Seasat-Type altimeter. *IEEE Trans. Antennas and Propag.*, **AP-30**, 726-733.

(17) Li, F.K., E. Im, W.J. Wilson, and C. Elachi, 1988: On the design issues for a spaceborne rain mapping radar. *Tropical Rainfall Measurements*, J.S. Theon and N. Fugono, eds. A. Deepak Publ., Hampton, VA, 387-393.

(18) Okamoto, K. et al., 1988: A feasibility study of the rain radar for tropical rainfall measuring mission. *J. Comm. Research Lab.*, **35**, 109-208. (This actually consists of six papers by K. Okamoto, J. Awaka, K. Nakamura, T. Ihara, T. Manabe and T. Kozu.)

(19) Goldhirsh, J., 1988: Analysis of algorithms for the retrieval of rain rate profiles from a spaceborne dual-wavelength radar. *IEEE Trans. Geosci. and Remote Sens.*, **GE-26**, 98-114.

(20) Im, E. and F. K. Li, 1989: Tropical rain mapping radar on the Space Station. *Proc. IGARSS'89*, Vancouver, Canada, 1485-1490.

(21) Marzoug, M., P. Amayenc, J. Testud, and N. Karouche, 1989: Conceptual design of the spaceborne rain radar for the B.E.S.T. project. Preprints, *24th Conf. Radar Meteor.*, Tallahassee, FL, Amer. Meteor. Soc., 597-600.

(22) Okamoto, K., J. Awaka, T. Ihara, K. Nakamura, and T. Kozu, 1989: Conceptual designs of rain radars in the Tropical Rainfall Measuring Mission and on the Japanese Experiment Module at the manned Space Station program. Preprints, *4th Conf. Satellite Meteor. and Oceanog.*, San Diego, CA, Amer. Meteor. Soc., 18-21.

(23) Nakamura, K., K. Okamoto, T. Ihara, J. Awaka, T. Kozu and T. Manabe, 1990: Conceptual design of rain radar for the Tropical Rainfall Measuring Mission. *Int. J. Satellite Communications*, **8**, 257-268.

(24) Okamoto, K., T. Ihara, J. Awaka, T. Kozu, K. Nakamura, and M. Fujita, 1991: Development status of rain radar in the tropical rainfall measuring mission. Preprints, *25th Conf. Radar Meteorol.*, Paris, Amer. Meteor. Soc., 388-391.

(25) Lhermitte, R., 1989: Satellite-borne millimetric wave doppler radar.*URSI Commission F, Open Symposium*, La Londe-Les-Maures, France, Sept. 11-15.

(26) Nathanson, F.E., T.H. Slocumb, S.W. McCandless, and R.K. Crane, 1989: A space based radar to measure clouds and rain. *Proc. IGARSS '89*, Vancouver, Canada, 1484.

(27) Im, E. and K. Kellogg, 1990; Spaceborne radar for rain and cloud measurements: A conceptual design. *Proc. IGARSS '90*, College Park, MD, 425-428.

(28) Atlas, D. and C.W. Ulbrich, 1974: The physical basis for attenuation-rainfall relationships and the measurement of rainfall parameters by combined attenuation and radar methods, *J. Res. Atmos.*, **8**, 275-298.

(29) _____, _____ and R. Meneghini, 1984: The multiparameter remote measurement of rainfall. *Radio Sci.*, **19**, 3-22. (This volume is a special issue on multiparameter radar rainfall measurement. Also see a series of papers in this issue.)

(30) Stout, G.E. and E. A. Mueller, 1968: Survey of relationships between rainfall rate and radar reflectivity in the measurement of precipitation. *J. Appl. Meteor.*, **7**, 465-474.

(31) Atlas, D. and C.W. Ulbrich, 1977: Path- and area-integrated rainfall measurement by microwave attenuation in the 1-3 cm band, *J. Appl. Meteorol.*, **16**, 1322-1331.

(32) Eccles, P.J. and E.A. Mueller, 1971: X-band attenuation and liquid water content estimation by a dual-wavelength radar. *J. Appl. Meteor.*, **10**, 1252-1259.

(33) Sachidananda, M. and D.S. Zrnic, 1986: Differential propagation phase shift and rainfall estimation. *Radio Sci.*, **21**, 235-247.

(34) Balakrishnan, N. and D.S. Zrnic, 1989: Correction of propagation effects at attenuating wavelengths in polarimetric radars, Preprints, *24th Conf. Radar Meteor.*, Tallahassee, FL, Amer. Meteor. Soc., 287-291.

(35) Okamoto, K., S. Yoshikado, H. Masuko, T. Ojima, N. Fugono, 1982: Airborne microwave rain scatterometer/radiometer. *Int. J. Remote Sens.*, **3**, 277-294.

(36) Fujita, M., K. Okamoto, S. Yoshikado, and K. Nakamura, 1985: Inference of rain rate profile and path-integrated rain rate by an airborne microwave scatterometer. *Radio Sci.* **20**, 631-642.

(37) _____, _____, H. Masuko, T. Ojima and N. Fugono, 1985: Quantitative measurements of path-integrated rain rate by an airborne microwave radiometer over ocean. *J. Atmos. Ocean. Tech.*, **2**, 285-292.

(38) Meneghini, R., K. Nakamura, C.W. Ulbrich, and D. Atlas, 1989: Experimental tests of methods for the measurement of rainfall rate using an airborne dual-wavelength radar. *J. Atmos. and Ocean. Tech.*, **6**, 637-651.

(39) Meneghini, R. and K. Nakamura, 1988: Some characteristics of the mirror image return in rain.*Tropical Rainfall Measurements*, J.S. Theon and N. Fugono, eds. A. Deepak Publ., Hampton, VA, 235-242.

(40) Weinman, J.A., R. Meneghini and K. Nakamura, 1989: Comparison of rainfall profiles retrieved from dual-frequency radar and from combined radar and passive microwave radiometer. Preprints, *4th Conf. Satellite Meteor. and Oceanog.* San Diego, CA, Amer. Meteor. Soc., 27-30.

(41) Meneghini, R. and K. Nakamura, 1990: Range profiling of the rain rate by an airborne weather radar. *Remote Sens. Environ.*, **31**, 193-209.

(42) Kozu, T., R. Meneghini, W. C. Boncyk, K. Nakamura, and T. T. Wilheit, 1989: Airborne radar and radiometer experiment for quantitative remote measurements of rain, *Proc. IGARSS '89*, Vancouver, Canada, 1499-1502.

(43) Meneghini, R., T. Kozu, H. Kumagai, and W. C. Boncyk, 1990: Analysis of airborne radar and radiometer rain measurements and their relationship to spaceborne observations. *Proc. IGARSS '90*, College Park, MD, 429-432.

(44) Elsberry, R. L., 1989: ONR tropical cyclone motion research initiative: Update on field experiment planning. Technical Report NPS-63-90-002, Naval Postgraduate School, Monterey, CA, 64 pp.

(45) Kumagai, H., R. Meneghini, and T. Kozu, 1991: Multi-parameter airborne rain radar experiment in the North Pacific. Preprints, *25th Conf. Radar Meteorol.*, Paris, Amer. Meteor. Soc., 400-403.

(46) Ulbrich, C.W. and D. Atlas, 1975: The use of radar reflectivity and microwave attenuation to obtain improved measurement of precipitation, Preprints, *16th Conf. Radar Meteorol.*, Houston, TX, Amer. Meteor. Soc., 496-503.

(47) ——— and ———, 1977: A method for measuring precipitation parameters using radar reflectivity and optical extinction, *Ann Telecommun.*, **32**, 415-421.

(48) ——— and ———, 1984: Assessment of the contribution of differential polarization to improved rainfall measurements. *Radio Sci.*, **19**, 49-57.

(49) Goldhirsh, J. and I. Katz, 1974: Estimation of raindrop size distribution using multiple wavelength radar systems. *Radio Sci.*, **9**, 439-446.

(50) ———, 1975: Improved error analysis in estimation of raindrop spectra, rain rate, and liquid water content using multiple wavelength radars. *IEEE Trans. Antennas Propag.*, **AP-24**, 718-720.

CHAPTER 2. PHYSICAL AND THEORETICAL BASES OF RADAR RAINFALL MEASUREMENT

2.1 Rainfall and DSD Parameters

2.1.1 Definitions of meteorological parameters

As a preparation for the discussion of radar rainfall measurements, it is helpful to summarize various radar and meteorological quantities. They include scattering and absorption cross sections of a particle, dielectric constant, size distribution of particles, and various integral rainfall parameters. Table 2-1 lists those parameters and their units used in this thesis. Although the units used here are very common, it should be noted that they are not unique. Care should be given to the difference in the units in comparing the results of this thesis to the results of other papers. More discussions on those parameters follow.

2.1.2 Dielectric constant

Dielectric constant, ε, is a fundamental parameter to characterize the attenuation and scattering properties of hydrometeors. It is often expressed as a value relative to that of free space, ε_0 (= 8.854×10^{-12} F/m). The relative dielectric constant ε_r (= $\varepsilon/\varepsilon_0$) is related to the complex index of refraction, m, by $m^2 = \varepsilon$. The ε_r or m of water and ice can be calculated if the temperature is given. The result by Ray[1] is shown in Table 2-2. For general nonliquid hydrometeors which are composed by water, ice and air, however, ε_r depends also on the mixing situation of the particle. Several formulae have been proposed to calculate the ε_r of such mixed hydrometeors, a discussion of which is found in Meneghini and Kozu[2]. In this thesis, the Wiener's formula[3,4] will be employed to calculate the ε_r of the bright band particles. In Appendix 2-1, an outline of this model to calculate ε_r is described.

2.1.3 Scattering, absorption and attenuation cross sections of a hydrometeor

The scattering, absorption and attenuation (or total) cross sections (σ_s, σ_a, and σ_t, respectively) of a single hydrometeor are dependent on the dielectric constant of a particle, particle size and shape, and the wavelength and polarization of the incident wave. Hydrometeors can be approximated as spherical or deformed (oblate spheroid or Pruppacher-Pitter[5] form) drop models. In most non-polarimetric radar measurements, the assumption of spherical shape may be sufficient[6]. The cross sections of a spherical particle can be calculated with

Table 2-1. Definitions and units of meteorological and radar quantities used in this thesis.

Quantity	Symbol	Definition	Unit
Frequency	f	-	Hz
Wavelength	λ	-	m
Speed of light	c	2.99792×10^8	m/sec
Refractive index	m	$m = m_R - im_I$	- *1
Real part of m	m_R	-	-
Imaginary part of m	m_I	-	-
Dielectric factor	K	$(m^2 - 1)/(m^2 + 2)$	-
Dielectric factor of water	K_w	-	-
Mass density	ρ	-	g/cm^3
Drop diameter	D	-	mm
Scattering cross section	σ_s	-	m^2
Absorption cross section	σ_a	-	m^2
Total cross section	σ_t	$\sigma_t = \sigma_s + \sigma_a$	m^2
Backscattering cross section	σ_b	-	m^2
Drop size distribution (DSD)	$N(D)$	-	mm^{-1}/m^3
Falling velocity	$v(D)$	-	m/sec
nth moment of DSD	M_n	$\int D^n N(D)\, dD$	mm^n/m^3
Radar reflectivity	η	$\int \sigma_b(D) N(D)\, dD$	m^{-1}
Radar reflectivity factor	Z	$\int D^6 N(D)\, dD$	mm^6/m^3
Effective radar reflect. factor	Ze	$10^{18} \lambda^4 \pi^{-5} \lvert K_w \rvert^{-2} \int \sigma_b(D) N(D)\, dD$	mm^6/m^3
Rainfall rate	R	$0.0006\pi \int v(D) D^3 N(D)\, dD$	mm/hour
Attenuation coefficient	k	$4343 \int \sigma_t(D) N(D)\, dD$	dB/km
Liquid water content	W	$\rho\pi/6 \times 10^{-3} \int D^3 N(D)\, dD$	g/m^3
Optical extinction	Σ	$\pi/2 \times 10^{-3} \int D^2 N(D)\, dD$	km^{-1}

*1 "m" is also used for a parameter of gamma dropsize distribution.

Table 2-2. Complex refractive indices of water and ice for several radar frequencies.

Frequency	Temperature	m_R	m_I	$\|K\|^2$
5.33 GHz	30°C	8.576	0.962	0.9249
	20°C	8.650	1.265	0.9279
	10°C	8.625	1.668	0.9307
	0°C	8.423	2.175	0.9332
	0°C (ice)	1.782	.003636	0.1767
10.00 GHz	30°C	8.185	1.649	0.9241
	20°C	8.032	2.059	0.9267
	10°C	7.682	2.507	0.9287
	0°C	7.087	2.907	0.9298
	0°C (ice)	1.781	0.002324	0.1764
13.80 GHz	30°C	7.786	2.066	0.9232
	20°C	7.465	2.462	0.9251
	10°C	6.938	2.815	0.9261
	0°C	6.221	3.034	0.9255
	0°C (ice)	1.781	.001848	0.1764
17.25 GHz	30°C	7.405	2.341	0.9221
	20°C	6.972	2.680	0.9234
	10°C	6.361	2.922	0.9232
	0°C	5.621	3.002	0.9205
	0°C (ice)	1.781	.001576	0.1764
24.15 GHz	30°C	6.684	2.661	0.9193
	20°C	6.133	2.851	0.9187
	10°C	5.482	2.902	0.9154
	0°C	4.791	2.802	0.9076
	0°C (ice)	1.780	.001241	0.1760
34.50 GHz	30°C	5.805	2.799	0.9137
	20°C	5.233	2.803	0.9093
	10°C	4.637	2.685	0.8998
	0°C	4.057	2.464	0.8819
	0°C (ice)	0.1780	.0009626	0.1760

the Mie theory. The description of the Mie theory can be found in a number of text books (e.g. Stratton[7]). Scattering coefficients of deformed drops have been calculated by employing several techniques such as point-matching and least-square fitting methods, spheroidal function expansions methods, and T-matrix methods [8,9]. Since the symmetry axes of falling raindrops are aligned along the vertical direction on average, the spherical particle model may be used for the study of down-looking radar measurement. This hypothesis will be evaluated later in this section.

According to the Mie theory, the scattering, absorption and total cross sections, σ_s, σ_a, and σ_t are given by

$$\sigma_s = \lambda^2/(2\pi) \sum_{n=1}^{\infty} (2n+1) (|a_n|^2 + |b_n|^2) \quad (2.1)$$

$$\sigma_t = -\lambda^2/(2\pi) \sum_{n=1}^{\infty} (2n+1) \mathrm{Re}[a_n + b_n] \quad (2.2)$$

$$\sigma_a = \sigma_t - \sigma_s \quad (2.3)$$

where λ is the wavelength in background medium. The expansion coefficients a_n and b_n are called Mie coefficients, and are expressed in terms of spherical Bessel functions and Hankel functions of the second kind with arguments χ (= $2\pi r/\lambda$, r being the radius of the particle) and the relative complex dielectric constant, ε_r. The a_n and b_n represent the scattered fields arising from the induced magnetic dipoles, quadrupoles, etc. and electric dipoles, quadrupoles, etc., respectively. Similarly, the Mie backscattering cross section, σ_b, is given by

$$\sigma_b = \lambda^2/(4\pi) \left|\sum_{n=1}^{\infty} (-1)^n (2n+1) (a_n - b_n)\right|^2 \quad (2.4)$$

- Rayleigh approximation

Much simplification is possible in the above expressions of σ_s, σ_a, σ_t and σ_b, when the particle size is much smaller than the wavelength λ, which is known as Rayleigh approximation. With this approximation, σ_s, σ_a, σ_t and σ_b are expressed as

$$\sigma_s = 2/3(\pi^5/\lambda^4) D^6 |K|^2 \quad (2.5)$$

$$\sigma_a = (\pi^2/\lambda) D^3 \mathrm{Im}[-K] \quad (2.6)$$

$$\sigma_t = \sigma_s + \sigma_a \quad (2.7)$$

$$\sigma_b = (\pi^5/\lambda^4) D^6 |K|^2 \quad (2.8)$$

with $$K = (\varepsilon_r - 1)/(\varepsilon_r + 2) \quad (2.9)$$

where D (= $2r$) is the diameter of the particle. A criterion of the diameter range where the Rayleigh approximation is valid is $|\sqrt{\varepsilon_r}\chi| < 0.5$ [10]. Eqs.(2.5) through (2.8) state that σ_s and σ_b are proportional to D^6, while σ_a is proportional to D^3 in the Rayleigh region. Because of the difference between the particle size dependences of σ_s and σ_a, σ_a is generally much greater than σ_s (i.e., $\sigma_t \approx \sigma_a$) when $D \ll \lambda$. The dielectric factor, K, for water (hereafter K_w) is later used to define the effective radar reflectivity, Ze:

$$K_w = (\varepsilon_r - 1)/(\varepsilon_r + 2), \quad \text{with } \varepsilon_r \text{ for water.} \quad (2.10)$$

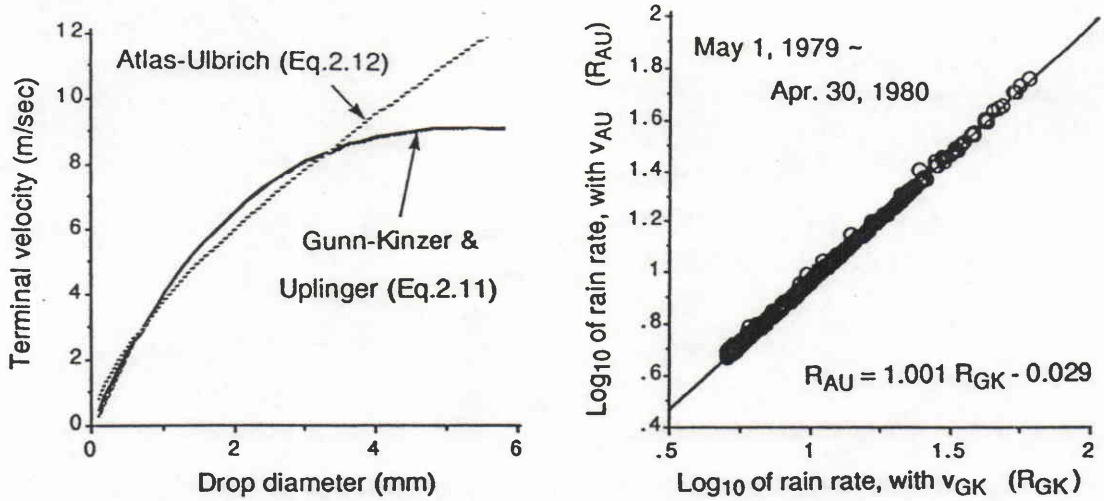

Figure 2-1 Terminal fall velocity of raindrops using different equations, and comparison of rain rates calculated from ground-measured DSDs using terminal velocities $v_{Up}(D)$ and $v_{AU}(D)$.

2.1.4 Terminal fall velocity

Rain rate is among the rain parameters most often required from meteorological, hydrological and cloud physics studies. Since the rain rate is the downward flux of water, it is essential to know the terminal fall velocity of hydrometeors. Gunn and Kinzer[11] data have widely been used as the raindrop terminal velocity on the ground. The height or air density dependence of the terminal velocity can be simply expressed by the factor $(\rho(0)/\rho(z))^{0.4}$, $\rho(z)$ being the air density at height z, multiplied to the Gunn-Kinzer velocity, $v_{GK}(D)$, which was given by Foote and du Toit [12]. It is sometimes convenient to approximate the $v_{GK}(D)$ by an analytic function. In this thesis, we use the following two functions:

$$v_{Up}(D) = 4.854\, D \exp(-0.195D) \tag{2.11}$$

$$v_{AU}(D) = 3.778\, D^{0.67} \tag{2.12}$$

where the velocity is in m/sec and the drop diameter is in millimeters. A comparison of v_{GK}, v_{Up} and v_{AU} is shown in Figure 2-1. The former, proposed by Uplinger[13], gives an excellent fit over the entire drop diameter range up to about 5.5 mm and will be used to calculate the rain rate from measured and theoretical DSDs. The latter, proposed by Atlas and Ulbrich[14], gives less accurate fit than the former; however, we will employ it in making approximate comparative analyses between rain rate and other rain parameters, since with $v_{AU}(D)$ rain rate is expressed as a quantity proportional to the 3.67th moment of DSD. In order to evaluate the validity of $v_{AU}(D)$, rain rates are calculated from DSDs measured on the ground using $v_{AU}(D)$ and $v_{GK}(D)$. The result, also shown in Figure 2-1, indicates that $v_{AU}(D)$ is sufficient for the purpose mentioned above.

2.1.5 Drop size distribution (DSD)

a. Importance of knowledge of DSD

Size distribution of precipitation particles (DSD) is a fundamental precipitation parameter by which all integral rain parameters (IRPs, see section 2.1.6) and relationships among them are characterized. Because the direct radar measurable, radar reflectivity, is approximately proportional to the 6th moment of DSD and different from the other IRPs of interest, the knowledge of DSD is essential to make an accurate radar estimation of IRPs. It is known that DSD is highly variable[15-18]. Examples of such DSD variation are shown in Figure 2-2, which were measured on the ground by a disdrometer (see Chapter 3 for the details). It changes from time-to-time and from one rain event to another. Although there have been numerous studies to understand, to parameterize and to estimate DSD, large uncertainties remain in temporal and spatial DSD variabilities and their dependence on rainfall type and climatological regimes.

b. DSD models

Although natural DSDs are highly variable, three-parameter models such as gamma and lognormal models are known to fit the natural DSDs well. Two-parameter models are less flexible but still provide good fitting to the natural DSD's in a limited domain. They are considered to provide a sufficient accuracy to relate rainfall parameters of practically interest such as radar reflectivity, rain rate, LWC and microwave attenuation[18,19]. The reason is that all of those rain parameters are mainly determined by distributions at intermediate to large drop diameters and therefore variations in distributions at small drops can be neglected.

The DSD model most frequently used to date is the gamma distribution:

$$N(D) = N_0 D^m \exp(-\Lambda D) = N_T \frac{\Lambda^{m+1} D^m}{\Gamma(m+1)} \exp(-\Lambda D) \qquad (2.13)$$

where $[N_0, m, \Lambda]$ or $[N_T, m, \Lambda]$ are parameters of the gamma model. Although N_T is the zeroth moment of the DSD modeled as gamma, we treat it also as a DSD parameter that can be used in place of N_0 [20]. The parameter m is often fixed for simplicity and for making it possible to estimate DSD from dual-parameter radar measurements. The exponential distribution is a special case ($m = 0$) of the gamma distribution and expressed as

$$N(D) = N_0 \exp(-\Lambda D) = N_T \Lambda \exp(-\Lambda D) \qquad (2.14)$$

where $[N_0, \Lambda]$ or $[N_T, \Lambda]$ are parameters of the exponential model.

Another DSD model that is sometimes employed is the lognormal distribution

$$N(D) = \frac{N_T}{\sigma D\sqrt{2\pi}} \exp(-\frac{(\ln D - \mu)^2}{2\sigma^2}) \qquad (2.15)$$

where $[N_T,\mu,\sigma]$ are parameters of the lognormal model. Similar to the m parameter of the gamma model, the parameter σ is often fixed[17,21].

The other problem in the DSD modeling is to characterize the spatial or temporal variation in DSD. For example, the Marshall-Palmer (MP) [22] DSD model

$$N(D) = N_0 \exp(-\Lambda D), \text{ with } N_0 = 8000 \text{ and } \Lambda = 4.1R^{-0.21} \qquad (2.16)$$

assumes that N_0 is constant and Λ is related to rain rate R by a negative power law. Similar DSD models were proposed by Joss et al.[15]:

$N_0 = 1400$ and $\Lambda = 3.0R^{-0.21}$	Joss-Thunderstorm (J-T)
$N_0 = 7000$ and $\Lambda = 4.1R^{-0.21}$	Joss-widespread (J-W)
$N_0 = 30000$ and $\Lambda = 5.7R^{-0.21}$	Joss-Drizzle (J-D).

It has been reported that the MP model fits well to natural DSDs if a large number of DSDs are averaged in spite of the large fluctuation in short term DSDs [18,23]. Since the Z factor or rain rate dependences of the DSD parameters are closely related to the relationships among various rain parameters, it is important to investigate such DSD fluctuation properties. In comparison to the modeling of individual DSD, the number of studies concerning to this problem is relatively small. Although there are many papers concerning the relationships among rainfall parameters (especially Z-R relation) [24,25] and although it is well known that such IRP relations are formed as a result of DSD variation, relatively limited number of papers give a quantitative discussion on the relation between "DSD variation" and the "relation between two rainfall parameters" [26,27]. We will consider this problem in detail and connect to the estimation of DSD parameters using a practically feasible radar system from space.

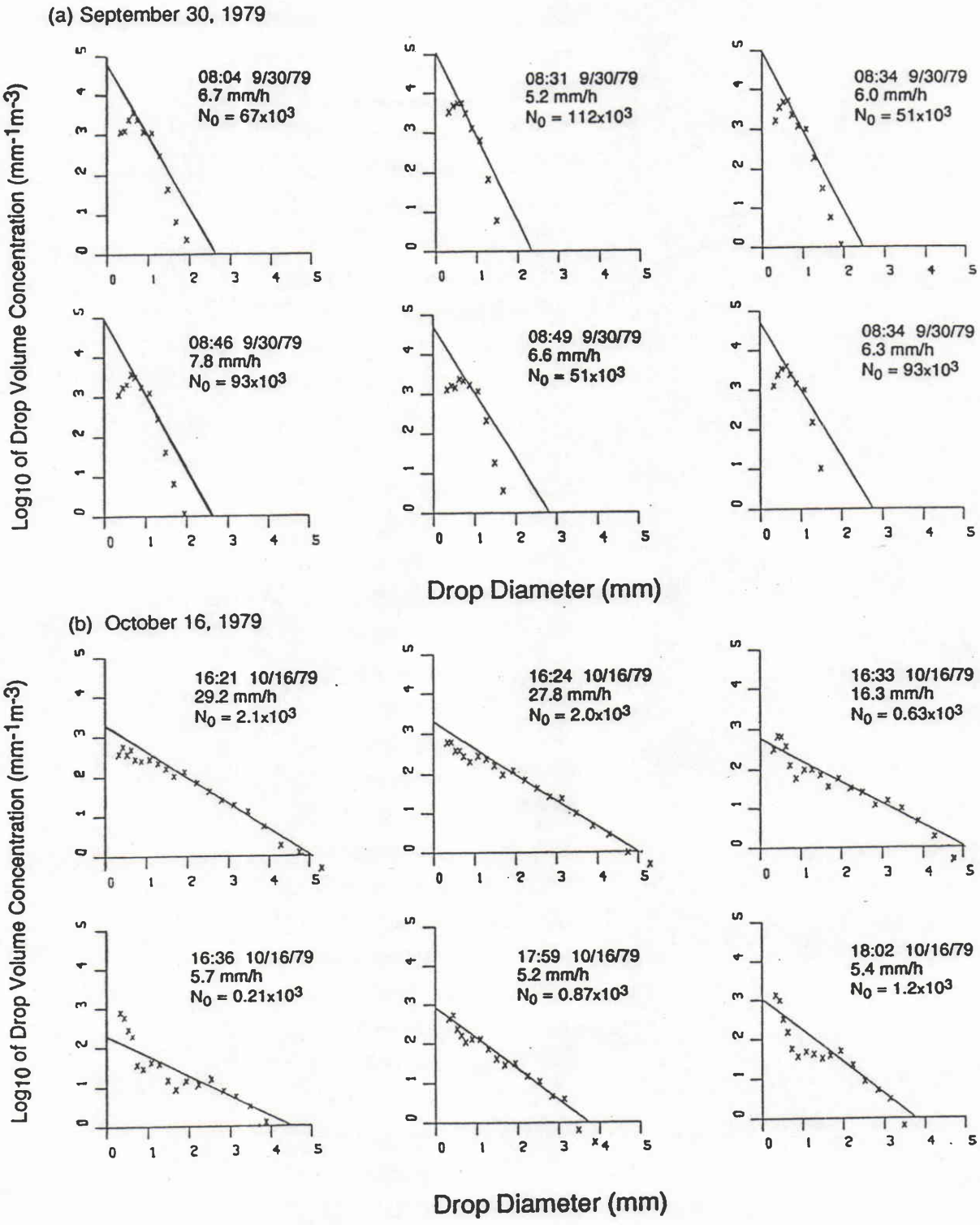

Figure 2-2. Examples of natural DSD measured by a disdrometer (see Chap.3). Solid line represents an exponential model fit using a moment method.

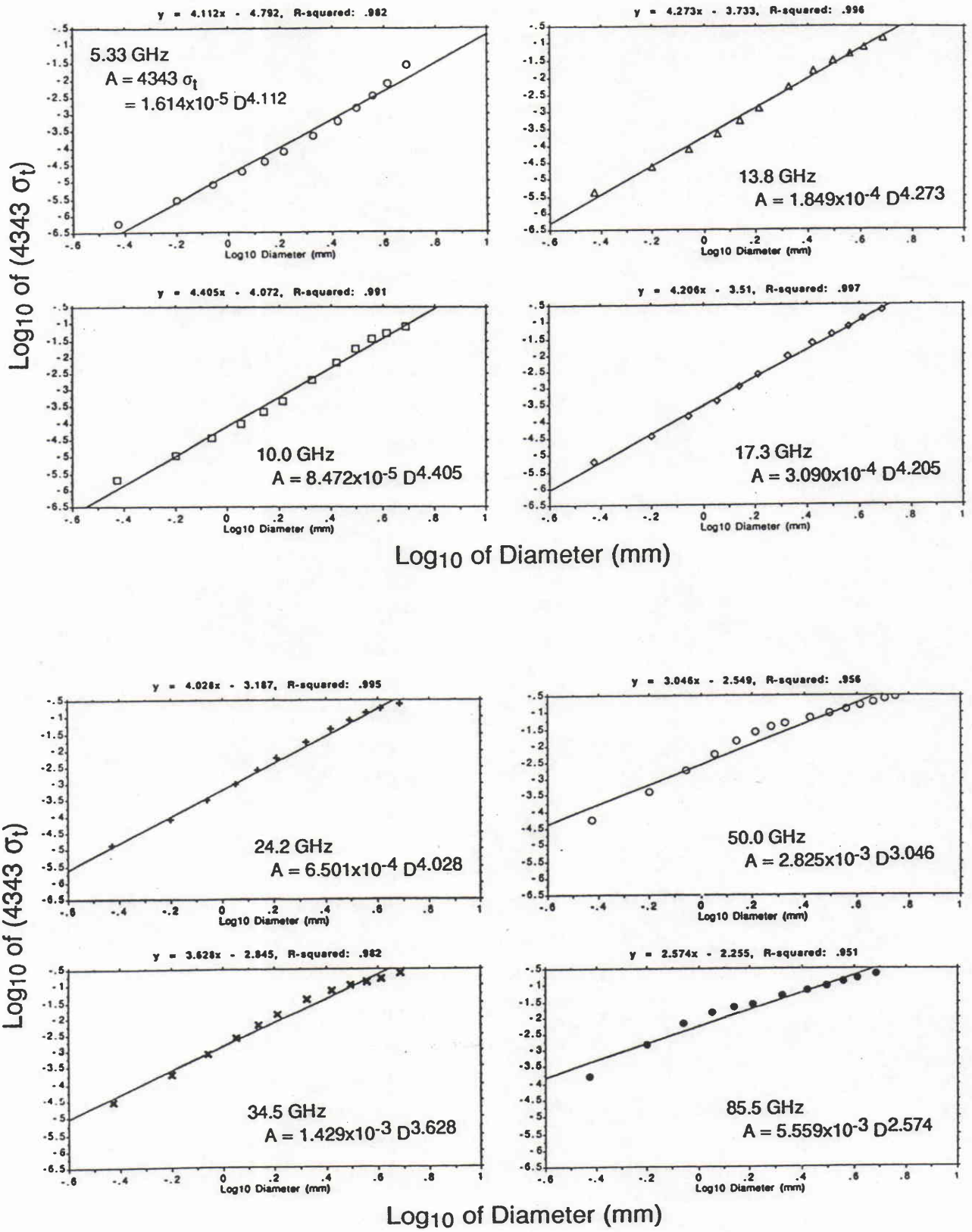

Figure 2-3. Regression results of the relation between logarithms of σ_t and D.
Please note that the exponent shifts with frequency, and that $A = 4343\sigma_t$.

2.1.6 Integral rainfall parameter (IRP)

As shown in Table 2-1, most of the rain parameters of scientists' and communications engineers' interest are defined as the integral of the product of a "kernel", $\kappa(D)$, and DSD, $N(D)$, over the drop diameter, D:

$$\mathrm{IRP} \equiv \int_0^\infty \kappa(D)\, N(D)\, dD. \tag{2.17}$$

Such quantities are called "integral rainfall parameters (IRP). A major task of radar rainfall measurement is to estimate IRPs of interest from IRPs directly obtained from radar measurements. (Note that the IRP can be defined regardless of particle phase even though we call it Integral "Rain" Parameter.) The IRPs most important for the radar rainfall measurement include radar reflectivity factor Z, effective radar reflectivity factor Ze, attenuation coefficient k, rain rate R, and liquid water content W, which are defined in Table 2-1.

For making studies on the IRPs and DSD, it is convenient to approximate the IRPs by the xth moment of DSD, M_x, which is defined by

$$M_x \equiv \int_0^\infty D^x N(D)\, dD \tag{2.18}$$

and expressed as the following equations for gamma and lognormal DSD models

$$M_{x,\mathrm{gamma}} = N_0 \frac{\Gamma(m+x+1)}{\Lambda^{m+x+1}} = N_T \frac{\Gamma(m+x+1)}{\Lambda^x\, \Gamma(m+1)} \tag{2.19a}$$

$$M_{x,\mathrm{lognormal}} = N_T \exp\left(x\mu + \frac{1}{2} x^2 \sigma^2\right) \tag{2.19b}$$

where x may be non-integer. In Table 2-3, such moment approximations are summarized. In the case of the moment approximation of attenuation coefficient, the order of the moment, x, depends on frequency. Around 10 GHz, x takes the maximum value of about 4.5. With decreasing or increasing the frequency, x decreases due to the increasing contribution of σ_a to σ_t at lower frequency and due to the increasing Mie scattering effect at higher frequency. Figure 2-3 shows regression results of the relation between logarithms of σ_t and D at several frequencies, from which the x value is obtained. The x value close to 3.67 at 35 GHz indicates that the attenuation measurement at around this frequency should provide an accurate rain rate estimate.

Table 2-3. Moment approximation of typical IRPs (IRP = $C M_n$).

Integral rain parameter	n	C	Unit	
Radar reflectivity factor, Z	6	1	mm^6/m^3	
Effective radar reflect. factor, Ze	~6	1	mm^6/m^3	
Rainfall rate, R	3.67	$6x3.78\pi x10^{-4}$	mm/hour	*1
Attenuation coefficient, k	3~4.5	4343 C_k	dB/km	*2
Liquid water content, W	3	$\rho\pi/6x10^{-3}$	g/m^3	
Optical extinction, Σ	2	$\pi/2x10^{-3}$	km^{-1}	

*1 See Eq.2.11. *2 $\sigma_t(D) = C_k D^{\nu}$, where $\nu = 3 \sim 4.5$ (dependent on frequency).

2.1.7 Melting layer (Bright band)

The information of thermodynamic phase is essential for accurate rainfall retrievals. The melting layer, at which frozen hydrometeors melt into rain, is very clearly seen by radar in stratiform rain. Because the melting process causes a clear enhancement in radar reflectivity for frequencies approximately less than 20 GHz, the melting layer is often called "bright band"[25]. For convective storms, it is generally difficult to identify where the melting occurs because of the strong updrafts in the cloud unless multi-frequency or polarimetric radars are employed. In this sense, the stratiform rain is easier to be modeled than the convective storms. Examples of radar reflectivity profile for stratiform and convective storm are illustrated in Figure 2-4.

During a stationary stratiform rain, it may be reasonable to assume that the water flux (i.e., rain rate) is constant from the top to the bottom of a storm. This assumption may be extended up to the bright band if water vapor condensation mainly occurs upper the bright band and if evaporation affects little to the flux.

Even with this constraint, there are many parameters characterizing the bright band in terms of scattering and attenuation properties. Those include drop size distribution, falling velocity, particle shape, orientation and dielectric constant. A number of bright band models have been proposed to date[28-32]. Although the shape of melting particle may be highly irregular, it is almost impossible to know the shape of each particle, shape distribution and orientation precisely. As a first approximation, therefore, spherical or spheroidal particle model has been used to calculate the scattering properties.

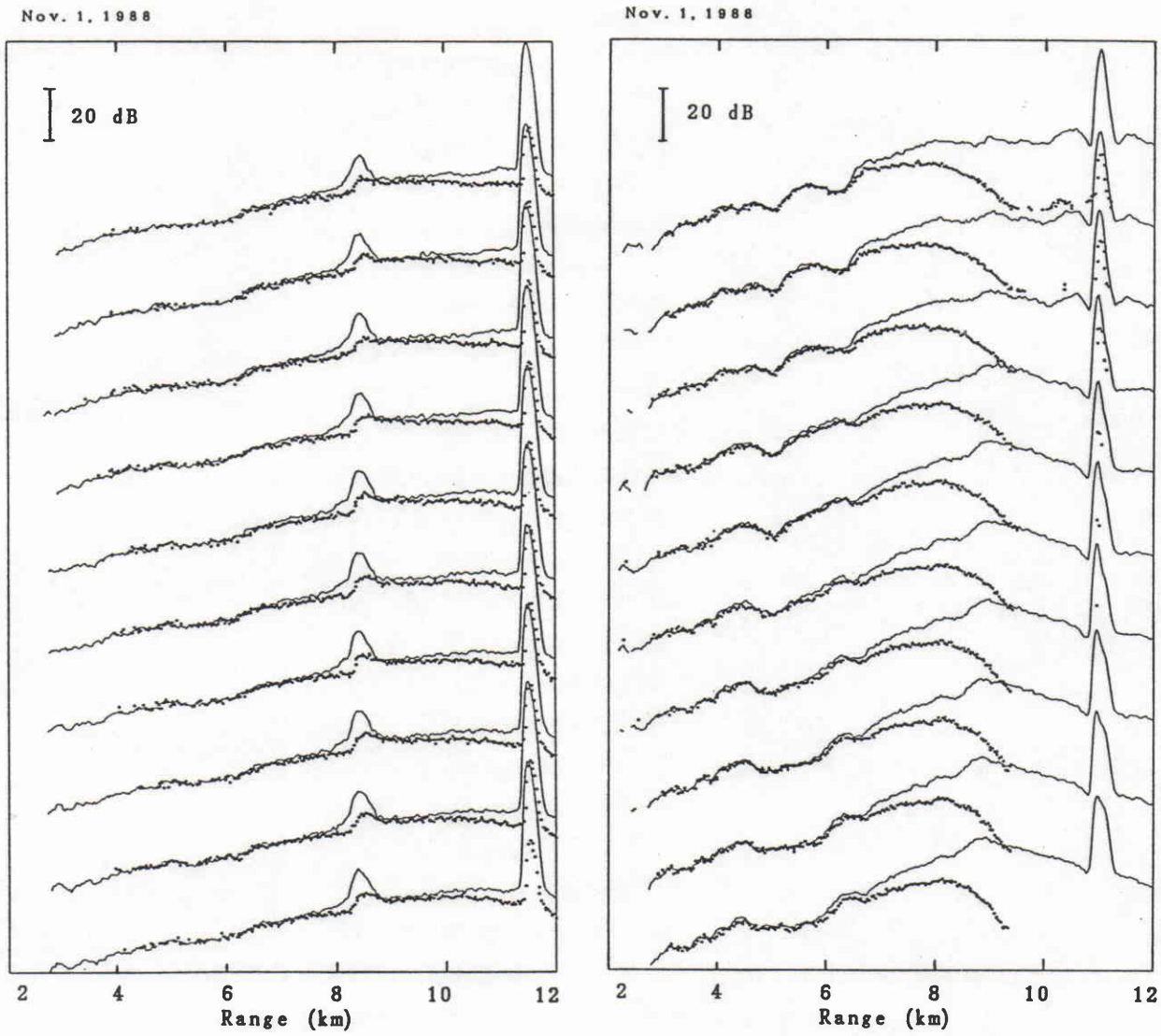

Figure 2-4. Examples of vertical radar reflectivity profile. Left: stratiform, and right: convective. Solid line and heavy dotted line represent X-band (10 GHz) and Ka-band (34.5 GHz) radar reflectivity factors (including attenuation), respectively. The sharp spike at around 11 ~ 11.5 km is the surface return.

Although there are two types of bright band particle model (concentric two-layer sphere and composite dielectrics models), no conclusion has been obtained which is better. In this thesis, we adopt the latter model together with a Noncoalescence/Nonbreakup (N/N) model to estimate the DSD in the bright band. These models have been studied by Awaka et al.[30]. They compared the N/N model with a modified Nishitsuji (M-N) model [4] in terms of the agreement with measured C-band Z factor profiles. Their conclusion is that the M-N model, which is considered to take physical processes in the bright band into account empirically, appears to be superior to the N/N model in the upper portion of the bright band. For the lower region of the bright band, however, the difference between the two models are small and the both models show good agreement with the measured profile. Since the major issue on the bright band in this thesis is to estimate the attenuation caused by the bright band that would occur at the lower portion of the bright band, for simplicity, we adopt the N/N model for the retrieval of bright band together with a composite dielectrics model for individual particle. The outline of the composite dielectrics model and the N/N model is outlined in Appendix 2-1.

2.1.8 Storm structure

In order to develop rainfall retrieval algorithms using a limited number of remote sensing data, the use of proper storm structure model is required and it should be as simple as possible while keeping a reasonable representation of microphysical phenomena. For example, vertical storm models used for passive microwave rainfall retrieval to date consist of one uniform rain region plus one or several ice and ice+rain mixing layers. Melting layer or bright band that is a distinct radar precipitation signature has been omitted in the passive rainfall sensing to simplify radiative transfer computations [33,34].

The radar, which has a capability of profiling, does not require such a simplification for vertical structure model. Yet, the knowledge of the storm structure is required to understand the radar signatures and estimate various precipitation parameters adequately, and to evaluate the effect of non-uniform beam filling on the accuracy of the algorithm. The modeling of stratiform type rain is fairly easy because of the existence of clear bright band; rainfall is horizontally uniform and understanding the vertical structure would suffice for most purposes. On the other hand, convective type storms are more difficult to model because the strong updraft causes the mixing of different hydrometeors such as supercooled water drop, ice and melting particles, and because the horizontal variability in rainfall is much larger than that of the stratiform rain. In Chapter 7, we will use simplified vertical rain structure models to

estimate path-integrated attenuation from Z-factor profile.

More generally, the modeling of a storm can be recognized as a parameterization of three dimensional (3-D) storm structure. Although individual storm structure is far more complicated than can be modeled by a reasonable number of parameters, at least statistically, extensive simplification should be possible. Several simplified 3-D models have been proposed in the field of microwave propagation studies and passive microwave rainfall retrievals. They have uniform or simply stratified vertical structures and rotationally symmetric[35], or rectangular horizontal structures[36]. Although they should be adequate for approximate estimation of the effect of non-uniform beam filling and for making radiative transfer models, more precise models depending on the type of storm system (tropical convection, wide spread rain associated with warm front, etc.) would be required for more realistic simulation of the spaceborne or airborne radar measurements.

2.2 Basic Theory of Radar Rainfall Measurement

2.2.1 Scattering and attenuation of radiowaves by hydrometeors

In section 2.1.3, we have considered the scattering and attenuation by a single hydrometeor. In practice, there are many such particles having various sizes and distributed randomly in space. Because of the randomness of the phases of scattered waves form particles, total scattered power is the incoherent sum of powers from individual particles. Therefore, the radar equation that relates the radar received power from the hydrometeors in a radar resolution volume can be expressed as a sum of the received power derived from the radar equation for a single hydrometeor. Although the meteorological radar equation may have a variety of forms depending on the radar polarization states, scattering geometry, etc.[2], we summarize here only the radar equations relevant to this study. The radar and scattering conditions we consider here are: monostatic radar, linear and copolarized signal, and the presence of rain attenuation to and from the radar resolution volume of interest. In such cases, the radar equation expressed as an integral of powers from the infinitesimal volume of $d\Omega dr$, Ω and r being solid angle and range, respectively, is given by

$$P_r(t) = \frac{\lambda^2 P_t}{(4\pi)^3} \int_V \frac{G^2(\Omega)\, \eta(r,\Omega)\, e^{-2\gamma(r,\Omega)}}{r^2} |u(t - 2r/c)|^2 \, d\Omega \, dr \qquad (2.20)$$

where λ is the radar wavelength, P_t is the peak transmit power, G is the one-way antenna

gain, $u(t)$ is the complex envelope of the transmitted pulse normalized to have the peak amplitude of unity. η and γ are radar reflectivity and optical depth of rain, respectively, which are given by

$$\eta = \int_0^\infty \sigma_b(D)\, N(D)\, dD = \pi^5 |K_w|^2 \lambda^{-4} Ze \tag{2.21}$$

$$\gamma(r) = 0.1 \ln 10 \int_0^r k(s)\, ds \tag{2.22}$$

where the definition of the quantities used in Eqs.(2.21) and (2.22) are given in Table 2-1.

The following approximations hold for most cases: (1) Most of the transmitted energy is concentrated in a narrow main beam so that the radar reflectivity and rain attenuation are independent of angular variations; (2) Antenna gain pattern is given by a two-dimensional Gaussian function and sidelobe contribution to the received power can be neglected. With these approximations, Eq.2.20 becomes

$$P_r(t) = \frac{C\,|K_w|^2}{r^2} Ze \exp\left[-0.2 \ln 10 \int_0^r k(s)\, ds\right] = \frac{C\,|K_w|^2}{r^2} Zm \tag{2.23}$$

with

$$C = \frac{\pi^3 P_t G_0^2 \theta_B^2 c\tau}{1024 \ln 2\, \lambda^2} \tag{2.24}$$

where G_0 is the peak antenna gain, θ_B is the half-power antenna beamwidth, c is the speed of light, and τ is the transmitted pulse width. For convenience, "apparent" or "measured" effective radar reflectivity factor, Zm, is also introduced. Zm is recognized as an estimate of Ze using a radar equation neglecting rain attenuation. Since Zm can be estimated with the radar system parameters only, it is convenient to begin the rain parameter estimation with this quantity and we will frequently use it in this thesis.

- Difference in Ze values between spherical and deformed drop models

Since the present study concerns the radar observation using near-nadir incidence angles at which there is little polarization difference in scattering properties, it may be sufficient to use the spherical model. The Mie theory may then be used to calculate all scattering and attenuation cross sections, which makes the calculation much easier than that for the deformed drop models. However, it may be required to check the difference between the spherical and

deformed drops having the same volume, because the effective diameter of the deformed drop is larger than that of the spherical drop when the drop is seen down or upward. For this purpose, comparisons are made for *Ze* factors calculated from the spherical and deformed (Pruppacher-Pitter) drops. For the calculation of the deformed drop case, we use the result from Oguchi's point-matching-and-least-squares method[37], (M. Satake, private communication). Since *Ze* is approximately proportional to the 6th moment and put the largest weight on the large drops among the IRPs of interest, it should be sufficient to check the difference in *Ze*. The result is shown in Figure 2-5 for 10 GHz and 35 GHz which are used in the airborne radar system we will employ later in this thesis. It is found that the differences in *Ze* factors (in dB unit) increase with rain rate to some extent depending on frequency and DSD. It appears, however, that the difference is minor in comparison to the large variation in DSD that causes large fluctuation in *Ze-R* and *k-Ze* relations, and that it can approximately be treated as a constant bias of several tenth of decibels.

Based on the above consideration, we use the spherical drop model both for raindrop and bright band particles.

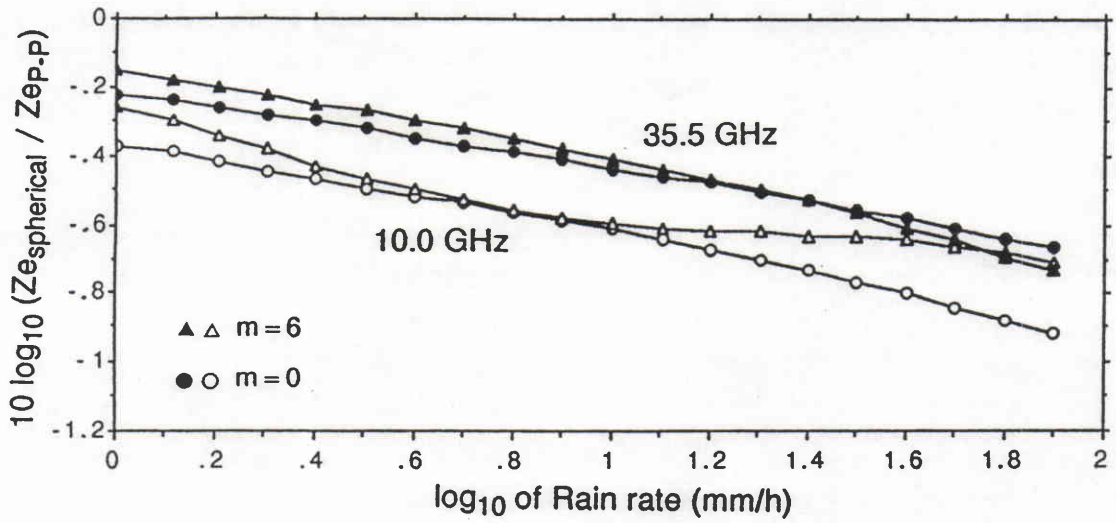

Figure 2-5 Difference in *Ze* factors of the spherical drop model and the deformed drop model at 10 GHz and 35.5 GHz assuming the two-parameter gamma DSD models given in Table 4-2, with $m = 0$ and $m = 6$.

2.2.2 Estimation of mean received power and radar reflectivity

Since the hydrometeors in a radar resolution volume are randomly distributed and fluctuating randomly, the radar precipitation return shows large fading due to the interference among return signals from each scatterer. The quantity that should be obtained by a radar precipitation measurement is the radar received power, P_r, that is defined by the radar equation described above; the sum of received powers from individual scatterers. The most common method to estimate P_r is to use the average of the fluctuating instantaneous received signal level. For the estimation, some assumptions are usually employed: (1) The fluctuating return signal is ergodic so that both ensemble and time averaging can be used; and (2) many small scatterers are randomly distributed in a resolution volume which is much larger in size than the radar wavelength, so that the phase of the composite return signal is uniformly distributed over 0 to 2π and the amplitude is Rayleigh distributed.

It follows from the assumption (2) that the instantaneous return power, P, is exponentially distributed; i.e. the probability density function (pdf) of P, $p(P)$, is given by

$$p(P) = P_r^{-1} \exp(-P/P_r). \tag{2.25}$$

The exponential pdf has the standard deviation equal to the mean value P_r and therefore the estimation of P_r from a single measurement suffers from a large error. In order to reduce the estimation error, many samples statistically independent should be averaged. The averaging is made after the detection of IF signal. The pdf of the averaged video signal depends on the type of detection. For a square-law detection, the pdf of the average of N independent video signals, $p_N(\xi)$, can be written in the form of the χ-squared distribution of $2N$ degrees of freedom[38]:

$$p_N(\xi) = \frac{N^N \xi^{N-1}}{P_r^N (N-1)!} \exp(-N\xi/P_r), \qquad \xi = N^{-1} \sum_{i=1}^{N} P_i \tag{2.26}$$

so that the expectation ($E(\cdot)$) and variance ($Var(\cdot)$) of ξ are P_r and P_r^2/N, respectively.

For the logarithmic detection that is frequently employed to increase the dynamic range, the pdf of the average of $\log_{10}(P/P_r)$, $p_{LN}(\zeta)$, is approximated by[39]

$$p_{LN}(\zeta) = \frac{aN[N(b - a)\zeta]^{3N-1}}{(3N-1)!} \exp[-N(b - a\zeta)], \quad \zeta = N^{-1}\sum_{i=1}^{N} \log(P_i/P_r) \qquad (2.27)$$

where a = 3.13, b = 2.215. It is shown that E(ζ) is about -0.25; i.e., the mean of log-converted power is 2.5 dB smaller than the log of true mean, P_r. Thus, a correction of 2.5 dB is needed in the radar equation when logarithmic detection and averaging are employed. Whereas, the standard deviation of ζ is approximated by $0.557/\sqrt{N}$ [40].

2.3 Rainfall and DSD Parameter Estimation

2.3.1 General discussion

The concept of "rainfall remote sensing", which is to estimate various rainfall parameters of interest from remote sensing techniques, is shown in Figure 2-6. The rainfall parameters to be estimated include rain rate, LWC, microwave attenuation, storm height, horizontal storm area, etc. The rain parameters to be measured include radar reflectivity, microwave/millimeter wave attenuation and brightness temperatures, differential Ze (Z_{DR}), differential phase shift, etc. For the estimation, it is common to model rainfall scene such as storm structure, DSDs (rain, bright band, and snow regions), fall velocity, etc. Techniques

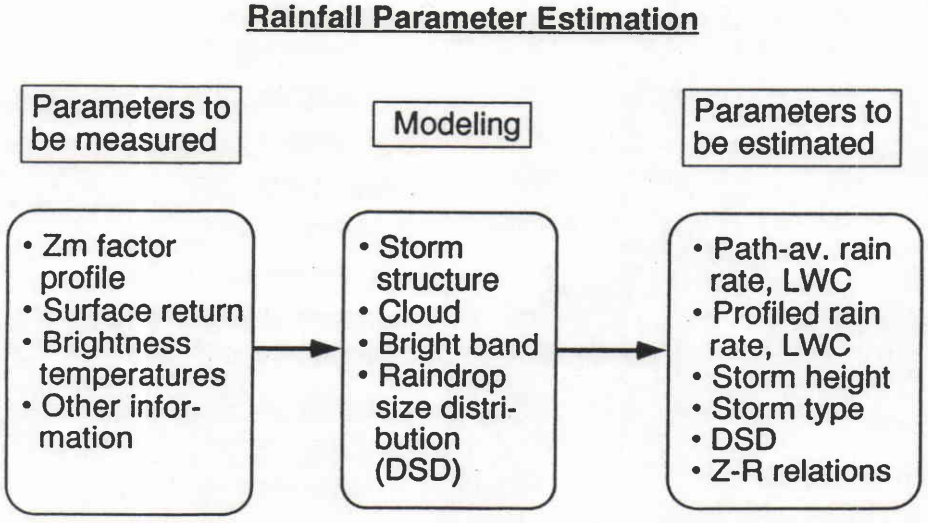

Figure 2-6 Concept of rain parameter estimation by means of remote sensing techniques.

to be employed are closely related to the requirements such as accuracy and spatial/temporal resolutions. For example, if only rainfall or rain rate statistics for a long period (e.g. a month) or a wide area are required, statistical properties of rainfall can be utilized to estimation techniques, which should reduce the difficulty in comparison to the estimation of instantaneous rain rate profile[41,42].

As can be seen from Table 1-2, there is a variety of requirements ranging from one month and 500 km to about a half an hour and several kilometers. In the case of radar measurements, it is the most basic problem to estimate rainfall parameters in a radar resolution volume which is approximately several hundred meters in range and several kilometers in horizontal dimension. Development of rainfall parameter estimation techniques with fine temporal/spatial resolutions is important, because the fine resolution rainfall mapping is a basis to understand large scale rainfall statistical properties and is essential for various climatological studies, short range weather forecast, and other cloud/rainfall microphysics. In this thesis, therefore, emphasis is given to the rainfall parameter estimation with high spatial/temporal resolution.

In the following, rainfall and DSD parameter estimation methods are classified in terms of the number of measurable rain parameters; single, dual and multi-parameter measurements. Methods to estimate rain rate by spaceborne radar measurements are also reviewed briefly and classified in this manner.

2.3.2 Single-parameter (SP) measurements

The conventional way to estimate rain rate and LWC, W, is to use empirical relationships between Z and R and between Z and W. Such methods are regarded as Single-Parameter (SP) measurements. In general, the SP measurement can be defined as estimating IRPs from a "single" IRP. Because of the difference in the weighting functions, the relationships between Z and other IRPs depend on DSD (see Figure 2-7). From the DSD parameter estimation point of view, the SP measurement has an ability to estimate only one DSD parameter. Since at least two parameters are required to express reasonably the natural DSD, it is anticipated that the SP measurement has a limited capability to estimate IRPs. If one can measure an IRP that has a kernel close to that of the IRPs to be estimated, estimating the two DSD parameters is not so essential to obtain sufficient accuracy; e.g. estimating rain rate from Ka-band ($\approx$ 35 GHz) attenuation[14]. However, such measurement can not always be accomplished.

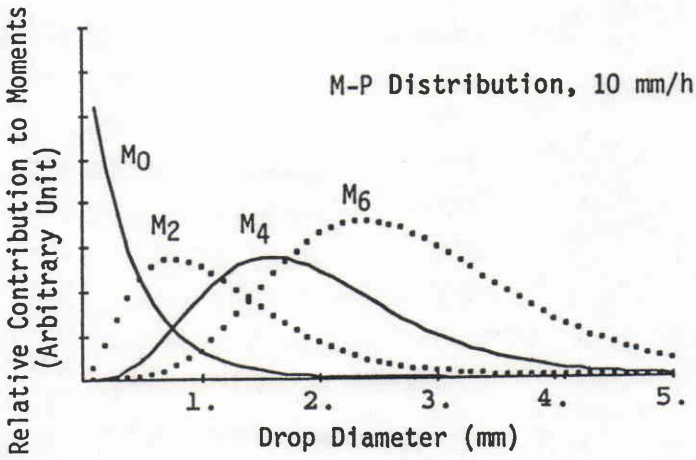

Figure 2-7 Distributions (weighting functions) for several moments of DSD.

2.3.3 Dual-parameter (DP) and multi-parameter measurements

The terms "dual-parameter" and "multi-parameter" have been used in various measurement configurations. For example, Doviak and Zrnic[43] describe the combination of a ground-based radar and raingage(s) set up far from the radar as one of the dual-parameter measurements. Atlas et al.[19], Rogers[44] and Hall[45] review various methods including dual-frequency, dual-polarization, Doppler, path-integrated microwave or optical attenuation and radiometry. In short, adding another measurement other than the radar reflectivity may be called "dual-parameter measurement". In this thesis, however, the terminology on the single-, dual- and multi-parameter measurements is redefined from the DSD parameter estimation (for a given spatial or temporal resolution) point of view, which is recognized as a narrow-sense definition and will make the discussion of the methods clear.

The basic concept (the narrow sense) of dual-parameter (DP) and multi-parameter rain measurements have been explored by Ulbrich and Atlas[19]. The terms "dual" and "multi" correspond to the number of "independent" IRPs to be measured. From such multiple measurements, DSD parameters can be estimated. Such estimation process is known as "inversion technique", and there are many applications such as retrievals of temperature profile from microwave radiometers around O_2 absorption line, of cloud dropsize spectra from multi-wavelengths/incidence angle lider measurements. For DSD estimation, Furuhama and Ihara[46] succeeded to estimate path-averaged DSD from multi-frequency attenuation measurements. For those methods, several inversion techniques such as Phillips-Twomey method (PTM) and Backus-Gilbert method (BGM) may be applied[47]. Those techniques have been employed to stabilize the result of the inversion because the inversions mentioned above are so-called "ill-

posed" problem. Differences between the above applications and the multi-parameter measurements using the radar are that the latter is not necessarily "ill-posed", and that the number of measurable independent rain parameters is very limited. Because of these facts in the dual- and multi-parameter radar measurements, the usual way to make the inversion is to solve simultaneous equations analytically or numerically. Of course, it is necessary to employ some averaging scheme in order to avoid a noisy result in the DSD estimation. The dual-polarization radar combining Ze and Z_{DR} [19,43-45,48,49] and the dual-frequency method studied by Goldhirsh and Katz[2,43,50] are typical examples of the DP measurement.

2.3.4 Semi dual-parameter measurement

In this thesis, a new concept, "semi" dual-parameter (SDP) measurement will be defined to generalize the concept of SP and DP measurements in terms of the resolutions of measurable IRPs and those of the DSD parameters to be estimated. The SDP measurement is defined as DP measurements in which one of the rain parameters to be measured has a spatial or temporal resolution coarser than that required. Various methods to improve the estimation accuracy of the Z-R method can be classified as SDP measurements. For example, the calibration of Z-factor-derived rain rate by comparing with rain gage data is an SDP measurement in which the rain gage data has a resolution much coarser than that of the Z-factor measurement. The adjustment of Z-R relation for each rain event basis may be an SDP measurement in which a rain parameter is estimated with the resolution of a storm so as to determine the Z-R relation. Similarly, most of the "dual" parameter measurements proposed for spaceborne radar measurements to date, briefly described in 2.3.7 and 2.3.8, are considered of this type.

2.3.5 Z-R method

The simplest way to estimate rain rate from Z-factor measurement would be to use an empirical relationship between Z and R, Z-R relation. It may be possible to argue that the history of radar meteorology is almost equivalent to the history to establish proper Z-R relations. Apart from various error sources affecting Z and R measurements, the estimation of R from Z is recognized as the estimation of 3.67th moment from 6th moment of DSD. Because of the high variability in DSD, it is impossible to fix the Z-R relation. Figure 2-8 shows typical power-law Z-R relationships reported by many researchers[51], which are also summarized by Battan[25]. We should note that, although most of the Z-R relations are of power-law, a single

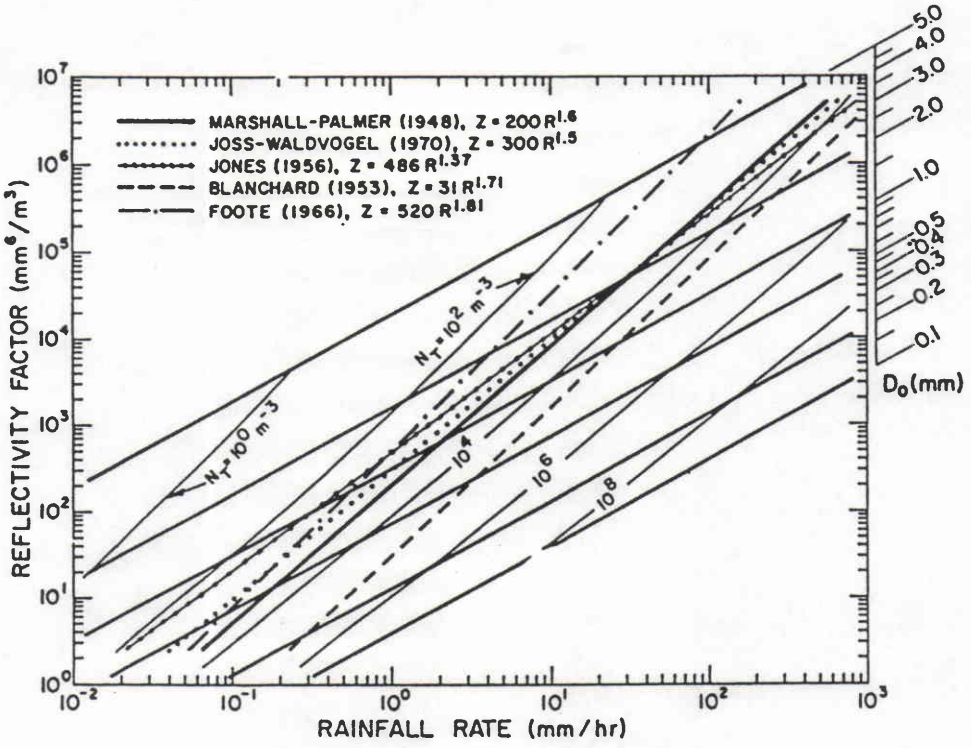

Figure 2-8. A comprehensive plots of Z-R relationships on a rain-parameter diagram [51].

power-law relation may not cover a full range of rain rate. The other uncertainty is the spatial and temporal variability in *Z-R* relation, although the variability should be much more moderate than that of DSD itself because a single *Z-R* relation allows a DSD parameter to vary.

As a result of numerous studies to establish proper *Z-R* relations, it appears that the adjustment of *Z-R* relations based on rain type, synoptic conditions, and climatological regimes can reduce the estimation error to some extent [24]. Even with such adjustment, instantaneous error can exceed ±10 dB. Major topics that have been argued in recent years include: (1) Climatological tuning of *Z-R* relationship — a standard linear regression of logarithms of *Z* and *R* may not be adequate and cumulative distribution matching schemes may improve the accuracy[52,53]; (2) linear *Z-R* relations have been measured in steady tropical rainfall[54,55], although measurements against this finding are also reported[56]. In short, the conventional Z-R method still need to be studied and refined because the improvement of this method relies heavily upon the information of detailed DSD and rainfall properties.

Although there are several problems mentioned above, it has the advantages of simplicity, range-profiling capability, large dynamic range, and the ability to work independent of background (both over land and ocean).

2.3.6 Surface reference target (SRT) method

The SRT method, a method to estimate path attenuation by using surface return as a reference, was first proposed by Meneghini et al.[57] and has been recognized as a method that has a potential to improve the spaceborne radar rainfall measurement accuracy to great extent; by using this method alone or by combining it with other methods[58-63]. The main reason is that this method can provide a rain rate estimate less sensitive to DSD variation than Z-R method. The second reason is that the path-integrated attenuation estimated from this method can be combined with the *Z*-factor profile to improve the range-profiling accuracy as described below. The derivation of path-integrated attenuation begins with a radar equation relating the surface return power P_1 to other parameters in the presence of rain (the subscript 1 denotes the quantities at the measurement in the presence of rain):

$$P_1 = C_1 r_1^{-2} \sigma^0_1 A_{a,1} A_r \tag{2.28}$$

where C is the radar constant, r is the range, and A_r and A_a represent path-integrated attenuation due to rain and other factors, respectively. The constant C may vary depending on the radar type and observation parameters. The problem is to estimate A_r from the measurement of P_1. One way is to measure a received power at an adjacent rain-free area or at the same area as the raining region but before or after the raining, P_2, which is given by

$$P_2 = C_2 r_2^{-2} \sigma^0_2 A_{a,2}. \tag{2.29}$$

Then, taking the ratio of P_1 to P_2 gives

$$P_1/P_2 = (C_1/C_2)\,(r_2/r_1)^2\,(\sigma^0_1/\sigma^0_2)\,(A_{a,1}/A_{a,2})\,A_r. \tag{2.30}$$

The radar constant C is usually constant except for some variation in transmit power and receiver gain which may be monitored, the range r can be measured accurately enough, and A_a may be steady enough or negligibly small in comparison to A_r. If one can assume that σ^0_2 is the same as σ^0_1 or the ratio is known, therefore, path-integrated rain attenuation A_r can be calculated from Eq.2.30. It is clear from the above discussion that this method requires only relative radar calibration and that σ^0 field should be homogeneous in space or steady in time. The latter also suggests that this method works fine for measurements over ocean with small incidence angles at which wind speed and direction dependence of σ^0 is relatively small[64]. Remaining uncertainties in this method include the contribution of bright band attenuation to the total attenuation and the effects of raindrop striking the water surface[65-66].

A dual-frequency version of the SRT method (DSRT method) has also been proposed by which a differential path attenuation can be estimated by taking the ratio of received powers of two different frequencies. The DSRT method has the advantage that the accuracy in attenuation estimate can be improved in proportion to the degree of correlation between σ^0s at the two frequencies [67].

2.3.7 Range profiling methods for attenuating-frequency radar

The term "range profiling" means that rain rate or other rain parameters are to be estimated as a function of range, perhaps with a range resolution within several hundreds of meters. The Z-R method can serve as a range profiling method when no rain attenuation exists. In heavy rainfall, however, the profile derived from the Z-R method would seriously underestimate the rain rate unless some attenuation correction is applied. Several methods have been proposed to improve the attenuation correction accuracy.

A. Hitschfeld and Bordan (H-B) solution

If we can apply a single k-Ze relation, $k = \alpha Ze^{\beta}$, for a path, the attenuating radar equation, Eq.2.23, can be analytically solved for Ze as follows [68,69].

$$Ze(r) = Zm(r) \left[1 - 0.2 \ln 10 \, \beta \int_0^r \alpha \, Zm(s)^{\beta} \, ds \right]^{-1/\beta}. \qquad (2.31)$$

This is known as the Hitschfeld-Bordan[68] (H-B) solution. This exact solution, however, tends to be very unstable when it is applied to cases of moderate to large attenuation because in such cases errors in k-Ze relation and radar constants are amplified significantly to cause very erroneous solutions. Hitschfeld and Bordan[68] suggested that the error should be reduced by using a reference rain rate constraint farther deep in the storm.

B. H-B solution with path-attenuation constraint

The constraint with rain gage data can be replaced by a path-integrated attenuation to stabilize the solution to the attenuating radar equation as proposed by several researchers [57,62,70-72]. There are some variations in the approaches taken to derive the rain rate and attenuation profiles; however, the basic concepts can be summarized in the following two points: (1) An "initial" value at the entrance of a storm (received power data without attenuation), or a "final" value at the range gate just above the surface (the 2-way path-attenuation up to the range gate can be derived from the surface return) has to be used. While

the former condition is the same as the H-B solution, the latter provides much more stable solution than the former[62]. (2) The path-integrated attenuation constrains the path-integrated quantities derived from the *Z*-factor profile. A problem is that the attenuation at the bright band or other hydrometeors aloft, at which *k-Ze* relations are not as clearly described as at rain region, has to be taken into account.

C. Differential received power profile with path-attenuation constraint

Instead of *Z*-factor profile itself, Fujita[61] proposed to employ the ratio between received powers at two adjacent range gates. Assuming power-law *Ze-R* and *k-R* relations, we obtain a set of n-1 equations that relates the received powers and rain rates at the two range gates. The path-integrated rain rate derived from the SRT method or microwave radiometers is then used to derive the rain rate profile of n range gates.

D. Problems in the methods B and C

Range-profiling methods described in *B* and *C* have advantages that the instability in the original H-B solution can be solved. The other advantage is that the accuracy in rain rate estimation can be improved through the use of attenuation having higher correlation with rain rate than *Z*. They essentially require only relative radar calibration because a path-attenuation derived from the SRT method or from microwave radiometry is used as a reference. However, these methods also have several problems:

(1) Since they rely on the DSD insensitivity of rainrate-attenuation relationships, estimation of rain parameters other than rain rate may have larger errors; e.g. estimating LWC.

(2) It may be difficult to use those methods over land and over ocean with large ($\gtrsim$10°) incidence angles because of the difficulty to apply the SRT method.

(3) The non-uniformity in rainfall over the cross-beam FOV causes errors in estimating rain rate and other rain parameters. It has been shown that the effects of the non-uniformity is more serious in the SRT method than in the Z-R method[73-75]. Thus, the applicability of these methods is questionable for storms having a large non-uniformity (e.g. storm edge).

2.3.8 DSD estimation methods

If we can estimate DSDs for each radar resolution volume, it would provide an "ideal" remote sensing data because the DSD is a fundamental rainfall parameter to determine IRPs of interest. However, it is very difficult to estimate the DSD profile precisely by remote sensing techniques.

In spite of the extensive work by Ulbrich and Atlas[19], little experimental work has been conducted for estimating DSD profile except for the dual-polarization radar studies. The difficulty of using dual-frequency radars for DSD estimation was addressed by Goldhirsh and Katz[50,76]. They assumed radars operating at (S and X bands), (S and K bands), and (X and K bands) to measure (*Ze* and X-band attenuation), (*Ze* and K-band attenuation), and (X and K-band attenuations), respectively, with the range resolution of 1 km. The radar reflectivity should be uniform within this resolution to measure the attenuation from the decrease in range-normalized received power. Although they conclude that an (S, K band) system may have an acceptable accuracy, the above assumptions required for this method are not always satisfied. The fundamental difficulty in this method is to measure an attenuation with a fairly high resolution of 1 km or so, and therefore this type of dual-parameter radar measurements to estimate DSD has not been considered as a practical system until now.

The DSD estimation method we propose in this thesis is based on the following facts:

(1) The original dual-frequency method tries to estimate the DSD independently for each resolution (~ 1 km or less); however, it may be reasonable that DSD is correlated to some extent in space so that estimating DSD with such a high resolution is not necessarily required.

(2) The combination of low resolution (path-integrated) *Z* factor and attenuation measurements can be employed to estimate a path-averaged DSD, if *Z* factor is measured without attenuation. However, such path-averaged DSD is not sufficient for profiling of rain parameters.

(3) A reasonable resolution in the DSD estimation would lie between (1) and (2); i.e. one of the DSD parameters varies with range gate but the other one is constant over the path. The parameters of such a "two-scale" DSD model can be estimated from the combination of a high resolution *Z*-factor and a low resolution attenuation measurements that has been used to improve the rain rate profiling as mentioned above.

This two-scale model approach is expected to provide useful DSD information without imposing strict radar system performance. In this sense, this method can be recognized as an extension of the range profiling methods studied by several researchers for spaceborne radars toward the original concept of DP measurement to estimate the DSD parameters[19,51]. The study of spatial and temporal DSD fluctuation properties is therefore important for developing a method to estimate the parameters of the two-scale DSD model.

2.3.9 Mirror image method

Meneghini and Atlas[77] proposed to utilize the "mirror" image of rain echo to derive a 4-way path-attenuation. The advantage of this method is the increased sensitivity for light rain and a potential to remove the unknown surface σ^0 from the algorithm by forming the ratio of direct to mirror image returns. Tests have been conducted using the data from the CRL/NASA joint aircraft experiment[78]. Although the test results are generally encouraging, it is premature to judge if this method is feasible or not. It may provide another tool to make an SDP measurement from space.

Appendix 2-1 Bright Band Model

1. Composite Dielectrics Model

The bright band model used for this thesis is outlined below referring to Awaka et al[30]. As a first step, a composite dielectrics model is used to calculate the dielectric constant of the bright band particle. We assume that bright band particle (snowflake) is composed of a uniform mixture of water, ice and air. Dielectric constants of water, ice, air (ε_w, ε_i, and ε_a, respectively) are related to the dielectric constant of their mixture, i.e. snow, (ε_s) with

$$\frac{\varepsilon_s - 1}{\varepsilon_s + U} = P_w \frac{\varepsilon_w - 1}{\varepsilon_w + U} + P_i \frac{\varepsilon_i - 1}{\varepsilon_i + U} + P_a \frac{\varepsilon_a - 1}{\varepsilon_a + U} \qquad (2.A1)$$

where U is a form factor, and P_w, P_i, and P_a are fractional volume contents of water, ice and air, respectively. By definition, $P_w + P_i + P_a = 1$. Also, letting ρ_w, ρ_i, and ρ_a be the density of water, ice and air, respectively, the density of snow, ρ_s, can be written

$$\rho_s = \rho_w P_w + \rho_i P_i + \rho_a P_a. \qquad (2.A2)$$

Noting that $\rho_w \approx 1$ g/cm^3, $\rho_i \approx 0.92$ g/cm^3 and $\rho_a \ll 1$ g/cm^3, we have $P_i \approx (\rho_s - P_w)/0.92$. Since there is an empirical relation $\rho_s \approx \sqrt{P_w}$ [3,4], we have the relation $P_i \approx (\sqrt{P_w} - P_w)/0.92$. Noting that the last term of Eq. (2.A1) can be omitted because $\varepsilon_a \approx 1$, and that ε_w and ε_i are uniquely determined by specifying the temperature of the particle, T, the quantities necessary to determine the dielectric constant of snow, ε_s, are P_w, T, and U. Table 2-A1 lists those parameters in the bright band as well as the resultant refractive indices of snow at several frequencies.

Table 2-A1. Parameters of the bright band particle model and refractive indices.

Height (km)	Temp. (°C)	P_W	U	Complex refractive indices at several frequencies 5.3 GHz	10.00	13.80	17.25	24.15	34.50
0.366	0.0	.017	3.4	1.125 -*i* 0.0013	1.125 -*i* 0.0020	1.125 -*i* 0.0027	1.125 -*i* 0.0032	1.124 -*i* 0.0043	1.123 -*i* 0.0057
0.183	0.0	.044	8.7	1.326 -*i* 0.0103	1.324 -*i* 0.0181	1.321 -*i* 0.0241	1.319 -*i* 0.0293	1.312 -*i* 0.0382	1.300 -*i* 0.0480
0.000	0.0	0.17	140	3.224 -*i* 0.4974	2.939 -*i* 0.7532	2.708 -*i* 0.8458	2.528 -*i* 0.8738	2.255 -*i* 0.8520	2.002 -*i* 0.7595
-.183	0.0	0.38	∞	5.298 -*i* 1.315	4.484 -*i* 1.746	3.959 -*i* 1.812	3.597 -*i* 1.783	3.102 -*i* 1.645	2.674 -*i* 1.421
-.366	0.0	0.85	∞	7.784 -*i* 2.001	6.555 -*i* 2.672	5.758 -*i* 2.786	5.206 -*i* 2.755	4.444 -*i* 2.568	3.772 -*i* 2.253
-.549	0.0 (Raindrop)	1.0	∞	8.423 -*i* 2.175	7.087 -*i* 2.907	6.221 -*i* 3.034	5.621 -*i* 3.002	4.791 -*i* 2.802	4.057 -*i* 2.464

2. Non-coalescence/Non-breakup (N/N) Model

The second step of the modeling is to determine the drop-size distribution. For simplicity, we assume that a particle changes its phase without any coalescence or breakup during its fall within the bright band, so that its melted diameter, D_m, is unchanged. It follows that the flux, i.e., rain rate, is constant over the bright band. Therefore, letting D_S, $N_S(D_S)$, $V_S(D_S)$ being the diameter, DSD, and falling velocity of a snowflake, and letting D_m, $N_R(D_m)$, $V_R(D_m)$ being the corresponding quantities of a melted particle (i.e., raindrop), we have

$$N_S(D_S)\, V_S(D_S)\, dD_S = N_R(D_m)\, V_R(D_m)\, dD_m. \tag{2.A3}$$

Since $D_S = D_m\, \rho_S^{-1/3}$,

$$N_S(D_S) = \rho_S^{1/3} V_R(D_m) V_S(D_S)^{-1}\, N_R(D_m). \tag{2.A4}$$

Eq.(2.A4) states that the DSD in the bright band is determined automatically from the dropsize and fall velocity distributions of raindrops, if we know the fall velocity distribution in the bright band.

The only remaining unknown quantity to determine the DSD in the bright band with this N/N model is the fall velocity distribution in the bright band. This is estimated from the falling velocity of dry to wet snowflakes obtained by Magono and Nakamura [79],

$$V_s(D_s) = 8.8 \times [0.1 D_s(\rho_s - \rho_a)]^{1/2} \qquad (0.05 \le \rho_s \le 0.3\ \mathrm{g/cm^3}) \qquad (2.A5a)$$

$$V_s(D_s) = 3.3 \times [\rho_s - \rho_a]^{1/2} \qquad (\rho_s \le 0.05\ \mathrm{g/cm^3}) \qquad (2.A5b)$$

and the falling velocity of raindrops, V_R (see Section 2.1.4), using the following interpolation scheme: Since usually $\rho_s \gg \rho_a$, Eq.(2.A5a) can be approximated as $Vs \approx 2.8\ \rho_s^{1/3}\sqrt{D_m}$. (Note that $D_s = D_m\ \rho_s^{-1/3}$.) This means that the fall velocity of a snowflake having a given D_m is proportional to $\rho_s^{-1/3}$ in the region, $0.05 \le \rho_s \le 0.3$ g/cm^3. If we assume that this ρ_s dependence of the fall velocity holds also in the region, $0.3 < \rho_s < 1$ g/cm^3, the following relation is obtained for a given D_m:

$$V_s = (V_R - V_{s0}) \times (\rho_s^{1/3} - 0.3^{1/3}) / (1 - 0.3^{1/3}) + V_{s0} \qquad (0.3 < \rho_s < 1\ \mathrm{g/cm^3}) \qquad (2.A6)$$

where V_{s0} is the fall velocity of a snowflake at $\rho_s = 0.3$ g/cm^3 given by Eq.(2.A5a). Since there is the relation $\rho_s \approx \sqrt{P_w}$, the fall velocity distribution at a specified altitude can be calculated from the P_w data given in Table 2-A1.

References

(1) Ray, P. S., 1972: Broadband complex refractive indices of ice and water. *Appl. Optics*, **11**, 1836-1844.

(2) Meneghini, R. and T. Kozu, 1990: *Spaceborne weather radar*. Artech House, Norwood, MA, 199pp.

(3) Matsumoto, A. and A. Nishitsuji, eds., 1971: SHF and EHF propagation in snowy districts, *Monograph Ser. of the Res. Inst. of Appl. Electricity*, Hokkaido Univ., (19).

(4) Nishitsuji, A. and M. Hirayama, 1971: On the anomalous attenuation of radio wave due to snowfall. *Trans. IECE Japan*, **54-B**, 22-29 (in Japanese).

(5) Pruppacher, H.R. and R.L. Pitter, 1971: A semi-empirical determination of the shape of cloud and rain drops. *J. Atmos. Sci.*, **28**, 86-94.

(6) Awaka, J., and T. Oguchi, 1982: Bistatic radar reflectivities of Pruppacher-and-Pitter form raindrops at 14.3 and 5.33 GHz. *J. Radio Res. Lab.*, **29**, (127), 125-150.

(7) Stratton, J.A., 1941: *Electromagnetic theory*, McGraw-Hill, New York.

(8) Oguchi, T., 1981: Scattering from hydrometeors: A survey. *Radio Sci.*, **16**, 691-730.

(9) _____, 1983: Electromagnetic wave propagation and scattering in rain and other hydrometeors. *Proc. IEEE*, **71**, 1029-1078.

(10) Ulaby, F.T., R.K. Moore, and A.K. Fung, 1981: *Microwave remote sensing: Active and Passive*. Vol.I. Artech House, Norwood, MA, 456pp.

(11) Gunn, K.L.S. and G.D. Kinzer, 1949: The terminal velocity of fall for water droplets in stagnant air. *J. Meteorol.*, **6**, 243-248.

(12) Foote, G.B. and P.S. du Toit, 1969: Terminal velocity of raindrops aloft. *J. Appl. Meteor.*, **8**, 245-253.

(13) Uplinger, W.G., 1981: A new formula for raindrop terminal velocity. Preprints, *20th Conf. Radar Meteor.*, Boston, MA, Amer. Meteor. Soc., 389-391.

(14) Atlas, D. and C.W. Ulbrich, 1977: Path- and area-integrated rainfall measurement by microwave attenuation in the 1-3 cm band. *J. Appl. Meteor.*, **16**, 1322-1331.

(15) Joss, J., J.C. Thams, and A. Waldvogel, 1968: The variation of raindrop size distribution at Locarono, *Proc. Int. Conf. Cloud Physics*, 369-373.

(16) Waldvogel, A., 1974: The N_0 jump of raindrop spectra. *J. Atmos. Sci.*, **31**, 1067-1078.

(17) Feingold, G. and Z. Levin, 1986: The lognormal fit to raindrop spectra from frontal convective clouds in Israel. *J. Climate Appl. Meteor.*, **25**, 1346-1363.

(18) Kozu, T. and K. Nakamura, 1991: Rainfall parameter estimation from dual radar measurements combining reflectivity profile and path-integrated attenuation. *J. Atmos. Ocean. Tech.*, **8**, 259-270.

(19) Atlas, D., C.W. Ulbrich and R. Meneghini, 1984: The multiparameter remote measurement of rainfall. *Radio Sci.* **19**, 3-22.

(20) Chandrasekar, V. and V.N. Bringi, 1987: Simulation of radar reflectivity and surface measurements of rainfall. *J. Atmos. Oceanic. Tech.*, **4**, 464-478.

(21) Feingold, G. and Z. Levin, 1987: Application of the lognormal raindrop size distribution to differential reflectivity radar measurement (Z_{DR}). *J. Atmos. Oceanic. Tech.*, **4**, 377-382.

(22) Marshall, J.S. and W.M. Palmer, 1948: The distribution of raindrops with size. *J. Meteorol.*, **5**, 165-166.

(23) Joss, J. and E.G. Gori, 1978: Shapes of raindrop size distributions. *J. Appl. Meteorol.*, **17**, 1054-1061.

(24) Stout, G.E. and E. A. Mueller, 1968: Survey of relationships between rainfall rate and radar reflectivity in the measurement of precipitation. *J. Appl. Meteor.*, **7**, 465-474.

(25) Battan, L.J., 1973: *Radar observation of the atmosphere*, The University of Chicago Press, Chicago, 324pp.

(26) Atlas, D. and C.W. Ulbrich, 1974: The physical basis for attenuation-rainfall relationships and the measurement of rainfall parameters by combined attenuation and radar methods, *J. Res. Atmos.*, **8**, 275-298.

(27) Ulbrich, C.W., 1983: Natural variations in the analytical form of raindrop size distributions. *J. Climate Appl. Meteor.*, **22**, 1764-1775.

(28) Dissanayake, A.W. and N.J. McEwan, 1978: Radar and attenuation properties of rain and bright band. *IEE Conf. Publ.* **169**, 125-129.

(29) Yokoyama, T., H. Tanaka, K. Nakamura, and J. Awaka, 1984: Microphysical processes of melting snowflakes detected by a two wavelength radar. Part II. Application of a two-wavelength radar technique. *J. Meteor. Soc. Japan*, **62**, 668-677.

(30) Awaka, J., Y. Furuhama, M. Hoshiyama, and A. Nishitsuji, 1985: Model calculations of scattering properties of spherical bright-band particles made of composite dielectrics. *J. Radio Res. Lab.*, **32**, 73-87.

(31) Bringi, V.N., R.M.Rasmussen, and J. Vivekanandan, 1986: Multiparameter radar measurements in Colorado convective storms. Part I: Graupel melting studies. *J. Atmos. Sci.*, **43**, 2545-2563.

(32) Klassen, W., 1988: Radar observations and simulation of the melting layer of precipitation. *J. Atmos. Sci.*, **45**, 3741-3753.

(33) Wilheit, T.T., 1986: Some comments on passive microwave measurement of rain. *Bull. Amer. Meteor. Soc.*, **67**, 1226-1232.

(34) Kummerow, C., R.A. Mack, and I.M. Hakkarinen, 1989: A self-consistency approach to improve microwave rainfall rate estimation from space. *J. Appl. Meteorol.*, **28**, 869-884.

(35) Capsoni, C., F. Fedi, and A. Paraboni, 1987: A comprehensive meteorologically oriented methodology for the prediction of wave propagation parameters in telecommunication applications beyond 10 GHz. *Radio Sci.*, **22**, 387-393.

(36) Kummerow, C. and J.A. Weinman, 1988: Determining microwave brightness temperatures from precipitating horizontally finite and vertically structured clouds. *J. Geophys. Res.*, **93**, (D4), 3720-3728.

(37) Oguchi, T., 1977: Scattering properties of Pruppacher-and-Pitter form raindrops and cross polarization due to rain: Calculations at 11, 13, 19.3 and 34.8 GHz. *Radio Sci.*, **12**, 41-51.

(38) Marshall, J.S. and Hitschfeld, W., 1953: The interpretation of the fluctuating echo for randomly distributed scatterers. Part I. *Can. J. Phys.* **31**, 962-994.

(39) Kodaira, N., 1960: The characteristics of the averaged echo intensity received by the logarithmic IF amplifier. *8th Weather Radar Conf.*, Amer. Meteor. Soc., Boston, 121-125.

(40) Joss, J., R. Cavalli and R. K. Crane, 1974: Good agreement between theory and experiment for attenuation data. *J. Res. Atmos.*, **8**, 299-318.

(41) Atlas, D., D. Rosenfeld, and D.A. Short, 1990: The estimation of convective rainfall by area integrals, 1. The theoretical and empirical basis. *J. Geophys. Res.*, **95**, (D3), 2153-2160.

(42) Rosenfeld, D., D. Atlas, and D.A. Short, 1990: The estimation of convective rainfall by area integrals, 2. The height-area rainfall threshold (HART) method. *J. Geophys. Res.*, **95**, (D3), 2161-2176.

(43) Doviak, R.J. and D.S. Zrnic, 1984: *Doppler radar and weather observations.* Academic Press, Orlando, FL, 458pp.

(44) Rogers, R.R., 1984: A review of multiparameter radar observations of precipitation. *Radio Sci.*, **19**, 23-36.

(45) Hall, M.P.M., 1984: A review of the application of multiple-parameter radar measurement of precipitation, *ibid*, 37-43.

(46) Furuhama, Y. and T. Ihara, 1981: Remote sensing of path-averaged raindrop size distribution from microwave scattering measurements. *IEEE Trans. Antennas. Propag.*, **AP-29**, 275-281.

(47) Ishimaru, A., 1978: *Wave propagation and scattering in random media.* Vol.2., Academic Press, Orlando, FL, 572pp.

(48) Seliga, T.A. and V.N. Bringi, 1976: Potential use of radar differential reflectivity measurements at orthogonal polarizations for measuring precipitation. *J. Appl. Meteor.*, **21**, 257-259.

(49) Holt, A.R., 1984: Some factors affecting the remote sensing of rain by polarization diversity radar in the 3- to 35-GHz frequency range. *Radio Sci.*, **19**, 1399-1412.

(50) Goldhirsh, J. and I. Katz, 1974: Estimation of raindrop size distribution using multiple wavelength radar systems. *Radio Sci.*, **9**, 439-446.

(51) Ulbrich, C.W. and D. Atlas: 1978: The rain parameter diagram: Methods and applications. *J. Geophys. Res.*, **83**, (C3), 1319-1325.

(52) Atlas, D., D. Rosenfeld, and D.B. Wolff, 1990: Climatologically tuned reflectivity-rain rate relation and links to area-time integrals, *J. Appl. Meteorol.*, **29**, 1120-1135.

(53) Rosenfeld, D., D.B. Wolff, and D. Atlas, 1991: Derivation of non-power law effective Z-R relation by PDF matching method, *J. Appl. Meteorol.*, accepted for publication.

(54) List, R., 1988: A linear radar reflectivity-rainrate relationship for steady tropical rain. *J. Atmos. Sci.*, **45**, 3564-3572.

(55) Zawadzki, I. and M. de A. Antonio, 1988: Equilibrium raindrop size distributions in tropical rain. *J. Atmos. Sci.*, **45**, 3452-3459.

(56) Willis, P.T. and P. Tattelman, 1989: Drop-size distributions associated with intense rainfall. *J. Appl. Meteorol.*, **28**, 3-15.

(57) Meneghini, R., J. Eckerman, and D. Atlas, 1983: Determination of rain rate from a spaceborne radar using measurements of total attenuation, *IEEE Trans. Geosci. Remote Sens.*, **GE-21**, 34-43.

(58) Fujita, M., K. Okamoto, S. Yoshikado, and K. Nakamura, 1985: Inference of rain rate profile and path-integrated rain rate by an airborne microwave scatterometer. *Radio Sci.* **20**, 631-642.

(59) Testud, J., P. Amayenc, and M. Marzoug, 1989: Stereo radar meteorology: A promising technique to observe precipitation from a mobile platform. *J. Atmos. Ocean. Tech.*, **6**, 89-108.

(60) Kozu, T., R. Meneghini, W. C. Boncyk, K. Nakamura, and T. T. Wilheit, 1989: Airborne radar and radiometer experiment for quantitative remote measurements of rain. *Proc. IGARSS'89*, Vancouver, Canada, 1499-1502.

(61) Fujita, M., 1989: An approach for rain rate profiling with a rain-attenuating frequency radar under a constraint on path-integrated rain rate, *Proc. GARSS'89*, Vancouver, Canada, 1491-1494.

(62) Marzoug, M. and P. Amayenc, 1991: Improved range profiling algorithm of rainfall rate from a spaceborne radar with path-integrated attenuation constraint. *IEEE Trans. Geosci. Remote Sens.*, **GE-29**, 584-592.

(63) Kozu, T., K. Nakamura, R. Meneghini and W.C. Boncyk, 1991: Dual-parameter radar rainfall measurement from space: A test result from an aircraft experiment. *IEEE Trans. Geosci. Remote Sens.*, **GE-29**, 690-703.

(64) Masuko, H., K. Okamoto, M. Shimada and S. Niwa, 1986: Measurement of microwave backscattering signatures of the ocean surface using X band and Ka band airborne scatterometers", *J. Geophys. Res.*, **91**, (C11), 13065-13083.

(65) Moore, R.K., Y.S. Yu, A.K. Fung, D. Kaneko, G.J. Dome, and R.E. Werp, 1979: Preliminary study of rain effects on radar scattering from water surfaces. *IEEE J. Oceanic Eng.*, **OE-4**, 31-32.

(66) Bliven, L.F. and G. Norcross, 1988: Effects of rainfall on scatterometer derived wind speeds. *Proc. GARSS'88*, Edinburgh, U.K., 565-566.

(67) Meneghini, R., J.A. Jones and L. H. Gesell, 1987: Analysis of a dual-wavelength surface reference radar technique", *IEEE Trans. Geosci. Remote Sens.*, **GE-25**, 456-471.

(68) Hitschfeld, W. and J. Bordan, 1954: Errors inherent in the radar measurement of rainfall at attenuating wavelengths. *J. Meteorol.*, **11**, 58-67.

(69) Meneghini, R., 1978: Rain rate estimates for an attenuating radar. *Radio Sci.*, **13**, 459-470.

(70) Lin, H., M. Xin, and C. Wei, 1985: Ground-based remote sensing of LWC in cloud and rainfall by a combined dual-wavelength radar-radiometer system. *Advances in Atmos. Sci.*, **2**, 93-103.

(71) Weinman, J. A., C. D. Kummerow, and C. S. Atwater, 1988: An algorithm to derive precipitation profiles from a downward viewing radar and multi-frequency passive radiometer. *Proc. GARSS'88*, Edinburgh, U.K., 229-234.

(72) Meneghini, R. and K. Nakamura, 1990: Range profiling of the rain rate by an airborne weather radar. *Remote Sens. Environ.*, **31**, 193-209.

(73) Nakamura, K., 1989: A comparison of the rain retrievals by backscattering measurement and attenuation measurement. Preprints, *24th Conf. Radar Meteorol.*, Tallahassee, FL, Amer. Meteor. Soc., 689-692.

(74) Amayenc, P., M. Marzoug and J. Testud, 1989: Non uniform beam filling effects in measurements of rainfall rate from a spaceborne radar. *ibid*, 569-572.

(75) _____, _____ and _____, 1990: Analysis of cross-beam resolution effects in rainfall rate profile retrieval from a spaceborne radar. *Proc. IGARSS'90*, College Park, MD., 433-436.

(76) Goldhirsh, J., 1975: Improved error analysis in estimation of raindrop spectra, rain rate, and liquid water content using multiple wavelength radars. *IEEE Trans. Antennas Propag.*, **AP-24**, 718-720.

(77) Meneghini, R. and D. Atlas, 1986: Simultaneous ocean cross section and rainfall measurements from space with a nadir-looking radar. *J. Atmos. Oceanic Tech.*, **3**, 400-413.

(78) Meneghini, R. and K. Nakamura, 1988: Some characteristics of the mirror image return in rain.*Tropical Rainfall Measurements*, J.S. Theon and N. Fugono, eds. A. Deepak Publ., Hampton, VA, 235-242.

(79) Magono, C. and T. Nakamura, 1965: Aerodynamic studies of falling snowflakes. *J. Meteor. Soc. Japan*, **43**, 139-147.

CHAPTER 3. THE USE OF GROUND-MEASURED DSD DATA FOR THE STUDY OF RADAR RAINFALL RETRIEVALS

For the study of rainfall retrievals by radar, the knowledge of DSD is essential. Numerous in-situ measurements of DSD have been made using various techniques. For the study of spaceborne radar remote sensing, it is desirable to make such measurements aloft. However, most of the DSD data presently available are those measured on the ground.

At Kashima Space Research Center of CRL, continuous DSD measurements were conducted between 1979 to 1981 using a Joss-Waldvogel type disdrometer, in order mainly to analyze slant-path microwave/millimeter wave propagation data. This large amount of DSD data should provide useful information for various applications. Problems are its accuracy and the correlation between the DSDs on the ground and aloft. To answer these questions, several tests have been performed. In particular, analyses of multi-frequency slant-path attenuation correlated with disdrometer data and a radar calibration employing the disdrometer data clearly indicate the validity of using the disdrometer data for propagation and rainfall remote sensing studies. In this chapter, the results of those analyses relating to the accuracy in the disdrometer DSD measurement are described.

3.1 The Joss-Waldvogel Type Disdrometer

3.1.1 Instrument description

The disdrometer, a raindrop impact type sensor to measure raindrop size distribution on the ground, was developed by J. Joss and A. Waldvogel[1)] and is manufactured by Distromet Ltd. in Switzerland [2)]. It has been used very widely to study DSD properties.

The disdrometer consists of a transducer, a processor and an analyzer. The transducer, a schematic drawing of which is shown in Figure 3-1, transforms the mechanical momentum of an impacting raindrop into an electric pulse. The amplitude of the pulse is roughly proportional to the momentum and has a dynamic range of 90 dB for raindrop diameters from 0.1 to 5 mm. The 90-dB dynamic range is compressed to about 36-dB by the processor. The processor also has a function to reduce acoustic noise. The output signals from the processor, U_c, is related to the drop diameter, D in mm, by $U_c = 0.94\, D^{1.47}$. U_c is then transferred to the signal analyzer, at which the signal is classified into 20 diameter channels. Table 3-1 lists the correspondence between channel number, drop diameter and terminal falling velocity.

Table 3-1 Diameter range of the disdrometer analyzer channels and drop terminal velocity at the geometrical center of the channels.

Channel No.	Drop diameter (mm)	Terminal velocity (m/sec)
1	0.3 ~ 0.4	1.40
2	0.4 ~ 0.5	1.84
3	0.5 ~ 0.6	2.27
4	0.6 ~ 0.7	2.67
5	0.7 ~ 0.8	3.07
6	0.8 ~ 1.0	3.65
7	1.0 ~ 1.2	4.34
8	1.2 ~ 1.4	4.91
9	1.4 ~ 1.6	5.41
10	1.6 ~ 1.8	5.87
11	1.8 ~ 2.1	6.40
12	2.1 ~ 2.4	6.99
13	2.4 ~ 2.7	7.49
14	2.7 ~ 3.0	7.88
15	3.0 ~ 3.3	8.21
16	3.3 ~ 3.7	8.51
17	3.7 ~ 4.1	8.77
18	4.1 ~ 4.5	8.95
19	4.5 ~ 5.0	9.05
20	5.0 ~	9.13

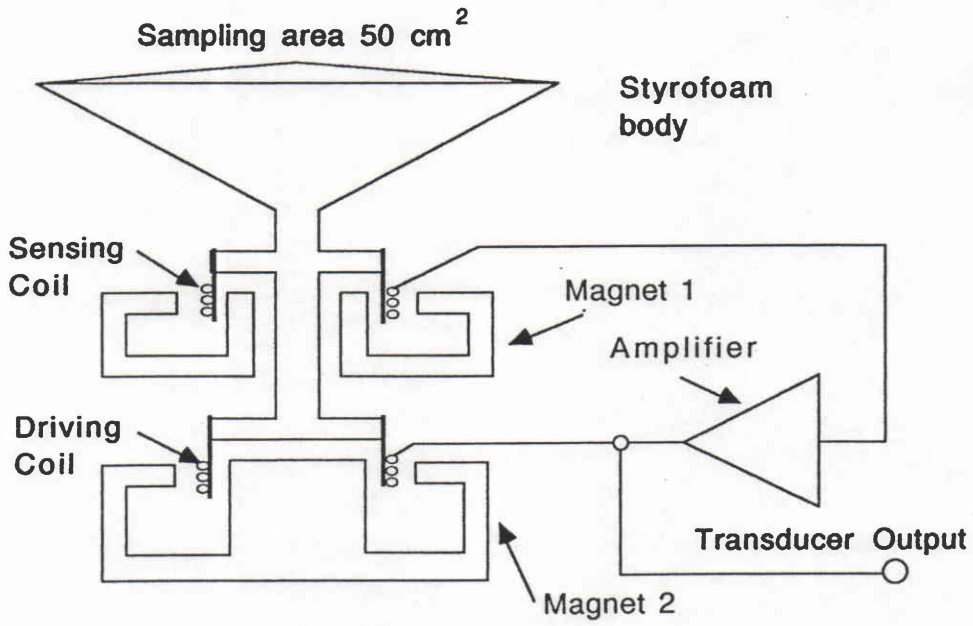

Figure 3-1. Schematic representation of the transducer for the Joss-Waldvogel disdrometer.

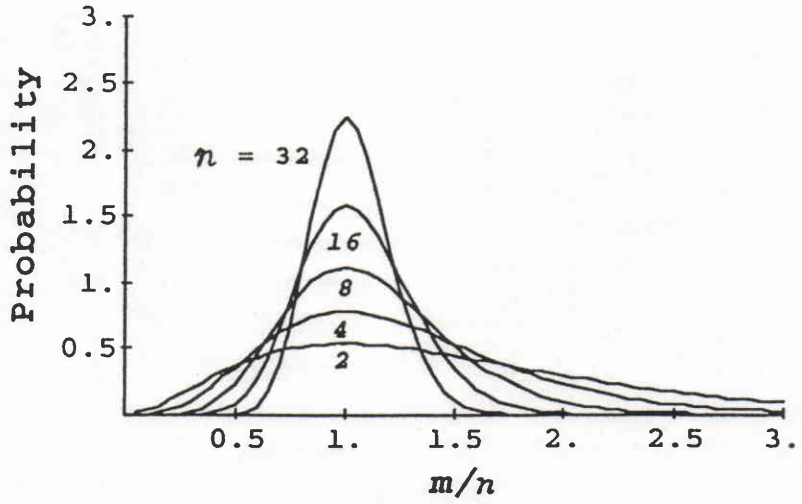

Figure 3-2. Distribution of normalized m (m/n) of Poisson-distributed random process.

3.1.2 Sampling error

It has been shown that the total number of raindrops observed by a drop sampling device under a uniform rain rate, n, is distributed according to the Poisson distribution[3)]

$$\Pi(n,m) = e^{-m} m^n / n! \tag{3.1}$$

where m is the mean value of the number of drops to be observed for a given sampling area and period. The standard deviation of Poisson distribution is $\sqrt{m}$. We can also recognize that Eq.3.1 is the probability of true mean m for a given observed number of drops n. The probability of the normalized m (m/n) is shown in Figure 3-2 for several n values. It is found that sampling error is significant if the number of samples is less than about 10. Therefore, data of large diameter disdrometer channels having less number of samples are generally more erroneous than smaller drop diameter channels.

In order to assess the effect of such sampling error, a simple test has been made using the measured disdrometer data. Let n_i be the number of drops measured at channel i. For this test, it is assumed that channels having n_i greater than 8 measure the drops correctly and that the true count number at the channels having n_i equal to or smaller than 8 may be $(n_i + \sigma_i)$ or $(n_i - \sigma_i)$ with $\sigma_i = \sqrt{n_i}$. The range of variation in 6th moment (Z factor) is calculated by

$$Z_{\pm\sigma} = \sum_{i \in \{i;\, n_i \le 8\}} (n_i \pm \sigma_i) D_i^6 + \sum_{i \in \{i;\, n_i > 8\}} n_i D_i^6. \tag{3.2}$$

$Z_{\pm\sigma}$ is recognized as the Z values to be obtained if the drop number observed is biased by σ_i.

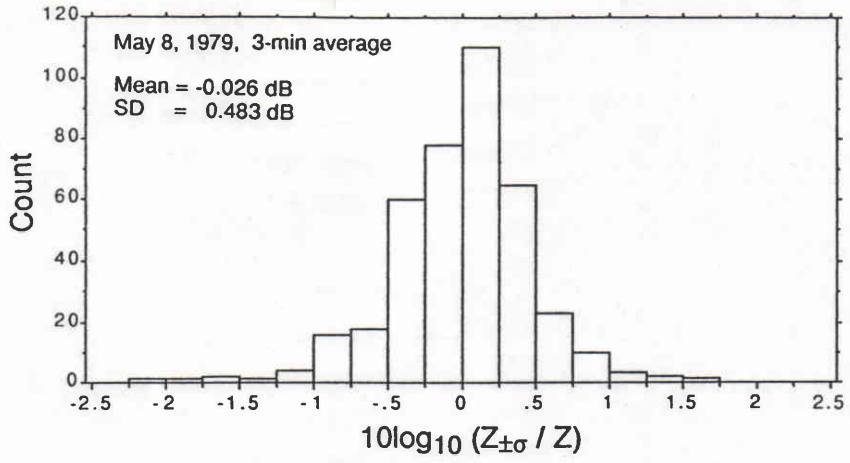

Figure 3-3. Effect of sampling error on calculated Z value.

Figure 3-3 shows the histogram of ($Z_{\pm\sigma}$ - Z), both $Z_{\pm\sigma}$ and Z in dBZ unit, obtained from 3-min averaged disdrometer data on May 8, 1979, where Z is the 6th moment directly calculated from disdrometer data. The standard deviation of ($Z_{\pm\sigma}$ - Z) is found to be about 0.5 dB indicating that the sampling error is not significant for 3-minute averaged disdrometer data. (Note that the effect of the sampling error on other lower-order moments is less than on Z.)

3.1.3 Sensitivity at small diameter channels

There have been arguments regarding the sensitivity degradation of the disdrometer at small drop diameter channels (smaller than about 0.8 or 1 mm). This may come from the "dead" time of the transducer during the impact of a large drop and a possible increase in the transducer surface friction by the wetness, especially in heavy rain conditions. The sensitivity degradation has been suggested by a comparison of DSDs measured by the disdrometer and other optical sensors [4]. There is no quantitative evaluation of the effect of wetness, however.

From an eye inspection of the Kashima disdrometer data, we have found decreases in drop density at small diameter channels in many cases although there are also a number of cases where exponential-like DSD shape extends down to about 0.5 or 0.3 mm diameter channels. This may suggest the existence of some sensitivity degradation at small diameter channels as has been suggested in past studies. However, it has also been shown that various DSD evolution processes from the bottom of the bright band to the ground would cause the DSD on the ground toward a "concave-down" shape; i.e., depletion of small and large drops in comparison to the exponential distribution [5-7]. Therefore, it may be concluded that the

depletion of small drops observed by the disdrometer represents natural DSD properties to some extent.

In order to assess the effect of this uncertainty in DSD shape at the small drop diameters, the following test is performed: We assume; that the DSD shape at the drop diameter range less than 0.9 mm (channel #6) follows an exponential distribution which is derived from a linear regression of diameter versus log of DSD weighted by the contribution of each channel to rain rate; and that the disdrometer measures the DSD correctly for the channels higher than #6. Examples of original and modified DSD's are shown in Figure 3-4. The modified DSD is then used to calculate rain rate, Z, and other rain parameters, and the results are compared with those obtained by the use of original DSD. Figure 3-5 shows the histogram of $10 \cdot \log(Y_{mod}/Y_{meas})$, where Y represents an IRP (moment or rain rate) and subscripts "meas" and "mod" indicate the value for measured and modified DSDs, respectively. It is found that the exponentiation of DSD at small drop diameters makes large differences in lower order moments but only a small or little difference in higher order moments. Considering that the exponentiation of the DSD used in this test probably overestimate the density of small drops to some extent, as discussed above, and that the DSD variation at intermediate to large drops is a dominating factor causing the fluctuation in the relation between higher order moments such as Z-R relation, we can conclude that the effect of uncertainty in the disdrometer data at the small drop channels is minor as far as our primary interest is focused on higher order moments such as R and Z.

3.2 DSD Measurement at Kashima

The disdrometer measurement at Kashima Space Research Center, CRL, started in May 1979 and was continued for several years; however, after the summer 1981, the sensitivity of the instrument has been degraded (K. Nakamura, private communication). Therefore, data from May 1979 until July 1981 are used in this study. The data consist of more than one hundred thousand 1-min integrated samples, about 70% of which have rain rate less than 1 mm/h. Since the rain rate range most important for climatological and hydrological studies is from about 1 mm/h to about 50 mm/h, and since the data at light rain rates have larger sampling error, we use the data having rain rates higher than 1 mm/h in this study. To reduce

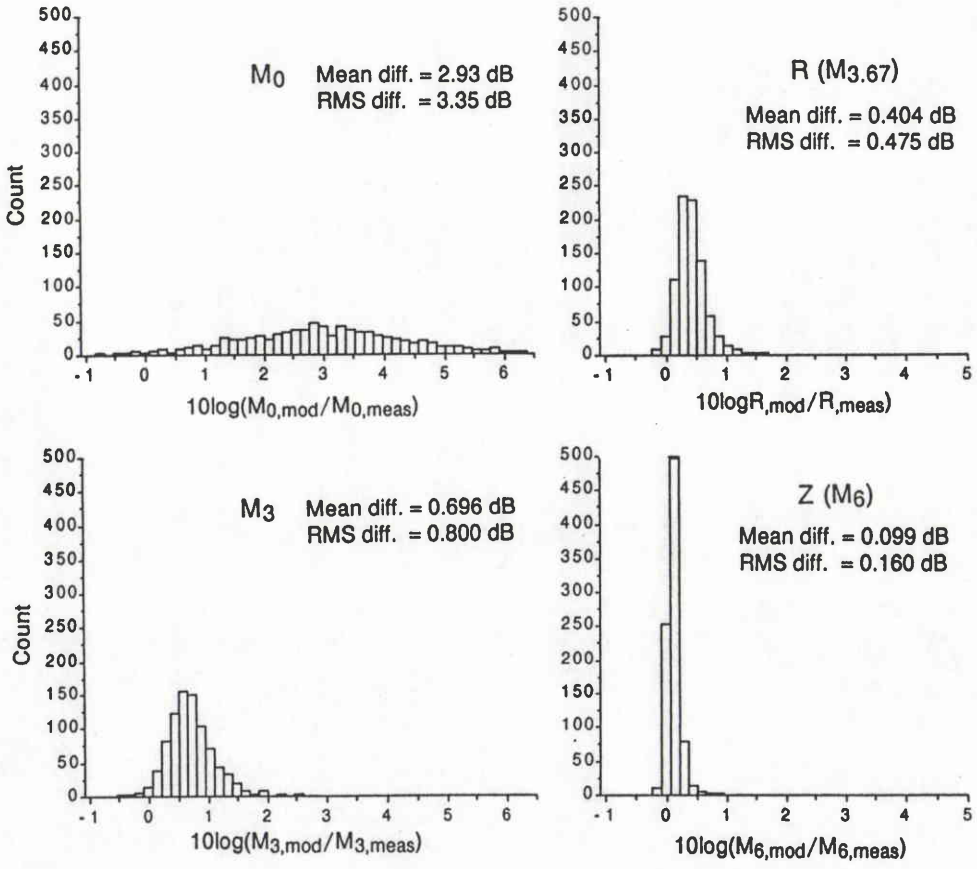

Figure 3-5. Histogram of the difference between IRPs calculated with the original and modified disdrometer data.

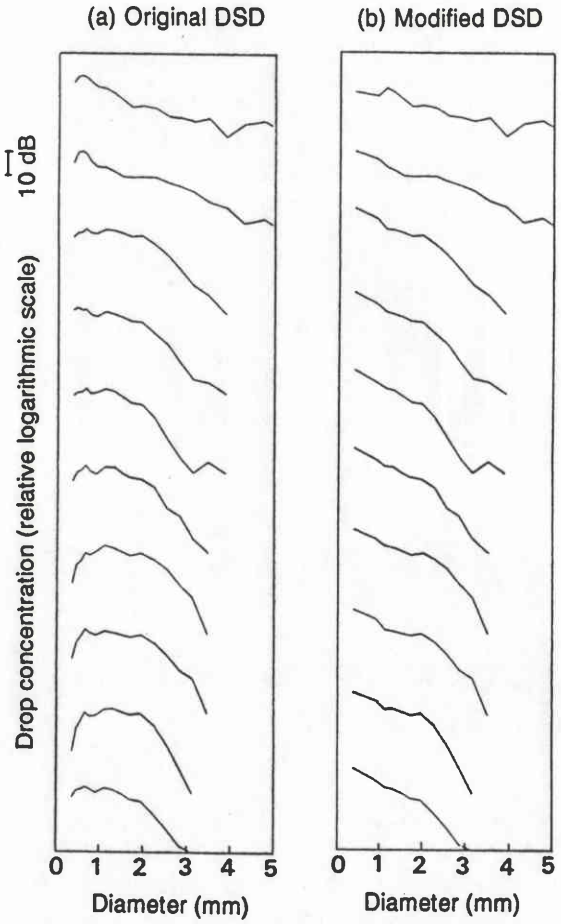

Figure 3-4. Example of disdrometer data modification: (a) Original, (b) exponentiation at small drop channels (< 1 mm).

the sampling error, moreover, we nominally use 3-min averaged data instead of the original 1-min data. The resulting number of 3-min data (higher than 1 mm/h) is about eleven thousand.

The location of the disdrometer and other related instruments at Kashima is illustrated in Figure 3-6 [8]. These instruments and facilities were originally set up for satellite to Earth path propagation experiments, and later used for making a simultaneous multi-frequency radar observation of rainfall [8]. The following two sections describe the results of the analyses through which the usefulness and validity of the disdrometer data for slant-path propagation and radar remote sensing studies are demonstrated.

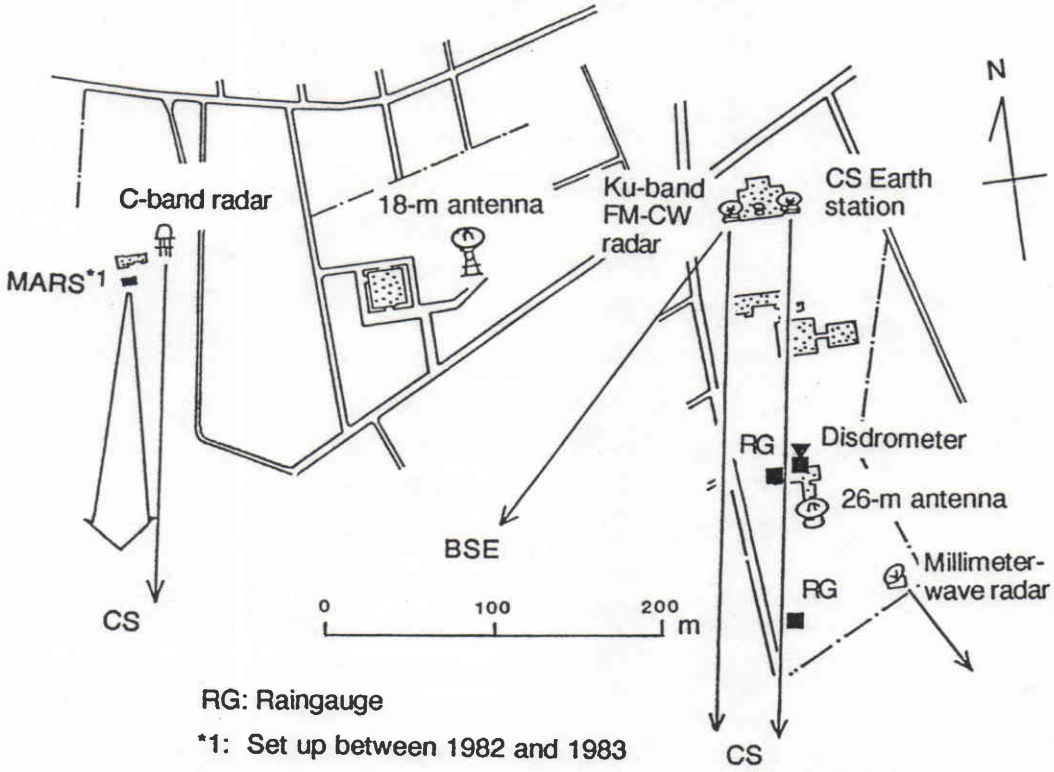

Figure 3-6. Location of the disdrometer and other related instruments at Kashima.

3.3 Analysis of Slant-path Rain Attenuation using Disdrometer Data

The knowledge of frequency dependence of rain attenuation is essential for accurate frequency scaling of attenuation, which is very useful to estimate rain attenuations at other frequencies from an attenuation record at a particular frequency [9]. Since the kernel of attenuation coefficient (Eq.2.17) depends on frequency, the ratio of rain attenuation at a frequency to that at another frequency also depends on DSD. Generally speaking, the larger the difference in the two frequencies, the greater the effect of DSD variation on the attenuation ratio.

A number of measurements of the attenuation ratio have been conducted both at terrestrial and satellite-Earth links[10-15]. In the case of the satellite link, analysis of measured attenuation ratio is difficult because of the difficulty in obtaining detailed precipitation properties on the slant path. Most of the slant-path propagation studies have described only measured results and/or empirical formulas of the attenuation ratio, which have been shown to vary widely from one rain event to another and within a rain event.

In the slant-path propagation experiments using CS and BSE satellites that we have carried out at Kashima Space Research Center, a large amount of down-link beacon attenuation data (CS 19.45 GHz, BSE 11.71 GHz) were obtained[16]. In addition, up-link attenuation data were obtained simultaneous with the down-link data for more than ten rainfall events for both CS and BSE. DSD's on the ground were also measured by the disdrometer.

In this section, the disdrometer-measured DSD data are employed for the analysis of measured attenuation ratios, and the feasibility of slant-path attenuation ratio estimation by ground-measured DSD data is examined. Because of the temporal and spatial discrepancies between the propagation paths and the disdrometer site, one-to-one correspondence of instantaneous attenuation values and disdrometer data may not give successful results. Therefore, the present analysis deals with event-scale properties[17].

Measurement parameters are summarized in Table 3-2. Up-link and down-link frequencies are 14.4 and 11.7 GHz for BSE and 28.9 and 19.5 GHz for CS. Signal levels received at the ground station were sampled every second and stored on magnetic tapes. Slant-path attenuations are obtained through the subtraction of received signal levels during rainfall from those for clear weather estimated from the levels just before and after the rainfall and/or those of the day following and preceding the rainfall day. It should be noted that a main point

Table 3-2 Parameters for up-link and down-link attenuation measurements.

	BSE	CS
Frequency, up, GHz	14.36	28.85
Frequency, down, GHz	11.71	19.45
Polarization	Vertical	Circular
Satellite Az, deg	225	189
Satellite El, deg	37	48
Satellite longitude, deg	110	135
Dynamic range, up, dB	12	18
Dynamic range, down, dB	30	35
Sample rate, sec	1	1
Average time, sec	32	32

of this analysis is the use of two frequency attenuation data along the same propagation path (i.e., each BSE and CS path), not the use of uplink and downlink signals.

3.3.1 Event-scale attenuation ratio properties

It has been reported that *Ze-R* and *k-Ze* relations can be adjusted for each rain event basis to give an improved accuracy in radar estimation of rain rate and attenuation[18,19]. Considering this fact, we examine event-scale attenuation properties.

To get an outline of event-to-event attenuation ratio variation, first we define the "event" attenuation ratio (AR_{ev}) by the slope of the best-fit regression line assumed to cross the origin;

$$AR_{ev} = \sum_j Y_j^2 / \sum X_j Y_j \qquad (3.3)$$

where Xj and Yj are instantaneous values of down- and up-link attenuations (measured or calculated from disdrometer data) for each rainfall event†. The other interpretation of AR_{ev} is the average of instantaneous attenuation ratio with the weighting factor of $XjYj$; that is, greater weight is given to larger attenuation values in the determination of AR_{ev}, which is adequate for most of practical purposes.

An example of AR_{ev} determination is shown in Figure 3-7. The left time charts show measured and disdrometer (DM) derived attenuations. AR_{ev}'s for measured and DM-derived attenuations are derived from respective instantaneous values by using Eq.3.3 as shown in the right scattergrams in Figure 3-7. For comparison, another AR_{ev} is also calculated assuming the Marshall-Palmer (MP) distribution [20]. In this calculation, attenuation pairs are calculated from the following 20 different MP distributions up to the maximum rain rate in that event (R_{max}):

$$N(D) = 8000 \exp(-4.1 R_j^{-0.21} D) \quad \text{with} \quad R_j = R_{max}\, 10^{-0.08(20-j)},\ j = 1,2,\ldots,20. \qquad (3.4)$$

These attenuation pairs are then used as the data for the regression to obtain the AR_{ev}.

Figure 3-8 shows the scattergrams of measured AR_{ev} versus DM-derived and MP-derived AR_{ev}'s. The result of the event attenuation ratio analysis is summarized in Table 3-3. For BSE, while the MP-estimated AR_{ev} has little correlation with measured AR_{ev}, DM-derived

† A similar quantity can be defined as $\Sigma X_j Y_j / \Sigma X_j^2$, which has been found to be very close to the value given by Eq.3.3 for all cases we have processed (within 2%).

values correlate well. The use of 10°C to 20°C raindrop temperature appears to be more suitable than 0°C. This is consistent with the ground temperature during the rainfall events, which ranged from 13°C to 25°C. In the case of CS, however, the DM estimation results in some overestimation, and the correlation coefficients are not as good as those for BSE. Nevertheless, the DM estimation provides higher correlation coefficients than MP estimation and the assumption of 10°C to 20°C drop temperature seems suitable, just as the BSE result.

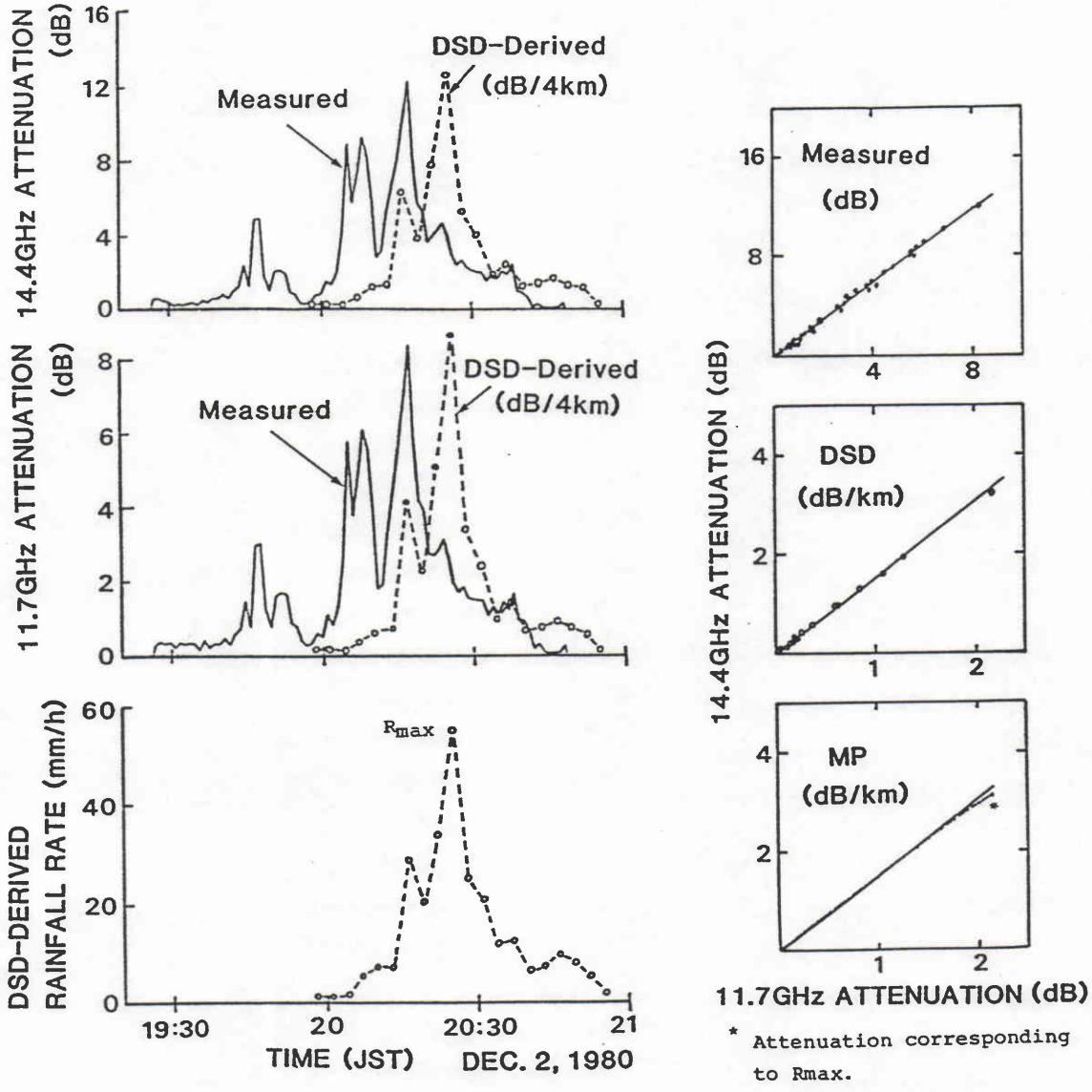

Figure 3-7. Example of the determination of "event" attenuation ratio (AR_{ev}) for measured and disdrometer-derived attenuation values.

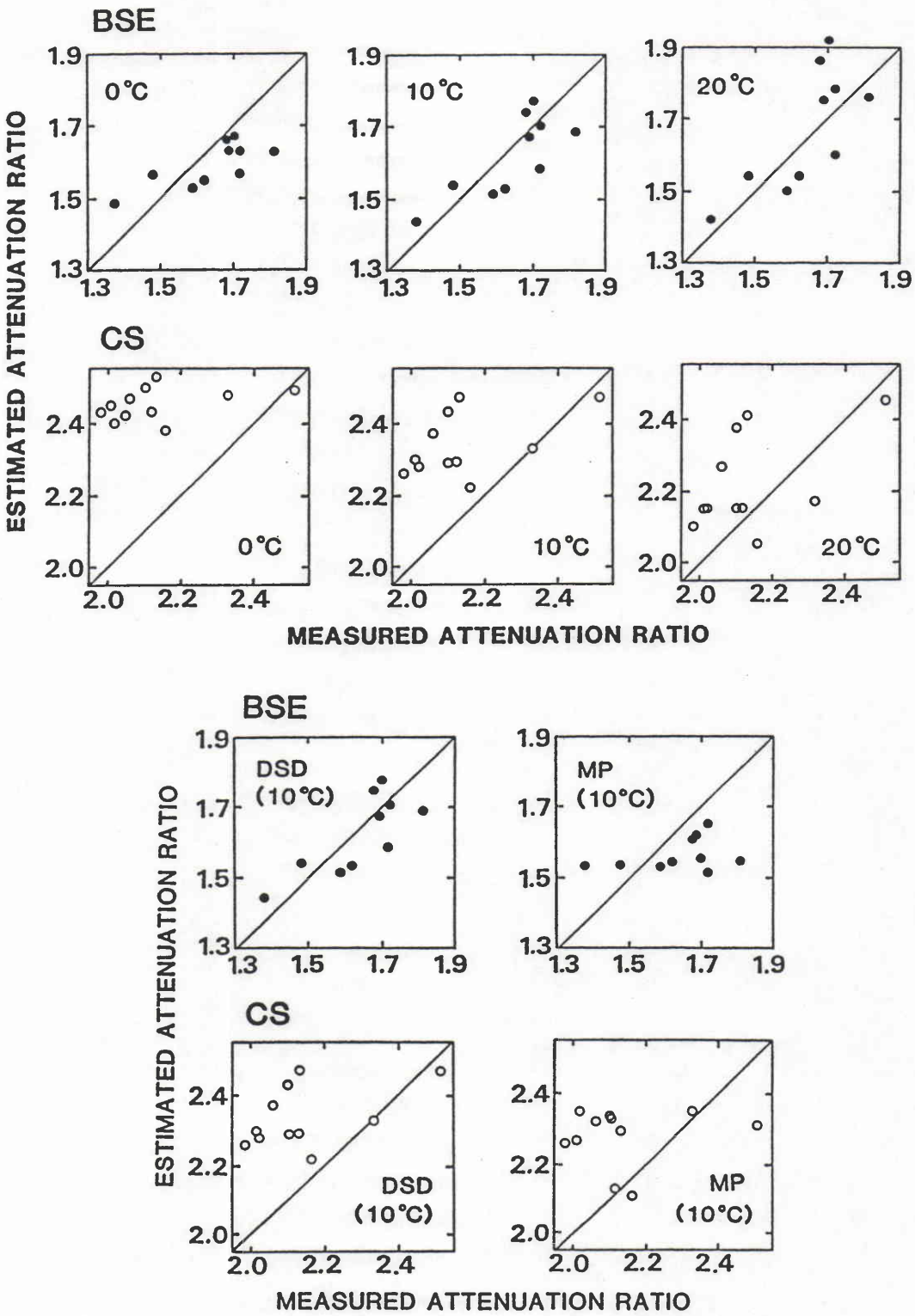

Figure 3-8. Upper: Scattergrams of measured vs. DM-derived AR_{ev} for drop temperature of 0 ~ 20°C. Lower: Comparison of correlations between measured and DM-derived AR_{ev}'s and between AR_{ev}'s measured and estimated with the assumption of Marshall-Palmer DSD model.

Table 3-3 Summary of the event attenuation ratio (AR_{ev}) analysis.

	Raindrop temperature, DM estimation, °C			Raindrop temperature, MP estimation, °C
	0	10	20	10
		BSE		
Average difference	-0.047	-0.023	0.028	-0.078
Correlation coefficient	0.760	0.764	0.737	0.344
		CS		
Average difference	0.314	0.200	0.088	0.128
Correlation coefficient	0.376	0.477	0.481	0.164

The variability in instantaneous attenuation ratio within a rain event, which is a measure of the validity of the event-scale attenuation ratio adjustment, is shown in Figure 3-9 together with AR_{ev}. Vertical bars in the figure indicate the maximum and the minimum values for down-link attenuation larger than 2 dB. For BSE, it is found that attenuation ratios are

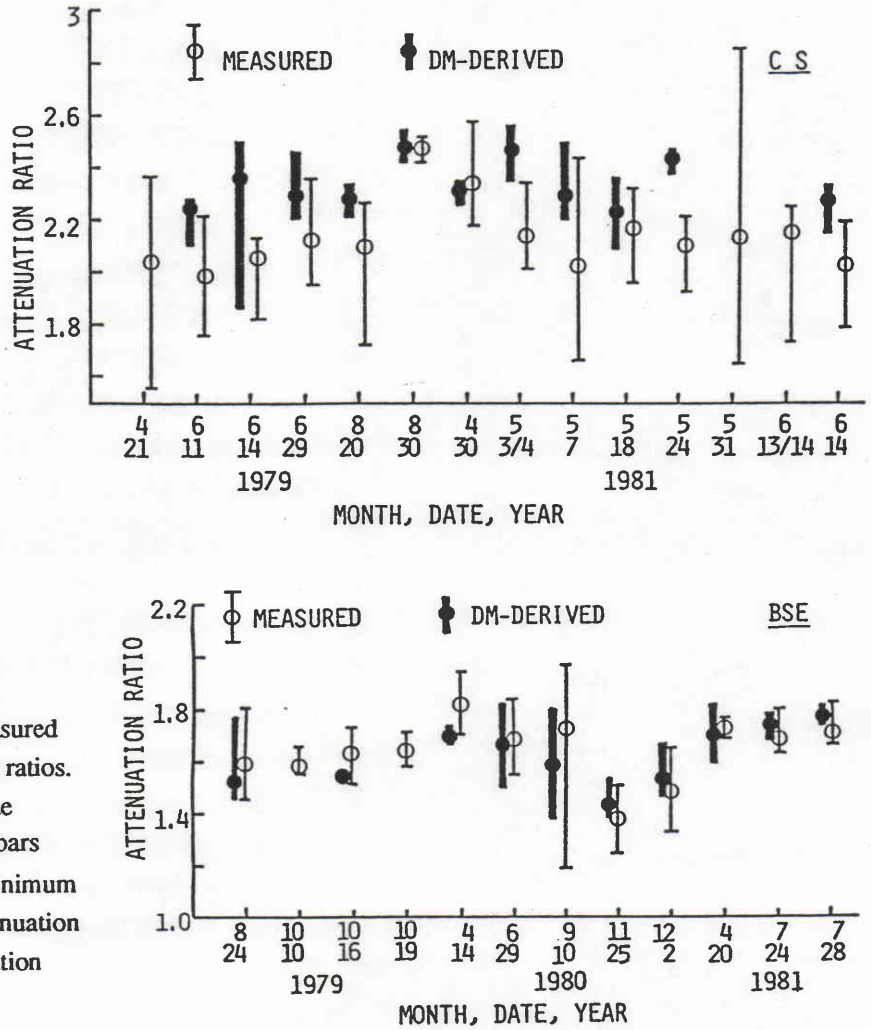

Figure 3-9. Comparison of measured and DM-derived attenuation ratios. Open and solid circles denote AR_{ev}, and heavy and light bars show the maximum and minimum values of instantaneous attenuation ratios for downlink attenuation larger than 2 dB.

relatively stable within one event except for a strong convective storms such as August 24, 1979 and September 10, 1980, and that the measured and DM-derived attenuation ratio variations correlate well. On the other hand, for CS, the correlation between measured and DM-derived attenuation ratio variations is not as good as the result of BSE. The larger variability in the measured values in CS suggests the existence of some causes of attenuation other than rain or some height dependence of DSD.

3.3.2 Discussion on the measured and DM-derived attenuation ratios

In this section, we examine the cause of the disagreement (that measured values are lower than the DM-derived ones) observed in the CS result. Similar results have also been observed for the low-attenuation range ($\lesssim 2$ dB) of BSE.

Gaseous attenuation: While the oxygen attenuation should be almost constant for rainy and fine days, the difference in humidity between rainy and fine days[21] can contribute to the attenuation ratio to small extent. The CS result can partly be explained by the water vapor attenuation because the water vapor absorption at 19.5 GHz is larger than at 28.9 GHz due to the 22.235 GHz absorption line; however, this is not the case for BSE.

Bright band attenuation: The other possible cause is the effect of bright band attenuation and/or other DSD properties related to rainfall type, since most of the CS measurements were made in stratiform rain. For BSE, no typical stratiform rain is included in the present analysis; even if bright band is observed in the Z factor profile measured by the C-band radar[22] (see Figure 3-6), temporal variation in measurable attenuation is very large and spiky in most cases.

The bright band attenuation and attenuation ratio are calculated with the bright band particle and its DSD model described in Chapter 2. Figure 3-10 shows the ratio of attenuation cross sections (Q_tR) of up- and down-link frequencies for raindrop and bright band particles. As shown in this figure, Q_tR's decrease with drop diameter, D, in general but have peaks at particular D values. Q_tR's are affected by drop temperature mainly in the small D region. This is because the temperature dependence of absorption cross section is larger than that of the scattering cross section and because absorption mainly contributes to total attenuation in the small D region. There is a difference in the location of peaks between Q_tR's of raindrops and of bright band particles. Attenuation ratio may be lowered by the existence of bright band attenuation if bright band particles of small and/or large diameter predominate. On the other hand, it may be increased if intermediate-sized particles do.

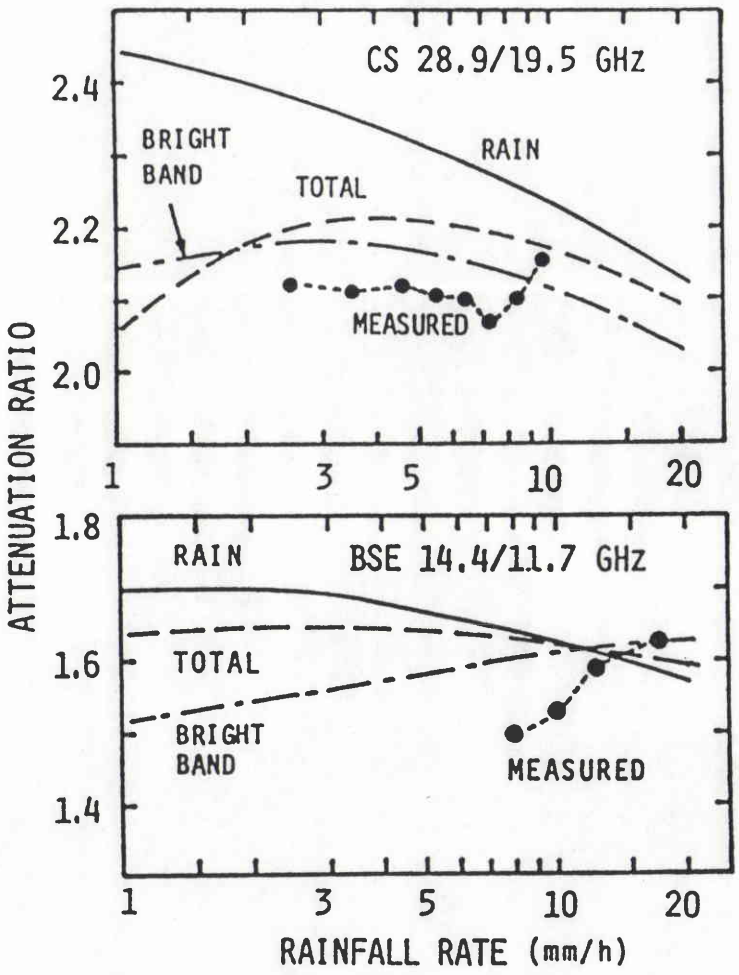

Figure 3-11. Results of slant-path attenuation ratio calculation: rain-only, bright-band-only, and total (including gas attenuation).

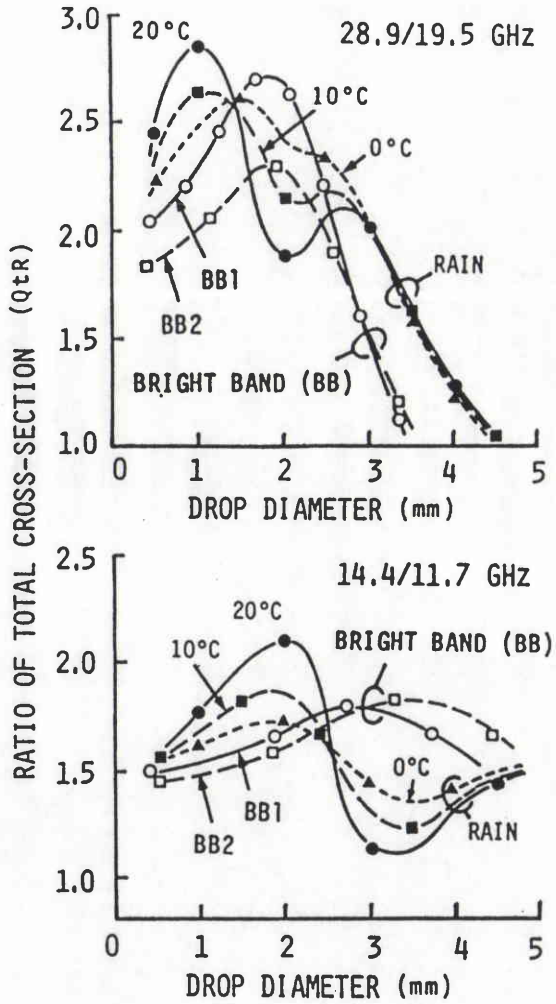

Figure 3-10. Ratio of attenuation cross sections at two different frequencies (QtR) as a function of drop diameter.

Figure 3-11 shows rain-only, bright-band only, and total (including gaseous attenuation) attenuation ratios as a function of rain rate for relatively light rain region, where the DSD of rain is assumed to be the MP distribution. Solid circles indicate the measured attenuation ratios for rainfall events during which clear bright band was observed. Rain height and bright band thickness are assumed to be 3 km and 0.5 km, respectively. For both CS and BSE, attenuation dependences of total and bright-band attenuation ratios are closer to the measured dependence than of rain-only cases.

Height dependence of DSD: DSDs would change systematically during their fall. In the case of stratiform rain, there have been a number of studies on this subject [5,7,23,24]. The physical processes relating to the DSD evolution include: breakup, coalescence, evaporation, accretion, etc. As a result of analytical and simulation studies, it is a consensus that the DSD shape in a stratiform rain would be more "concave down" near the ground than aloft[7]. Therefore, the attenuation ratio calculated from the disdrometer data may not represent the overall attenuation ratio properties along the slant-path. That is, there may be larger number of large and small drops aloft than on the ground. To study this height dependence of DSD in detail, we have to develop a method to estimate the original DSD from the final DSD measured on the ground, which is a complicated inverse problem. For an approximate evaluation of the DSD change with height, DSD is modified by the same method as used for the disdrometer sensitivity degradation test (see 3.1.3) except that DSDs are exponentiated at both small and large drop regions in this case. Such modification is qualitatively similar to the natural one occurring in stratiform rains and the calculated attenuation ratio may be a limiting value considering the continuous change in DSD from the exponential shape to the measured DSD on the ground. The calculated attenuation ratio is generally smaller than that obtained from the original DM data by about 0.05 to 0.15, which is consistent with the difference between the estimated (total) and the measured attenuation ratios shown in Figure 3-11.

3.4 Ku-band FM-CW Radar Calibration using Disdrometer Data

3.4.1 Outline of the FM-CW radar

A Ku-band FM-CW radar was developed at Kashima Space Research Center in order mainly to study microwave propagation characteristics for slant paths [25,26]. The major advantage of this radar for the propagation studies is that the radar signal is transmitted from the same antenna installed for the propagation data acquisition such as receiving a satellite

beacon signal and measuring slant-path brightness temperature, thereby enabling close comparative analyses of the radar and propagation data. The radar was originally developed as an FM-CW type, and later a pulse-compression (PC) system was added to increase the sampling rate. Another objective of the radar development is to evaluate quantitatively the performance of the radar system for rainfall observation because at that time no report and only a few report have been published on the rain observation by FM-CW and PC radars, respectively.

Table 3-4 Major parameters of FM-CW radar.

Center frequency	14.3625 GHz	
Polarization	Vertical	
Antenna	Transmit	Receive
Diameter	13 m	30 cm
Gain	63.1 dB	29.0 dB
HPBW	0.10°	4.6°
Output power	49.1 dBm	
Frequency deviation	7.5 MHz p-p	
Modulation signal	Triangular	
Modulation frequency	300 Hz	
Range resolution	100 m	
Measurable range	0.25 ~ 15 km	
Dynamic range	80 dB	
Numb. of indep. samples	~ 300	
Scan time	60 sec	

The major parameters of the radar is listed in Table 3-4. Basically the radar was constructed by utilizing an FM-TV transmitter and a 13-m Cassegrain antenna installed for the BSE (Broadcasting Satellite for Experimental Purposes) experiment [27]. A 12.0-GHz sky noise temperature and an 11.7-GHz BSE beacon signal (during the BSE experiment only) were also measured by the same antenna. Since the beamwidth of the 13-m antenna is extremely narrow (0.1°), it is safe to assume that the cross-beam non-uniformity of rain in a resolution volume is negligible. The signal backscattered from rain is received by a 30-cm parabolic antenna. This antenna size was selected so that the scattered signals from range gates between 0.25 and 15 km, which include all the precipitation regions along the slant-path, can be received without scanning the receiving antenna. In Appendix 3-1, a radar equation relevant to this system is derived.

3.4.2 Calibration method

Absolute radar calibration is essential to obtain quantitative radar reflectivity that is required to estimate microwave rain attenuation and rain rate. However, it is not easy to make an accurate calibration because of a number of error sources, and an overall external calibration using reference targets is usually required. One type of the reference targets is point targets such as metal spheres and corner reflectors, scattering cross sections of which are calculated accurately[28]. A problem in using such point targets is that the radar equation for the point target is different from that for volume targets. Some of system constants such as antenna pattern and pulse width can not be calibrated with the use of the point target. The most direct way to make the overall rain radar calibration is to use rain itself as a reference target. Therefore, this scheme has been widely used in spite of several error sources. The usual method in this scheme is to compare the rain rates as measured by ground-based rain gages and those estimated from the radar assuming a *Ze-R* relation. Clearly, there are two major error sources in this method. One is the spatial discrepancy between the observing volume by radar and that by the gages; and the other is the uncertainty in *Ze-R* relation or DSD.

In order to reduce those errors, a new scheme has been developed for calibrating the FM-CW radar. The main points are: 1) Path attenuation derived from a satellite beacon signal or from the 12-GHz radiometer is used as a reference instead of raingage data; and 2) the relation between attenuation coefficient versus *Ze* (*k-Ze* relation) derived from the disdrometer data is employed for estimating slant-path attenuation, which is compared with the radiometer-derived path attenuation to obtain a correction factor of the radar system constant, *F*.

As described in Chapter 2 (Eq.2.24) , the radar equation including attenuation effect on received power is

$$P_r(r) = \frac{C\,|K_w|^2}{r^2} Zm \tag{3.5}$$

where the radar constant C, which was given in Eq.2.24 for a typical radar configuration, may have a different form in this case, and is expressed by the "original" or uncalibrated radar constant, C_0, and a correction factor, F, as $C = C_0/F$. A flowchart of the calibration is shown in Figure 3-12. The reference quantity, 11.7-GHz path-attenuation derived from the 12-GHz sky noise temperature (A_{RM}), was calibrated using the BSE beacon attenuation [29]. Whereas,

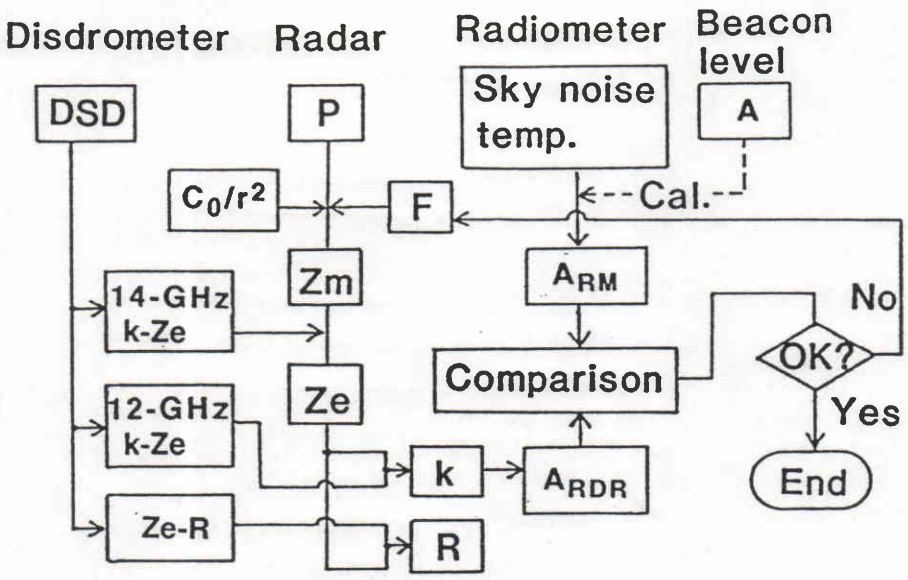

Figure 3-12. Flowchart of radar calibration.

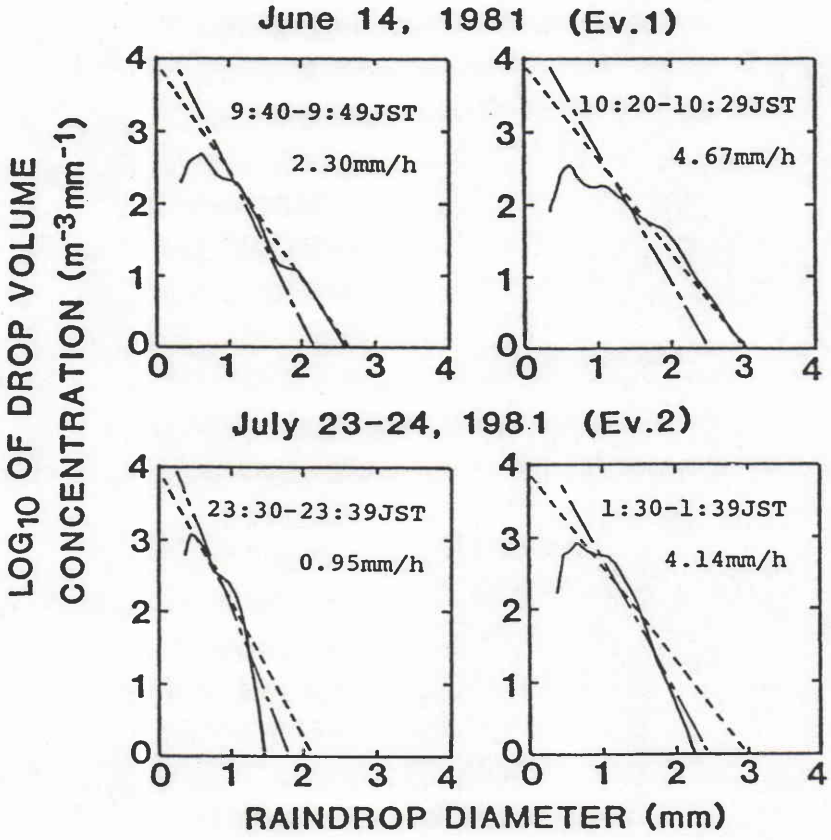

Figure 3-13. Example of disdrometer-measured DSDs during Ev.1 and Ev.2. Broken and dot-dash lines show MP and J-D distribution.

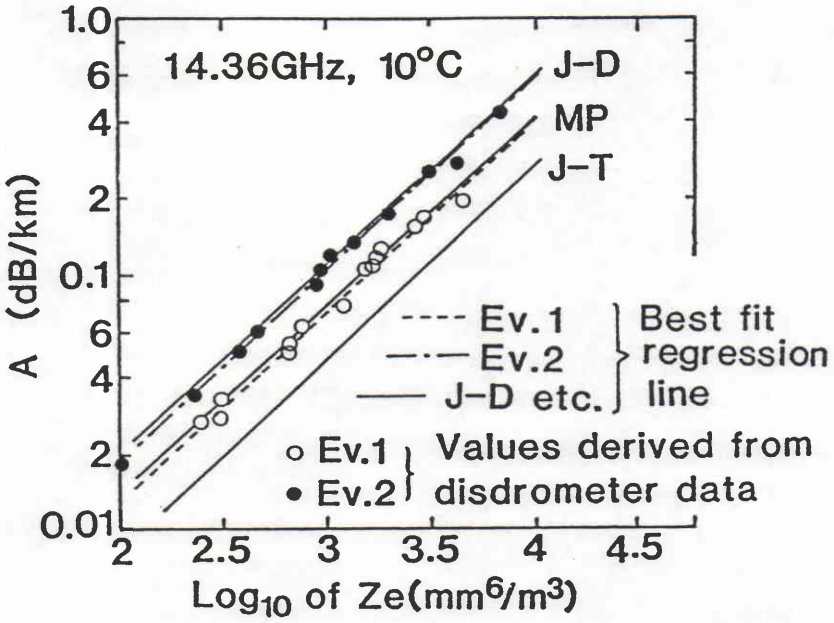

Figure 3-14. Attenuation coefficient (*A*, in this figure) vs. *Ze* relationships measured in Ev. 1 and Ev.2. The curves for MP, J-D and J-T distributions are also shown.

k_{14} (14.4 GHz)-*Ze*, and k_{12} (11.7 GHz)-*Ze* relations required for estimating path attenuation from the radar received power profile are obtained from the disdrometer data by a linear regression of log *k* and log *Ze* values within a rainfall event. The k_{14}-*Ze* relation is used to calculate *Ze*'s together with C_0 and a given *F* value. An estimate of 11.7-GHz path attenuation (A_{RDR}) is then calculated with the k_{12}-*Ze* relation. The final F value is selected as a value that gives the best agreement between A_{RM} and A_{RDR}; i.e., the value that minimizes the RMS deviation (*RMS-dev*)

$$RMS\text{-}dev^2 = N^{-1} \sum_{i=1}^{N} [A_{RDR_i} - A_{RM_i}]^2 \qquad (3.6)$$

where the summation from *i* to *N* spans over a rain event but only cases where both A_{RDR} and A_{RM} are higher than 0.5 dB.

We use two rainfall events for the calibration; one is on June 14, 1981 (Ev.1) and the other is on July 23-24, 1981 (Ev.2). During both events, *k-Ze* relations calculated from the disdrometer data are stable, which would lead to a good accuracy in the calibration. Examples of disdrometer-measured DSD are shown in Figure 3-13. It has been found that the *k-Ze* relations for Ev.1 and Ev.2 are close to those for Marshall-Palmer (MP) and Joss-Drizzle (J-D) distributions (see Section 2.1.5), as shown in Figure 3-14.

One problem in the derivation of path-attenuation from radar is how to evaluate the attenuation due to bright band particles. Goldhirsh[19] obtained the best result for stratiform rain when he omitted the bright band attenuation in his analysis using an S-band radar data. As Dissanayake and McEwan [30] pointed out, this may be due to the fact that the increase in S-band *Ze* at bright band is so large that the attenuation is significantly overestimated when the same *k-Ze* relation as that for rain is used for bright band. However, the degree of the overestimation should be relaxed with increasing frequency; the same *k-Ze* relation may be applied both to rain and bright band when we use an X-band radar [30]. For the Ku-band radar, we calculate the bright band attenuation employing the particle and DSD models described in Chapter 2. The resultant *k-Ze* relation for the values averaged over the bright band is found to give somewhat (about 1.5 times) larger attenuation coefficients than that for rain for a given Ze. However, the properties of bright band particles still need clarification and the bright band k-Ze relation may vary from case to case. Therefore, the following three *k-Ze* relations are used for the evaluation of bright band attenuation: (1) no attenuation at bright band; (2) the same *k-Ze* relation as that for rain; and (3) the above mentioned bright band *k-Ze* relation.

3.4.3 Result of the calibration

Figure 3-15 shows the relation between the RMS-deviation and F value used to calculate A_{RDR}. The curves designated as "DSD-Ev" represent the results using the disdrometer-derived *k-Ze* relations. For comparison, the results using the *k-Ze* relations for J-D, MP and Joss-Thunderstorm (J-T) distributions are also plotted in the figure. The F value that gives the minimum RMS-deviation for each curve, F_m, differs by about 2 dB for each event when J-D, MP or J-T distribution is assumed for both rain events. On the other hand, F_m is almost constant when the disdrometer data are employed for estimating event-scale *k-Ze* relations. This indicates the usefulness of disdrometer data to estimate DSDs on slant paths. For Ev.1, about 1-dB difference appears between the DSD-Ev F_m values obtained from the assumption of bright band attenuation (1) and (3), while for Ev.2, the difference is only about 0.3 dB. This is due to the difference in the magnitude of bright band *Ze*'s between Ev.1 and Ev.2. However, it appears that the large event-by-event variability in DSD causes much larger error in estimating F_m than the uncertainty in evaluating bright band attenuation. Consequently, we have chosen F = 1.5 dB for the FM-CW radar.

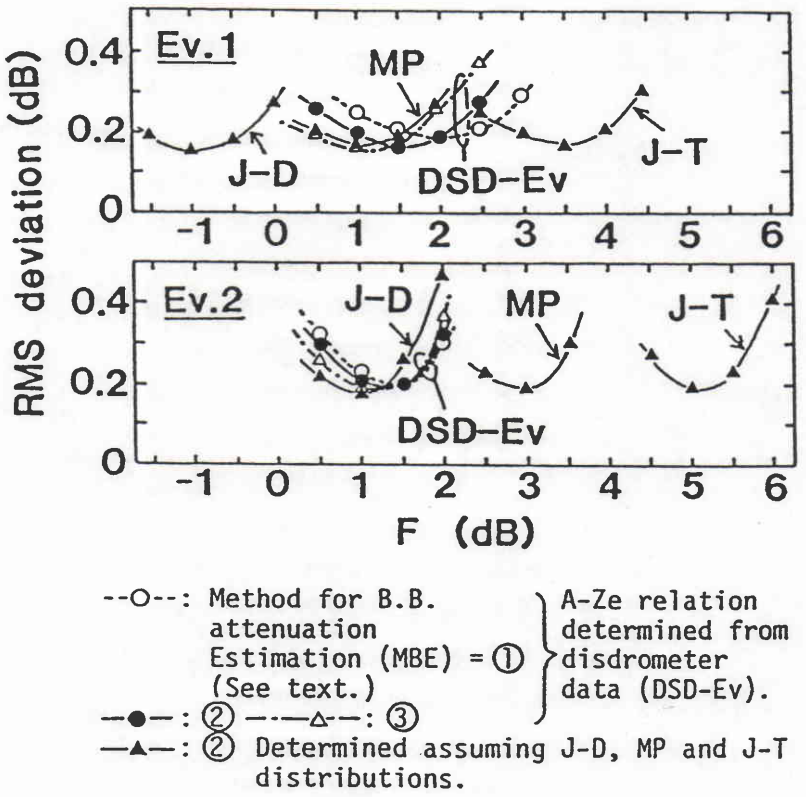

Figure 3-15. F value versus RMS deviation between A_{RDR} and A_{RM}.

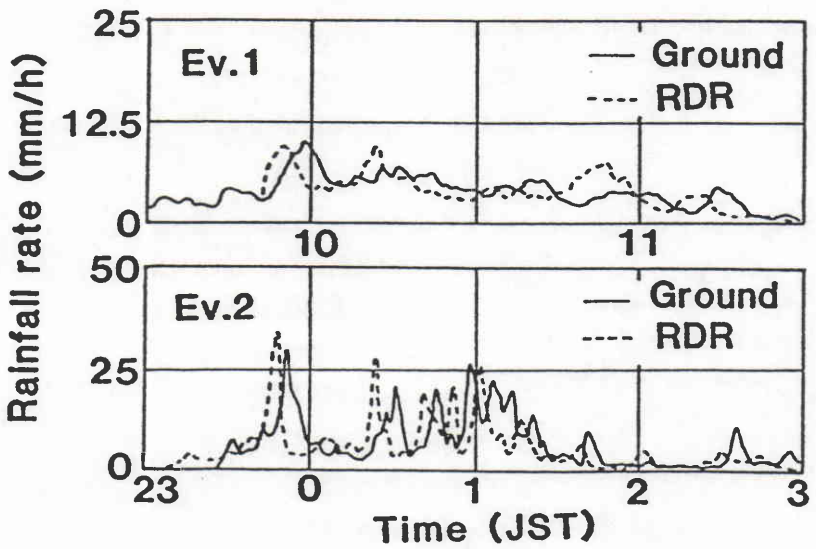

Figure 3-16. Comparison of radar-derived rain rate on the BSE path with ground-measured rain rate.

To verify the calibration result, comparisons are made between rain rates measured by a raingage and those from the calibrated radar data using the *Ze-R* relation derived from the disdrometer. The rain gage is installed at about 2 km from the radar and about 1.5 km below the BSE propagation path. Figure 3-16 shows the comparison of rain rates derived from the radar reflectivity at the range bin just above the rain gage and those measured by the rain gage. Several minutes' shifts of the time at which peaks of rain rates occur are probably due to the 1.5-km height difference. Including these time shifts, the radar derived rain rates are very consistent with the rain gage data for both events.

3.5 Conclusions

We have examined the validity to use DSDs measured on the ground by a disdrometer for studying spaceborne radar rainfall measurements. Sampling errors and possible sensitivity degradation of the disdrometer were examined. It was found that those errors are not negligible but the uncertainty in the measured DSD due to those errors are much smaller than natural DSD variabilities.

We have used the disdrometer data to analyze the slant-path rain attenuation ratios and to improve the accuracy in the calibration of the radar for rain measurement on a slant-path. It was found that the event-averaged attenuation ratios are well correlated with the values estimated from the disdrometer data, and that a reasonable radar calibration result is obtained by the use of disdrometer-derived *k-Ze* relations. Although a correction may be required for the attenuation caused by the bright band in the case of stratiform rain and further study may be required to model a height dependence of DSD shape, the results of these studies indicate the validity of using the disdrometer data not only for ground based radar studies but also for aircraft and spaceborne radar studies.

In the above studies, successful results have been obtained by employing the disdrometer data to estimate event-scale relations between rain parameters such as attenuation ratio and *k-Ze* relation. This suggests that the magnitude of the event-by-event variability in DSD, which can be estimated from the disdrometer measurement, is a dominating factor to determine the total variability of rain parameter relations rather than other sources such as short-term or small scale variations of DSD within a rain event, height dependence of DSD and effects of bright band attenuation. It may therefore be possible to model the rainfall in such a way that some of the rain parameters vary more slowly than the variability in rain rate and *Ze*.

Appendix 3-1: Derivation of radar equation for the Ku-band FM-CW radar

As shown in Figure 3-A1, we consider a cylindrical scattering volume ΔV the length of which is equal to the range resolution, Δr, and we assume that the rain in ΔV is uniform and that all of the power transmitted forward pass through the cross section of ΔV, S. Since the beamwidth of the receiving antenna (4.6°) is much wider than that of the transmitting antenna (0.1°), receiving antenna gain (G_r) can be approximated to be constant over the ΔV. The power of the received signal, $P(r)$, scattered from raindrops in ΔV is expressed as

$$P(r) = (\lambda/4\pi)^2 \eta G_r \int_{r-\Delta r/2}^{r+\Delta r/2} \iint_S Q \, ds \, w^{-2} \, dw \qquad (3.A1)$$

where λ is the radar wavelength, r is the distance from the radar to the center of ΔV, η is the back-scattering cross section of rain per unit volume, and Q is the power flux density illuminating an infinitesimal volume dV (= $ds\, dw$) at the distance w. Rain attenuation along the path has been neglected.

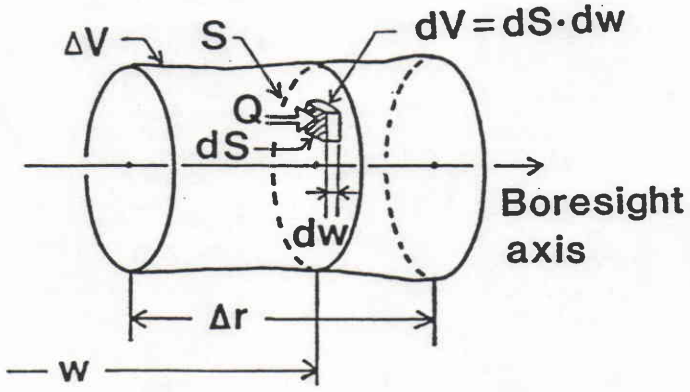

Figure 3-A1. Scattering volume ΔV for the calculation of radar received power.

From the above assumption, the surface integral of Q on S is almost equal to the effective transmitted power ξP_t, ξ being the antenna efficiency. Thus, when $r \gg \Delta r$, Eq.3.A1 is approximated as

$$P(r) \approx (\lambda/4\pi)^2 \eta\, G_r\, \xi P_t\, \Delta r / r^2 = \pi^3 |K_w|^2 (16\lambda^2)^{-1}\, G_r\, \xi P_t\, \Delta r\, Ze / r^2 \qquad (3.A2)$$

where $|K_w|$ and Ze are defined in Table 2-1 (also by Eqs.2.10 and 2.21). A merit to use a wide beamwidth receiving antenna is that neither transmitting antenna gain nor pattern appears in the radar equation because almost all transmitted power can be received by the receiving antenna with approximately a constant gain, G_r. This means that the above radar equation works even in a near field region. Substituting $|K_w|^2 = 0.93$, $\lambda = 2.09$ cm, $G_r = 29.0$ dB and $\xi P_t = 46.4$ dBm ($\xi = 0.54$), which are the parameters of the FM-CW radar, we have

$$P(r)\ (\mathrm{dBm}) = -128.4 - 20 \log r + 10 \log \Delta r + 10 \log Ze(r) \qquad (3.A3)$$

where units of r, Δr, and Ze are km, m, and $\mathrm{mm^6/m^3}$, respectively.

References

(1) Joss, J. and A. Waldvogel, 1967: Ein Spektrograph fur Neiderschlagstropher mit Automatischer Auswertung. *Pure Appl. Geophys.*, **68**, 240-246.

(2) Distromet Ltd.: *Distrometer RD-69 and Analyzer AD-69 Instruction Manuals.* P.O. Box 33, CH-4020 Bassel, Switzerland.

(3) Cornford, S.G., 1967: Sampling errors in measurements of raindrop and cloud droplet concentrations. *Meteor. Mag.*, **96**, 271-282.

(4) List, R., 1988: A linear radar reflectivity-rainrate relationship for steady tropical rain. *J. Atmos. Sci.*, **45**, 3564-3572.

(5) Caton, P.G.F., 1966: A study of raindrop-size distributions in the free atmosphere. *Quart. J. Roy. Meteor. Soc.*, **92**, 15-30.

(6) Cataneo, R. and G.E. Stout, 1968: Raindrop-size distributions in humid continental climates, and associated rainfall rate-radar reflectivity relationships. *J. Appl. Meteor.*, **7**, 901-907.

(7) Ulbrich, C.W., 1983: Natural variations in the analytical form of the raindrop size distribution., *J. Climate Appl. Meteor.*, **22**, 1764-1775.

(8) Nakamura, K., H. Inomata, T. Kozu, J. Awaka, and K. Okamoto, 1990: Rain observation by an X- and Ka-band dual-wavelength radar. *J. Met. Soc. Japan*, **68**, 509-521.

(9) CCIR, 1990: Propagation data and prediction methods required for Earth-space telecommunication systems. Report 564-3, Dusseldorf.

(10) Ippolito, L.J., 1971: Effects of precipitation on 15.3- and 31.65 GHz Earth-space transmissions with the ATS-V satellite. *Proc. IEEE*, **59**, 189-205.

(11) Howell, R.G., J. Thirlwell, and N.G. Golfin, 1977: Simultaneous 20 and 30 GHz attenuation measurements on a satellite-Earth path. *Electron. Lett.*, **13**, (21), 640-642.

(12) Fang, A.J., and J. M. Harris, 1979: Precipitation attenuation studies based on measurements of ATS-6 20/30-GHz beacon signals at Clarksburg, MD. *IEEE Trans. Antennas Propagat.*, **AP-27**, 1-11.

(13) Nackoney, O.G., and D. Davidson, 1979: Rain attenuation of 12/14 GHz satellite video transmissions. *Electron. Lett.*, **15** (22), 703-704.

(14) Thirlwell, J., and R.G. Howell, 1981: Slant-path attenuation measurements in the range 12-30 GHz using OTS and passive radiometers at Martlesham Heath, England. *IEE Conf. Publ.*, **195**, 29-35.

(15) Altshuler, E.E., and L.E. Telford, 1980: Frequency dependence of slant path rain attenuation at 15 and 35 GHz. *Radio Sci.* **15**, 781-796.

(16) Fukuchi, H., T. Kozu, K. Nakamura, J. Awaka, H. Inomata, and Y. Otsu, 1983: Centimeter wave propagation experiments using the beacon signals of CS and BSE satellites. *IEEE Trans. Antennas Propag.*, **AP-31**, 603-613.

(17) Kozu, T., J. Awaka, H. Fukuchi, and K. Nakamura, 1988: Rain attenuation ratios on 30/20- and 14/12-GHz satellite-to-Earth paths. *Radio Sci.*, **23**, 409-418.

(18) Stout, G.E. and E. A. Mueller, 1968: Survey of relationships between rainfall rate and radar reflectivity in the measurement of precipitation. *J. Appl. Meteor.*, **7**, 465-474.

(19) Goldhirsh, J., 1979: Predictive methods for rain attenuation using radar and in-situ measurements tested against the 28-GHz COMSTAR beacon signal. *IEEE Trans. Antennas Propag.*, **AP-27**, 398-406.

(20) Marshall, J.S. and W.M. Palmer, 1948: The distribution of raindrops with size. *J. Meteorol.*, **5**, 165-166.

(21) Itoh, S., 1987: A method for estimating atmospheric attenuation on Earth-space paths in fair and rainy weather. *Trans. IEICE Japan*, **J70-B**, 1407-1414, (in Japanese).

(22) Tanaka, H., T. Shinozuka, K. Nakamura, K. Koike, and H. Kuroiwa, 1980: ETS-II experiments, Part II, weather radar system. *IEEE Trans. Aerosp. Electron. Syst.*, **AES-16**, 567-580.

(23) Srivastava, R.C., 1971: Size distribution of raindrops generated by their breakup and coalescence. *J. Atmos. Sci.*, **28**, 410-415.

(24) Brazier-Smith, P.R., S.G. Jennings, and J. Latham, 1973: The influence of evaporation and drop-interactions on a rainshaft. *Quart. J. Roy. Meteor. Soc.*, **99**, 704-722.

(25) Kozu, T., K. Nakamura, J. Awaka, and M. Takeuchi, 1983: 14-GHz FM-CW radar for observation of precipitation.*Trans. IECE Japan*, **J66-B**, 1394-1401 (in Japanese).

(26) ——, ——, ——, and ——, 1987: Development of Ku-band FM-CW/Pulse-compression radar for rain observation on a slant-path. *J. Radio Res. Lab.*, **34**, (143), 95-113.

(27) Imai, N., Y. Otsu, and T. Tanaka, 1980: Main transmit and receive station in Japanese BSE program. *IEEE MTT-S Int. Microwave Symp.*, Washington, D.C., 281-283.

(28) Ulaby, F.T., R.K. Moore, and A.K. Fung, 1982: *Microwave remote sensing: Active and Passive*. Vol.II. Artech House, Norwood, MA, 457-1064pp.

(29) Kozu, T., H. Fukuchi, and Y. Otsu, 1986: Comparison of antenna noise temperature with rain attenuation of a satellite beacon signal at 12 GHz. *Electron. Lett.*, **22**, (24), 1274-1275.

(30) Dissanayake, A.W. and N.J. McEwan, 1978: Radar and attenuation properties of rain and bright band. *IEE Conf. Publ.* **169**, 125-129.

CHAPTER 4. STATISTICAL PROPERTIES OF DSD PARAMETERS

Natural DSDs are highly variable; however, it is known that they can be modeled reasonably well by three-parameter models such as gamma and lognormal models. In this chapter, we show the result of statistical properties of the gamma and lognormal DSD parameters derived from the Kashima disdrometer data described in Chapter 3. The knowledge of statistical properties of such DSD parameters are required to assess the values derived from a remote sensing technique, to make further modeling of DSD in terms of rain rate or Z factor dependences, temporal or spatial variations, and reducing the three-parameter model to a two-parameter model. Those modeling may provide a better accuracy in a wide range of radar rainfall measurements as well. Statistical analyses in this chapter include:

(1) Statistics of parameters of the gamma and lognormal DSD models; (2) rain rate and Z-factor dependences of the DSD parameters; (3) correlations among the DSD parameters; and (4) statistics of IRP relationships. We also check the validity of using the gamma and the log-normal models by means of a comparison of rain rates directly calculated from the disdrometer data and from estimated DSDs. There are several time scales in statistical analyses; long term (a season ~ a year) and short term (one rainfall event or less). In this chapter, we mainly deal with the long term statistics. The short term statistics will be studied in Chapter 5.

4.1 DSD Models and the Parameter Estimation Methods

We use gamma and lognormal distributions both of which have been used for the modeling of DSD (e.g. Ulbrich[1] and Feingold and Levin[2]). Especially, the gamma distribution has extensively been used in recent years as an alternative of the conventional exponential distribution. The gamma and lognormal models are given by

$$N(D) = N_0 D^m \exp(-\Lambda D) = N_T \frac{\Lambda^{m+1} D^m}{\Gamma(m+1)} \exp(-\Lambda D) \tag{4.1a}$$

$$N(D) = \frac{N_T}{\sigma D \sqrt{2\pi}} \exp\left(- \frac{(\ln D - \mu)^2}{2\sigma^2} \right) \tag{4.1b}$$

where D is drop diameter, $\Gamma(x)$ is the complete gamma function, [N_0, m and Λ] or [N_T, m and Λ] are parameters of the gamma model, and [N_T, μ and σ] are parameters of the

lognormal model. The parameters m+1 and Λ^{-1} are also called the shape parameter and the scale parameter, respectively. Although the parameter N_T, zeroth moment of the gamma or the lognormal model, is also recognized as an integral rain parameter (IRP), we treat it as a DSD parameter as well. Note that the zeroth moment of actual DSD is generally different from the parameter N_T obtained from the parameterization.

To estimate those DSD parameters from the disdrometer data, several methods have been employed; fitting the measured DSD directly with some weighting[2,3], Maximum Likelihood Estimation (MLE)[4,5], and Method of Moment (MoM)[6,7]. Although MLE is considered to provide more stable estimates than others, it is not practical for the estimation using remote sensing data because actual DSD samples are required for this method. (The same problem applies to the direct fitting method.) Since most remote sensing data are IRPs approximately proportional to moments of DSD, MoM is considered to provide the estimates most resemble to those obtained from actual radar measurements. A variety of combinations of the moments can be used for the DSD parameter estimation. Although the conventional MoM uses 0th, 1st and 2nd moments, for the present study, we use higher order moments; attenuation and Z factor approximated by 3rd and 4th moments for attenuation and 6th moment for Z factor. The assumption for attenuation corresponds to the situation in which rain attenuations are measured at two different frequencies; around 24 GHz and a millimeter wave (see Figure 2-3). Although using a millimeter-wave radar seems to be difficult at present, this may not be the case in the future[8]. For the DP measurement, we assume that only 4th and 6th moments are measured. For more precise radar measurement simulation, the orders of the moments for attenuation (and perhaps radar reflectivity, too) should be tuned more precisely depending on frequency; however, the use of the 3rd and 4th moments should be sufficient for the purpose of this chapter; to examine the variability in DSD parameters and their effects on multi-parameter radar measurements.

For the gamma DSD model, the xth moment of DSD, M_x, is expressed as

$$M_x = N_0 \frac{\Gamma(m+x+1)}{\Lambda^{m+x+1}} = N_T \frac{\Gamma(m+x+1)}{\Lambda^x \Gamma(m+1)} \tag{4.2a}$$

While for the lognormal model,

$$M_x = N_T \exp(x\mu + \frac{1}{2}x^2 \sigma^2). \tag{4.2b}$$

M_y and M_z are given similarly. For deriving Eq.4.2, we have assumed that the integral over drop diameter can be extended from zero to infinity. By knowing these DSD moments, and by solving the three simultaneous equations for the DSD parameters, estimates of DSD parameters may be obtained. Using $x = 3$, $y = 4$ and $z = 6$, together with the gamma model, estimates of the DSD parameters are obtained as follows (see Appendix 4-1 for the derivation):

$$m = \frac{11G - 8 + \sqrt{G(G+8)}}{2(1-G)}, \quad \text{with } G = \frac{M_4^3}{M_3^2 M_6} \tag{4.3}$$

$$\Lambda = (m+4)\, M_3/M_4 = (m+4)/D_m \tag{4.4}$$

$$N_0 = \Lambda^{m+4}\, M_3/\Gamma(m+4) \tag{4.5a}$$

$$N_T = \Lambda^3\, M_3\, \Gamma(m+1)/\Gamma(m+4) \tag{4.5b}$$

where D_m ($= M_4/M_3$) is the mass-weighted average diameter, and G is the inverse of the parameter G' in Ulbrich[1] that is the 3rd moment of the mass spectrum normalized by D_m^3. Similarly, letting L_x be the natural logarithm of M_x, lognormal DSD parameters are written

$$N_T = \exp[(24\, L_3 - 27\, L_4 - 6\, L_6)/3] \tag{4.6}$$

$$\mu = (-10\, L_3 + 13.5\, L_4 - 3.5\, L_6)/3 \tag{4.7}$$

$$\sigma^2 = (2\, L_3 - 3\, L_4 + L_6)/3. \tag{4.8}$$

One advantage to use the gamma model is that this model can be considered as an extension of the exponential distribution, the most widely used DSD model to date. Whereas, the log-normal model has advantages that each of the DSD parameters has clear physical meaning and that the DSD parameters ($\log N_T$, μ and σ^2) are linearly related to the moments of DSD[2].

In the case of dual-parameter measurement simulation for which two-parameter gamma or lognormal DSD model should be employed, we use only M_6 and M_4. Considering that the two-parameter gamma is an extension of the conventional exponential DSD model, we fix the parameter m. In this case, N_0 (or N_T) and Λ are given by

$$\Lambda = [(m+5)(m+6)\, M_4/M_6]^{1/2} \tag{4.9}$$

$$N_0 = \Lambda^{m+5}\, M_4/\Gamma(m+5) \tag{4.10a}$$

$$N_T = M_4\, \Lambda^4\, \Gamma(m+1)/\Gamma(m+5). \tag{4.10b}$$

Similarly, we fix σ for the lognormal model according to Feingold and Levin[2]. In this case, N_T and μ are given by

$$N_T = \exp(3L_4 - 2L_6 + 12\,\sigma^2) \tag{4.11}$$

$$\mu = (L_6 - L_4 - 10\,\sigma^2)/2. \tag{4.12}$$

As mentioned above, the DSD parameters derived by this method are similar to those to be estimated through the dual-parameter radar measurement combining radar reflectivity and microwave or millimeter wave attenuations.

Examples of the model fitting of disdrometer-measured DSD are shown in Figure 4-1.

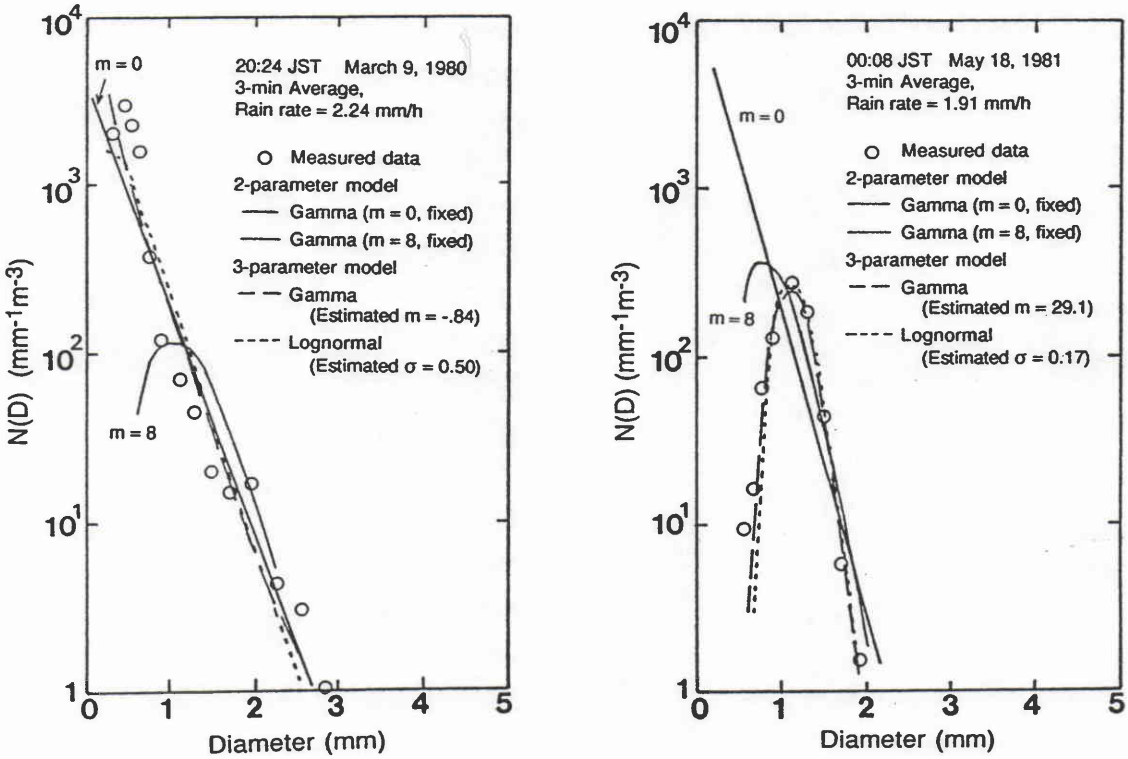

Figure 4-1. Examples of model fitting of measured DSD with the higher-order moment estimation.

The right example shows the result for very large m and very small σ, while the left one shows small (negative) m and large σ. It is found that the three parameter models are flexible enough to fit these two extreme DSDs very well. On the other hand, the two-parameter models do not seem to work well for the wide variability in DSD shape. As shown later, however, the two-parameter models can be used fine at least to estimate other IRPs the kernels of which are not different much from those of the measurables.

4.2 Statistics of DSD Parameters

Figures 4-2 to 4-4 show the histograms of the exponential, gamma and lognormal model parameters, respectively, as derived from Eqs.4.3~4.5 for the disdrometer data over the two years. Note that the logarithms of the DSD parameters have been used to make the histograms for N_0, N_T and Λ. In Figure 4-5, the cumulative distribution of N_0 of the exponential model for the data having rain rates higher than 3 mm/h is plotted on a normal distribution scale, showing that N_0 is approximately log-normally distributed. The histogram of N_0 in Figure 4-2 has some skewness, which is caused by the DSD variation at light rain rates. Similar properties have been observed for the N_T's of the gamma and lognormal models. Roughly speaking, it can be said that the pdf's of N_0 (gamma model, with $m \approx 0$~3 fixed), N_T's, and Λ are approximately log-normal. The same is true for $\log(m+4)$ as suggested by Eq.4.4. Major statistical quantities of those DSD parameters are listed in Table 4-1.

One of the interest in the DSD modeling with the gamma distribution is the values of m naturally found. It is shown that the values are clearly larger than zero (exponential distribution) and are sometimes very large (> 20). It should be noted that the m value is obtained from the higher order moments and may not represent the DSD shape at small to intermediate drop diameter region. As indicated from Eq.4.3, m can be extremely large as the parameter G approaches unity. Since G is determined by a relative magnitude among M_3, M_4 and M_6, it is expected that only a small DSD change causes a large variation in m when the DSD has a narrow standard deviation and therefore that such a large change in m is not significant in fitting the DSD. For comparison, we have derived m values from lower-order moments (e.g. M_0, M_1 and M_2) and have found that they are somewhat smaller and more stable than the m value derived from M_6, M_4 and M_3. This means that a part of the variation in m comes from natural and/or sampling fluctuations of DSD at larger drops. Later in this chapter, more discussion is made on the m value relating to the accuracy in rain rate estimation.

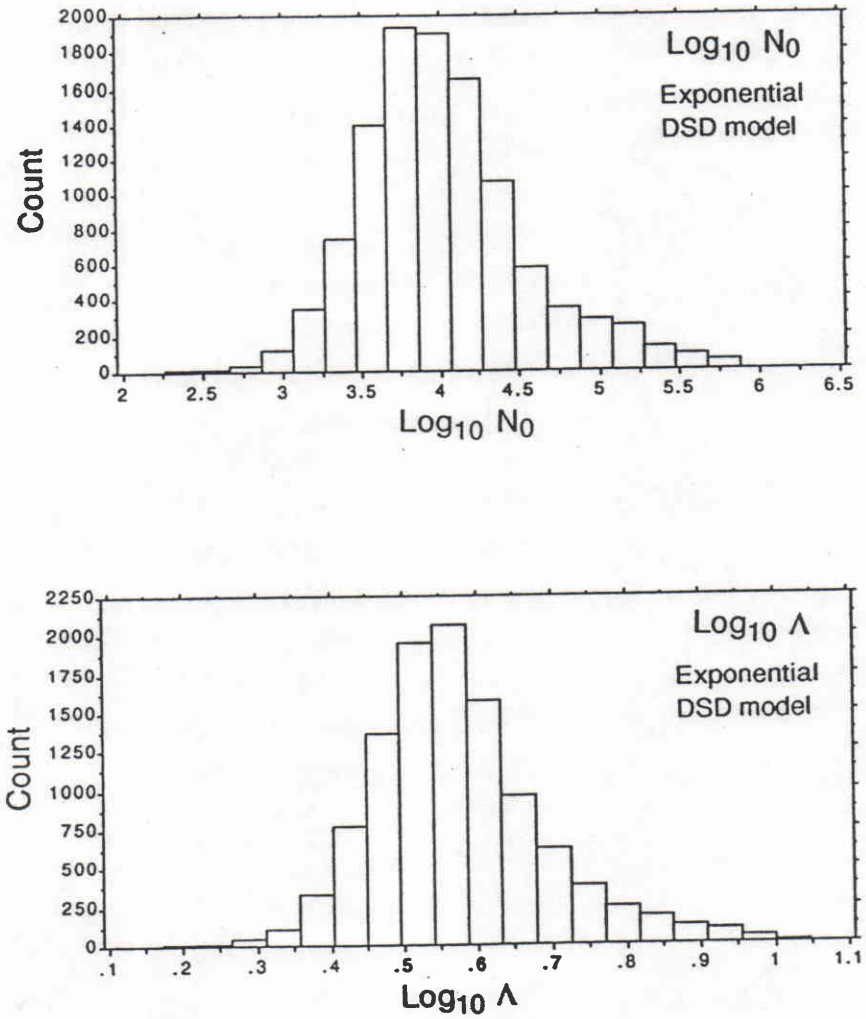

Figure 4-2. Histogram of exponential DSD model parameters.

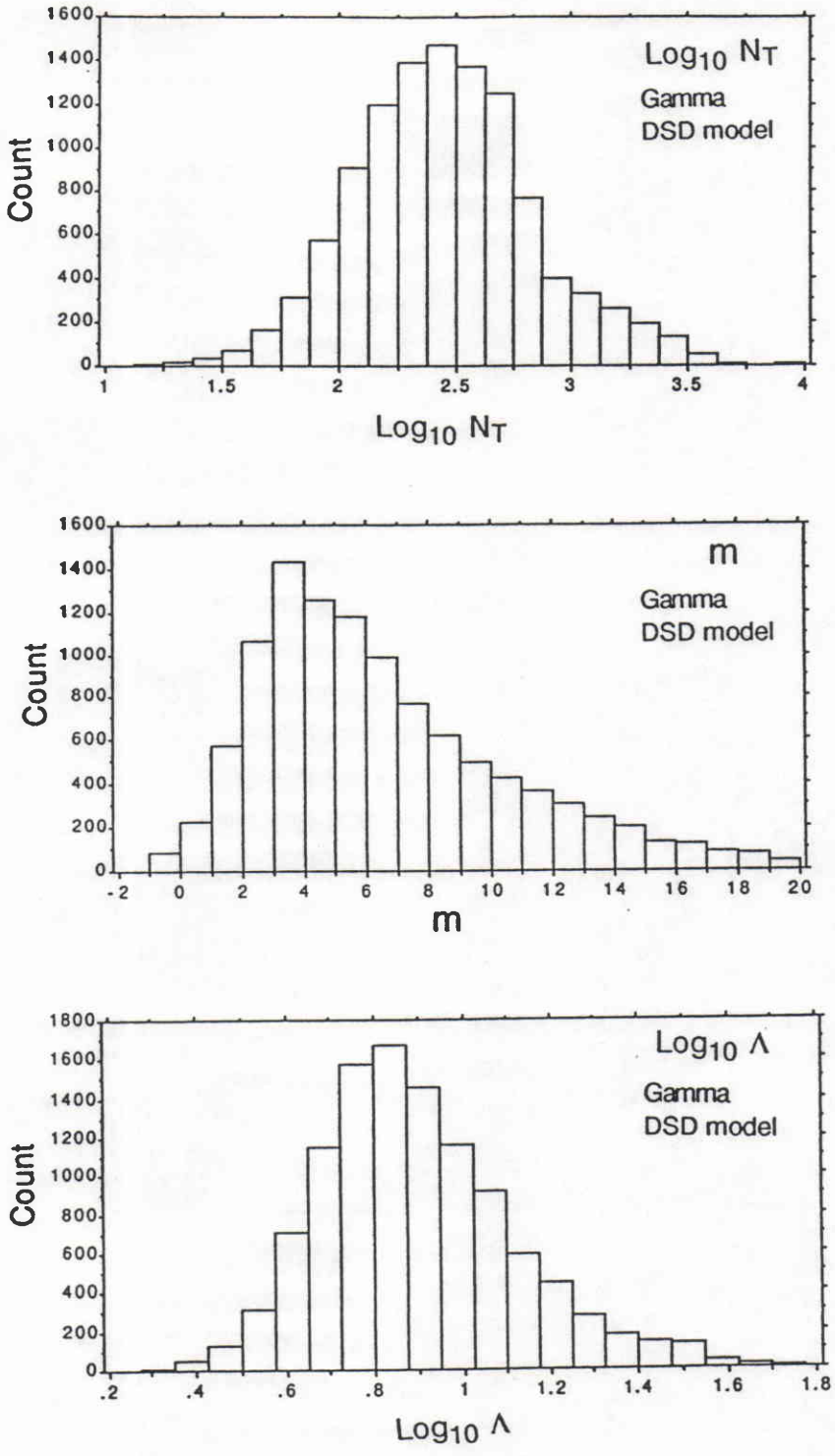

Figure 4-3. Histogram of gamma DSD model parameters.

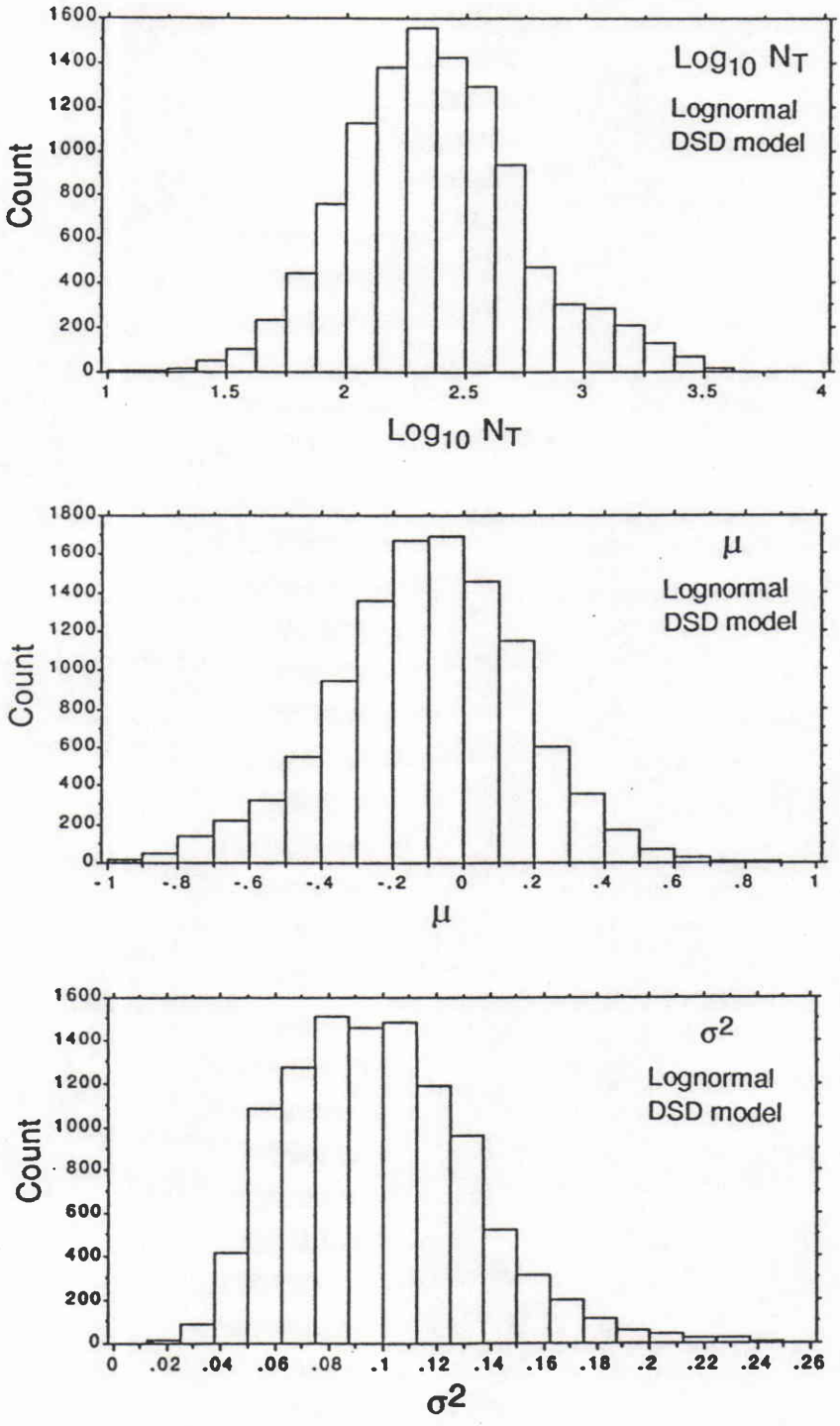

Figure 4-4. Histogram of lognormal DSD model parameters.

Table 4-1. Statistics of DSD parameters derived from disdrometer data.
(May 1979 ~ July 1981, 3-min averaged data, rain rate > 1 mm/h, total number of data = 10841)

Parameter	Mean	SD	Min	Max	Percentiles			Kurtosis	Skewness	
					10%	50%	90%			
$\log N_{0,exp}$	4.00	0.50	1.96	5.81	3.43	3.95	4.65	0.74	0.56	
$\log \Lambda_{exp}$	0.567	0.113	0.126	1.00	0.437	0.556	0.715	0.93	0.59	
$\log N_{T,gma}$	2.46	0.413	0.662	6.09	1.98	2.44	2.95	6.50	1.05	
$\log \Lambda_{gma}$	0.889	0.211	0.125	1.54	0.639	0.866	1.02	0.118	0.438	
m_{gma}	6.71	4.52	-0.99	30.0	2.22	5.65	12.8	3.29	1.47	*1
$\log (m_{gma}+4)$	1.00	0.17	0.478	1.53	0.794	0.985	1.23	0.02	0.21	
$\log N_{0,gma}$	6.09	2.22	1.72	16.0	4.03	5.50	8.99	3.35	1.69	
$\log N_{T,lgn}$	2.37	0.377	0.651	3.98	1.92	2.35	2.85	0.45	0.29	
μ_{lgn}	-0.102	0.272	-2.08	1.05	-0.441	-0.089	0.221	1.10	-0.33	
σ^2_{lgn}	0.099	0.036	0.012	0.550	0.057	0.095	0.143	6.02	1.23	
$\log N_{T,gma0}$	3.43	0.409	1.78	4.85	2.96	3.39	3.98	0.42	0.46	*2
$\log N_{T,gma3}$	2.65	"	0.993	4.06	2.17	2.61	3.19	"	"	
$\log N_{T,gma6}$	2.39	"	0.741	3.81	1.92	2.35	2.94	"	"	
$\log \Lambda_{gmao}$	0.567	0.113	0.126	1.00	0.437	0.556	0.715	0.93	0.59	*4
$\log \Lambda_{gma3}$	0.758	"	0.316	1.19	0.627	0.746	0.905	"	"	
$\log \Lambda_{gma6}$	0.889	"	0.448	1.32	0.759	0.878	1.04	"	"	
$\log N_{T,lgn1}$	2.21	0.409	0.560	3.63	1.74	2.17	2.76	0.42	0.46	*3
$\log N_{T,lgn2}$	2.28	"	0.626	3.70	1.80	2.24	2.83	"	"	
$\log N_{T,lgn3}$	2.45	"	0.794	3.87	1.97	2.41	2.99	"	"	
μ_{lgn1}	0.050	0.261	-0.949	1.06	-0.290	0.076	0.350	0.93	-0.59	
μ_{lgn2}	-0.013	"	-1.01	0.999	-0.351	0.013	0.289	"	"	
μ_{lgn3}	-0.174	"	-1.17	0.846	-0.517	-0.149	0.126	"	"	
cf. $\log M_0$ (meas'd)	2.48	0.360	0.656	3.57	2.03	2.49	2.94	0.27	-0.06	

*1 In the estimation of m, the value is limited between -0.99 and 30.0.

*2 gma0, gma3, gma6 represent the gamma model with fixed m values of 0, 3, and 6, respectively.

*3 lgn1, lgn2, lgn3 represent the lognormal model with fixed σ values of 1.30, 1.33, and 1.40, respectively.

*4 Λ_{gma0} is the same as Λ_{exp}.

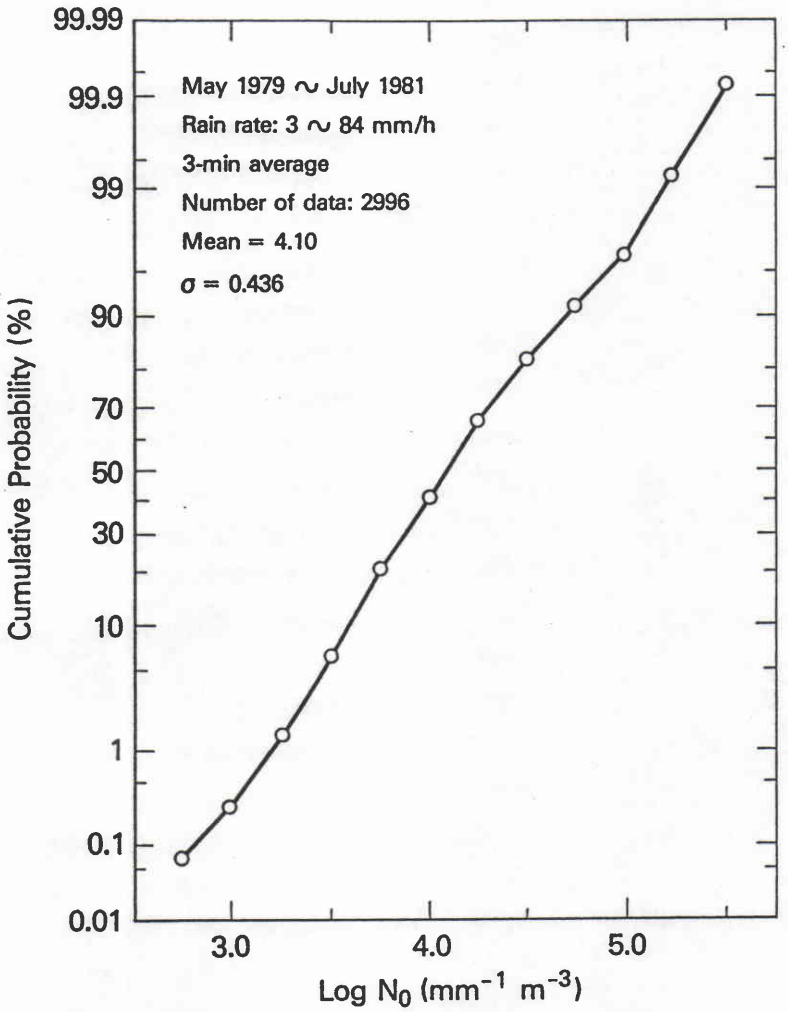

Figure 4-5. Cumulative distribution of N_0 of the exponential DSD model.

4.3 Interrelations among DSD Parameters and DSD Moments

4.3.1 Rain rate and Z factor dependences of DSD parameters

There has been a wide range of interest in the problem how DSD parameters change with rain rate, the most widely used rain parameter. This is because the knowledge of such relationships is useful to estimate various IRP relations such as Z-R relation, and to model DSD's at other locations where only rain rate data are available. Similarly, the Z factor dependence would be useful to make a modeling of DSD in radar measurements in which Z factor profile is a primary output.

Figures 4-6 to 4-8 show respectively the rain rate dependences of the exponential, gamma, and lognormal model parameters. The large variabilities in these DSD parameters are also clear in these figures. It is also found that the variability is generally larger in light ($\lesssim$3 mm/h) to moderate (3 ~ 15 mm/h) rain rates; at heavy rain rates ($\lesssim$ 15 mm/h), the DSD parameters are much less variable. This suggests that physical processes producing heavy rain rates at Kashima are relatively similar. On the other hand, light to moderate rain rates should be generated from various precipitation processes which result in the large variation in DSD. Similar properties have also been obtained for the relations between the DSD parameters and Z. From those results, the following conclusions are drawn (subscripts "exp", "gma" and "lgn" represent the values for the exponential, gamma and lognormal models, respectively):

(1) Λ_{exp} and Λ_{gma} are clearly dependent on R and Z.

(2) N_{0exp} has only a small and little dependences on R and Z, respectively.

(3) N_{Texp}, N_{Tgma} and N_{Tlgn} have similar properties to N_{0exp} but for somewhat larger dependences on R and Z.

(4) The parameter m has small R and Z dependences, indicating that DSD is somewhat more concave-down at heavy rain rates than light rain rates, although the variability of m at light rain rates is very large.

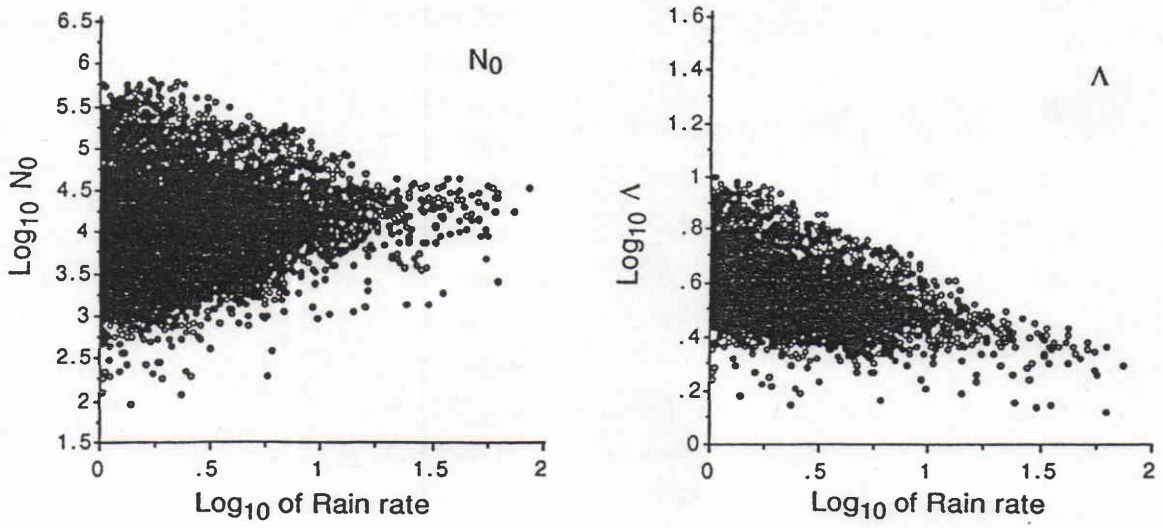

Figure 4-6. Rain rate dependences of the exponential DSD parameters, May 1979 ~ July 1981.

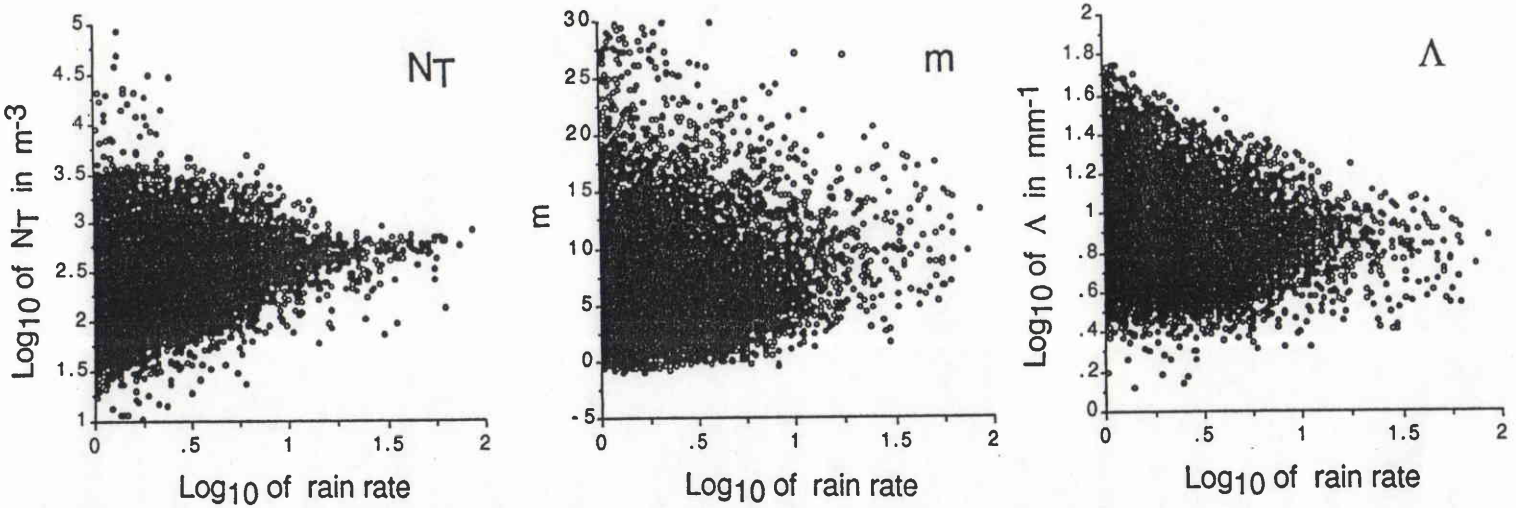

Figure 4-7. Rain rate dependences of the gamma DSD model parameters, May 1979 ~ July 1981.

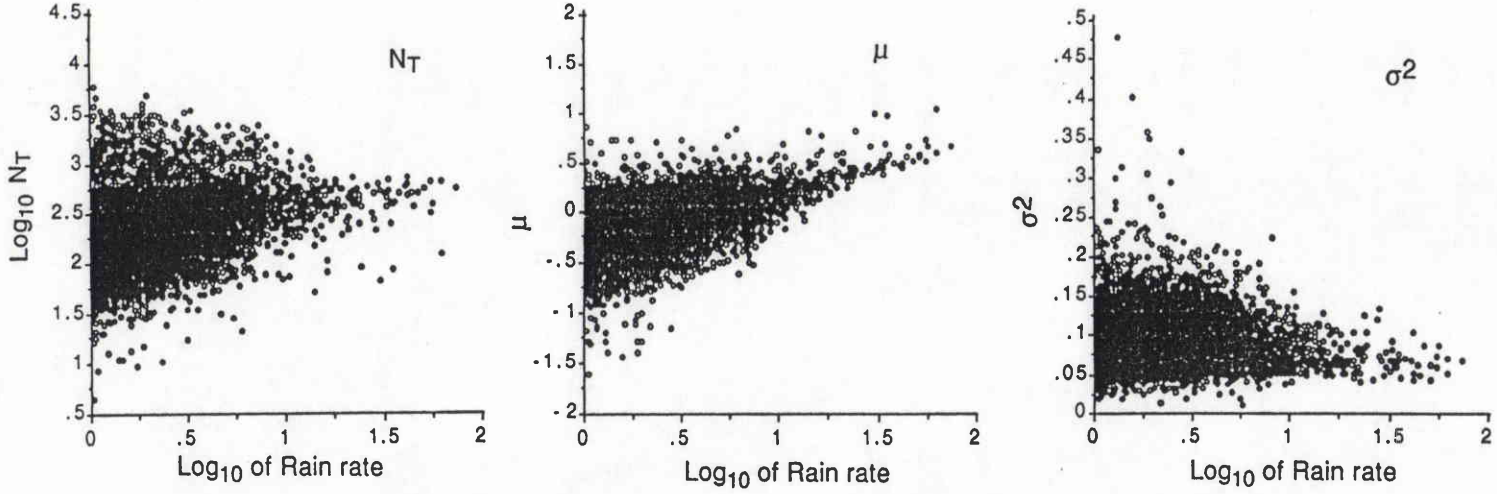

Figure 4-8. Rain rate dependences of the lognormal DSD model parameters, May 1979 ~ July 1981.

The clear correlation between Λ_{exp} and R (and Z) and the less clear correlation between N_{0exp} and R (and Z) are partly caused by the functional relation between the DSD parameters and the xth moment of DSD, M_x:

$$\log M_x = \log \Gamma(x+1) + \log N_{0exp} - (x+1) \log \Lambda_{exp} \qquad (4.13)$$

which states that the greater the value of x is, the more the effect of variations in Λ_{exp} due to the coefficient $(x+1)$ is, while the effect of variations in N_{0exp} is independent of the order of the moment. Similar explanation may be applied to the gamma distribution, although the situation is somewhat more complicated in the case of the 3-parameter gamma model because the parameter m is also variable. Physical DSD properties may force the N_{0exp} value constant regardless of R or Z, as proposed in earlier works by Marshall and Palmer[3], and Joss et al.[9]. Table 4-2 lists least-square regression results of relations between DSD parameters and rain rate. Since the distribution of rain rate is very nonuniform, weighting factors inversely proportional to the density of rain rate have been used for the regression. We have found that the DSD models shown in Table 4-2 (except the 3-parameter gamma) have excellent consistencies between assumed and calculated rain rates (within 3%), and therefore they can be used as typical gamma DSD models in place of the conventional exponential models such as MP and J-D models to calculate various IRPs.

Table 4-2 Rain-rate dependence of DSD parameters for two-parameter gamma, and three-parameter gamma and lognormal models.

Two-parameter gamma			
$m = 0$	$N_0 = 9057\, R^{0.177}$,	$N_T = 2046 R^{0.365}$,	$\Lambda = 4.37\, R^{-0.176}$
$m = 3$	$N_0 = 1.19\times10^5\, R^{-0.352}$,	$N_T = 337 R^{0.365}$,	$\Lambda = 6.78\, R^{-0.176}$
$m = 6$	$N_0 = 1.44\times10^6\, R^{-0.880}$,	$N_T = 189 R^{0.365}$,	$\Lambda = 9.16\, R^{-0.176}$
Three-parameter gamma and lognormal			
Gamma	$N_T = 255\, R^{0.187}$,	$\Lambda = 8.37\, R^{-0.0715}$,	$m + 4 = 9.02 R^{0.114}$
Lognormal	$N_T = 202\, R^{0.231}$,	$\mu = 0.523 \log_{10} R - 0.312$,	
	$\sigma^2 = -0.0238 \log_{10} R + 0.108$		

4.3.2 Correlations between DSD parameters and between IRPs

In the previous section, we have studied the relation between DSD parameters and rain rate or Z factor. The other interest has been if all the three DSD parameters in the gamma or the lognormal models should be treated as independent parameters, and if one of the three

parameters can be fixed or not. It should be noted that answers to these questions generally depend on the combination of IRPs to be employed to derive the DSD parameters. For example, if all IRPs of interest are only higher order moments, simple two-parameter models (e.g. exponential model) may be enough because the DSD modeling need not take care of the variation in DSD at small drop diameters, enabling the modeling much simpler. Figure 4-9 shows the correlations between m and log N_0 and between m and log Λ for the gamma distribution. As shown in these figures, there are high correlations between m and other parameters. The existence of the N_0-m relation was suggested by Ulbrich[1] to reduce the three-parameter gamma to the two-parameter gamma distribution; however, it has also been pointed out that such a relation could come from a statistical correlation between DSD parameters rather than due to physical DSD properties[10]. The Λ-m relation is also due to a statistical correlation between Λ and m, and expected from Eq.4.4 which states that Λ is given by the product of m+4 and D_m^{-1}. Since D_m is fairly stable, the large variation in m as seen in Figures 4-3 and 4-7 is directly reflected to the variation in Λ. These correlations are also recognized as a "compensation" effect to give reasonable IRP values. On the other hand, there are little correlation between N_T and Λ and N_T and m, as shown in Figure 4-10. This may be due to the fact that the total drop concentration, N_T, follows the Poison distribution and independent of the physical processes producing the "shape" of DSD and determine the other DSD parameters, Λ and m. For this reason, Chandrasekar and Bringi[10] recommend the use of N_T rather than N_0 as one of the gamma DSD parameters.

It is not clear at present that the relationships shown above are useful to reduce the three parameter DSD model to a two-parameter model because the high correlations are essentially caused by the large variation in m. Considering that the large m value is caused by a minor fluctuation in G (see Eq.4.3) and it is not so essential to fit the natural DSD reasonably, we can restrict the m value within a range between 0 to 8, for example. In such case, correlations in the N_0-m relation and the Λ-m relation are not high as can be seen from Figure 4-9. More study is needed on the problem how the gamma DSD parameters should be defined and on the same problem for the lognormal model.

Later in this chapter, we will test more straightforward scheme to reduce the three parameter DSD model to a two-parameter model; to fix one of the three DSD parameters as has been tried by many researchers.

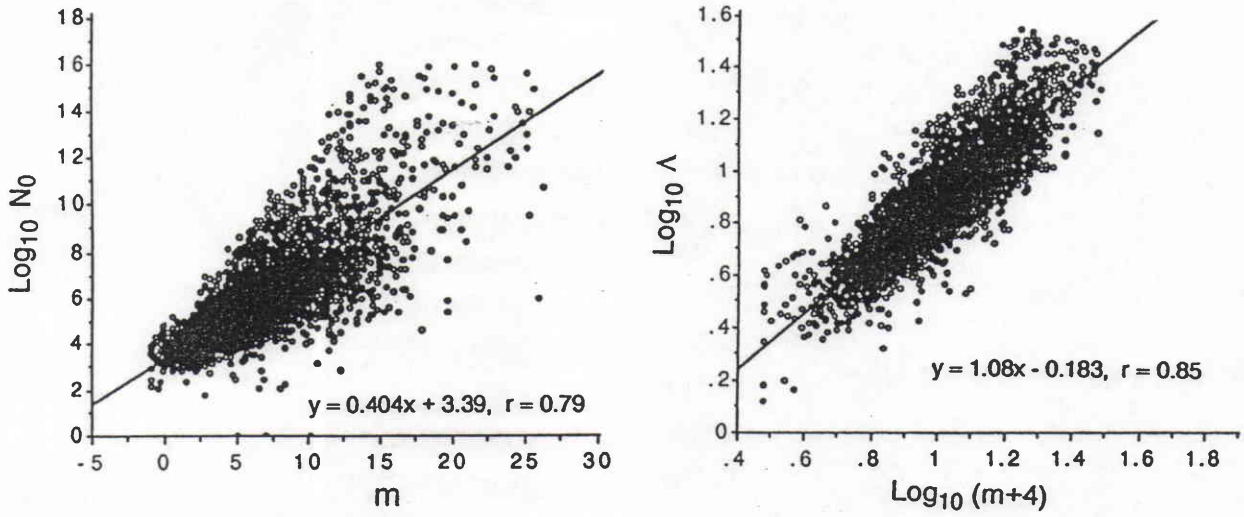

Figure 4-9. Scattergrams of the gamma DSD model parameters; m vs. log N_0 and log (m+4) vs. log Λ.

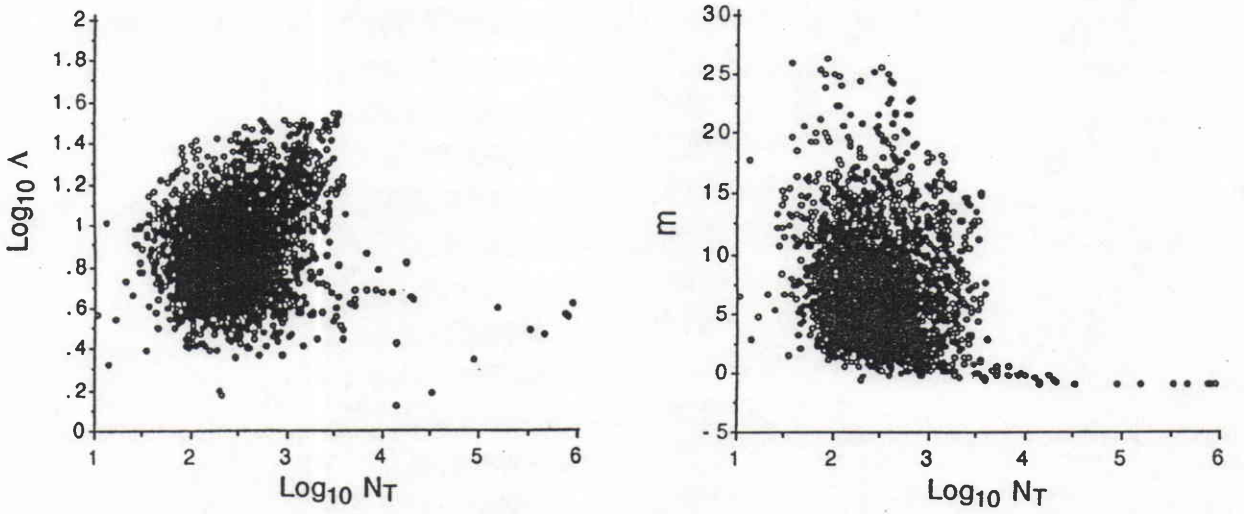

Figure 4-10. Scattergrams of the gamma DSD model parameters; log N_T vs. log Λ and log N_T vs. m.

4.3.3 Relations between IRPs

A. Correlation between two different moments

Because of the fluctuation in DSD, the relationship between different moments changes from time to time. Figure 4-11 shows scattergrams of rain rate versus several moments ranging from M_0 to M_6. It is clearly shown that the correlation becomes low when the order of the moment departs from that for rain rate (≈ 3.67). Chandrasekar and Bringi[10] derived the correlation coefficient between M_x and M_y, r_{xy} in the case where DSD fluctuation is solely due to statistical sampling error:

$$r_{xy} = \frac{\Gamma(m+x+y-b+1)}{\Gamma(m+2x-b+1)^{1/2}\,\Gamma(m+2y-b+1)^{1/2}} \tag{4.14}$$

where m is the gamma DSD parameter, and b (= 0.67) is the exponent of a power-law relation between the terminal velocity of raindrops versus drop diameter (Eq.2.12). For deriving Eq.4.14, it is assumed that the DSD follows a gamma distribution, that total number of raindrops follows Poisson distribution, that sampling volume (for a given diameter range) is proportional to the terminal velocity (Eq.2.12), and that realizations of DSD are independent and identically distributed[10].

It should be noted that r_{xy}'s between higher-order moments are fairly high even when only statistical DSD fluctuations exist (see Fig.4-12). Thus, we should be careful in interpreting IRP relationships derived from DSD data with a small sampling volume (or short integration time) in which the sampling error can be a dominant cause of DSD variation. As discussed in 3.1.2, however, the sampling fluctuation (for Poisson process) in the 3-min averaged disdrometer data is relatively minor, and therefore the data should well represent physical DSD variations as well as the sampling fluctuation regarding the gamma pdf (if any).

Correlation analyses are made of the moments calculated from disdrometer data. The resultant correlation coefficients are then compared with the value calculated with Eq.4.14. To investigate short-term and long-term DSD fluctuations, three kinds of time segments have been used; short-term (0.5 ~ 1.5 hours within a rain event), intermediate term (several days) and long-term (several months). The results obtained from each time segment are then averaged, and plotted on Figure 4-12 as well as the theoretical curve (Eq.4.14). It is found that in general the correlation coefficients obtained from the disdrometer data are higher than the theoretical results assuming reasonable m values of 0 ~ 8, especially for short-term

correlation coefficients and the values between higher order moments. One simple example of "physical" DSD variation would be the Marshall-Palmer (MP) distribution (Eq.2.16) in which the parameter N_0 is constant. Correlation coefficients between IRPs obtained from the DSD variation according to the MP distribution are almost unity (see 5.2). The result shown in Figure 4-12 suggests the existence of such systematic DSD change due to some physical precipitation processes causing the higher correlation, especially for intermediate to large drops within a rain event.

B. Relations between Ze, R, attenuation coefficient and liquid water content

It is convenient to derive power law relationships between physically meaningful IRPs; effective radar reflectivity factors (*Ze*), attenuation coefficients (*k*) at several frequencies, rain rate (*R*) and liquid water content (*W*). Table 4-3 summarizes the resulting power law relations as derived from linear regression between logarithms of two different IRPs. For calculating those IRPs, equations summarized in Table 2-1 have been used together with the two-year disdrometer data, σ_b and σ_t values calculated with the Mie theory, and the raindrop terminal velocity given by Eq.2.11. For comparison, the relations obtained with assuming typical exponential distributions (MP, J-D and J-T distributions, see Section 2.1.5) are also shown. Table 4-4 summarizes RMS errors to estimate *Ze* form *R* and *k* from *R* using the *Ze-R* and *k-R* relations shown in Table 4-3 (actually, the errors to estimate logarithms of those values). We can see that estimating *k* from *R* (and vice versa) is much less erroneous than estimating *Ze* from *R* (and vice versa). RMS errors to estimae *k* from *Ze* using the *k-Ze* relations have been found to be 1.4 ~ 1.5 dB.

Since DSD may be dependent upon rainfall type, there may be some seasonal variation in the relation between IRPs. As one example of the relations sensitive to the DSD variation, Figure 4-13 shows the seasonal variation of the relation between *Z* and rain rate derived from the 2-year disdrometer data. In the figure, open circles and associated bars represent the mean and ± standard deviation of $\log_{10} Z$ corresponding to the rain rate range shown in the figure. It is found from the results for the two lower rain rate ranges that the mean and the standard deviation of *Z* factor for the same rain rate in winter season are, respectively, higher and smaller than those in other seasons. Those results suggest that winter rainfall at Kashima has relatively similar characteristics (i.e. *Z-R* relation) giving rather higher *Z* factor. The larger standard deviation of *Z* factor for rainfalls in other seasons should be a consequence of the fact that there are various types of rainfall from spring to fall.

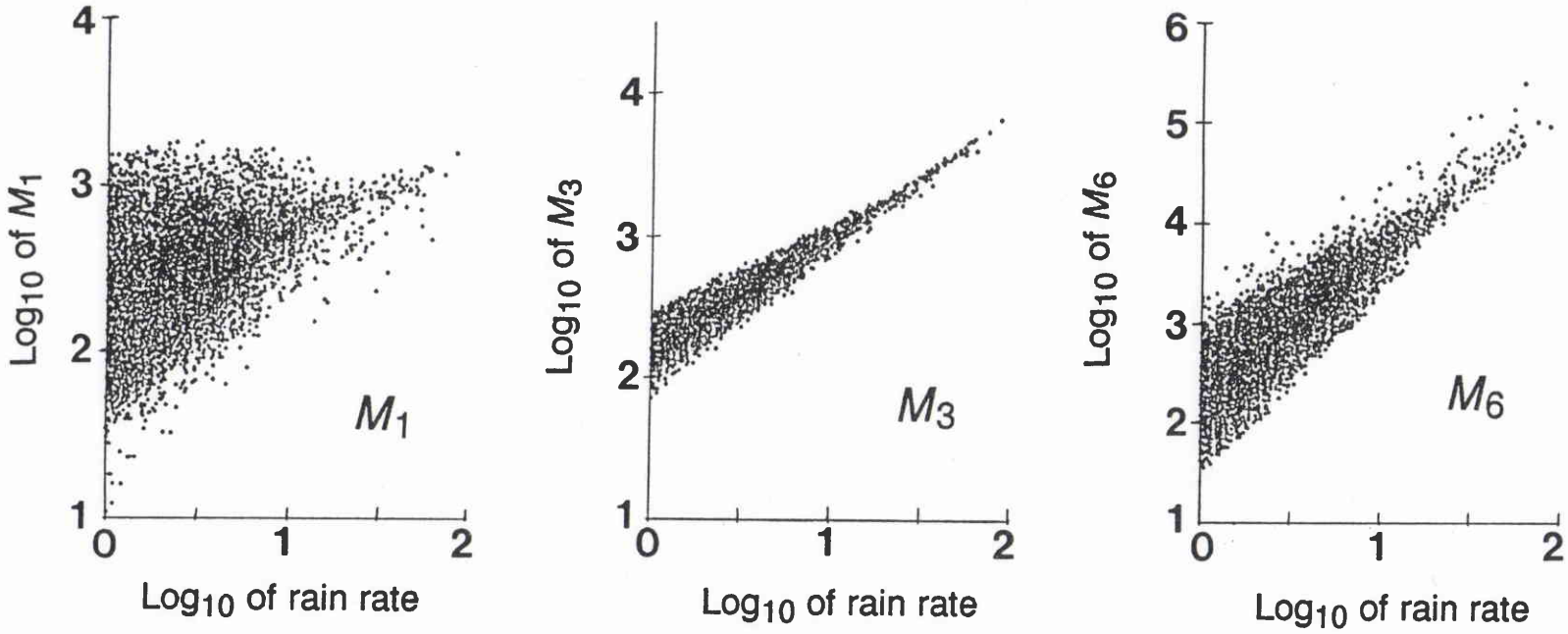

Figure 4-11. Scattergrams of rain rate versus moments; M_1, M_3, M_6.
(Disdrometer data, May 1979 ~ July 1981)

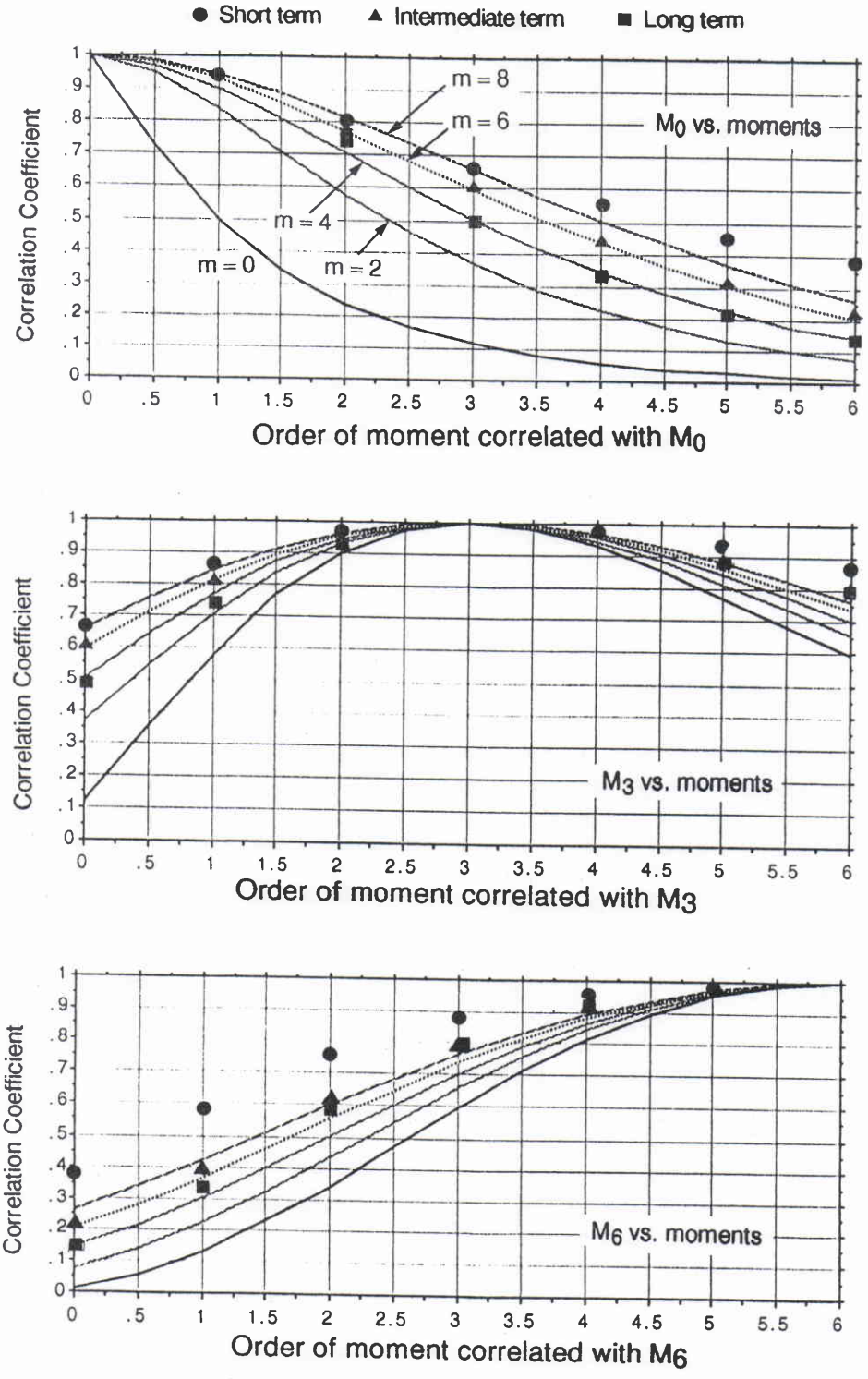

Figure 4-12. Correlation coefficients between moments of DSD; theoretical calculation (curves) and those obtained from disdrometer data for several temporal scales.

Table 4-3. Important IRP relationships derived from linear regressions between the logarithms of IRPs. Rain rate 1 ~ 100 mm/h, drop temperature 10°C.

• Disdrometer data

	Rain rate range	
Ze-R relations	1 ~ 100 mm/h	3 ~ 100 mm/h
Z (Rayleigh) - *R*	$Z = 224\ R^{1.37}$	
Ze (5.30 GHz) - *R*	$Ze = 217\ R^{1.36}$	$Ze = 227\ R^{1.33}$
Ze (10.0 GHz) - *R*	$Ze = 209\ R^{1.38}$	$Ze = 209\ R^{1.37}$
Ze (13.8 GHz) - *R*	$Ze = 217\ R^{1.42}$	$Ze = 220\ R^{1.41}$
Ze (17.2 GHz) - *R*	$Ze = 235\ R^{1.44}$	$Ze = 244\ R^{1.42}$
Ze (24.2 GHz) - *R*	$Ze = 270\ R^{1.43}$	$Ze = 296\ R^{1.38}$
Ze (34.5 GHz) - *R*	$Ze = 284\ R^{1.33}$	$Ze = 332\ R^{1.24}$
k-R relations		
k(10.0 GHz) - *R*	$k = 0.00988\ R^{1.13}$	$k = 0.00914\ R^{1.17}$
k(13.8 GHz) - *R*	$k = 0.0239\ R^{1.14}$	$k = 0.0230\ R^{1.16}$
k(17.2 GHz) - *R*	$k = 0.0421\ R^{1.13}$	$k = 0.0415\ R^{1.14}$
k(24.2 GHz) - *R*	$k = 0.0924\ R^{1.11}$	$k = 0.0927\ R^{1.10}$
k(34.5 GHz) - *R*	$k = 0.209\ R^{1.08}$	$k = 0.215\ R^{1.06}$
k-Ze(13.8 GHz) relations		
k(10.0 GHz) - *Ze*	$k = 0.000191\ Ze^{0.743}$	
k(13.8 GHz) - *Ze*	$k = 0.000448\ Ze^{0.748}$	
k(17.2 GHz) - *Ze*	$k = 0.000816\ Ze^{0.741}$	
k(24.2 GHz) - *Ze*	$k = 0.00190\ Ze^{0.728}$	
k(34.5 GHz) - *Ze*	$k = 0.00440\ Ze^{0.721}$	
W-R relation	$W = 0.0674\ R^{0.872}$	$W = 0.0664\ R^{0.881}$

• Typical exponential distribution (MP, J-D and J-T). Rain rate, 0.5 ~ 80 mm/h.

Ze-R relations	J-D		MP		J-T	
($Ze = a\ R^b$)	*a*	*b*	*a*	*b*	*a*	*b*
Ze(10.0 GHz) - *R*	115	1.51	211	1.59	557	1.62
Ze(13.8 GHz) - *R*	119	1.55	234	1.59	661	1.55
Ze(17.2 GHz) - *R*	126	1.56	258	1.55	713	1.46
Ze(24.2 GHz) - *R*	141	1.51	290	1.44	692	1.27
Ze(34.5 GHz) - *R*	149	1.42	270	1.29	467	1.09
k-R relations ($k = a\ R^b$)	J-D		MP		J-T	
k(10.0 GHz)-*R*	.00952	1.12	.0101	1.20	.0136	1.23
k(13.8 GHz)-*R*	.0212	1.13	.0237	1.17	.0317	1.16
k(17.2 GHz)-*R*	.0363	1.12	.0411	1.14	.0530	1.13
k(24.2 GHz)-*R*	.0794	1.10	.0897	1.11	.1103	1.07
k(34.5 GHz)-*R*	.1782	1.08	.204	1.05	.236	.974

Table 4-4. RMS dB errors to estimate Z from R, and k from R using the IRP relations shown in Table 4-3. (disdrometer data, R = 1 ~ 100 mm/h, May 1979 ~ July 1981).

Estimating k		Estimating Ze	
		Ze (5.3 GHz)	2.4 dB
k (10.0 GHz)	0.88 dB	Ze (10.0 GHz)	2.5 dB
k (13.8 GHz)	0.91 dB	Ze (13.8 GHz)	2.8 dB
k (17.3 GHz)	0.83 dB	Ze (17.3 GHz)	2.9 dB
k (24.2 GHz)	0.67 dB	Ze (24.2 GHz)	2.9 dB
k (34.5 GHz)	0.54 dB	Ze (34.5 GHz)	2.5 dB

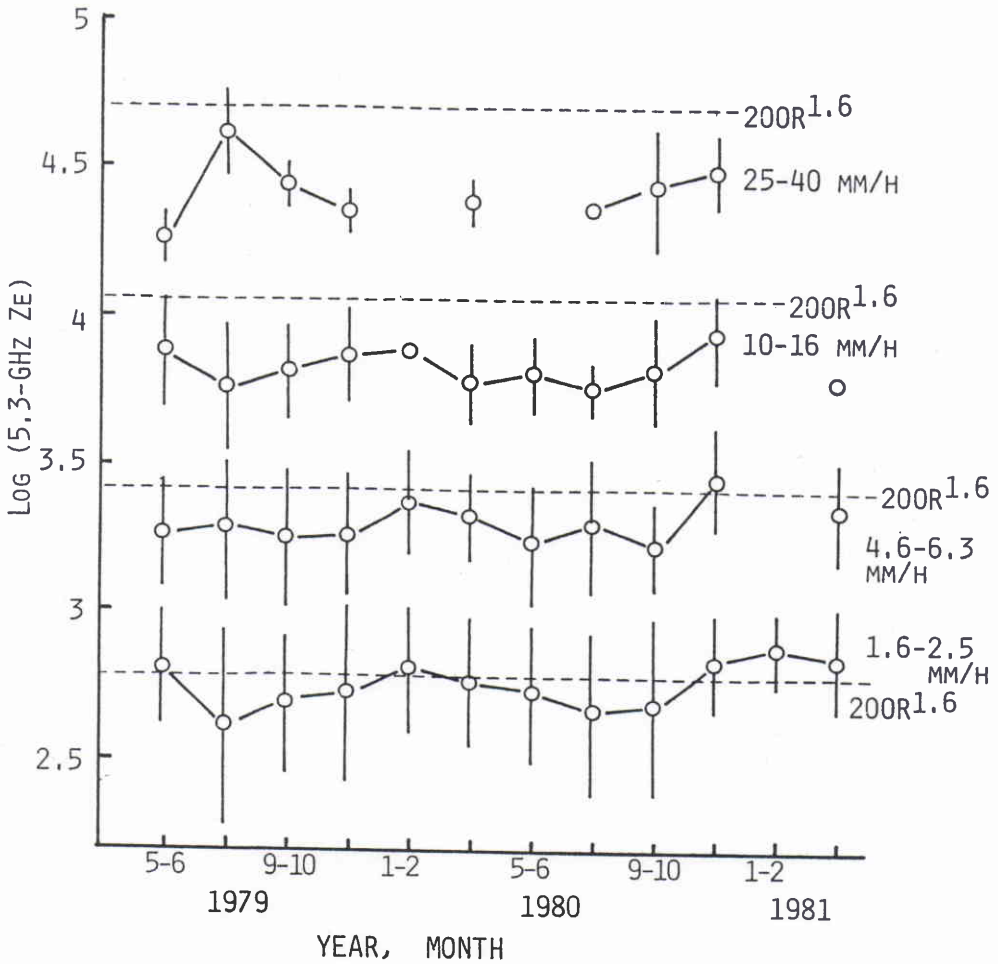

Figure 4-13. Seasonal variation in the relation between Z factor and rain rate derived from the 2-year disdrometer data.

4.4 Tests of Rain Rate Estimation Accuracy by SP and DP Measurements

A major purpose to estimate DSD by radar measurements is to improve the accuracy in estimating meteorological quantities of interest. In this section, we test the validity of using the three-parameter or two-parameter gamma and lognormal models by means of comparisons of estimated rain rate with "measured" (i.e., directly calculated from the measured DSD) one. Those rain rates are calculated using the raindrop terminal velocity approximated by Eq.2.11. Figure 4-14 shows the scattergrams of "measured" rain rate versus rain rates estimated by an SP measurement (Z-R method), a DP measurement using the exponential model, and two TP measurements using the gamma and lognormal models. To evaluate the accuracy in the rain rate estimation, we use RMS deviation (*RMS-dev*) in dB unit and Average Probability Ratio (*APR*). The former is defined by

$$RMS\text{-}dev = 10\sqrt{\frac{1}{n}\sum_{i=1}^{n}(\log_{10} R_{est,i} - \log_{10} R_{meas,i})^2} \qquad (4.15)$$

where n is the number of data points, R_{est} and R_{meas} are estimated and "measured" rain rates, respectively. The latter is defined by

$$APR = \frac{1}{N}\sum_{i=1}^{N}(P_{est,i} / P_{meas,i}) \qquad (4.16)$$

where P_{est} and P_{meas} denote the cumulative probabilities of estimated and measured rain rates, respectively, and i stands for the value at rain rate R_i. The sampling from $i = 1$ to N is made appropriately over the cumulative distributions. *APR* is a measure of bias error, giving larger weight to higher rain rates.

It is shown that significant improvement is achieved by increasing the number of estimated DSD parameters from one to two. Further improvement is obtained by increasing the number from two to three although the improvement is not as drastic as the former case. This feature is similar to the results shown in Atlas et al.[11].

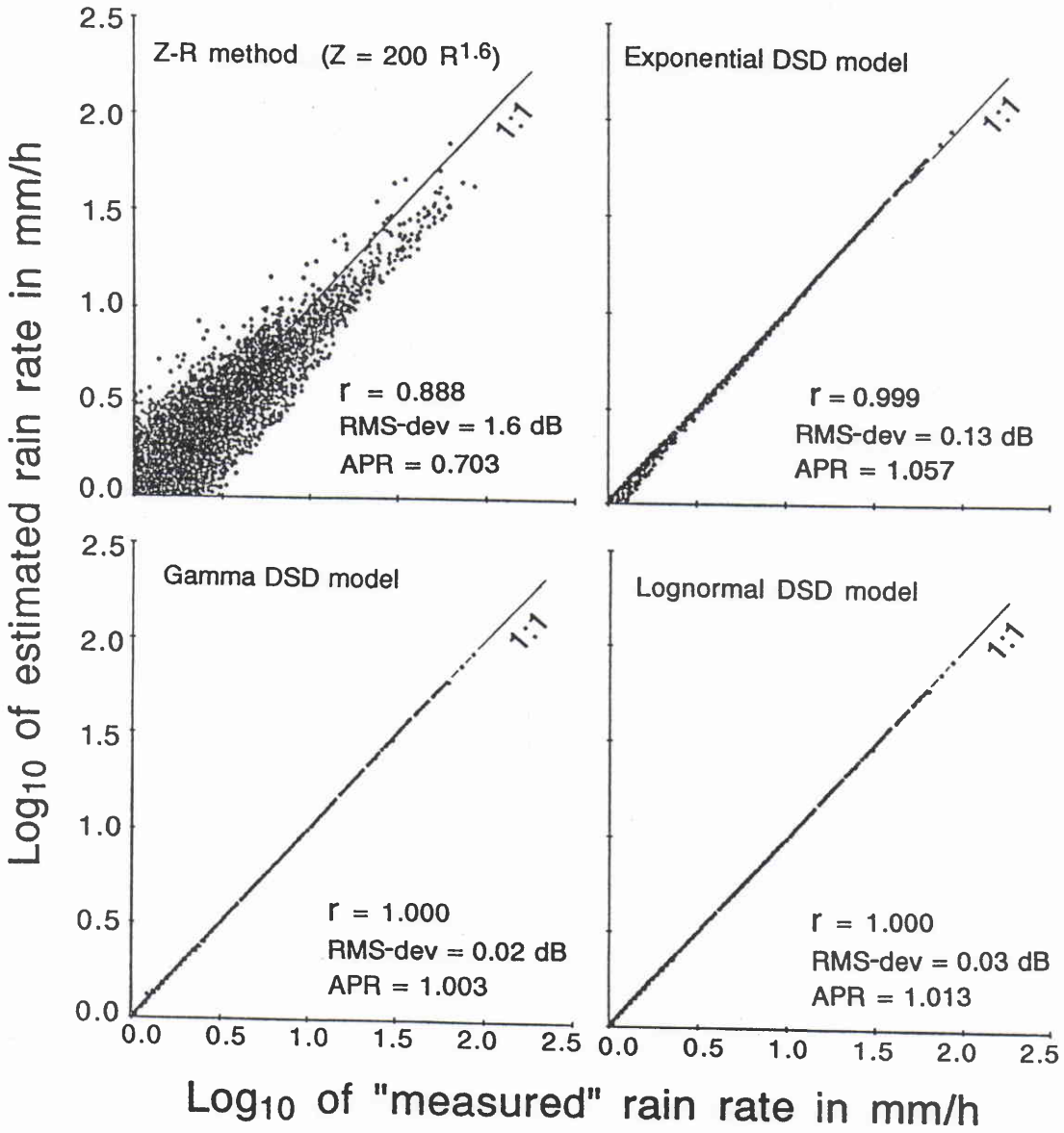

Figure 4-14. Comparison of rain rate estimates by an SP measurement (Z-R method), a DP measurement using the exponential DSD model, and two TP measurements using the gamma and lognormal DSD models.

For reducing the number of independent DSD parameters, it has been common to fix one of the parameters, specifically m for gamma[12-14] and σ for lognormal models[2,15]. Dependence of rain rate estimation accuracy on m or on σ is examined by a simulation of DP measurements using M_4 and M_6. The results, which are summarized in Figure 4-15, indicate that m from 6 to 8 and σ from 0.28 to 0.29 give the lowest RMS and bias errors, although the accuracy is not very sensitive to the shift in m and σ. The similarity in the kernel between k and R probably contributes to this insensitivity, because a comparison of rain rate estimates deduced from various combinations of moments, (M_0,M_6), (M_2,M_6), etc., has indicated that the estimation accuracy becomes more sensitive to the choice of m when the kernel of the moment combined with M_6 becomes far from that for rain rate (≈ 3.67).

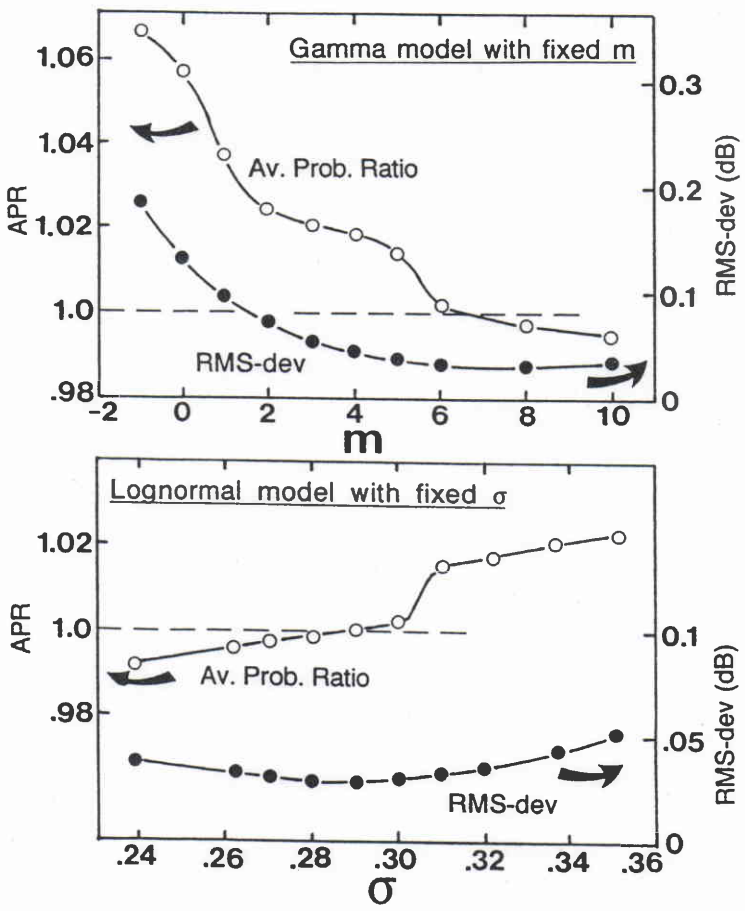

Figure 4-15. Dependence of rain rate estimation accuracy on the gamma DSD parameter m and on the lognormal DSD parameter σ.

- *Discussion on the "best" m value*

The best m and σ values (in the sense that they provide the lowest RMS deviation) obtained here are somewhat different from the results of previous works using Z and Z_{DR} combinations ($m = 2 \sim 5$ [12-14]: $\sigma = 0.34$ [15] †). Although the accuracy remains excellent over fairly wide ranges of m and σ (see Figure 4-15), it may be worth making some comments on the m and σ values obtained here. We make comments only on the m value since the same discussion can be made just by noting that "large" m corresponds to "small" σ.

We should note that the quantities of interest here are all higher order moments. As mentioned earlier in this chapter, the use of lower-order moments for the DSD estimation does lower the m estimate. This suggests that the DSD properties at large drop diameters contribute to the large m value rather than those at small drop diameters. Even so, it may be worth while to check the effect of DSD at drop diameter less than about 1 mm where the Joss-Waldvogel type disdrometer may have a degraded sensitivity because in many cases DSDs measured by our disdrometer show a decrease in drop density with diameter at the small diameter region (see Chapter 3). For this purpose, we use the same test method described in Section 3.1; i.e., the disdrometer-measured DSD is artificially modified so that the DSD at less than 1 mm diameter is exponentially distributed. The modified DSD is then used to derive the DSD parameters. It is found that the exponentiation of the DSD at the small diameter region approximately halves the m value when the original one is 6 to 8; i.e. the modified DSDs have m values of 3 to 4. However, it should also be noted that in general natural DSDs tend to have a "concave-down" shape due to various raindrop evolution processes[1] rather than the exponential shape assumed for the test. Thus, we may conclude that, if there is some instrument sensitivity degradation at the small diameter region, the "best" m value would be about 4 to 6.

The other aspect to be considered is the accuracy in estimating lower order moments. As a limiting case, we test the zeroth moment estimation. The result, shown in Table 4-5, indicates that the $m = 3 \sim 6$ are best to minimize the RMS deviation, while $m = 6 \sim 8$ gives the APR close to unity, and that the accuracy is much worse than that in the rain rate estimation. Although there is some difference in the "best" m in terms of RMS deviation and APR, on average, this conclusion is similar to that obtained in the rain rate estimation.

---

† The definition of σ in this thesis is different from that used in Feingold and Levin[15]. Their "best" σ of 1.4 corresponds to $\sigma = 0.336$ by our definition. (Letting their "σ" be σ', $\sigma = \ln\sigma'$).

Table 4-5. Results of zeroth moment (M_0) estimation from DP measurements combining M_6 and M_4.

DSD model	*RMS-dev* (dB)	*APR*
Gamma, $m = 0$	9.43	44
Gamma, $m = 3$	2.82	3.7
Gamma, $m = 6$	2.67	1.3
Gamma, $m = 10$	3.61	0.68
cf. Gamma, 3-parameter	1.29	1.86
Lognormal, 3-parameter	1.61	0.91

4.5 Error Analysis

In this section, we consider the effect of measurement errors on the estimates of rain rate (R) and liquid water content (W). For this analysis, we assume the two-parameter gamma distribution with m fixed, and we use the moment approximation to IRPs; Z, R and W are proportional to M_6, $M_{3.67}$ and M_3, respectively, and the attenuation coefficient (k) is proportional to $M_3 \sim M_{4.3}$. Through these assumptions, the problem is reduced to an estimation of M_u from the measurements of M_x and M_y. For simplicity, we consider the errors in "logarithm of normalized x th moment", X:

$$X = 10\cdot\log_{10}(M_x) - 10\cdot\log_{10}(\Gamma(m+x+1))$$

$$= 10\cdot\log_{10} N_0 - 10\cdot(m+x+1)\log_{10}\Lambda. \qquad (4.17a)$$

Y and U can be defined similarly:

$$Y = 10\cdot\log_{10} N_0 - 10\cdot(m+y+1)\log_{10}\Lambda \qquad (4.17b)$$

$$U = 10\cdot\log_{10} N_0 - 10\cdot(m+u+1)\log_{10}\Lambda. \qquad (4.17c)$$

From Eq.4.17, we have the linear relation between the dual-parameter estimate of U, U_D

$$U_D = (u-y)/(x-y)\cdot X - (u-x)/(x-y)\cdot Y. \qquad (4.18)$$

By expressing X and Y as $X = X_0 + \delta_X$ and $Y = Y_0 + \delta_Y$ where X_0 and Y_0 are true values, and δ_X and δ_Y are corresponding errors, the error in U_D, δ_{UD}, becomes

$$\delta_{UD} = (u-y)/(x-y)\cdot\delta_X - (u-x)/(x-y)\cdot\delta_Y. \qquad (4.19)$$

Assuming that δ_X and δ_Y are independent random variables with mean values of Δ_X and Δ_Y and standard deviations of σ_X and σ_Y, respectively, we have the mean and variance of δ_{UD} (Δ_{UD} and σ_{UD}^2, respectively):

$$\Delta_{UD} = (u-y)/(x-y)\cdot\Delta_X - (u-x)/(x-y)\cdot\Delta_Y \tag{4.20}$$

$$\sigma_{UD}^2 = [(u-y)/(x-y)]^2\cdot\sigma_X^2 + [(u-x)/(x-y)]^2\cdot\sigma_Y^2 \tag{4.21}$$

It is clear from Eq.4.19 that the dual-parameter estimation becomes more accurate with increasing $|x-y|$; i.e., the orders of the two measurable moments should be apart from each other in order not to amplify the measurement error. For comparison, a single-parameter estimate of U using X (U_{SX}) and that using Y (U_{SY}) are derived:

$$U_{SV} = (v-u)\cdot(m+v+1)^{-1}N_{0,\mathrm{dB}} + (m+u+1)\cdot(m+v+1)^{-1}\,X \tag{4.22}$$

where $V = X$ or Y and $v = x$ or y, and $N_{0,\mathrm{dB}} = 10\cdot\log_{10} N_0$. Letting the mean and the standard deviation of the error in $N_{0,\mathrm{dB}}$ be Δ_{N0} and σ_{N0}, respectively, we have the mean (Δ_{USV}) and variance (σ_{USV}^2) of the error in U_{SV} , δ_{SV}:

$$\Delta_{USV} = (v-u)\cdot(m+v+1)^{-1}\Delta_{N0} + (m+u+1)\cdot(m+v+1)^{-1}\,\Delta_V \tag{4.23}$$

$$\sigma_{USV}^2 = (v-u)^2\cdot(m+v+1)^{-2}\,\sigma_{N0}^2 + (m+u+1)^2\cdot(m+v+1)^{-2}\,\sigma_V^2 \tag{4.24}$$

Note that $\Delta_V = \Delta_X$ or Δ_Y, and that $\sigma_V = \sigma_X$ or σ_Y.

We assume here that the attenuation is estimated by means of the SRT method (see Section 2.3.6). The values of Δ_X and Δ_Y, which depend on the methods for radar calibration and "reference" surface σ^0 determination, are difficult to specify but it is easy to calculate Δ_{UD} and Δ_{USV} once Δ_X, Δ_Y and Δ_{N0} are specified. Thus, we consider only the random errors in the estimates of U (σ_{UD} and σ_{USV}).

For calculating the standard deviation of δ_{UD} and δ_{USV}, we specify the standard deviations of errors in X, Y and N_0 as follows: $\sigma_Y = 0 \sim 2.0$ (dB), which corresponds to the received power fluctuation for the number of independent samples of $\infty \sim 8$; $\sigma_X = 0.17 \sim 0.61$ dB, which approximately corresponds to the standard deviation of surface σ^0 from 1.0 to 3.5 dB for the two-way path attenuation of 25 dB; and $\sigma_{N0} = 2.5 \sim 6.5$ dB, which is chosen referring to the statistical analysis of the N_0 (for $m = 0$) derived from the disdrometer data ($\sigma_{N0} \approx 4.3$ and ≈ 5.1 for rain rates higher than 3 mm/h and 1 mm/h, respectively; see Section

4.2). As mentioned earlier in this section, x = 3.0 ~ 4.3, y = 6, and u = 3.67 or 3.0. Using these values, the standard deviations, σ_{UD} and σ_{USV}, are calculated. The following conclusions can be drawn from the result that is shown in Figure 4-16 and summarized in Table 4-6:

(1) The SP estimation using Z (U_{SY}) is generally much worse than the DP estimation and the SP estimation using attenuation (U_{SX}).

(2) When x is close to u, the difference in the accuracies of U_{DP} and U_{SX} are small.

(3) The DP estimation is generally superior to the SP estimation using X when σ_{N0} is large ($\sigma_{N0} \gtrsim 4.5$) and x is much different from u (= 3.67 or 3.0). In the case of rain rate estimation (u = 3.67), the superiority is enhanced when $x < u$ and reduced when $x > u$. In the case of W estimation (u = 3), on the other hand, the superiority is maintained over a wide range of x.

(4) The rain rate estimation from the combination of radar reflectivity and an attenuation coefficient becomes insensitive to the measurement error when the attenuation coefficient is proportional to a moment lower than rain rate ($M_{3.67}$). Although an attenuation measurement at millimeter wavelength (40 ~ 50 GHz or higher) is required to achieve this condition, adding such millimeter wave rain measurements should be useful to improve the rain retrieval accuracy especially for light rain rate region.

Table 4-6 Summary of R and W estimation error. (SD of random error in dB)
σ_X = 0.5 (SD(σ^0) = 2 dB with path-attenuation 25 dB), σ_Y = 0.5, σ_{N0} = 4.5.

Order of M_x	R ($M_{3.67}$) estimation			W (M_3) estimation		
	DP (U_D)	SP with k (U_{SX})	SP with Z (U_{SY})	DP (U_D)	SP with k (U_{SX})	SP with Z (U_{SY})
3.0	0.28	0.84	1.53	0.34	0.33	1.95
3.3	0.30	0.52	1.53	0.38	0.45	1.95
3.7	0.34	0.33	1.53	0.46	0.74	1.95
4.0	0.40	0.44	1.53	0.56	0.95	1.95
4.3	0.50	0.62	1.53	0.71	1.14	1.95

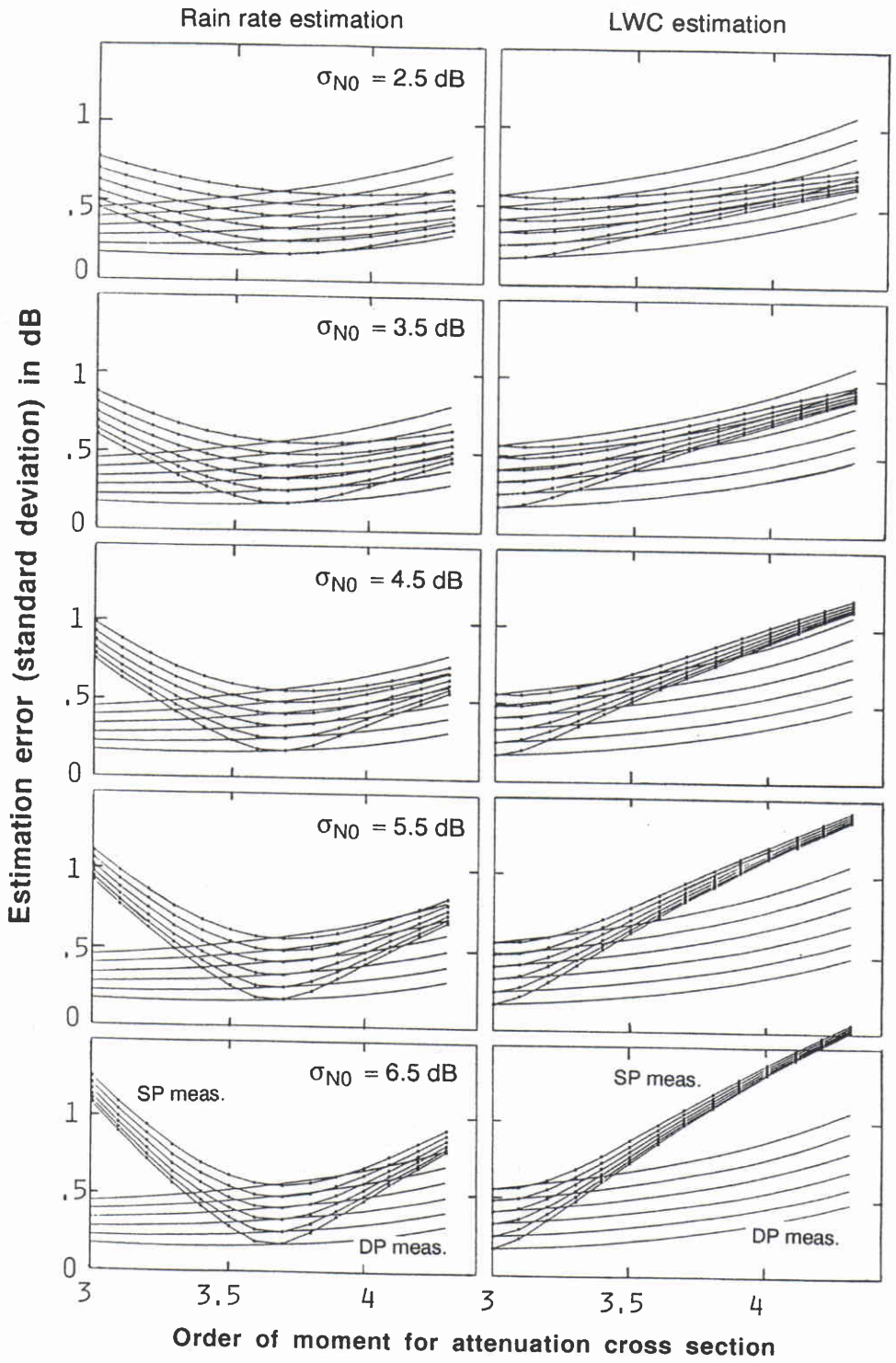

Figure 4-16. Rain rate and LWC estimation error (random) caused by errors in Z-factor and attenuation measurements, and in natural DSD fluctuation. Five curves in each figure correspond to $\sigma_X = 0.17 \sim 0.61$. $\sigma_Y = 0.5$.

4.6 Conclusions

In this chapter, we have investigated statistical properties of the parameters of DSD modeled by the exponential, the gamma and the lognormal models, and of several important IRPs such as Z factor and rain rate. The DSD parameters have been derived by means of the MoM (the method of moments) using two or three higher order moments.

It is found that the gamma and exponential DSD parameters are approximately lognormally distributed except for the shape parameter, m, which has both positive and negative values. The pdf's of the gamma DSD parameter m and the lognormal DSD parameter σ^2 have long tail at their large values, which is caused by a small fluctuation in the DSD shape at intermediate to large drop diameters and it may not be essential to use such large m and σ values to estimate other IRPs through DSD parameter estimation.

The parameter Λ has a clear negative correlation with R and with Z, while N_0 (for gamma models with m fixed to a small value of $0 \sim 3$) and N_T's show no or only a small positive correlation. This is partly caused by the fact that the higher order moments are generally more sensitive to the variation of Λ than those of N_0 or N_T. Physical DSD evolution processes may also contribute to the higher correlation between Λ and Z (or R).

Several important IRP relationships including *Ze-R*, *k-R* and *k-Ze* relations have been obtained through a regression analysis of IRPs derived from the disdrometer data. The resultant IRP relations (particularly *Ze-R* relation) are somewhat different from those obtained assuming the typical exponential DSD models, which is a result of the departure of DSD shape from the exponential form (more concave-down). This suggests that the use of the conventional exponential DSD models are not necessarily the best to assess various IRP relationships. As an alternative, we suggest the use of the "two-parameter" gamma DSD models with m fixed to 3 or 6 shown in Table 4-2 as typical gamma DSD models. From the regression analysis between Z and R with a 2-month segmentation, it was found that there is some seasonal dependence of *Z-R* relation; *Z-R* relations for winter rainfall are generally less variable and give higher Z factors for the same rain rate value than those in other seasons.

In order to test the validity of dual-parameter (DP) and triple-parameter (TP) measurements combined with the assumption of the gamma and lognormal DSD models more precisely, a simulation of rain rate estimation has been made. From the simulation, it is shown that if we can make a TP measurement using two kinds of attenuation in addition to Z, the estimation is nearly perfect, and that even a DP measurement, in which only a kind of

attenuation can be measured , provides excellent estimation over a fairly wide range of m and σ values. The m values of 6~8 and σ values of 0.28~0.29 are found to give the lowest RMS errors in rain rate estimation. Those "best" m (σ) values may shift to small (large) values to some extent, by considering the possible sensitivity degradation of the disdrometer. In such cases, the "best" m would be 4~6. When other lower order moments are estimated from the same DP and TP measurements instead of rain rate, the accuracy is degraded and the choice of DSD model becomes more critical to avoid large errors. According to the result of a zeroth moment estimation, the m values of around 6 are found to provide the minimum error, which is similar to the case of rain rate estimation.

Finally, an error analysis has been made to assess the effects of errors in DP measurements. The results indicate that the DP estimation of rain rate and LWC is generally superior to the SP estimation under typical measurement error conditions. The superiority of the DP estimation is reduced to some extent if the attenuation coefficient is proportional to the moments higher than $M_{3.67}$ (rain rate), while the DP estimation becomes insensitive to the measurement error and the superiority is greatly enhanced if the moment lower than 3.67, i.e., millimeter wave attenuations, can be measured together with Z factor.

Appendix 4-1 Derivation of DSD parameters

- Gamma parameters

From the expression of xth moment of the gamma DSD given by Eq.4.2a, 3rd, 4th and 6th moments of DSD are written

$$M_3 = N_0 \Gamma(m+4) \,/\, \Lambda^{m+4} \tag{4.A1a}$$

$$M_4 = N_0 \Gamma(m+5) \,/\, \Lambda^{m+5} = N_0 (m+4) \Gamma(m+4) \,/\, \Lambda^{m+5} \tag{4.A1b}$$

$$M_6 = N_0 \Gamma(m+7) \,/\, \Lambda^{m+7} = N_0 (m+6)(m+5)(m+4) \Gamma(m+4) \,/\, \Lambda^{m+7}. \tag{4.A1c}$$

Eliminating $N_0\Gamma(m+4)$ from Eqs. 4.A1a and 4.A1b gives

$$M_4 = (m+4)\Lambda^{-1} M_3. \tag{4.A2}$$

Similarly, from Eqs.4A.1b and 4.A1c,

$$M_6 = (m+5)(m+6)\Lambda^{-2} M_4. \tag{4.A3}$$

Eliminating Λ from Eqs.4.A2 and 4.A3 provides the expression of m in terms of the moments,

$$(m+4)^2/[(m+6)(m+5)] = M_4^3/[M_3^2 M_6] = G. \tag{4.A4}$$

Eq.4.A4 yields the solution for m that is given by Eq.4.3. Once we have the value of m, the parameters Λ and N_0 are readily obtained from Eq.4.A2 and then 4.A1a.

- Lognormal parameters

From Eq.4.2b, the natural logarithms of xth, yth and zth moments of the lognormal DSD, L_x, L_y, L_z, are written

$$L_x = L_N + x\mu + 1/2\, x^2 \sigma^2 \tag{4.A5a}$$

$$L_y = L_N + y\mu + 1/2\, y^2 \sigma^2 \tag{4.A5b}$$

$$L_z = L_N + z\mu + 1/2\, z^2 \sigma^2 \tag{4.A5c}$$

where $L_N = \ln N_T$. Eq.4.A5 constitutes a linear simultaneous equation of L_N, μ, and σ^2, which is easily solved for those DSD parameters. Substituting $x = 3$, $y = 4$, and $z = 6$, we have the expressions of N_T, μ and σ^2 given by Eq.4.6 through 4.8.

References

(1) Ulbrich, C.W., 1983: Natural variations in the analytical form of raindrop size distributions, *J. Climate Appl. Meteor.*, **22**, 1764-1775.

(2) Feingold, G. and Z. Levin, 1986: The lognormal fit to raindrop spectra from frontal convective clouds in Israel. *J. Climate Appl. Meteor.*, **25**, 1346-1363.

(3) Marshall, J.S. and W.M. Palmer, 1948: The distribution of raindrops with size. *J. Meteorol.*, **5**, 165-166.

(4) Mielke, P.W., Jr., 1976: Simple iterative procedures for two parameter gamma distribution maximum likelihood estimates. *J. Appl. Meteor.*, **15**, 181-183.

(5) Wong, R.K.W. and N. Chidambaram, 1985: Gamma size distribution and stochastic sampling errors. *J. Climate Appl. Meteor.*, **24**, 568-579.

(6) Waldvogel, A., 1974: The N_0 jump of raindrop spectra. *J. Atmos. Sci.*, **31**, 1067-1078.

(7) Ajayi, G.O., and R.L. Olsen, 1985: Modeling of a tropical raindrop size distribution for microwave and millimeter wave applications. *Radio Sci.*, **20**, 193-202.

(8) Im, E. and K. Kellogg, 1990: Spaceborne radar for rain and cloud measurements: A conceptual design. *Proc. GARSS'90*, College Park, MD, 425-428.

(9) Joss, J., J.C. Thams, and A. Waldvogel, 1968: The variation of raindrop size distribution at Locarono, *Proc. Int. Conf. Cloud Physics*, 369-373.

(10) Chandrasekar, V. and V.N. Bringi, 1987: Simulation of radar reflectivity and surface measurements of rainfall. *J. Atmos. Oceanic. Tech.*, **4**, 464-478.

(11) Atlas, D., C.W. Ulbrich and R. Meneghini, 1984: The multiparameter remote measurement of rainfall. *Radio Sci.* **19**, 3-22.

(12) Ulbrich, C.W., and D. Atlas, 1984: Assessment of the contribution of differential polarization to improved rainfall measurements, *Radio Sci.*, **19**, 49-57.

(13) Bringi, V.N., T.A. Seliga, and W.A. Cooper, 1984: Analysis of aircraft hydrometeor spectra and differential reflectivity (Z_{DR}) radar measurements during the Cooperative Convective Precipitation Experiment, *Radio Sci.*, **19**, 157-167.

(14) Goddard, J.W.F. and S. M. Cherry, 1984: Quantitative precipitation measurements with dual linear polarisation radar, Preprints, *22nd Conf. Radar Meteorol.*, Zurich, Amer. Meteor. Soc., 352-357.

(15) Feingold, G. and Z. Levin, 1987: Application of the lognormal raindrop size distribution to differential reflectivity radar measurement (Z_{DR}). *J. Atmos. Ocean. Tech.*, **4**, 377-382.

CHAPTER 5. SDP MEASUREMENT AND TWO-SCALE DSD MODEL

5.1 Concept

In the discussion in Section 2.3.3, we have assumed that the DP measurement measures two kinds of integral rain parameters (IRPs) in a radar resolution volume. The DP measurement has been tested in terms of rain rate estimation accuracy in Chapter 4. In many cases, however, such "complete" DP measurements are difficult to perform. The resolution of IRP measurements combined with the radar reflectivity measurement are usually coarser than the resolution required for the rainfall profiling. This configuration is different from the complete DP measurement. As briefly mentioned in Section 2.3.4, we call this type of dual-parameter measurements "Semi" DP (SDP) measurement[1)].

Let Δr and ΔR be the resolutions for the first and second measurements, respectively, and let us assume that Δr is the resolution required for the profiling. In DP measurements, $\Delta r = \Delta R$, and in SDP measurements, $\Delta R = n \cdot \Delta r$ where $n \geq 2$. Similar definitions apply to the time resolution. Considering that SP measurements need the estimation of one of the two DSD parameters based on empirical or theoretical models, an SDP measurement with $n \rightarrow \infty$ may approach an SP measurement. The concept of DP, SDP and SP measurements is illustrated in Figure 5-1.

Even from the SDP measurement, through proper DSD modeling, it is possible to obtain DSD information with the resolutions ΔR or Δr. Since the first rain parameter is measured with the resolution Δr, one DSD parameter can be estimated with the same resolution, while the other DSD parameter can only be estimated with the resolution ΔR. Thus the parameters of a DSD model used for the SDP measurement should have two scale spatial variability; Δr and ΔR. We hereafter call this type of DSD model defined over a time or spatial region (or both) "two-scale" DSD model. Examples of SDP measurements by a spaceborne radar combining Z factor profile and a low resolution attenuation data are illustrated in Figure 5-2(a). It should be noted that the DSD parameters used for a two-scale model need not be the parameters appearing in the original expression of the model for individual DSD. We could select the DSD parameters in such a way that one of them is most variable and the other is least variable, or that one of them is most sensitive and the other is least sensitive to the IRPs of interest.

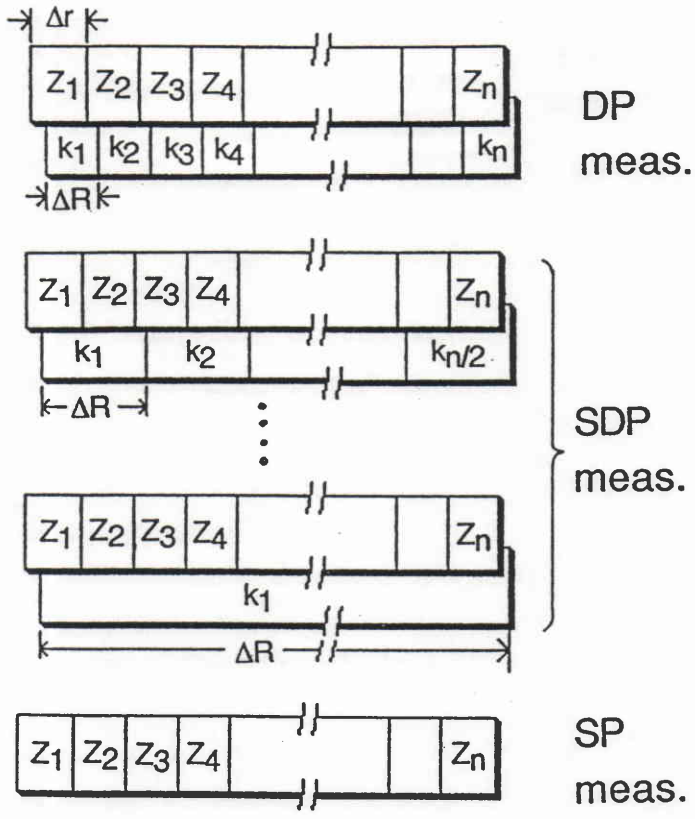

Figure 5-1. Concept of DP, SDP and SP measurements using radar reflectivity factor (Z) and microwave attenuation (k) for rainfall profiling with the resolution Δr.

In a wide sense, the SDP measurement may be recognized as an addition of a broad rain parameter characterized over a space or time (need not be a radar measurable quantity) to the original SP radar measurement with high resolution, and the two-scale model parameters may be recognized as the conversion of those measured quantities to more fundamental or useful rain parameters. For example, let us consider the radar-gage comparison illustrated in Figure 5-2(b). The radar measurement would provide a 4-D map of Z factor with a high spatial and temporal resolution, while the rain gage would provide a 1-D (on the time axis) profile of the other IRP, rain rate, at a certain spatial location. However, a sequence of gage samples has to be employed to estimate a time invariant rain parameter such as Z-R relation to avoid errors caused by a spatial discrepancy between the gage and radar measurement volumes. Thus, the gage data are recognized as a quantity having a crude temporal resolution, and we have to assume that the parameter estimated at the gage site is applicable to an entire raining area and/or storm life. In summary, the 4-D Z-factor map and the rain gage data at a point are connected in terms of a two-scale DSD model, in which one of the two DSD parameters is assumed to be constant over the 4-D raining space.

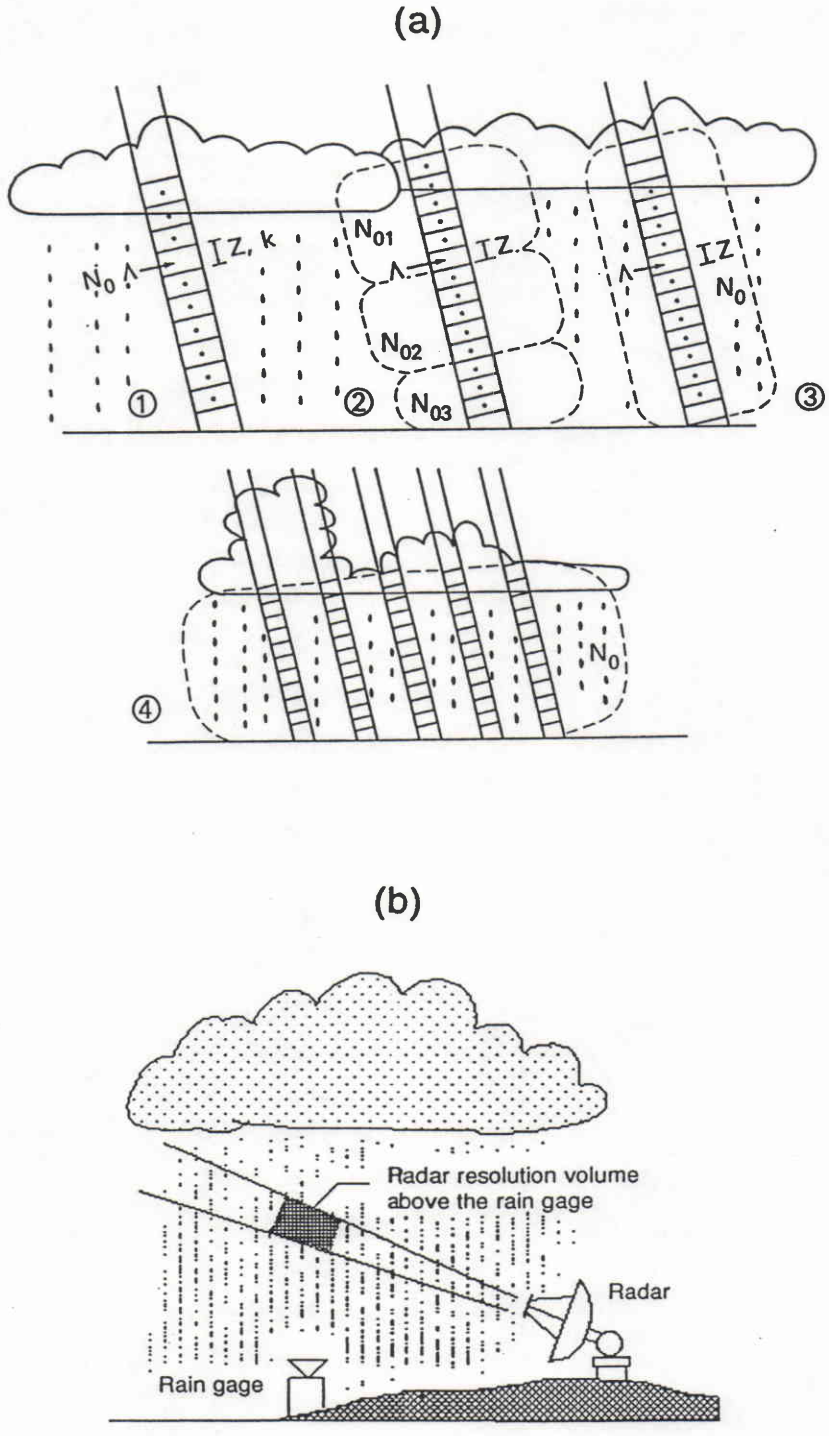

Figure 5-2. Illustration showing examples of SDP measurement by a spaceborne radar (a), and by a combination of ground-based radar and a raingage (b).

It should be noted that if a radar system constant required to obtain the quantitative rain parameters is unknown, such unknown system parameter needs to be incorporated in the modeling of the radar measurement. For example, if the radar calibration is the purpose of the radar-gage comparison, a radar system constant is to be estimated with assuming the DSD parameter. (In fact, we have determined the calibration factor, F, of a Ku-band FM-CW radar employing the DSD measured by a disdrometer in Chapter 3.) Such an SDP measurement may not have the ability to estimate the two-scale DSD model parameters. Similar problem happens in cases where other factors such as the existence of non-liquid hydrometeors affect the "kernel" of a rain parameter itself. In actual DSD estimation algorithms, those uncertainties should be corrected in advance or should be included in the modeling. For simplicity, however, we continue to assume in this chapter that the the kernels of IRPs are known and solely determined by the DSD parameters.

5.2 Two-scale DSD Model and Relations between IRP's

We should note that, if a DSD parameter is constant over ΔR, relationships between IRPs are also fixed over ΔR. Since IRPs are given as a function of two DSD parameters, by eliminating the parameter changing with range, we have a relation which contains only the other parameter constant over ΔR. If we assume the gamma DSD model with a fixed m (Eq.4.1a) and two IRPs, I_x and I_y, proportional to xth and yth moments of DSD (i.e., $I_x = c_x M_x$ and $I_y = c_y M_y$ where c_x and c_y are constants), the relation between I_x and I_y is expressed in the form

$$I_y = \alpha I_x^{\beta} \tag{5.1}$$

The coefficient, α, and the exponent, β, are generally functions of the DSD parameter kept in the expression of Eq.5.1. Table 5-1 lists the pairs of (α,β) for the gamma DSD model. Similar power-law forms can be derived for the lognormal model[2]. Atlas and Ulbrich[3,4] have already noticed in their earlier studies regarding the "rain-parameter diagram" that the all IRP relationships can be derived from a known IRP relation, e.g., Z-R relation. However, their interest was in the "complete" DP measurement rather than the nature of the DSD variation causing such IRP relations.

Table 5-1 Coefficient α and exponent β in the rain parameter relationships for the gamma DSD model.

	Parameter kept in α		
	N_0	N_T	Λ
α	$(C_y/C_x^{\beta})N_0^{1-\beta}$	$(C_y/C_x^{\beta})N_T^{1-\beta}$	$(C_y/C_x)\Lambda^{x-y}$
β	$(m+y+1)/(m+x+1)$	y/x	1

Note: $C_x = c_x\,\Gamma(m+x+1)$, $C_y = c_y\,\Gamma(m+y+1)$

Although in most profiling algorithms, power-law IRP relations (Eq.5.1) are assumed without detailed discussion on their relation to the DSD[5-10], we see that such an assumption implies the use of a "two-scale" DSD model and that all IRP relations are determined from the two-scale model parameter assumed to be constant over ΔR. A preliminary study to determine a path-averaged DSD parameter from joint measurements of the Ku-band FM-CW radar (see Chapter 3) and a 12-GHz radiometer has been performed by Kozu et al.[11]. Their result appears to support the validity of the method, although they did not generalize the nature of such DSD estimation processes.

Let us consider two-scale models assuming a gamma DSD with m fixed in which N_0, N_T or Λ is constant over ΔR (see Table 5-1). In these two-scale models, β depends only on m and the two-scale model assumed, and α depends on the DSD parameter (N_0, N_T or Λ) as well. Thus, estimating the DSD parameter constant over ΔR is equivalent to estimating α. The estimation of α from an SDP measurement was proposed by Meneghini et al.[5], Lin et al.[6] and Meneghini and Nakamura[10]. The concept of the two-scale model gives a physical basis for such IRP relation adjustment. Instead of adjusting α, it should be possible to adjust β or to adjust both α and β by employing other two-scale models.

5.3 Proper Two-Scale Model: Empirical Evidence

The question that arises is what is the proper two-scale model. For example, if we assume that Λ is constant over ΔR, then we have linear IRP relations. The same happens if we assume a very large m value. These assumptions, however, do not seem to apply to many cases. Let us consider Z-R relations where $x = 3.67$ and $y = 6$. If N_T is constant, we have the exponent β of 1.63 (see Table 5-1). Whereas if N_0 is constant with m values between 0 and 8, we have the exponents between 1.5 and 1.18.

- From Z-R relations

Since the exponent of *Z-R* relations commonly measured is between 1.2 and 1.7 except for a few cases[12], the assumptions of "constant N_T" and "constant N_0" appear to be reasonable. The validity of these assumptions can be checked from an event-scale regression analysis between Z and R. Since the estimation of R from Z is required in radar remote sensing, the regression coefficients from Z to R are used for this analysis. Figure 5-3 shows the mean and standard deviation of β in $Z = \alpha R^{\beta}$ relation as well as the mean of α. Each (α,β) pair is derived from 3-min averaged DSD samples within a rainfall event which lasts between 30 and 96 minutes and has a maximum rain rate higher than 5 mm/h. From the 2-year data set, 139 such rain events are obtained. Although the data processing for Figure 5-3 is different from that for Figure 4-13, similar seasonal dependence of *Z-R* relations can be seen; in winter, α or β is larger than the values for other seasons to give higher Z factor values for given R's.

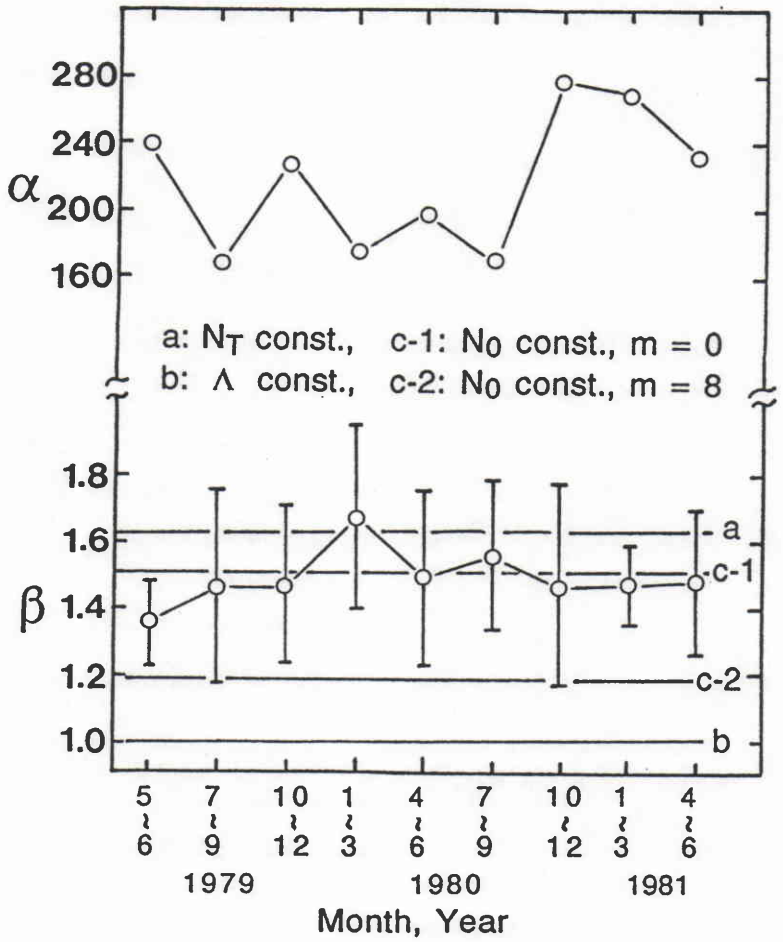

Figure 5-3. Event-scale *Z-R* relationship derived from disdrometer data: The mean and standard deviation of the exponent β and the mean of the coefficient α, as a function of season.

We see that although there are some event-by-event fluctuation and seasonal variation in β, average β values are consistent with the assumption of "constant N_0 with small m" and "constant N_T". The β value given by the *constant N_T* model (= 1.63) is slightly larger than the disdrometer result shown in Figure 5-3. This is caused by a small positive correlation between N_T and R obtained from the disdrometer data. In fact, if we express $N_T = a \cdot R^b$, then substituting this relation into the original Z-R relation in which α is a function of N_T (Eq.5.1 and Table 5-1) yields

$$Z = (C_y/C_x^{\beta})\,(a\,R^b)^{1-\beta} R^{\beta} = (C_y/C_x^{\beta})\,a^{1-\beta}\,R^{\beta+b(1-\beta)},\ \beta = 6/3.67 = 1.63. \qquad (5.2)$$

If we use b = 0.36 (see Table 4-2), then the new exponent $\beta+b(1-\beta)$ is 1.4 which is consistent with the result shown in Figure 5-3.

- *From principal component analysis*

It should be noted that the above models are based on the correlation analysis between two higher-order moments, Z and R, and would not be valid for relating lower-order moments of DSD. In order to clarify this point, a principal component (or EOF) analysis between two moments is performed, in which pairs of two moments (e.g. M_0 and M_1) in a rain event are used to obtain the direction of the first principal component, defined as an angle measured from x axis, as illustrated in Figure 5-4. The reason to use the principal component analysis rather than the regression analysis is that the regression lines can differ significantly depending on the choice of independent variable when correlation coefficient is low. The first and the second principal components correspond to the DSD parameter that explains most the DSD variation on the Z-R plane and the DSD parameter that is least correlated with the DSD variation (i.e., that should be fixed), respectively.

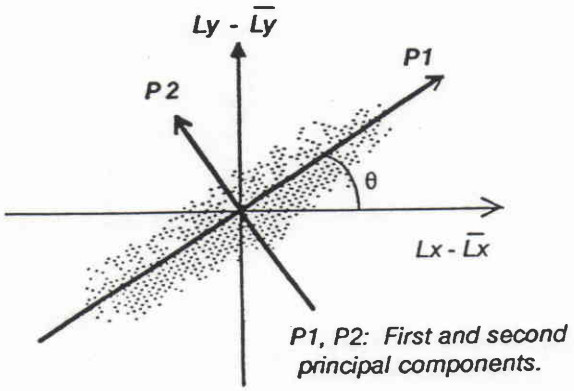

Figure 5-4.
Concept of principal component analysis to see the proper two-scale DSD model

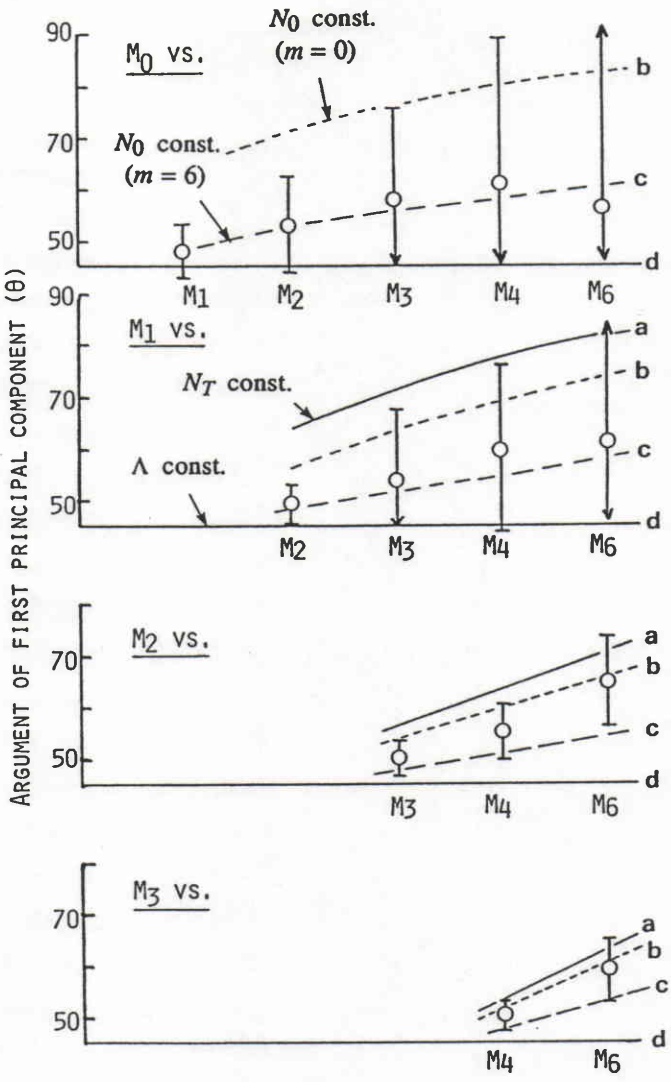

Figure 5-5. Argument of the first principal component of two moments obtained from event-scale analysis together with the arguments assuming typical two-scale models.

Figure 5-5 shows the result of the EOF analysis for various combinations of moments. Curves in the figure represent the arguments assuming several two-scale models; "constant N_0 ($m = 0$)", "constant N_T " and "constant Λ". As indicated in the figure, the two-scale model which is consistent with the result of the principal component analysis depends on the moments of interest; the "constant Λ" model is suitable to explain the relation between lower order moments, while the "constant N_0 ($m = 0$)" and "constant N_T" models are suitable for higher order moments just as we have seen in the regression analysis of Z and R.

The above conclusion on the two-scale models suitable for relating higher order moments may be due to the following facts:

(1) As discussed earlier, higher-order moments are less sensitive to the variation in N_0 or N_T and more sensitive to the variation in Λ than lower-order moments. In other words, Λ generally has higher correlation with R and Z than N_0 and N_T.

(2) It is well known that N_0 and N_T change significantly. However, it has also been known that a large and sudden change in these parameters is associated with the change in rain type or a transition from one mesoscale area to another within a rain area[13]. Therefore, the above "constant N_0" and "constant N_T" model may be justified in a short time and a limited spatial scale, and probably within a rain event.

It should be noted that the N_0 value in Waldvogel[13] is also derived from two higher order moments, M_3 and M_6, and therefore the conclusion of his and our analyses may be applicable only to the N_0 and N_T values derived from higher order moments. Moreover, the event-by-event fluctuation in β shown in Figure 5-3 indicates that the "best" two-scale model, i.e., the DSD parameter to be fixed over ΔR, varies from one rain event to another. It also suggests the existence of a systematic rain type dependence of the "best" two-scale model. Therefore, detailed analyses of DSD properties with a rain-type classification should be useful to refine the two-scale model. Appendix 5-1 outlines a preliminary analysis of rain-type dependence of *Z-R* relations, which suggests the usefulness to use different two-scale models depending on rainfall type.

5.4 Simulation of SDP Measurements

As discussed above, the accuracy of rain parameter profiling by the SDP measurement should depend on the spatial and/or temporal DSD variation properties. In order to investigate the performance of the SDP measurement and to test the validity to use the two-scale DSD model, a simulation is performed using the disdrometer dataset.

5.4.1 Simulation method

Based on the above conclusion on the two-scale model (Section 5.3), we use the "constant N_T and N_0" models for the SDP measurement simulation. The m value is fixed to be 0 or 6. Although the "constant N_0 with m = 6" model gives somewhat small β value (≈ 1.2) and may not be a reasonable model, it is used for comparison.

The concept of the simulation is illustrated in Figure 5-6. For the simulation, we use disdrometer data which give rain rates higher than 1 mm/h and are continuous for t_{av} times N_r, where t_{av} is the averaging time for disdrometer data representing the DSD in the interval Δr. Longer t_{av} is preferable to reduce the sampling error in DSD measurement; however, the longer the t_{av} is, the less the number of data which can be employed for the simulation of length N_r. As a compromise, we adopt t_{av} = 3 min.

The total time to construct a radar measurement path of $N_r = 32$ is 96 minutes, which may correspond to an attenuation measurement integrated over a storm; i.e., estimating IRP relations on a storm basis. On the other hand, since the 3-min average implies that DSD is averaged over about 1 km in range (assuming the drop fall velocity is 6 m/s), smaller N_r values (2 to 4) may represent a single observation by spaceborne or airborne radars in which path lengths are short.

We assume that the Z ($= c_z \cdot M_6$) profile and path-averaged attenuation coefficient $\bar{k}$ ($= c_k \cdot M_4$) can be measured. Path-integrated attenuation, A, is related to $\bar{k}$ by $\bar{k} = A/(N_r \cdot \Delta r)$. First, we derive an N_0 estimate. Using the k-Z relation shown in Table 5-1, we have

$$\bar{k} = \frac{1}{N_r} C_{N_0} \sum_{i=1}^{N_r} N_{0,i}^{1-b} Z_i^b = \frac{1}{N_r} C_{N_0} \langle N_0^{1-b} \rangle \sum_{i=1}^{N_r} Z_i^b \qquad (5.3)$$

where $b = (m+5)/(m+7)$, $C_{N_0} = [c_k \cdot \Gamma(m+5)] \cdot [c_z \cdot \Gamma(m+7)]^{-b}$ and $\langle N_0^{1-b} \rangle$ is the path-averaged N_0^{1-b} weighted by Z^b. Eq.5.3 states that the N_0 estimate $\langle N_0^{1-b} \rangle$ is expressed as a function of $\bar{k}$ and a Z-factor profile, that is

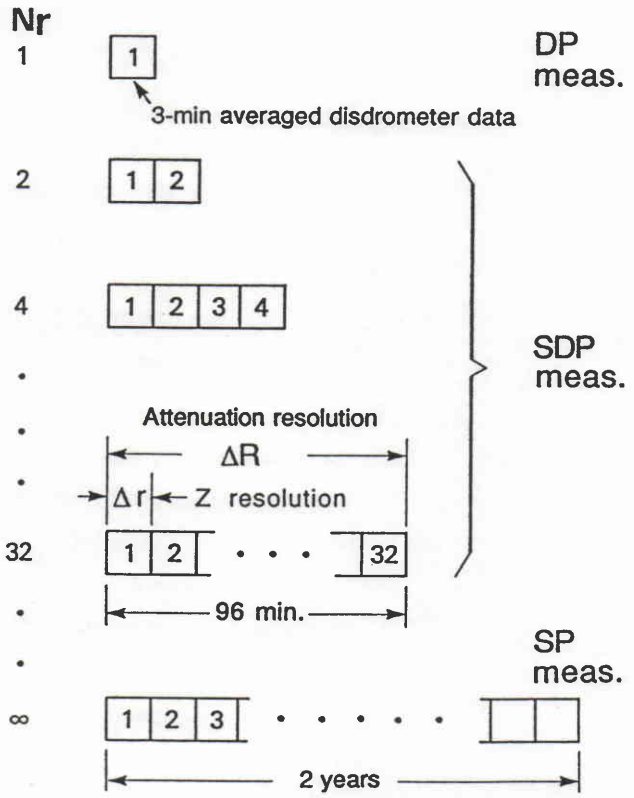

Figure 5-6. Concept of SDP measurement simulation with the disdrometer data.

$$\langle N_0^{1-b} \rangle = C_{N0}^{-1} N_r \bar{k} \; / \sum_{i=1}^{N_r} Z_i^b \tag{5.4}$$

Similarly, the $Z^{2/3}$-weighted path-averaged $N_T^{1/3}$, $\langle N_T^{1/3} \rangle$, is given by

$$\langle N_T^{1/3} \rangle = C_{NT}^{-1} N_r \bar{k} \; / \sum_{i=1}^{N_r} Z_i^{2/3} \tag{5.5}$$

where $C_{NT} = [c_k \cdot \Gamma(m+5)] \cdot [c_z \cdot \Gamma(m+7)]^{-2/3} \cdot \Gamma(m+1)^{1/3}$. Using the N_0 or N_T estimates, Λ profile is calculated

$$\Lambda_i = \left(\frac{c_z \, \Gamma(m+7)}{Z_i} \right)^{\frac{1}{m+7}} \langle N_0^{1-b} \rangle^{1/2} \tag{5.6a}$$

$$\Lambda_i = \left(\frac{c_z \, \Gamma(m+7)}{\Gamma(m+1) \, Z_i} \right)^{1/6} \langle N_T^{1/3} \rangle^{1/2} \tag{5.6b}$$

Further, a rain rate profile is obtained with the DSD parameters; using a moment approximation to rain rate, i.e. $R = c_R M_\gamma$ where c_R is a constant and $\gamma = 3.67$

$$R_i = c_R \, \Gamma(m+\gamma+1) \langle N_0^{1-b} \rangle^{1/(1-b)} / \Lambda_i^{\,m+\gamma+1} \tag{5.7a}$$

$$R_i = c_R \, [\, \Gamma(m+\gamma+1) / \Gamma(m+1) \,] \langle N_T^{1/3} \rangle^3 / \Lambda_i^{\,\gamma} \tag{5.7b}$$

or using the direct integration over D,

$$R_i = \frac{\pi}{6} \langle N_0^{1-b} \rangle^{1/(1-b)} \int_0^\infty v(D) \, D^{m+3} \exp(-\Lambda_i D) \, dD \tag{5.8a}$$

$$R_i = \frac{\pi}{6} \langle N_T^{1/3} \rangle^3 \int_0^\infty \frac{v(D) \, D^{m+3} \, \Lambda_i^{m+1}}{\Gamma(m+1)} \exp(-\Lambda_i D) \, dD \tag{5.8b}$$

where Λ_i is given by Eq.5.6a or 5.6b, and $v(D)$ is the drop terminal velocity (Eq.2.11).

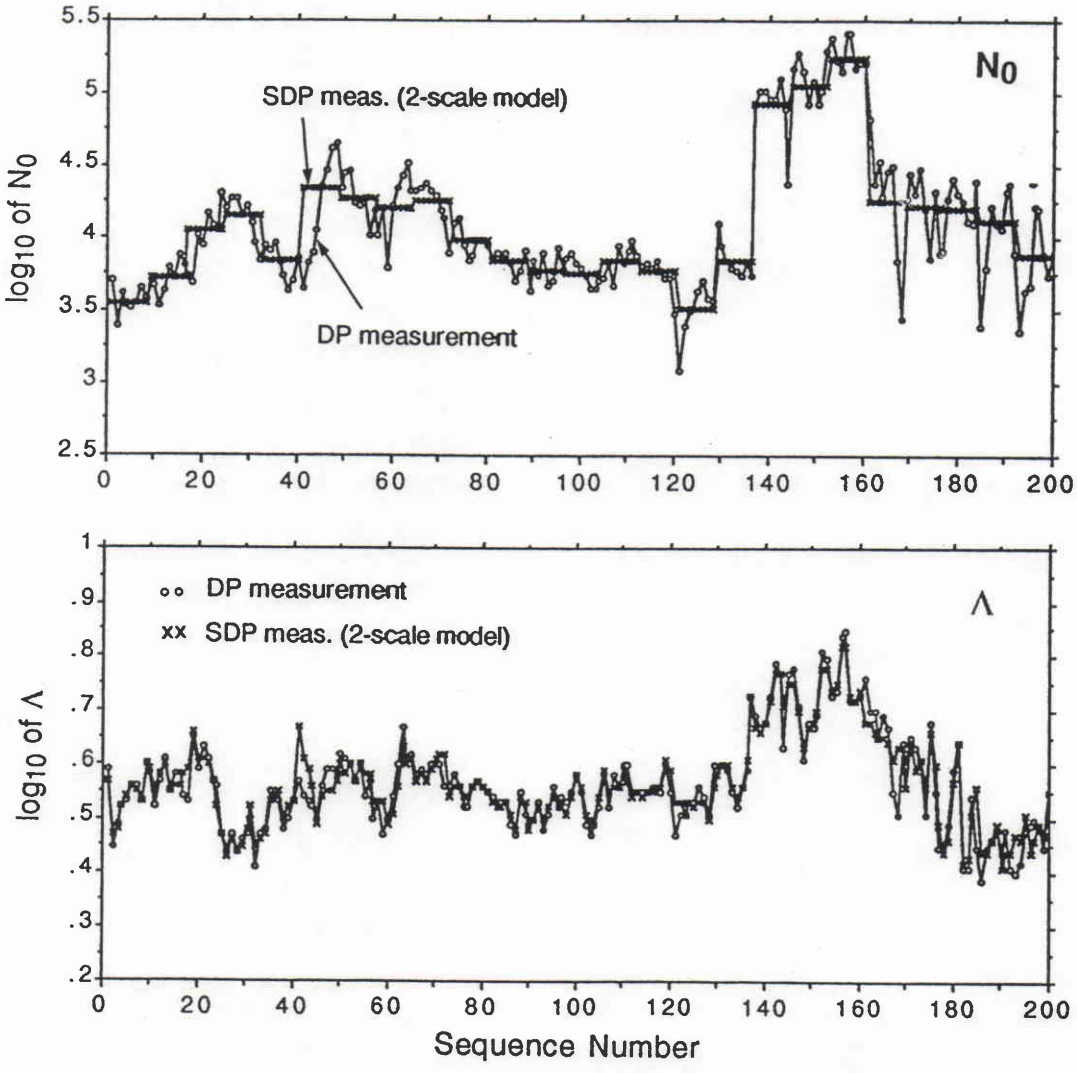

Figure 5-7. Example of estimates of "path-averaged" (low resolution) N_0 and corresponding Λ profile.

5.4.2 Simulation result; rain rate profile

An example of path-averaged N_0 and corresponding Λ profile estimated through the SDP measurement simulation is shown in Figure 5-7. Note that a time segment in which the path-averaged N_0 is constant represents a profile. In the figure, the DSD profile as estimated by the DP measurement (the same as the result of the SDP measurement with $N_r = 1$) is also shown for comparison. It is found that in general the SDP estimates agree well with the DP estimates. DSD profiles of various resolutions ($N_r = 2 \sim 32$) are estimated for the two-year

disdrometer data set. Some of rain rate estimation results are shown in Figure 5-8 including a DP measurement, SDP measurements (N_r = 2 and 32), and an SP measurement using a *Z-R* law derived from a linear regression of log *Z* and log *R* over the entire two-year period. As expected, the DP estimation of rain rate is nearly perfect, the SP estimation results in a large error, and the SDP measurements provide accuracies in between.

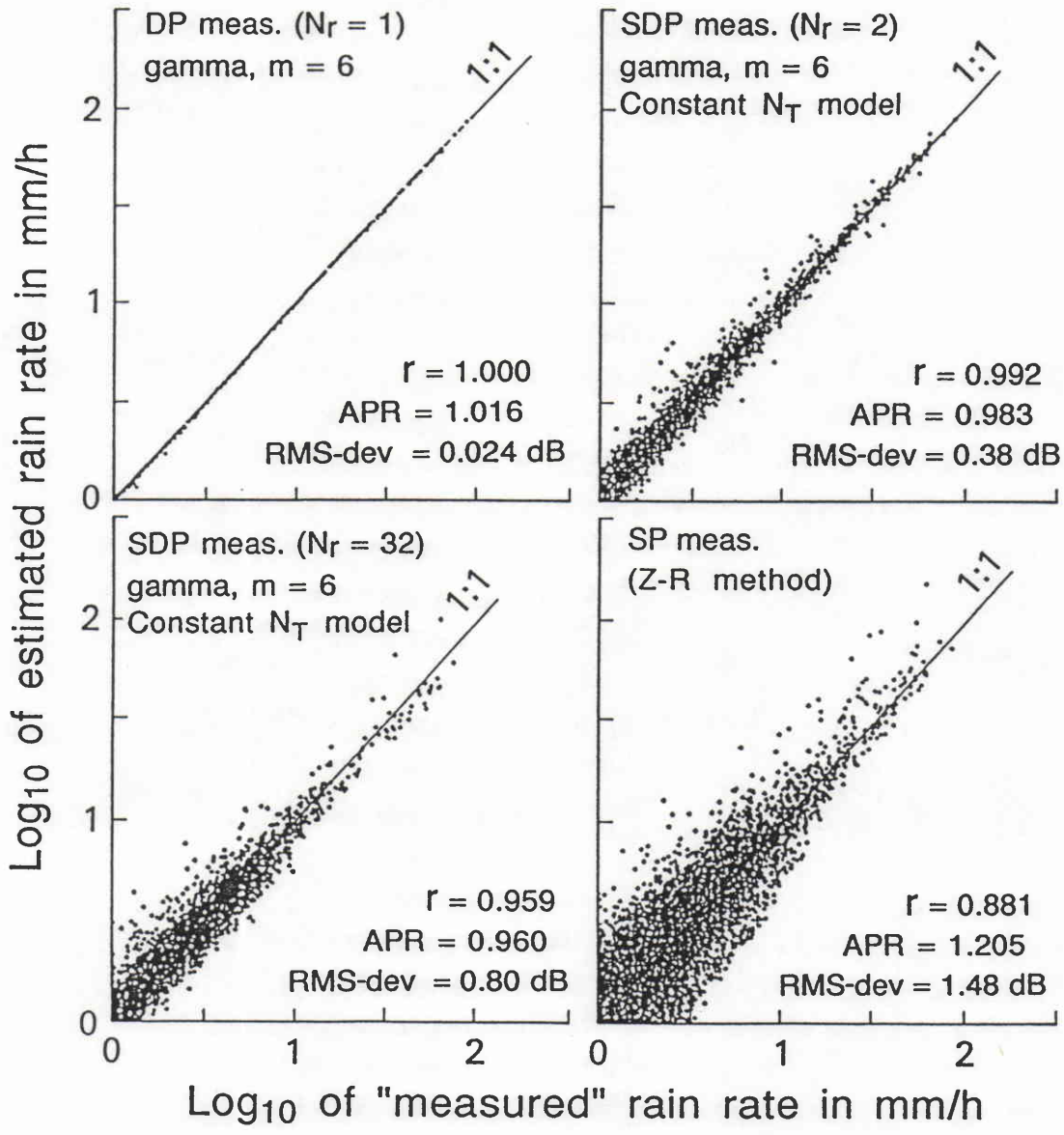

Figure 5-8. Comparison of rain rate estimation results by a DP measurement using the gamma DSD model with a fixed *m* (= 6), two SDP measurements ("constant N_T, m = 6" model with N_r = 2 and N_r = 32), and an SP measurement (Z-R method).

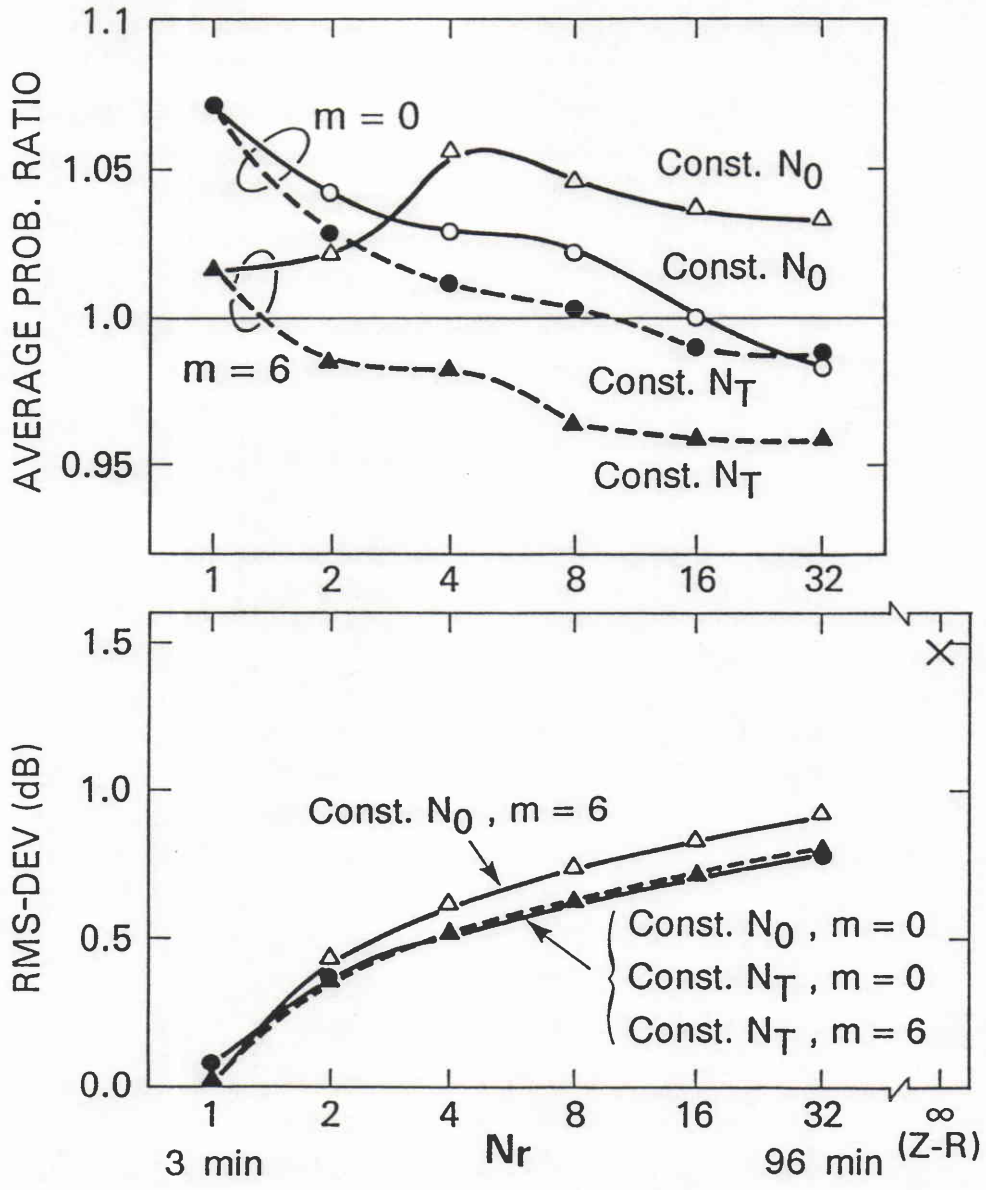

Figure 5-9. *Nr* dependence of rain rate estimation accuracy (*APR* and *RMS-dev*). $Nr = 1$ represents "complete" DP measurement and $Nr = \infty$ an SP measurement using a *Z-R* relation.

The dependence of rain rate estimation accuracy (*RMS-dev* and Average Probability Ratio, *APR*) on N_r is shown in Figure 5-9. It is interesting that the accuracy changes significantly between $N_r = 1$ and 2, and that the RMS deviation seems to saturate from $N_r = 2$ to 32. Even when $N_r = 32$, a twofold improvement can be obtained in comparison to the SP measurement. This indicates the usefulness of adding an attenuation measurement integrated over a storm; i.e., the usefulness of event-scale adjustments of IRP relations.

Table 5-2. A result of path-averaged rain rate estimation. SDP_{av} results using other three two-scale models are very close to the result shown here.

	RMS deviation	Av. Prob. Ratio
- SP measurement		
Z-R method	1.40 dB	1.333
k-R method	0.22 dB	1.010
- SDP_{av} measurement†		
SDP_{av}-1	0.021 dB	0.999
SDP_{av}-2	0.020 dB	1.003

† "Constant N_T, m = 6" model, $N_r = 4$.

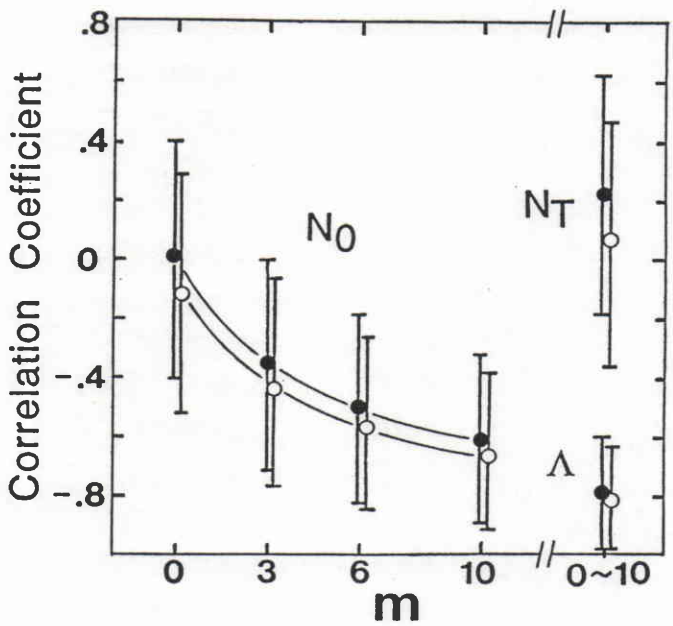

Figure 5-10. Mean and standard deviation of correlation coefficients between logarithms of N_0 and Z, N_T and Z, and Λ and Z. Each sample is obtained from a 30 ~ 90 minute rainfall event. Filled circles represent the result when only rainfall events which have a maximum rain rate higher than 5 mm/h are included.

We also see that the RMS deviation of the "constant N_0 with m = 6" model is somewhat worse than the others. In addition, the dependence of APR on N_r is different from the others, which is consistent with the small β value given by this DSD model. This result can also be explained from the Z-factor dependence of N_0 and N_T shown in Figure 5-10. Since N_0 (m = 6) has a clear negative correlation with Z, if a path-averaged N_0 is used for different Z values on a path, N_0 is overestimated and underestimated at greater and smaller Z

values, respectively. This results in overestimation and underestimation of rain rate at higher and lower rain rates, respectively. Accordingly, *APR*, which gives larger weights on higher rain rates, increases. The result shown in Figure 5-9 indicates that an unreasonable two-scale model would degrade the rain rate estimation accuracy.

5.4.3 Estimation of path-averaged rain rate

It should be noted that the above results are those for the rain rate estimation for each resolution cell; i.e. profiling. In estimating a path-averaged rain rate, the SDP measurement works as a DP measurement since the radar resolution required is now ΔR, not Δr. There may be two options for estimating the path-averaged value: (1) Z-factors are averaged and combined with the path-averaged attenuation ($SDP_{av}1$); (2) rain rate profile obtained from the SDP measurement is then averaged over the path ($SDP_{av}2$).

A simulation of these "averaged" SDP measurements has been performed and the path-averaged rain rate estimation accuracy compared with two kinds of SP measurements; Z-R method and k-R method. For the SP measurements, Z-R and k-R relations derived from the two-year disdrometer data are used. The result, which is summarized in Table 5-2, shows that the two SDP_{av} methods give nearly perfect estimation just as the complete DP measurement. The k-R method gives slightly larger RMS error than the SDP_{av} measurements; however it still provides an excellent estimation. This is due to the similarity in the kernels of rain rate and attenuation (assumed to be proportional to M_4). The bias error seen in the Z-R method may be due to the difference in the data bases for obtaining the Z-R relation and for the simulation.

5.5 Validity of the two-scale model

The validity of the two-scale DSD model can be seen by some different ways. One is to see the variation of N_0 or N_T with range. In SDP measurements, a path-averaged N_0 (or N_T) is estimated and used for all range bins. Although this is not true, our interest is how high the correlation remains with range. Figure 5-11 shows the scattergram of "true" (the value estimated by a complete DP measurement) versus path-averaged N_0 values for $N_r = 2$ and $N_r = 32$ cases. We can see that even when $N_r = 32$, a high correlation remains. Therefore in contrast with SP measurements which always assume a fixed N_0 or N_T value, SDP measurements estimating N_0 or N_T with a low resolution can improve the rain rate estimation accuracy depending on the measurement resolution and the spatial correlation of the DSD parameters.

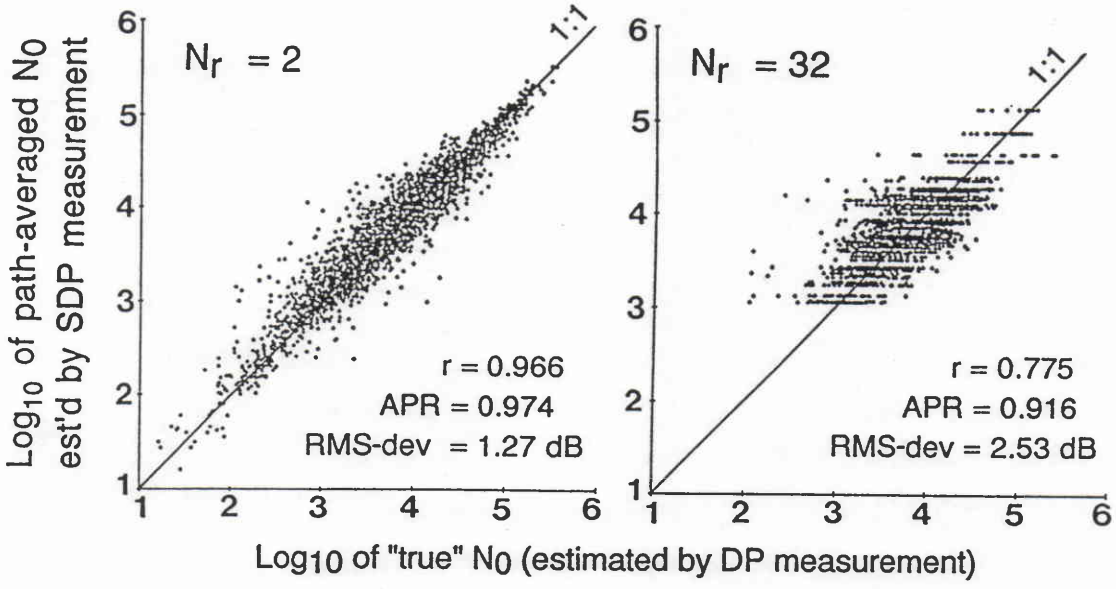

Figure 5-11. Correlations between N_0 derived from a DP measurement and that derived from SDP measurements with N_r = 2 and 32. The former N_0 can be recognized as a "true" value in the sense that it provides a nearly perfect rain rate estimation.

The other interpretation is to compare the magnitude of "short-term" and "long-term" variations in DSD parameters. Let us assume that the fluctuation in a DSD parameter (e.g. N_0) consists of two spatial or temporal variabilities; the fluctuation within a ΔR and that for values averaged over a ΔR. Let the variances for the former (short-term fluctuation) and the latter (long-term fluctuation) be σ_S^2 and σ_L^2, respectively. Since these fluctuations should be independent, SP measurements suffer the total variance, σ_T^2 (= $\sigma_S^2 + \sigma_L^2$). Whereas SDP measurements, which can estimate a long-term fluctuation with the resolution ΔR, suffer only σ_S^2. The rain rate estimation accuracy obtained by an SDP measurement depends on the relative magnitude of σ_S^2 to σ_T^2. If ΔR is so short that the DSD parameters correlate well in the ΔR (i.e. $\sigma_S^2 \ll \sigma_T^2$), SDP measurements should work desirably. Whereas, if ΔR is as coarse as the period that includes many different storms, σ_S^2 would be close to σ_T^2 and therefore SDP measurements would not improve the accuracy.

To examine the N_r dependence of the magnitude of σ_S^2 relative to σ_T^2, the two-year disdrometer data set is divided into many time segments each of which consists of N_r DSD samples. A statistical analysis is then performed for the σ_S^2 of a DSD parameter obtained from each time segment. Figure 5-12 shows the ratio of σ_S to σ_T derived from the two-year disdrometer data set as a function of N_r (corresponds to the length of ΔR), where σ_S represents the square-root of the average σ_S^2 and σ_T represents the standard deviation of samples included in all time segments. Plots at the left part of the figure (N_r = 6 to 32) represent the result obtained only by using the time segments each of which has a sequence of N_r samples continuous in time; i.e., σ_S should represents the fluctuation within a rain event or shorter period. Whereas the right plots (N_r = 32 to 2000) represent the result without the above data continuity check; i.e. the N_r samples in a time segment include the DSD for different storms. In fact, data sets of N_r = 32, 200, and 2000 without the continuity check consist of DSDs sampled over 1.5 hours to a few days, one or two weeks, and several months, respectively.

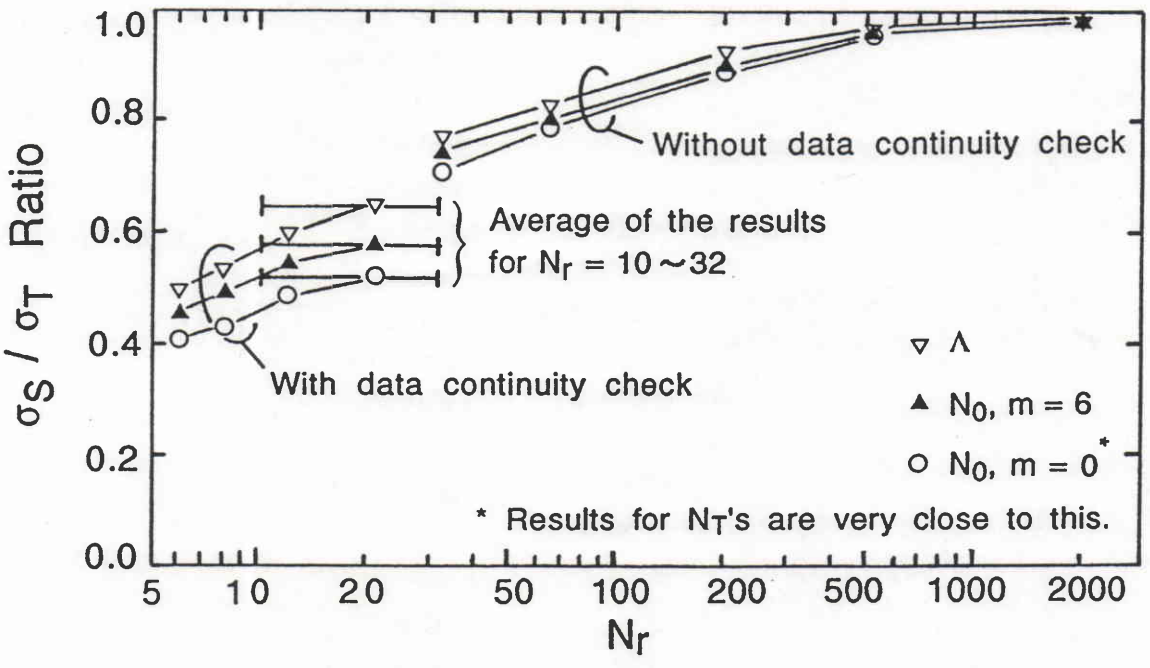

Figure 5-12. Dependence of σ_S/σ_T ratio on N_r. For obtaining σ_S and σ_T, the two-year disdrometer data time series is divided into N segments with the length N_r. Variance $\sigma_{S_i}^2$ is calculated for each segment ($i = 1 \sim N$), and σ_S is obtained from the average variance σ_S^2 ($= 1/N \sum_{i=1}^{N} \sigma_{S_i}^2$). σ_T is directly calculated from the all data included in the N segments.

The following conclusion can be drawn from Figure 5-12: (1) σ_S/σ_T approaches unity, i.e. SDP measurements approach SP measurements with increasing N_r; (2) there appears a gap between the results obtained from the data sets with and without the continuity check, indicating the existence of large event-by-event DSD variations; (3) N_0 ($m = 6$) and Λ have larger σ_S/σ_T ratios than N_0 ($m = 0$) and N_T; and (4) SDP measurements should improve the rain rate estimation accuracy by about a factor of two, with some dependence on the assumed two-scale model. The latter two conclusions, which indicate the necessity to use a "good" two-scale model and the validity of applying a two-scale model within a rain event, are consistent with the result shown in Figure 5-9. In the case of N_0 ($m = 0$), for example, σ_T is as large as 5 dB (see Table 4-1); however, σ_S within a rain event is only about 2 ~ 2.5 dB. The gap in the σ_S/σ_T ratio mentioned in (2) suggests that the rain rate estimation accuracy would be degraded if the resolution ΔR (in this test, a time segment of length N_r) spans over two or more different rain events.

5.6 Conclusions

In this Chapter, we have investigated rain rate estimation properties of the "semi" dual-parameter (SDP) radar measurement combining radar reflectivity factor (Z) and a path-integrated microwave attenuation through a simulation using a disdrometer data set collected over 2 years. This type of measurement applies to most of spaceborne radar measurements, and has properties between " complete" DP and single-parameter (SP) measurements. We have proposed a concept of "two-scale" DSD model, the parameters of which can be derived from the SDP measurement.

It has been shown that the SDP measurement provides an RMS error ranging from 0.4 to 0.8 dB for the estimation of log of rain rate in contrast with 0.03 dB and 1.5 dB for a DP measurement and an SP measurement (Z-R method), respectively. The degradation in the accuracy from DP to SDP measurements comes mainly from the decorrelation in DSD parameters. An interesting result is that even when the resolution of attenuation measurement is as coarse as N_r = 32 (96 minutes), the SDP measurement clearly provides a better estimation than the SP measurement. This indicates the usefulness of "event-scale" adjustment of IRP relations. It is shown that the SDP measurement can also improve the accuracy in comparison to SP measurements (k-R and Z-R methods) in the estimation of path-averaged rain rate.

The ability of the SDP measurement to estimate DSD parameters should generally be desirable for introducing a clear physical background into rain parameter estimation algorithms and for deeper understanding of precipitation properties. For rain rate estimation, the usefulness of the SDP measurement should be enhanced as the kernel of attenuation differs from that of rain rate. If the difference is small, like 35-GHz attenuation, the SDP measurement would not be so useful; i.e. DSD estimation may not be necessary. Moreover, the usefulness should depend on the relative magnitude of the "long-term" DSD variation and measurement errors as we have studied in Chapter 4 for the dual-parameter measurement. If the former is very large, even somewhat poor measurements should be useful. If DSD is stable, the SDP measurement may be more erroneous than the SP measurement.

In the present study, we have assumed that IRPs are proportional to DSD moments to simplify the formulation. Although this is approximately true for many cases, in general we have to use more sophisticated or numerical techniques to derive DSD parameters; particularly when effects of Mie scattering and rain attenuation up to a radar scattering volume become significant. Through such generalization, however, various rain rate profiling methods combining a Z-factor profile and a path attenuation could be recast in terms of the parameter estimation of a two-scale DSD model. An approach that is applicable to more general conditions will be proposed later in Chapter 7 as well as a test of the method using an aircraft dataset.

Although the two scale models used in the present study should be adequate ones as a first approximation, the accuracy in estimating rain rate and other rain parameters should be improved by refinements of the two-scale model. Such refinements include DSD modeling incorporating a rainfall-type dependence of the two-scale model and a height dependence of DSD caused by evaporation, coalescence, breakup, etc., and modeling the DSD of bright-band particles especially for the application to spaceborne radar measurements. As an extension of the SDP measurement, combining two (or more) kinds of path-integrated quantities with a Z-factor profile is also worth studying for obtaining a better estimation of the DSD parameters.

Appendix 5-1 Preliminary analysis of rain-type dependence of Z-R relation

- Rain-type classification

In order to perform the classification automatically, the method used to analyze the ETS-II[14] and CS/BSE[15] propagation experiments is employed here, which is illustrated in Figure 5-A1. Although this method may not work to distinguish convective storm and shallow rain, it was successfully used to extract rain-type dependence of slant-path attenuation and cross-polarization properties[14,15]. Further detailed classification is a subject of future study. Reflectivity profiles along the CS and BSE paths observed by the C-band radar (Figure 3-6) have been used for the classification. To quantify the rain type, the following numbers are specified; "stratus" = 1, "others" = 2, and "cumulus" = 3. Since the classification result changes from time to time, the values are averaged over a rain event to give an "average" rain type for the event, which ranges between 1 and 3.

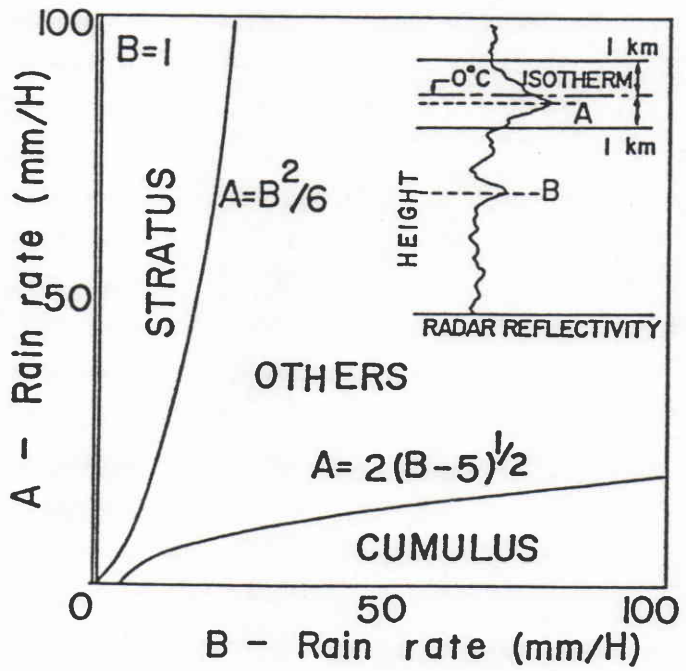

Figure 5-A1. Rain-type classification method[14]

- Disdrometer data processing

As with the processing used in Section 5.3, disdrometer data (from May to November 1980, for this analysis) are segmented into "rainfall event", and a regression analysis is performed to derive event-scale Z-R relations. The resulting α and β in $Z = \alpha R^{\beta}$ are then

analyzed against the rain type. Among the total 91 rain events, only (α,β) pairs obtained from rain events having correlation coefficients higher than 0.9 (total 79 events) are used for the analysis. Figure 5-A2 shows scattergrams between rain-type and the maximum rain rate observed within a rain event, and between rain-type and the exponent β. As expected, the "cumulus" type rain is more intense than the "stratus" type rain. It is found that many of the exponent β are distributed around 1.4 ~1.6, which is consistent with the result obtained in Section 5.3. While the β value in the "stratus" rain is widely scattered, it is more stable in the case of the "cumulus" rain. This suggests that the two-scale models used in this chapter may be sufficient for the "cumulus" rain, but more study is required to model the DSD in the "stratus" rain. Figure 5-A3 shows the scattergram between β and α for typical "stratus" ("rain type" < 1.6) and "cumulus" ("rain type" > 2.4) cases. The high negative correlation between β and α appeared in this figure is a natural consequence that Z-R relations should give physically reasonable Z and R values naturally found. Although the coefficient α appears to vary widely not only in the "stratus" but the "cumulus" rain, we should note that α can be estimated from the SDP measurement described in this chapter. In Table 5-A1, statistics of the α and β values are summarized.

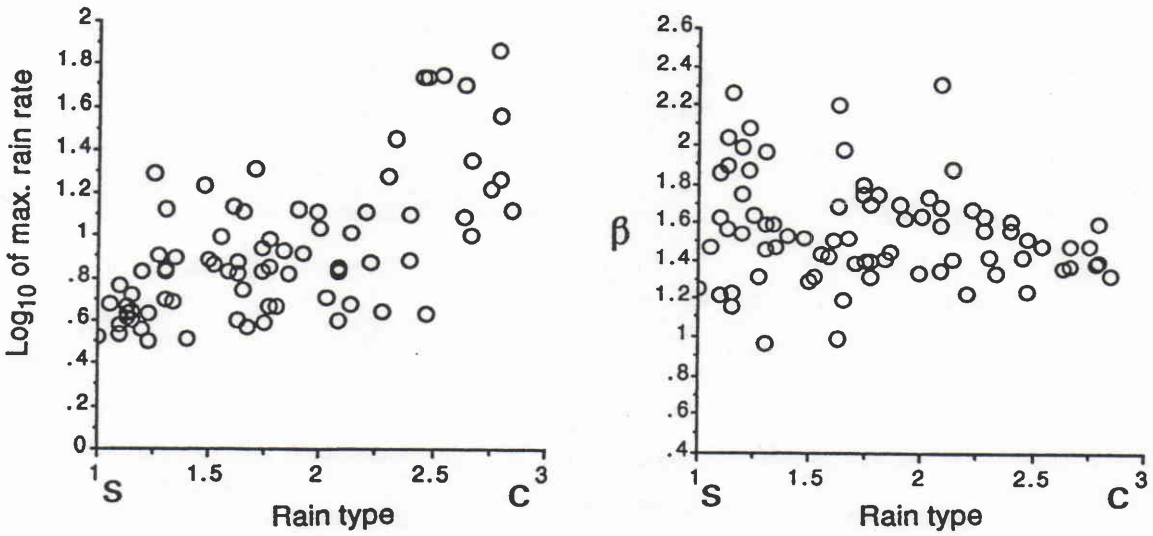

Figure 5-A2. Scattergrams of rain-type versus maximum rain rate observed within a rain event, and of rain-type versus β.

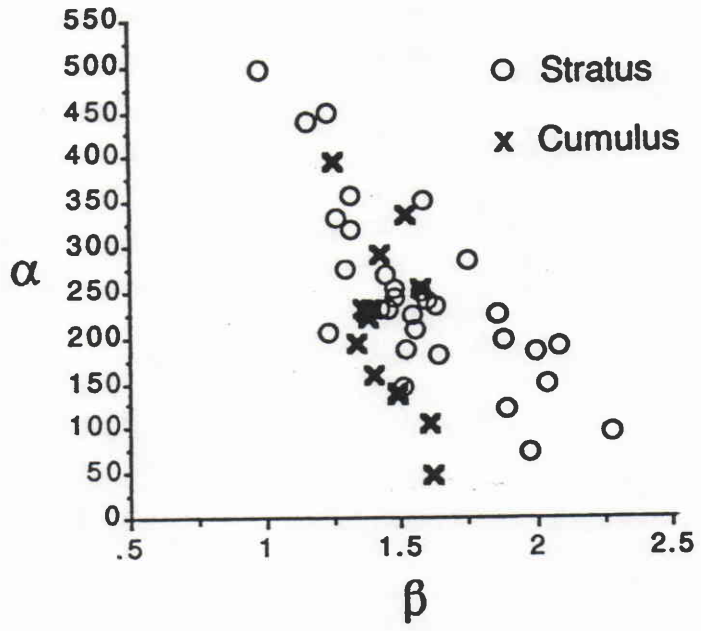

Figure 5-A3. Scattergram of β versus α for typical "stratus" rain (rain type < 1.6, open circles) and "cumulus" rain (rain type > 2.4, "X").

Table 5-A1. Statistics of the coefficient α and the exponent β in *Z-R* relation. (Correlation coefficient > 0.9 only)

	Number of data	Mean	SD	Min	Max	Percentiles 10%	50%	90%
All rain	79							
α		225	103	41.5	679	114	215	345
β		1.55	0.27	0.97	2.31	1.25	1.52	1.94
Stratus	31							
α		246	98.5	73.0	498	136	230	390
β		1.57	0.30	0.97	2.27	1.22	1.53	2.01
Cumulus	14							
α		212	92.2	47.3	394	99.8	225	342
β		1.44	0.11	1.24	1.61	1.32	1.41	1.60

References

(1) Kozu, T. and K. Nakamura, 1991: Rainfall parameter estimation from dual radar measurements combining reflectivity profile and path-integrated attenuation. *J. Atmos. Ocean. Tech.*, **8**, 259-270.

(2) Feingold, G. and Z. Levin, 1986: The lognormal fit to raindrop spectra from frontal convective clouds in Israel. *J. Climate Appl. Meteor.*, **25**, 1346-1363.

(3) Atlas, D. and C.W. Ulbrich, 1974: The physical basis for attenuation-rainfall relationships and the measurement of rainfall parameters by combined attenuation and radar methods. *J. Res. Atmos.*, **8**, 275-298.

(4) Ulbrich, C.W., and D. Atlas, 1978: The rain parameter diagram: Methods and applications. *J. Geophys. Res.*, **83**, (C3), 1319-1325.

(5) Meneghini, R., J. Eckerman, and D. Atlas, 1983: Determination of rain rate from a spaceborne radar using measurements of total attenuation, *IEEE Trans. Geosci. Remote Sens.*, **GE-21**, 34-43.

(6) Lin, H., M. Xin, and C. Wei, 1985: Ground-based remote sensing of LWC in cloud and rainfall by a combined dual-wavelength radar-radiometer system. *Advances in Atmos. Sci.*, **2**, 93-103.

(7) Weinman, J. A., C. D. Kummerow, and C. S. Atwater, 1988: An algorithm to derive precipitation profiles from a downward viewing radar and multi-frequency passive radiometer. *Proc. GARSS'88*, Edinburgh, U.K., 229-234.

(8) Fujita, M., 1989: An approach for rain rate profiling with a rain-attenuating frequency radar under a constraint on path-integrated rain rate, *Proc. GARSS '89*, Vancouver, Canada, 1491-1494.

(9) Marzoug, M. and P. Amayenc, 1991: Improved range profiling algorithm of rainfall rate from a spaceborne radar with path-integrated attenuation constraint. *IEEE Trans.Geosci. Remote Sens.*, **GE-29**, 584-592.

(10) Meneghini, R. and K. Nakamura, 1990: Range profiling of the rain rate by an airborne weather radar. *Remote Sens. Environ.*, **31**, 193-209.

(11) Kozu, T., J. Awaka, K. Nakamura, and H. Inomata, 1986: Improved estimation of rain attenuation and rainfall rate for slant-paths by simultaneous radar and radiometer measurements. Preprints, *23rd Conf. Radar Meteor.*, Snowmass, CO, Amer. Meteor. Soc., 104-107.

(12) Battan, L.J., 1973: *Radar observation of the atmosphere*. The University of Chicago Press, Chicago, 324pp.

(13) Waldvogel, A., 1974: The N_0 jump of raindrop spectra. *J. Atmos. Sci.*, **31**, 1067-1078.

(14) Furuhama, Y., T. Ihara, T. Shinozuka, K. Nakamura, and J. Awaka, 1981: Propagation characteristics of millimeter and centimeter waves of ETS-II classified by rainfall types. *Ann. Telecomm.*, **36**, 24-32.

(15) Fukuchi, H., T. Kozu, K. Nakamura, J. Awaka, H. Inomata, and Y. Otsu, 1983: Centimeter wave propagation experiments using the beacon signals of CS and BSE

CHAPTER 6. AIRBORNE RADAR RAINFALL MEASUREMENT

For testing and improving the rainfall retrieval methods, data from aircraft radar experiments are important, because the down-looking spaceborne radar measurements can well be simulated by airborne radars. CRL and NASA have been conducting a series of joint aircraft experiments using the microwave airborne rain-scatterometer/radiometer (MARS) developed at CRL. The history of the joint experiment was outlined in Chapter 1. In this chapter, a description is given of the instruments used for the experiment in 1988 and 1989, the data from which are used to test the DSD estimation method proposed in this study[1,2]. The aircraft used in this experiment is the NASA T-39 jet airplane that can fly much higher than those used in previous experiments thereby enabling a study of heavier convective storms and upper precipitation structure. Observations from such high altitude is also an excellent simulation of those from space. Major specifications of the T-39 aircraft are listed in Table 6-1. Two instruments were used in this experiment (hereafter, the T-39 experiment); a modified version of the MARS [3] and a NASA 19-GHz dual-polarization radiometer[4]. Figure 6-1 shows the T-39 aircraft at WFF and the instruments installed on the T-39.

Table 6-1. Major specifications of NASA/T-39 aircraft

Official name	T-39 Subliner (NASA 431)
Nominal speed	385 knots (198 m/sec)
Maximum speed	440 knots (226 m/sec)
Maximum payload	1,500 lbs (680 kg)
Maximum cruise time	2.5 hours
Empty weight	9,965 lbs (4.52 tons)
Cabin size	60 x 40 x 100 inches (1.52 x 1.02 x 2.54 m)

6.1 Airborne Radar/Radiometer

The MARS comprises dual-frequency (10.00 GHz and 34.45 GHz) radars and dual-frequency radiometers (9.86 GHz and 34.21 GHz), the original version of which was developed in 1979. For the T-39 experiment, extensive modifications have been made in order to achieve higher sensitivity and horizontal resolution, to improve accuracies in both precipitation and surface echo measurements, and to improve real-time monitoring capabilities.

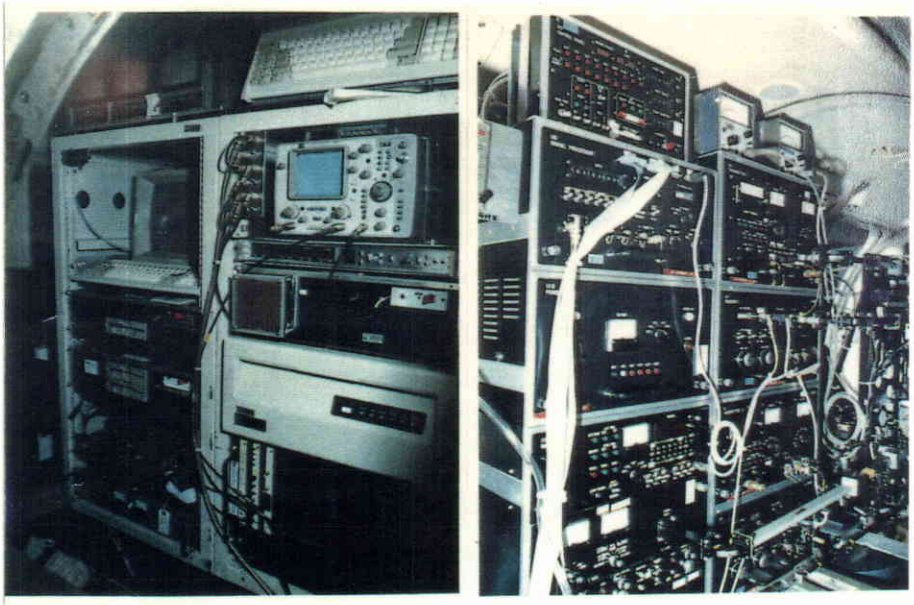

Figure 6-1. NASA T-39 aircraft at WFF and instruments installed on the aircraft.

Major parameters of the instruments for the T-39 experiment are summarized in Table 6-2. The block diagram of the system is shown in Figure 6-2. The system consists of antennas, X-band and Ka-band radars (RF and IF units), an X/Ka-band radiometer, a 19-GHz radiometer (NASA's), a signal processor/radar controller (original one), a CAMAC [5] digital/analog I/O system, a digital tape drive, a pitch/roll gyro, a loran receiver, a video camera and recorder, an oscilloscope, and three IBM PC's (for radar data collection, for 19-GHz radiometer data collection, and for real-time monitoring, respectively). The major items of the system upgrade for the T-39 experiment are:

• Antenna: Original offset parabolic antennas were changed to a pair of matched beam horn-lens antennas having 5-degree half-power beam width (HPBW) and 30-dB gain. Those provide about 4-dB better sensitivity than and about 40 percent reduction in foot print size from the values of the original antennas.

• Data processing system: An IBM PC-based new data processing system was developed. To support various analog and digital I/O's, CAMAC instruments and an internal I/O board are used to make interfaces to other equipments.

• Real-time monitoring: Another IBM-PC was installed to provide versatile real-time monitor functions including two types of color displays; a radar/radiometer system status summary and color-coded 2-D display of the measured radar reflectivity profiles. Data for this real-time monitor are transmitted from the data acquisition computers through RS-232 interfaces.

• Radar/radiometer data are stored on a 1600-BPI magnetic tape. The summary data sent to the monitor computer are also stored on a floppy disk to allow a quick review of a flight.

• A CAMAC high-speed 8-bit A/D converter provides a radar signal sampling rate of 0.2 μsec that is 2.5 times oversampling in comparison to the radar pulse width. The integrator connected directly to the A/D converter allows a variable number of pulse integration, N_{integ}, from 1 to 65536, although N_{integ} of 128 is nominally used. The oversampling is useful to improve the accuracy in measuring surface return signal level because the surface return is usually very spiky for near-nadir incidence.

• Data sampling window was expanded from the original one (9 km) to 22.5 km (X band) and 20.25 km (Ka band) in order to measure entire storm including mirror image.

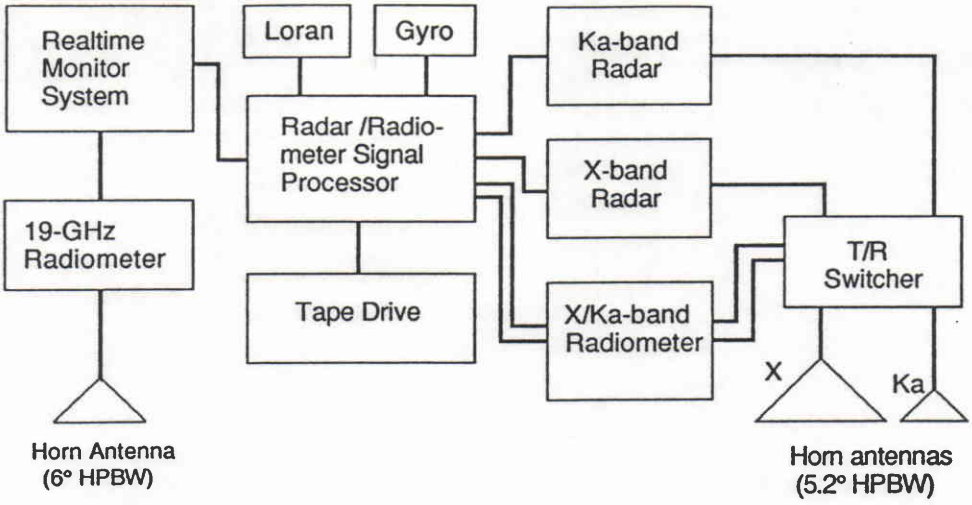

Figure 6-2. Block diagram of the instruments for the T-39 experiment.

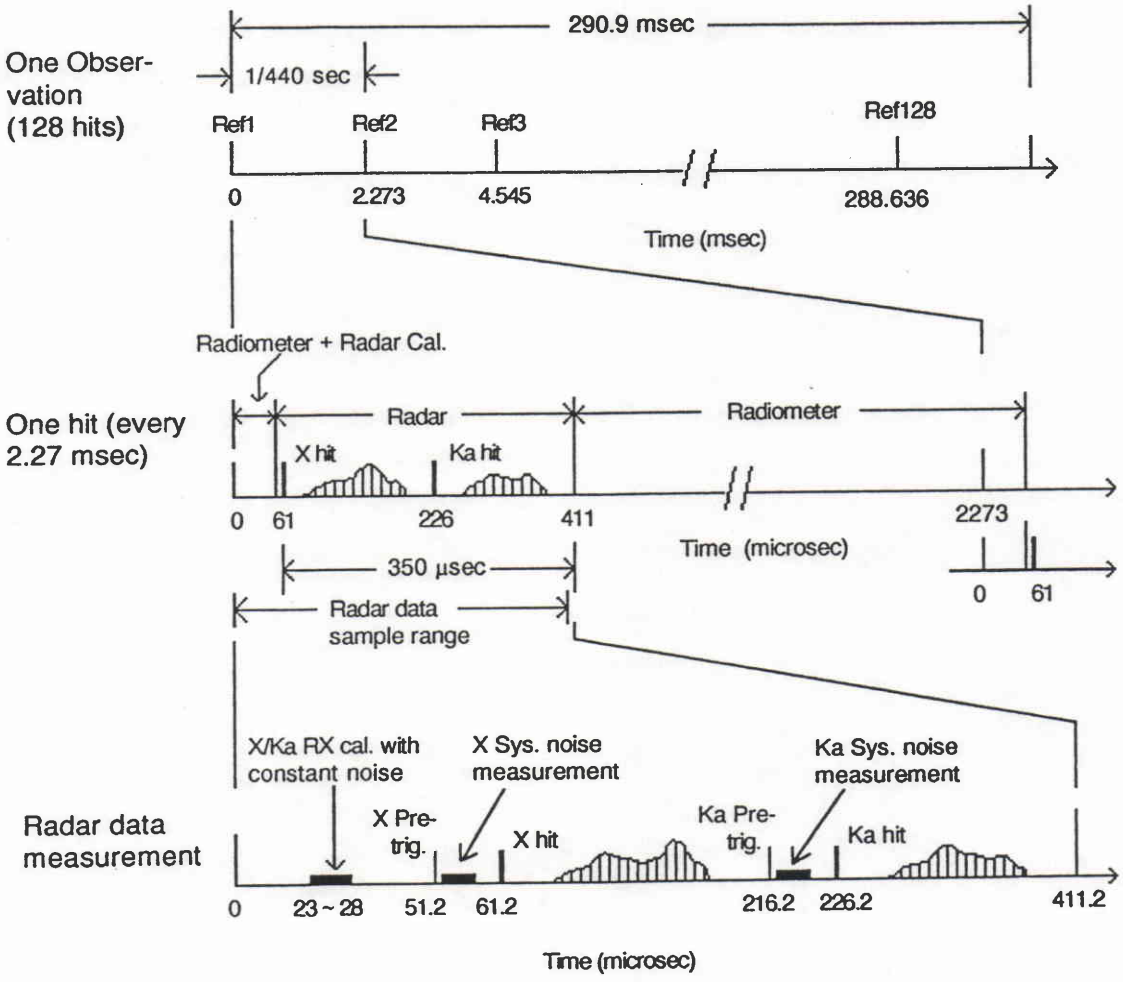

Figure 6-3. Data acquisition timing chart of the dual-frequency radar/radiometer.

• Extended noise monitoring function: Two types of noise level monitoring were added; one is to measure the receiver noise plus a noise from an internal terminator that is used to monitor short-term (a few minutes to one flight) receiver gain fluctuation (*Noise-cal*), and the other is to measure the receiver noise plus the antenna noise which varies depending on microwave emission properties of the surface (*Noise-sys*). This is used to extract the signal level from the measured total (signal + noise) level.

The data acquisition timing chart is shown in Figure 6-3. The data sampling starts from 51.2 μsec before the X-band pulse hit in order to measure the noise levels and a leak signal directly coming from the transmitter. The latter is used to monitor the radar transmit timing.

Table 6-2 Major system parameters for the T-39 experiment

RADAR

	X band	Ka band
Center frequency	10.00 GHz	34.45 GHz
Antenna		
Type	Horn lens	Horn lens
Aperture	42 cm	13 cm
Gain	30.3 dB	30.4 dB
HPBW	5.2 deg	5.1 deg
Transmitter		
Peak power	20 kW	10 kW
PRF	440 Hz	440 Hz
Pulse width	0.5 μsec	0.5 μsec
Receiver		
Noise figure	5.3 dB	9.6 dB
Detection	Logarithmic	Logarithmic
Dynamic range	80 dB	80 dB
Signal Processor		
Sample interval	0.2 μsec	0.2 μsec
Range window	22.5 km	20.25 km
Number of indep. samples (nominal)	128	128

RADIOMETER

	X band	Ka band	K band
Center frequency	9.86 GHz	34.21 GHz	18.70 GHz
Antenna	Same as the radar antenna		Horn lens
IF bandwidth	100 MHz	100 MHz	200 MHz
Integ. time	0.25 sec	0.25 sec	0.1 sec
Resolution	0.5 K	0.5 K	0.3 K

6.2 Outline of the Experiment

Tables 6-3 and 6-4 summarize a series of flights in October through December, 1988, and meteorological conditions measured at WFF during the flights. The experiment was based at Wallops Flight Facility (WFF) of NASA, Virginia, where the T-39 aircraft has been maintained. The flight was mainly conducted over the Atlantic Ocean around WFF; however, an over-land flight was also successfully conducted on October 21, 1988. An S-band ground-based radar (SPANDAR) at WFF was used to find rain cells and to direct the aircraft to them. Raingages were also employed to obtain truth data.

Table 6-3 Summary of the T-39 experiment, fall 1988.

No.	Date, Time (UT / EDT or EST)		Remarks
1.	10/19	1537-1735/1137-1335	1st observation flight. Over ocean, Ka-band RX good, light rain, Ka-band TX power too high. Anyway everything worked.
2.	10/21	1919-2125/1519-1725	Stratiform rain. Over ocean and land (raingage, disdrometer and SPANDAR). X radiometer failed. Ka RX not good.
3.	10/22	1323-1520/0923-1120	Over land/ocean. No rain. Retrace the same ground track as the flight on 10/21.
4.	10/28	2003-2146/1603-1746	Over ocean. Norfolk area. Some localized convective storms.
5.	11/01	1544-1758/1044-1258	Over land/ocean. Mainly stratiform rain.
6.	11/01	1955-2230/1455-1730	Over ocean. Northeast of WFF. Some heavy storms. Good! But too far from SPANDAR.
7.	11/05	1819-2100/1319-1600	Over ocean. Some heavy storms. But they escaped into restricted areas. Both Ka and X-band Both Ka TX and RX bad.
8.	11/17	1655-2123/1155-1423	Over ocean. Some heavy storms. Ka RX recovered somewhat.
9.	12/13	1859-2049/1359-1549	2nd calibration flight over ocean. Cloudy. At the end of the flight, cloud-free data was obtained

Table 6-4. Meteorological data during the flights, fall 1988 measured at WFF (average of the data taken every hour during the time period shown for each flight).

Date	Time (UT)	Temperature (°C)	Dew Point (°C)	Pressure (mb)	Wind Velocity (m/s)	Wind Direction (Az, deg.)
10/19	16 - 18	13.9	7.8	1015.4	3.8	320
10/21	19 - 20	13.9	12.5	1014.4	2.6	050
10/22			No data available.			
10/28	19 - 20	18.3	15.0	1017.2	6.7	180
11/1a	16 - 17	10.6	9.7	1011.1	5.7	020
11/1b	20 - 21	10.6	8.9	1006.2	3.1	325
11/05			No data available.			
11/17	17 - 20	11.1	5.2	1017.1	4.9	330
12/13	19 - 21	-1.1	-5.5	1010.7	4.0	320

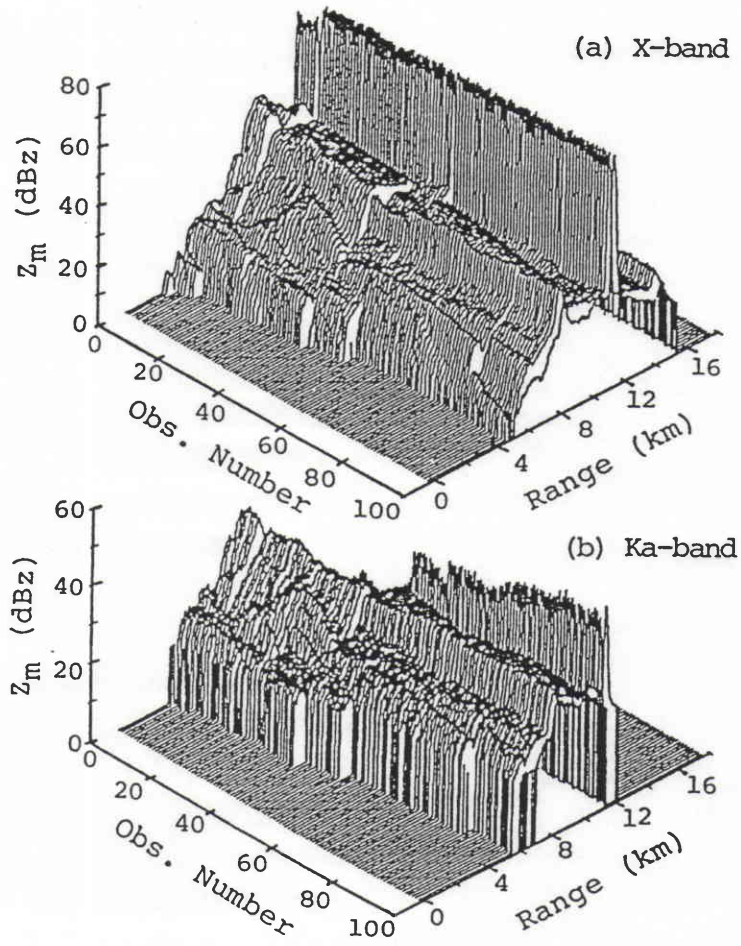

Figure 6-4. Example of 3-D plot of X and Ka-band *Zm* profiles on November 1, 1988.

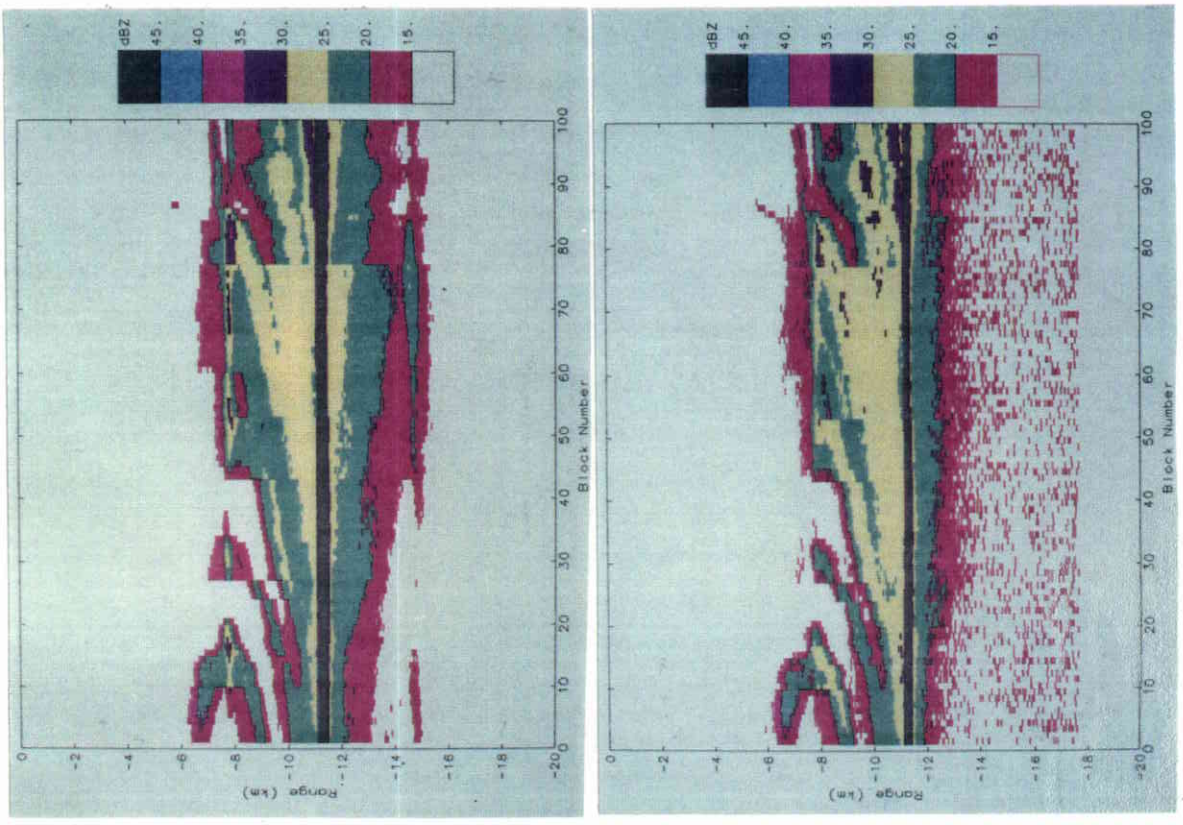

(b) Upper, X band. Lower, Ka band.

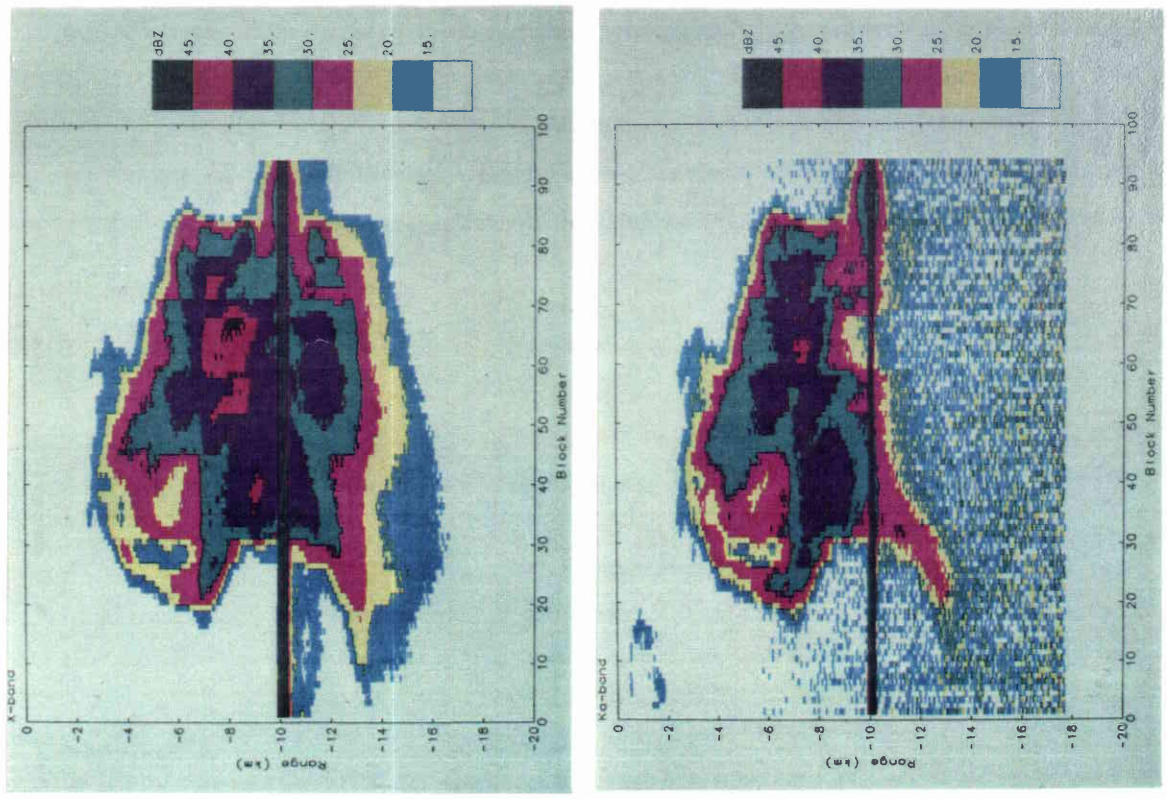

(a) Upper, X band. Lower, Ka band.

Figure 6-5. Example of contour plots of *Zm*. (a) Convective rain; October 28, 1988. (b) Stratiform rain; November 17, 1988.

Figure 6-4 shows an example of 3-D plot of X-band and Ka-band Zm profiles measured on October 1, 1988, over the Atlantic Ocean. A single observation, which was taken approximately every 0.4 seconds, represents an average of 128 pulse hits. Since the aircraft nominal speed is about 200 m/sec, 100 observations correspond to about 8 km if the observation is continuous. For data processing, however, those observations which were interrupted by radio interference, taken during aircraft attitude fluctuation and banking, and taken over some of non-raining areas have been skipped in order to guarantee the quality of processed data and to reduce the data volume. The abscissa "observation number" represents the sequential number after the data skip, and therefore the actual distance is generally larger than the value simply measured by the above conversion factor (80 meters per observation.)

The sharp large spike at about 11-km below the aircraft shown in Figure 6-4 is the surface return. Although the quantity *Zm* for the surface return is meaningless, it is shown to see its relative magnitude. In most cases, the X-band surface return is almost constant indicating little rain attenuation at X-band. In the corresponding Ka-band plot, much stronger rain attenuation is evident from the large variation in the surface return. Below the surface, mirror image return appears for X-band. For Ka-band, on the other hand, no mirror image appears due to the strong rain attenuation at this frequency. This feature can be more clearly seen from the contour plots of *Zm* values. Figure 6-5 shows an example of such plots for typical convective cell and stratiform rains over the Atlantic Ocean. In the Ka-band plot of the convective storm, some mirror image appears at the leading edge of the storm at which no rain exists between the precipitation aloft and the surface.

6.3 Radar Equation and Processing of Level "zero" Data

The first step of the radar data processing is the conversion of a "count" value stored on the tape to the apparent effective radar reflectivity factor, *Zm* (see Eq.2.23). To do this, radar equation appropriate to the radar observation condition should be established, and the radar system constants appearing in the equation should be quantified as well as their temporal drifts during a time period of interest. Since the radar equation relates the *Zm* value to the radar received power, it is necessary to establish another relation; i.e. the relation between the received power and the count value.

- Radar equation used to obtain Zm value

From Eq.(2.23), the radar equation, written in decibel unit, relevant to the observation condition for the T-39 experiment can be written

$$P(r) = C + 10 \cdot \log_{10} Zm - 20 \cdot \log_{10} r \tag{6.1}$$

with

$$C = 10 \cdot \log_{10}(\pi^3/(1024 \ln 2)) + 2 \cdot G + 20 \cdot \log_{10} \theta_b + 10 \cdot \log_{10} (c\tau) + P_t + 10 \cdot \log_{10} |K_w|^2 - 20 \cdot \log_{10} \lambda - L - 180.0 \tag{6.2}$$

where Zm (mm^6/m^3) is the apparent radar reflectivity factor, r (m) is the range from the radar to a target, G (dB) is the antenna gain, θ_b (rad) is the half-power beamwidth of the antenna, c (m/sec) is the speed of light, τ (sec) is the pulse width, P_t (dBm) is the radar peak transmit power, K_w is the dielectric factor of water (Eq.2.10), λ (m) is the radar wavelength, L (dB) is the total system loss, and C is the radar system constant. Note that "-180.0" is necessary to convert the unit of Zm from mm^6/m^3 to m^3.

- Radar received power calibration

The relation between radar received power and count value stored on the tape can be determined by injecting RF signals of known levels into an input port of the receiver and by measuring the corresponding count values. Such receiver calibration has been performed by using a microwave frequency synthesizer as a source. Since the receiver has a logarithmic detector, the relation between the input signal level, P, and the count value, Y, is expressed as

$$Y = a P + b \tag{6.3}$$

where a and b are coefficients to be determined through the linear regression of the measured values of P and Y. It should be noted that a and b are usually determined through the calibration using a continuous wave of a single frequency rather than an incoherent signal like rain echo, and that Y represents the video voltage after the incoherent integration of log-converted power. Therefore, an end-to-end radar equation to obtain Zm is given by

$$10 \cdot \log_{10} Zm = a Y + b + F_{log} - C + 20 \cdot \log_{10} r \tag{6.4}$$

where F_{log} (= 2.5 dB) is the bias caused by integrating the logarithm of power rather than the power itself (Section 2.2.3). In practice, there is a small fluctuation in a, b and C. According

to our experience, however, the coefficient a is almost constant for a given logarithmic detector. The fluctuation in C is mainly caused by that in the transmit power, and can be monitored by measuring P_t periodically. Whereas, the fluctuation in b is caused by the gain drift in the receiver (including the log detector). Assuming that the noise figure of the receiver is almost constant at least within a flight (several hours), we can use the noise level output from the receiver as a tool to monitor receiver gain drift when a constant noise power is injected to the receiver (e.g., the noise from a terminator with temperature controlled). The *Noise-cal* measurement mentioned above is made for this purpose. Such monitoring of relative variation in the transfer function from Y to Zm allows an accurate measurement of "relative" Zm values.

6.4 External Radar Calibration

The absolute Zm measurement is more difficult than the relative measurement because the bias errors in a, b and C as well as the "relative" fluctuation of those values have to be taken into account. In practice, however, the bias error in a is minor and the error in b can effectively be combined with that in C. Thus, the problem reduces to the determination of the system constant C. Since the antenna characteristics have to be known to determine C, it is necessary to employ an external calibration scheme using a reference target. Although there are several candidates for the reference target such as metal spheres and corner reflectors[6], it may be said that the rain itself is the best target in the sense that the same radar equation as that used for actual rain observation can be used to determine the error in C.

The radar is externally calibrated by using the data obtained during the over-raingage flight on October 21, 1988 (see Figure 6-6). As the rain was widespread and stratified, DSD is assumed to follow the Marshall-Palmer (MP) distribution[7] from which a 10-GHz Ze (calculated with Mie theory) vs. rain rate relation of $203 \cdot R^{1.6}$ is derived. A correction factor, F, in the radar equation, expressed as $10 \cdot \log_{10} Ze_{true} = 10 \cdot \log_{10} Ze_{meas} + F$, is estimated from the comparison of Ze_{meas} and Ze_{gage} assuming $Ze_{gage} = Ze_{true}$, where Ze_{meas} represents the average of Ze's just above the surface (altitudes 300~600 m) and where $Ze_{gage} = 203\, R_{gage}^{1.6}$, R_{gage} being the gage-measured rain rate. Among the raingages shown in Figure 6-6, nine aircraft passages over raingages #4 ~ #10 are used for the calibration. Time trends of the raingage-measured rain rates and timing of aircraft passages are shown in Figure 6-7. The rain rates observed by the gages range from 3 to 18 mm/h. In order to reduce the statistical

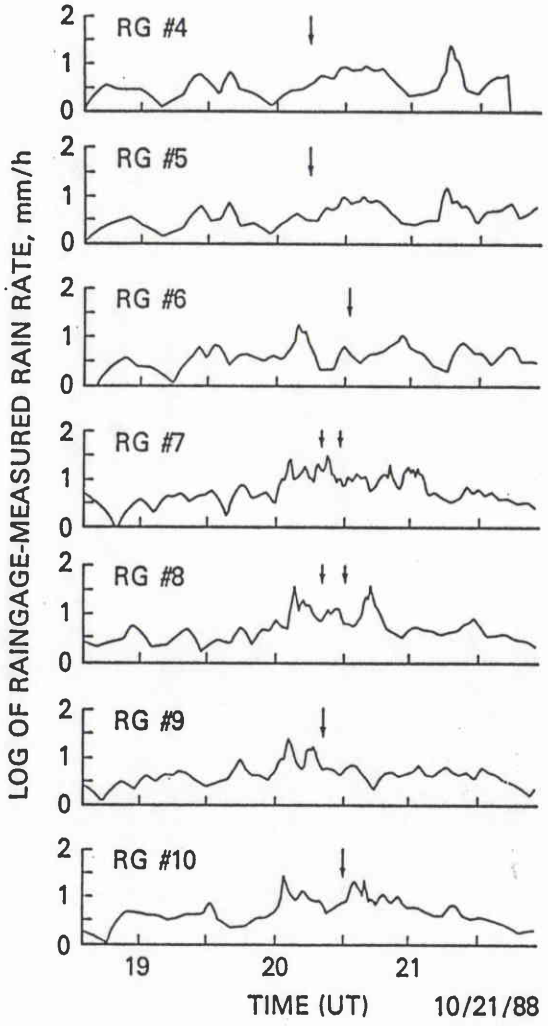

Figure 6-7. Time trend of rain rates measured by raingages and the timing of aircraft passage.

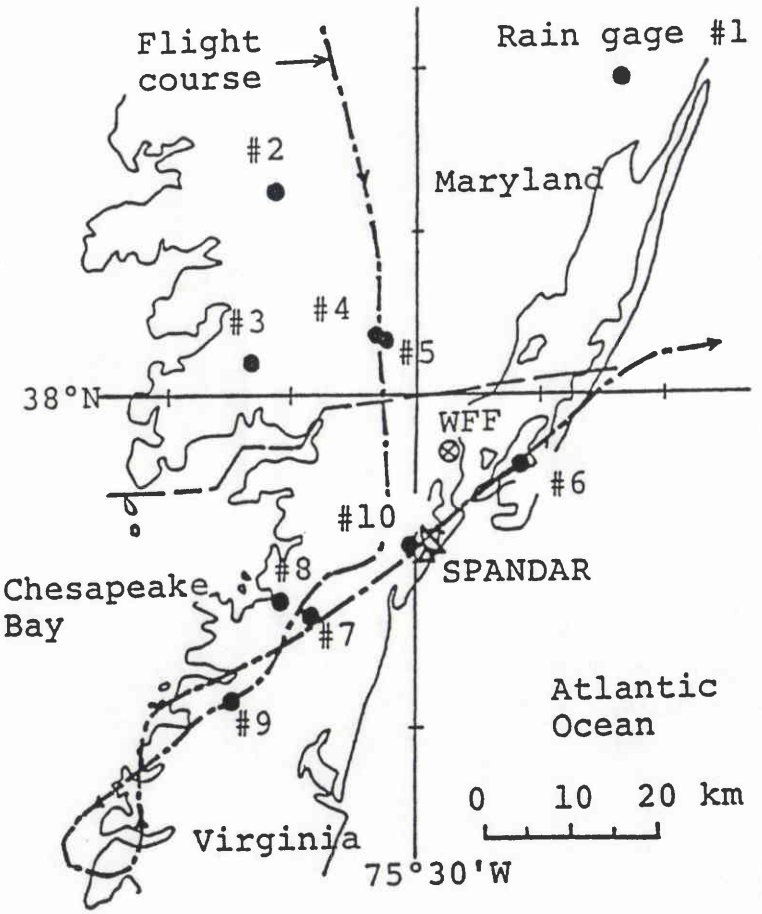

Figure 6-6. Ground track of the flight on October 21, 1988, and the location of raingages.

rain rate variability, temporal averaging (~2 minutes) and spatial averaging (~2 km, along the flight direction) have been applied to raingage and radar data, respectively. The final F value is obtained by the average of F values obtained from the 9 passes, using a weighting factor approximately proportional to the inverse of the sum of three factors; variances of the radar and gage-derived Ze's and a factor proportional to the distance between raingage site and the ground foot print of the radar. This method is applied only to the X-band radar and yields an F value of 1.32 (1.2 dB). The calibrated radar constant gives the RMS decibel deviation of 1.6 dB for the 9 pairs of R_{gage} and radar estimated rain rate. Figure 6-8 shows the correlation between rain rates as measured by the raingages and those estimated from the radar with the calibrated system constant.

To calibrate the Ka-band radar, we use Ze values far above the bright-band during light stratiform rains, where it is reasonable to assume that the scatterers are small ice particles which should satisfy an excellent Rayleigh scattering approximation and cause little attenuation even at Ka-band. Comparing Ka-band Ze's with the calibrated X-band ones provides an F value of 0.65 (-1.9 dB) for the Ka-band data. When the same Ka-band radar calibration scheme is applied to rainfalls observed in other flights, however, approximately ±1 dB variation has been found in the Ka-band F value, which is probably caused by an unstableness of Ka-band receiver that we have encountered throughout the experiment. For the Ka-band data processing, therefore, the F value is tuned once for each flight.

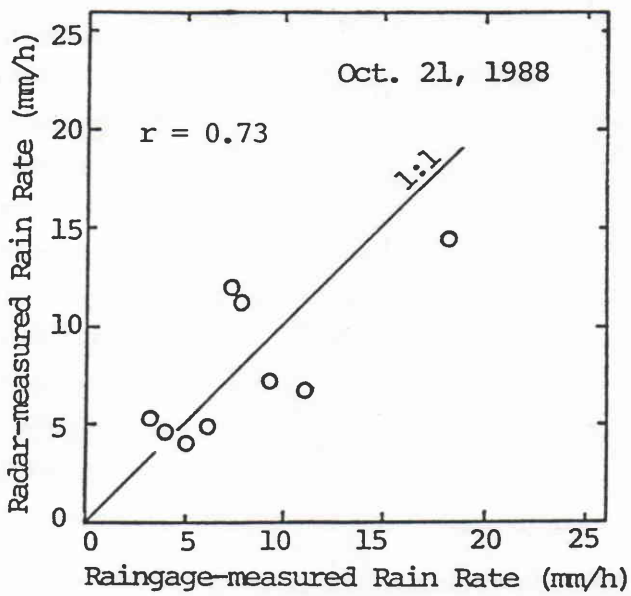

Figure 6-8. Correlation between rain rates measured by raingages and those estimated by the calibrated X-band radar using a MP Ze-R relation.

6.5 Conclusions

The CRL microwave airborne rain scatterometer/radiometer (MARS) was upgraded to make high altitude aircraft rainfall measurements using the NASA T-39 aircraft. Although the Ka-band radar transmitter and receiver have sometimes had troubles, the system has worked well during the fall 1988 experiment. The system upgrade has provided wider range window, higher sensitivity, and probably higher accuracy in the *Zm* and surface σ^0 measurements than the original MARS. An external radar calibration has been successfully performed by employing the rain rate data measured by a raingage network. The calibration of the Ka-band radar, which is generally difficult due to the large rain attenuation, has been made through a new scheme; the comparison of Ka-band *Zm* values with the X-band ones far above the bright band. This scheme appears to work reasonably well, which leads to the quantitative analysis of *Zm* values that will be described in the next chapter.

The T-39 experiment provided quantitative multiparameter radar and radiometer data sets from high altitude which is an excellent simulation tool for the measurement from space. The data would therefore be valuable to test various rainfall retrieval algorithms from space. We will test the DSD estimation method proposed in Chapter 5 using the T-39 experimental data.

Appendix 6.1 Parameters in the radar equation for the T-39 experiment

From Eq.6.4 and the F value determined by the radar calibration, Zm (in dBZ) is written

$$10\cdot\log_{10} Zm = a\,Y + b + F_{log} + F - C + 20\cdot\log_{10} r. \qquad (6.A1)$$

with

$$C = 10\cdot\log_{10}(\pi^3/(1024\ \ln 2) + 2\cdot G + 20\cdot\log_{10}\theta_b + 10\cdot\log10\ (c\tau) + P_t + 10\cdot\log_{10}|K_w|^2 - 20\cdot\log_{10}\lambda - L - 180.0 \qquad (6.A2)$$

The parameters required to calculate Zm from the count value Y are summarized below.

- *System constant C:*

	X band	Ka band	Remarks
$10\cdot\log_{10}(\pi^3/(1024\ \ln 2))$	-13.60	-13.60	
$2\cdot G$ (dB)	60.60	60.80	
$20\cdot\log_{10}\theta_B$	-20.84	-21.01	HPBW = 5.2°, 5.1°
$10\cdot\log_{10}(c\tau)$	21.76	21.76	τ = 0.5 μsec
P_t (dBm)	73.0	70.0	Nominal value
$10\cdot\log_{10}\lvert K_w\rvert^2$	-0.32	-0.46	
$-20\cdot\log_{10}\lambda$	30.46	41.20	λ = 3.0 cm, 0.871 cm
$-L$ -180	-181.4	-183.4	
Total	-30.34	-24.71	

- *Coefficients a and b:* These values depend somewhat on the result of internal calibration. The nominal values are a = 0.098 and b = -111 for X band, and a = 0.107 and b = -101 for Ka band.

- F_{log} *and F:* As mentioned in the text, F_{log} = 2.5 dB, and F = 1.2 dB for X band. For Ka band, nominal F value is -1.9 dB (it has been adjusted once per flight based on the comparison of X and Ka-band Zm values far above the bright band).

Consequently, Zm in dBZ is given by

$$Zm\ (\text{dBZ, X band}) = (0.098Y - 111) + 3.7 + 30.34 + 20\log_{10} r = 0.098Y - 77.0 + 20\log_{10} r \qquad (6.A3)$$

$$Zm\ (\text{dBZ, Ka band}) = (0.107Y - 101) + 0.6 + 24.71 + 20\log_{10} r = 0.107Y - 75.7 + 20\log_{10} r \qquad (6.A4)$$

where the range r is in meters. Note that Eqs.6.A3 and 6.A4 are "nominal" relations; the coefficients change somewhat due to the fluctuations in transmit power, receiver gain, etc.

References

(1) Kozu, T., R. Meneghini, W. C. Boncyk, K. Nakamura, and T. T. Wilheit, 1989: Airborne radar and radiometer experiment for quantitative remote measurements of rain. *Proc. IGARSS '89*, Vancouver, Canada, 1499-1502.

(2) Kozu, T., K. Nakamura, R. Meneghini, and W.C. Boncyk, 1991: Dual-parameter radar rainfall measurement from space: A test result from an aircraft experiment. *IEEE Trans. Geosci. and Remote Sens.*, **GE-29**, 690-703.

(3) Okamoto, K., S. Yoshikado, H. Masuko, T. Ojima, N. Fugono, 1982: Airborne microwave rain scatterometer/radiometer. *Int. J. Remote Sens.*, **3**, 277-294.

(4) Spencer, R.W., T. T. Wilheit, R. Hood, and A. Chang, 1987: Precipitation detection with the ER-2 microwave precipitation radiometers. *Proc. 2nd Airborne Science Workshop*, Miami, FL, 93-95.

(5) Cleart, R. T., 1986: The IEEE-583 Bus -- CAMAC, A versatile interface standard. *BUSCON, The Users' Conference*, San Jose, CA, 1-12.

(6) Ulaby, F.T., R.K. Moore, and A.K. Fung, 1982: *Mirowave remote sensing: Active and Passive*. Vol.II. Artech House, Norwood, MA, 457-1064pp.

(7) Marshall, J.S. and W.M. Palmer, 1948: The distribution of raindrops with size. *J. Meteorol.*, **5**, 165-166.

CHAPTER 7. EXPERIMENTAL TESTS OF SEMI DUAL-PARAMETER MEASUREMENT

As shown in previous chapters, statistical analyses of DSD parameters and a simulation of SDP measurements using the disdrometer data set have revealed that the semi dual-parameter (SDP) measurement combining a *Zm* profile and a path-integrated attenuation can provide a reasonable improvement in rain rate estimation accuracy through the estimation of two-scale DSD model parameters. If such SDP measurements could be performed from space, various useful rainfall properties including *Ze-R* relations for each observation could be obtained in addition to the improved rain rate estimates. In practice, however, there has been no successful experimental result of such DSD estimation until now.

In this chapter, we test the SDP measurement using the data obtained from a joint aircraft experiment described in Chapter 6 in order to evaluate the performance and limitations, and further to improve the method. For this test, the SDP measurement is constructed by the combination of an X-band (10 GHz) radar reflectivity profile and either X- or Ka-band (34.5 GHz) path attenuation obtained from sea-surface echo (i.e., by the SRT method). One of the major problems in such testing is that it is usually very difficult to obtain a good "reference" measurement. Although the raingage (or disdrometer) data may serve as such reference, spatial and temporal variability in rainfall can cause a significant error in the comparison of such point measurements and airborne radar data. The same applies to the comparison of the ground-based and airborne radars because of the different radar resolution volumes. In the latter case, the calibration accuracy of the ground-based radar is also a problem. Therefore, we will employ another approach; consistency between independent measurements. Specifically, we will use the Ka-band *Zm* profile for this consistency check [1-3].

7.1 Methods of the Test and the DSD Model

7.1.1 General discussion

In the simulation described in Chapter 5, we have assumed that the radar reflectivity *Ze* and path-integrated attenuation are proportional to 6th and 4th moments of DSD and that *Ze* is measured without attenuation in order to simplify the discussion and to obtain an analytical solution to the equation for the DSD parameters. These assumptions approximately hold for light to moderate rain rate cases in which the X-band attenuation is negligible and Ka-band

path attenuation can be measured from the surface return. To handle heavy rain cases, however, we need more generalized approach, which will be discussed in this section.

As for the two-scale DSD model necessary for the DSD estimation, we refer the results obtained in Chapter 5, and use the exponential "two-scale" DSD model in which Λ is variable with range whereas N_0 is constant over the path for each observation. By combining X-band Zm profile and X or Ka-band path-integrated attenuation, the two-scale DSD model parameters are derived. In general, a numerical technique is required to derive the DSD parameters; however, with the assumption of power-law IRP relations (see Eq.5.1), a simplification is possible, and in some special conditions, the DSD parameters can be derived analytically as described in Chapter 5. An outline of these procedures is shown below.

We begin with the radar equation using "apparent" Ze's at X and Ka band, Zm_y, y being a subscript representing the value at X or Ka band (y = X or Ka):

$$P_y(r_i) = C_y |K_y|^2 Zm_y(r_i) / r_i^2 \tag{7.1}$$

where C_y is a radar constant, $|K_y|^2$ is a dielectric factor of water, r_i is the range from radar to the ith resolution volume, and $P_y(r_i)$ is a radar received power. Since Zm is a quantity that can be obtained without any assumption of DSD, apart from bias or random errors in $P(r)$ or C, a Zm profile (i.e. n Zm's, n being the number of range bins) is recognized as a "measurable" quantity by a radar. The "true" Ze's, $Ze_y(r_i)$, may be related to Zm by

$$Zm_y(r_i) = Ze_y(r_i) \exp[-0.2\ln 10\, A_y(r_i)] \tag{7.2}$$

with

$$A_y(r_i) = \sum_{j=1}^{i} \varepsilon_{ij}\, k_y(r_j)\, \Delta r \tag{7.3}$$

where $k_y(r_j)$ is the rain attenuation coefficient in dB/unit distance, Δr is the interval between radar range bins, and ε_{ij} = 1 when $j < i$ and 0.5 when $j = i$. (ε_{ii} = 0.5 means that $A_y(r_i)$ represents the attenuation up to the "center" of the range bin i.)

The other quantity we employ here for the DSD estimation is a path-integrated attenuation derived from surface echo ($A_{SR,y}$) that can be estimated from a difference between surface return powers (in dB unit) within and outside the rain. $A_{SR,y}$ is expressed as

$$A_{SR,y} = \sum_{j=1}^{n} k_y(r_j)\, \Delta r. \tag{7.4}$$

Noting that $Ze_y(r_j)$ and $k_y(r_j)$ are functions of DSD parameters at r_j, i.e. $\Lambda(r_j)$ and N_0, we see that $Zm_y(r_j)$ is a function of $\Lambda(r_1)$ through $\Lambda(r_j)$ and N_0, and $A_{SR,y}$ is a function of $\Lambda(r_1)$ through $\Lambda(r_n)$ and N_0. Thus, generic equations relating measurable quantities and DSD parameters are

$$\left.\begin{aligned} Zm_X(r_1) &= f_{X1}(\Lambda_1; N_0) \\ Zm_X(r_2) &= f_{X2}(\Lambda_1, \Lambda_2; N_0) \\ &\cdots\cdots\cdots\cdots \\ Zm_X(r_n) &= f_{Xn}(\Lambda_1, \Lambda_2, \ldots, \Lambda_n; N_0) \end{aligned}\right\} \quad (7.5a)$$

$$\left.\begin{aligned} Zm_{Ka}(r_1) &= f_{Ka1}(\Lambda_1; N_0) \\ Zm_{Ka}(r_2) &= f_{Ka2}(\Lambda_1, \Lambda_2; N_0) \\ &\cdots\cdots\cdots\cdots \\ Zm_{Ka}(r_n) &= f_{Kan}(\Lambda_1, \Lambda_2, \ldots, \Lambda_n; N_0) \end{aligned}\right\} \quad (7.5b)$$

$$A_{SR,X} = g_X(\Lambda_1, \Lambda_2, \ldots, \Lambda_n; N_0) \quad (7.5c)$$

$$A_{SR,Ka} = g_{Ka}(\Lambda_1, \Lambda_2, \ldots, \Lambda_n; N_0) \quad (7.5d)$$

The functions f_{Xi}, f_{Kai}, g_X, and g_{Ka} are the same as Eqs.7.2 and 7.4 in nature, but they are expressed in terms of DSD parameters. In other words, Eq.7.5 is based on the assumption that the backscattering and extinction cross sections of the hydrometeors are known so that Ze_y and k_y are expressed solely as functions of the DSD parameters. Although the back-scattering and extinction cross sections of raindrops depend on temperature to some extent and there is a small atmospheric gaseous attenuation, the above assumption approximately holds for the frequencies we consider here. Later in this chapter we discuss the attenuation caused by non-liquid hydrometeors. At present, we continue to assume that the precipitation particles along the path are all raindrops.

The concepts of the estimation of DSD parameters and other rain parameters are shown in Figure 7-1. If we employ either the X-band or the Ka-band Zm profile (Eq.7.5a or 7.5b) and either $A_{SR,X}$ or $A_{SR,Ka}$ (Eq.7.5c or 7.5d), it is theoretically possible to obtain the n+1 DSD parameters along the path ($\Lambda(r_1)$ through $\Lambda(r_n)$ and an N_0) by inversion techniques from the n+1 measurable quantities. It could also be possible to employ all X and Ka-band

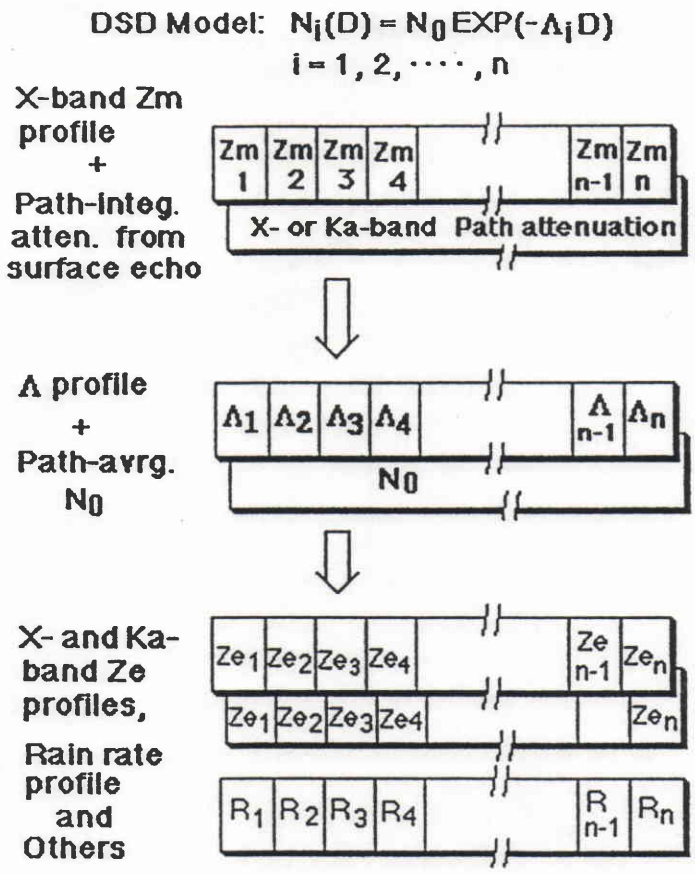

Figure 7-1. Concept of estimating DSD parameters, Ze and rain rate profiles by SDP measurement.

measurements to estimate the (n+1) DSD parameters using least-square or other estimation techniques[4]. In many cases, however, only a single-frequency radar will be onboard a spacecraft and such a least-square scheme may not be applicable. In our dual-frequency system, moreover, it is almost impossible to use Eqs.7.5c and 7.5d at the same time because of the insufficient receiver dynamic range; at light to moderate rainfall the X-band path attenuation is too small, and at heavy rainfall the Ka-band path attenuation is too large to be measured. In addition, the Ka-band *Zm* profile is only partially obtained due to excessive rain attenuation in a heavy rainfall. Thus, we use Eq.7a and Eq. 7c or 7d (depending on rain intensity) for the DSD parameter estimation. As shown later, we will use the Ka-band *Zm*'s to make a consistency check.

There are several methods to solve Eq.7.5a and 7.5c (or 7.5d) for $\Lambda(r_1)$, $\Lambda(r_2)$, . . ., $\Lambda(r_n)$ and N_0. The first method is a fully numerical one, in which a Λ profile is numerically calculated sequentially from the first range bin for a given N_0, and the resulting DSD profile is substituted into the right-hand side of Eq.7.5c (or 7.5d) to get an estimate of X-band (or Ka-band) path-attenuation ($A_{RD,X}$ or $A_{RD,Ka}$); this procedure is repeated with changing N_0 until the estimate becomes equal to $A_{SR,X}$ (or $A_{SR,Ka}$).

The second method makes use of the power-law approximations to solve Eq.7.5a. For a given N_0 value, we can obtain best-fit power-law relations from pairs of IRPs which are theoretically calculated using DSDs having the constant N_0. Using the relation between k_X and Ze_X, we have an exact solution of Eq.7a for Ze_X. This is known as the Hitschfeld-Bordan solution[5]. Once we have the X-band Ze profile, $A_{RD,X}$ (or $A_{RD,Ka}$) can easily be calculated using a k_X-Ze_X (or k_{Ka}-Ze_X) relation for the N_0 specified, which is compared with $A_{SR,X}$ (or $A_{SR,Ka}$). This is repeated until we have an N_0 that gives the best agreement with $A_{SR,X}$ (or $A_{SR,Ka}$). Λ profile is also calculated using the Ze_X profile and the "best-fit" N_0, although the Λ profile is not necessary to calculate other rain parameters as far as power-law relations between the rain parameters and Ze_X can be applied.

The third option is a fully analytic approach. As indicated in Chapter 5 and in Meneghini and Nakamura[6], it is possible to solve Eq.7.5a and Eq.7.5c or 7.5d analytically in some cases: (1) Cases where X-band attenuation is negligible, β_{Ka} is independent of N_0 and α_{Ka} is a monotonic function of N_0; (2) Cases where X-band attenuation is present but β_X is independent of N_0 and α_X is a monotonic function of N_0. In these cases, the problem reduces to an estimation of α_{Ka} or α_X instead of N_0.

7.1.2. Description of the power-law approximation method

Among the three methods, we use the second option because even though Ze_X, k_X or k_{Ka} is not perfectly proportional to a moment of DSD, the power-law relations are found to be excellent approximations to exact relations between them. Moreover, the assumptions required for the third option seem to be too stringent; in fact, as shown in Table 7-1, β_{Ka} has a fairly strong dependence on N_0. For the second method, all power-law relations, which are stored in a look-up table (Table 7-1), are used to calculate Ze_X, k_X, k_{Ka}, Λ, rain rate and other rain parameter profiles for a given N_0. The values in the look-up table are obtained as follows: First, we prepare 20 DSDs having a constant N_0 and different Λ's (i.e. different rain rates) in the range shown in Note 2 of Table 7-1. Twenty IRP pairs of interest (e.g. Ze and R) are then calculated from the DSDs (using the Mie theory for Ze and k). Those IRPs are log-converted and then used for a linear regression to obtain the power-law relation. For simplicity, a raindrop temperature of 0°C is assumed for the calculation of back-scattering and attenuation cross sections. Although the attenuation coefficients are fairly sensitive to temperature at light rain rates where absorption is dominant, for the cases of moderate to high rain rates considered here, the temperature dependence can be neglected.

Table 7-1. Coefficients of the power-law relations for some N_0 values obtained by linear regressions of logarithms of k, Ze, R and Λ values. In the look-up table, coefficients for other N_0's are also stored.

	k-Ze relations				Ze-R relations				Λ-Ze relation	
	k_X-Ze_X		k_{Ka}-Ze_X		R-Ze_X		R-Ze_{Ka}		Λ-Ze_X	
N_0	α_X ($\times10^{-3}$)	β_X	α_{Ka} ($\times10^{-2}$)	β_{Ka}	a_X ($\times10^{-1}$)	b_X	a_{Ka} ($\times10^{-2}$)	b_{Ka}	ζ_X	η_X
1×10^5	.5502	.7175	.8509	.7177	.5446	.6848	5.087	.6796	13.17	-.1423
5×10^4	.3732	.7296	.6631	.7262	.4714	.6732	3.830	.6907	11.82	-.1408
3×10^4	.3111	.7343	.5788	.7248	.4289	.6626	2.995	.7050	10.89	-.1394
1.5×10^4	.2520	.7370	.5180	.7114	.3799	.6470	2.035	.7336	9.731	-.1371
8×10^3	.2092	.7392	.4993	.6894	.3374	.6337	1.361	.7689	8.807	-.1354
4×10^3	.1653	.7447	.4973	.6594	.2864	.6230	.8274	.8181	7.952	-.1345
1.4×10^3	.1050	.7627	.4778	.6167	.1994	.6201	.3577	.9122	7.013	-.1367

Note 1: Raindrop temperature of 0°C is assumed.

Note 2: The regressions are made using the values corresponding to the following rain rate range.
k_X-Ze_X : 5 - 100 mm/h, k_{Ka}-Ze_X and R-Ze_{Ka} : 0.5 - 20 mm/h, R-Ze_X and Λ-Ze_X : 0.5 - 50 mm/h.

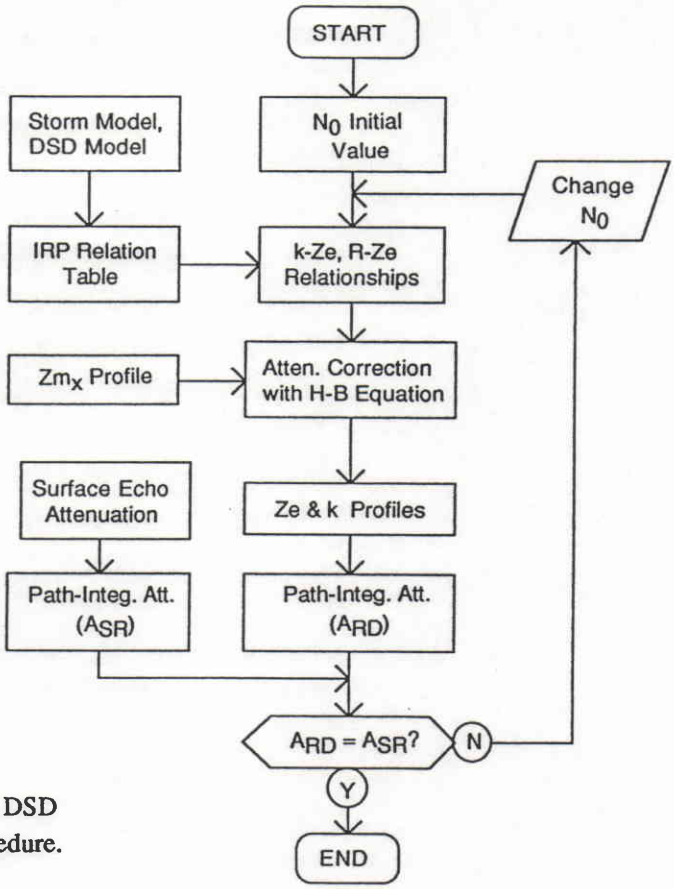

Figure 7-2. Flowchart of DSD estimation procedure.

A flowchart of the estimation procedure is shown in Figure 7-2. For a given N_0 (i.e. a set of power-law relations listed in Table 7-1), an estimate of Ze_X profile is calculated with a Hitschfeld-Bordan solution

$$Ze_X(r_i; N_0) = Zm_X(r_i)\,[1 - q\,S_X(r_i; N_0)]^{-1/\beta X(N_0)} \tag{7.6}$$

with

$$S_X(r_i; N_0) = \sum_{j=1}^{i} \varepsilon_{ij}\ \alpha_X(N_0)\,Zm_X(r_j)^{\beta X(N_0)}\,\Delta r \tag{7.7}$$

where $q = 0.2 \cdot \ln 10 \cdot \beta_X(N_0)$, and α_X and β_X are, respectively, the coefficient and the exponent of k_X - Ze_X relation, $k_X = \alpha_X\,Ze_X^{\beta X}$. A similar pair ($\alpha_{Ka}$, β_{Ka}) can be defined for k_{Ka} - Ze_X relation, $k_{Ka} = \alpha_{Ka}\,Ze_X^{\beta Ka}$.

Using the estimated Ze_X profile (Eq.7.6) and the k_X - Ze_X and k_{Ka} - Ze_X relations for the same N_0, estimates of X-band and Ka-band attenuation coefficient profiles are obtained:

$$k_Y(r_i; N_0) = \alpha_Y(N_0)\,Ze_X(r_i; N_0)^{\beta Y(N_0)}. \tag{7.8}$$

Estimates of X-band or Ka-band path-integrated attenuations are then

$$A_{RD,y} = \sum_{j=1}^{n} k_y(r_j; N_0)\,\Delta r. \tag{7.9}$$

$A_{RD,y}$ is known to be unstable when X-band radar wave is highly attenuated[5]. Thus, we force it equal to the surface echo-derived attenuation, $A_{SR,y}$, and find a solution for N_0 that satisfies the equation

$$A_{RD,y} = A_{SR,y}. \tag{7.10}$$

Due to the fluctuation of surface scattering cross section (σ^0), $A_{SR,y}$ is not accurate when the path-attenuation is small. For example, it has been found from a statistical analysis of surface returns in no-rain conditions that the standard deviation of surface σ^0 is 1 ~ 1.5 dB for the flights used for the DSD estimation test. The same thing happens when path-attenuation is so large that signal-to-noise ratio (S/N) becomes small. To avoid a noisy result of the DSD estimation, the processing is done only when $A_{SR,y}$ is greater than 3 dB (2-way path attenuation > 6 dB) and the effective S/N[7] of the surface echo is greater than 6 dB. If $A_{SR,Ka}$ satisfies this criterion, it is employed for the processing (y = Ka in Eq.7.10). If not, $A_{SR,X}$ is then checked by means of the same criterion.

An approximate solution can be found by selecting a "best-fit" N_0 from 13 N_0 candidates ranging from $1.4\text{x}10^3$ to $100\text{x}10^3$ $\text{mm}^{-1}\text{m}^{-3}$ (see Table 7-1). The maximum N_0 error in this approximate solution is about ±0.7 dB. When the X-band path-attenuation is negligible, this N_0 error corresponds to about ±0.2 dB error in $A_{RD,y}$. With increasing path-attenuation, the error in $A_{RD,y}$ increases for a given N_0 error; however, the approximate N_0 solution has been found acceptable up to about 10-dB X-band 2-way path-attenuation, corresponding to about 65 mm/h rain rate with a rain height of 3 km.

Once we obtain the N_0 estimate, $\tilde{N}_0$ (the solution to Eq.7.10), we also have a set of estimates of rain-parameter profiles including Ze_X, k_X, and k_{Ka}, just by substituting $\tilde{N}_0$ into Eqs. 7.6 and 7.8. Similarly, profiles of the other DSD parameter, Λ, and rain rate (and any other integral rain parameters) can be calculated with the corresponding power-law relations

$$\Lambda(r_i; \tilde{N}_0) = \zeta_X(\tilde{N}_0)\, Ze_X(r_i; \tilde{N}_0)^{\eta_X(\tilde{N}_0)} \tag{7.11}$$

$$R(r_i; \tilde{N}_0) = a_X(\tilde{N}_0)\, Ze_X(r_i; \tilde{N}_0)^{b_X(\tilde{N}_0)}. \tag{7.12}$$

It should be noted that rain rate can also be obtained from a k-R relation for $\tilde{N}_0$ or from an integral of the product of drop water volume, drop terminal velocity and DSD over the diameter D, and all the results should be consistent with one another. The same applies to any rain parameter calculations, because all rain parameters are now mutually related in terms of the DSD profile we have estimated.

7.1.3. Melting layer attenuation

In the above formulation, we have assumed that the hydrometeors along the path are all raindrops having DSDs with a single N_0. Actually, however, other hydrometeors may exist. In such cases, the modeling of DSD along the path and the calculation of path-integrated attenuation from the Zm_X profile requires modification. In the present analysis, we use the following scheme to incorporate the effect of non-liquid hydrometeors.

(1) For the processing of aircraft data, a Zm profile is classified into three regions; ice, melting layer, and rain. For a stratiform rain in which a bright-band is evident from the Zm profile, the classification is relatively easy. In the case of other rain types, we make the classification based on the 0°C isotherm height derived from the bright band observed at other stratiform rains observed in the same flight.

(2) Radiowave attenuation in the ice region is negligible both at X and Ka-band.

(3) To evaluate the melting layer attenuation and k-Ze relations, we assume that the melting layer particles are spherical composite dielectrics and their DSD is given by a Nonbreakup-and-Non-coalescence model[8] (see Appendix 2.1). For stratiform rain, the thickness of the melting layer is chosen to be 900 m (bright band Zm peak ± 450 m), in which the particles change their fractional volume content of water from 0.017 to 0.85 corresponding to wet to watery snow [8]. Since it has been found that k_X - Ze_X and k_{Ka} - Ze_X relations averaged over the melting layer are close to those for rainfall, for simplicity, we use the same k-Ze relations both for the rain region and the melting layer.

(4) In the case of convective rain, we assume that the particles start melting at 2-km above the 0°C isotherm height (i.e. "melting layer" for the convective rain is between 2-km above and 450-m below the 0°C height). This is based on an analysis of X- and Ka-band Zm profiles of heavy convective storms observed in the flight on November 1, 1988, which indicates that Ka-band radiowave starts attenuating around 2-km above the estimated 0°C isotherm height. This model is clearly too simple to represent the physical phenomena above the 0°C height in

the convective storm. In this region, attenuation may be caused by wet growth of ice or snow and supercooled raindrops; dense water cloud can also cause a significant Ka-band attenuation in some cases. Therefore, *k-Ze* relations for this region may not be the same as those for rain. Depending on the convective activity, the rain top height may also differ from case to case. Such a detailed convective storm modeling is beyond the scope of the present study. Instead, we will evaluate the effect of storm modeling on the N_0 estimate by comparing the results obtained with the above simple convective model and those with the stratiform model that assumes the melting layer thickness of 900 m (0°C isotherm height ± 450 m).

(5) In any case, the "path-averaged" rain rate shown later is defined as the average over the rain region only. The *Zm* values of the melting layer are used only to evaluate the attenuation of radiowaves passing through them.

The storm model used here is illustrated in Figure 7-3.

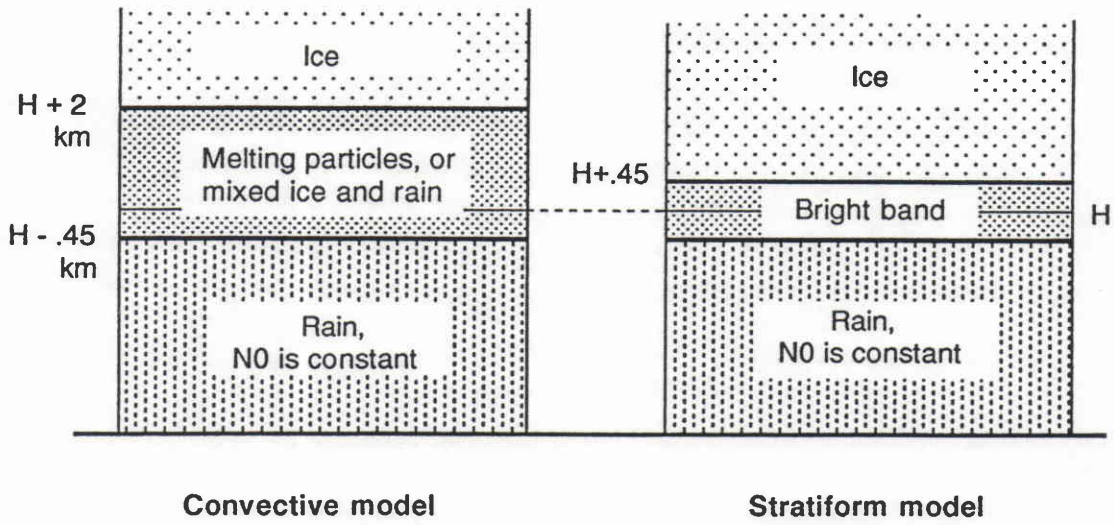

Figure 7-3. Storm model used to calculate path-attenuation and path-averaged rain rate from *Zm* profile.

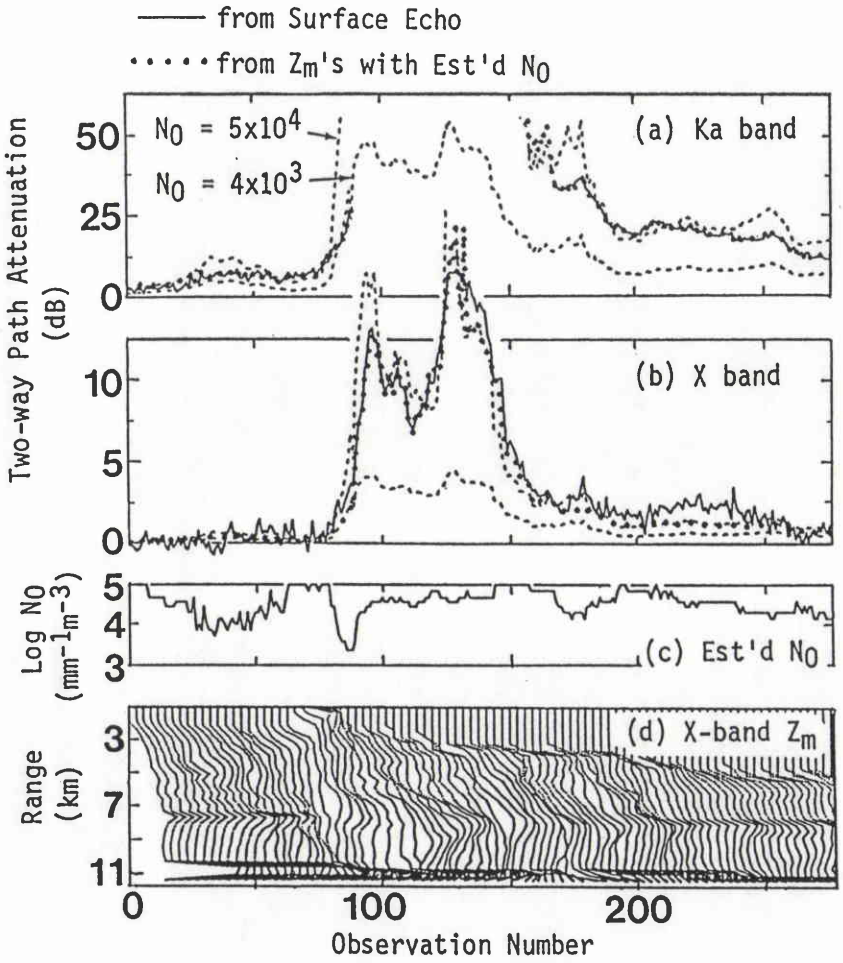

Figure 7-5a. The same as Fig.7-4 except on November 1, 1988.

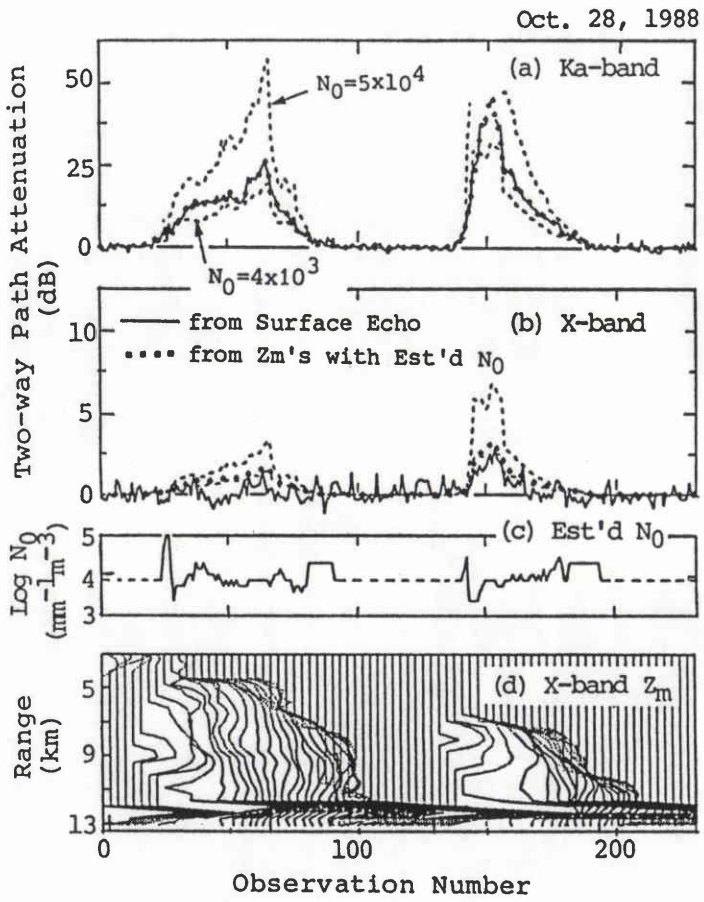

Figure 7-4. Comparisons of 2-way path attenuations derived from surface echoes, the estimated N_0, and the corresponding X-band Zm profile on October 28, 1988. See the text for the details of the notation for the path attenuation.

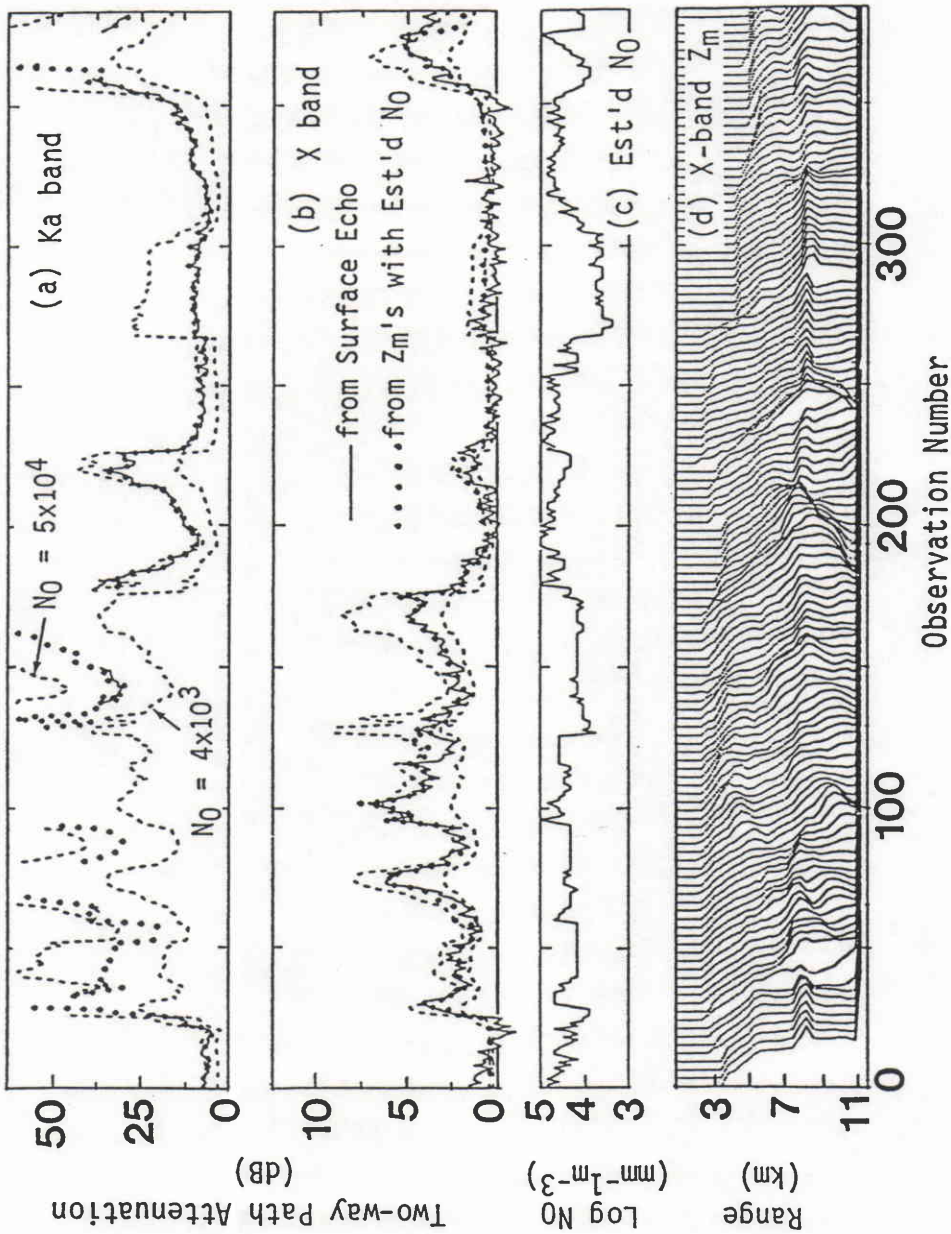

Figure 7-5b. (Cont'd)

7.2 Results and Discussion

The DSD estimation is tested using the data obtained from the flights over the Atlantic Ocean on October 28 and November 1, 1988. The storms observed on the former date were localized convective cells, while on the latter date, mixed convective and stratiform rains were observed.

7.2.1 Spatial trend of N_0

Results of path-averaged N_0 estimation are shown in Figures 7-4 and 7-5. In the figures, the plots labeled (a) and (b) represent the 2-way path attenuations at Ka-band and X-band, respectively. The curves in (a) and (b) include: the attenuation derived from the surface echo; the value obtained by selecting the best N_0 ($\tilde{N}_0$); and values obtained by using fixed N_0 values of 5×10^4 and 4×10^3 $mm^{-1}m^{-3}$, for a guideline of upper and lower boundaries of N_0 naturally found. These limits are selected based on a statistical analysis of disdrometer data at Kashima, and represent the 10 % and 90 % ranges of the distributions of N_0 values. The estimated N_0's are shown in (c). To provide a qualitative indication of the storm structure, the X-band *Zm* profile versus range from the aircraft is shown in (d).

It is found that $\tilde{N}_0$ is almost everywhere bounded by the two extremes (5×10^4 and 4×10^3 $mm^{-1}m^{-3}$) suggesting that the estimation procedure gives reasonable results. The data also show that $\tilde{N}_0$ undergoes gradual spatial variations that are probably caused by internal storm structure. It is also found that a sharp spike in $\tilde{N}_0$ sometimes appears at the edge of an intense region. This phenomenon might be related to DSD properties specific to the storm edge or to the partial beam filling[9-11]. Although the -3 dB beamwidths of X and Ka-band antennas are almost the same, a slight misalignment of antenna direction or a small difference in antenna patterns may also be a problem at the storm edge.

For the heavy convective rains, the N_0 estimation is also made using the stratiform model as mentioned in Section 7.1.3. The $\tilde{N}_0$'s are found to be 0 ~ 2 dB (about 1 dB on average) larger than those using the convective model. Although the difference is small compared with the variability in natural N_0's and comparable in magnitude to the errors due to other causes (described later), more study of the convective storm structure is required to improve the accuracy in the N_0 estimation.

7.2.2 Consistency with Ka-band *Ze*

In order to further evaluate the validity of the estimated N_0, we make a consistency check using Zm_{Ka} profile that is independent of the DSD estimation. The Zm_{Ka} profile is converted to a Ze_{Ka} profile by making the attenuation correction

$$Ze_{Ka}(r_i) = Zm_{Ka}(r_i) \exp[0.2\ln 10\, A_{Ka}(r_i; \tilde{N}_0)] \tag{7.13}$$

with

$$A_{Ka}(r_i; \tilde{N}_0) = \sum_{j=1}^{i} \varepsilon_{ij}\, k_{Ka}(r_j; \tilde{N}_0)\, \Delta r \tag{7.14}$$

$$k_{Ka}(r_i; \tilde{N}_0) = \alpha_{Ka}(\tilde{N}_0)\, Ze_X(r_i; \tilde{N}_0)^{\beta Ka(\tilde{N}_0)}. \tag{7.15}$$

We analyze here only the data for which $\tilde{N}_0$ is derived by using the Ka-band surface echo attenuation, since the $\tilde{N}_0$ thus obtained guarantees an excellent stability in the attenuation correction for Ka-band *Zm*'s.

- Ratio of Ka-band Ze to X-band Ze :

Since Ze_{Ka} is subject to larger Mie scattering effects than Ze_X, the ratio of Ze_{Ka} to Ze_X depends on DSD. The Ka/X *Ze* ratio obtained from the measured (and attenuation corrected) *Ze*'s should be consistent with the estimated $\tilde{N}_0$ value. Examples of *Zm* and *Ze* profiles for three different $\tilde{N}_0$'s are shown in Figure 7-6[7]. The Ze_X and Ze_{Ka} in this figure are calculated with Eq.7.6 (letting $N_0 = \tilde{N}_0$) and Eq.7.13, respectively. The profile (a) is obtained from the October 28 flight. In this case, $\tilde{N}_0$ is 8000 $mm^{-1}m^{-3}$. The other two, (b) and (c), are obtained from the November 1 flight and have, respectively, large and small $\tilde{N}_0$'s. As shown in Figure 7-6, the Ka/X *Ze* ratio in the rain region appears to change from case to case.

Figure 7-7 shows the scattergram between path-averaged *Ze* ratio (ZeR_{meas}) and $\tilde{N}_0$ for light to moderate rain rate region shown in Figure 7-5, during which Ka-band path-attenuation is available from the surface echo (Observation number 200 ~ 330 in Figure 7-5b). The ZeR_{meas} is calculated from the equation

$$ZeR_{meas} = 1/n \sum_{i=1}^{n} [Ze_{Ka}(r_i; \tilde{N}_0)/Ze_X(r_i; \tilde{N}_0)] \tag{7.16}$$

where the summation from $i = 1$ to n extends only over those n gates that span the rain region.

Also shown in the figure are theoretical curves assuming the exponential DSD model

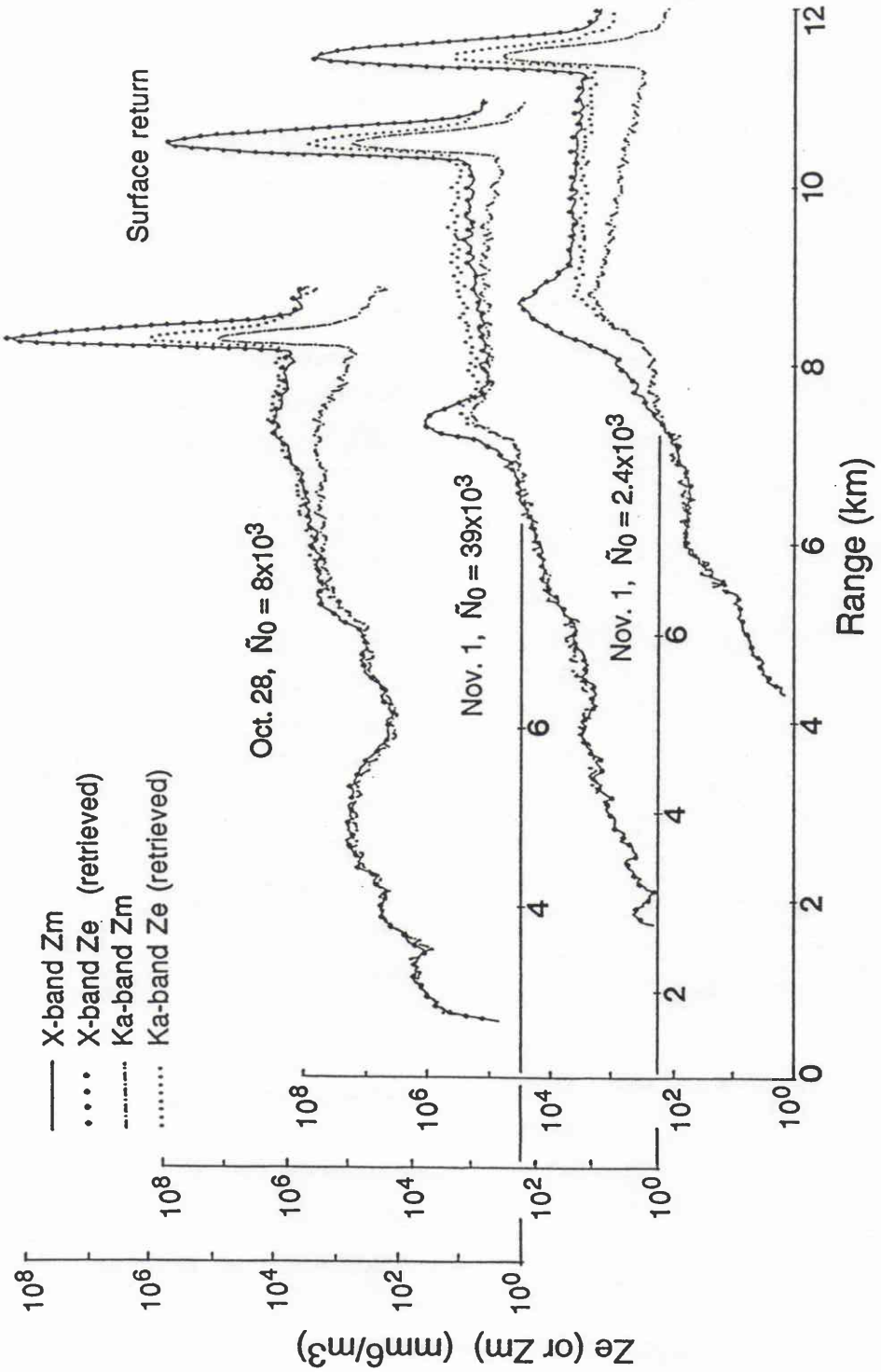

Figure 7-6. Examples of X- and Ka-band *Zm* and *Ze* profiles including surface return.

for given Ze_X's which correspond approximately to the values observed in the same period. For larger N_0's ($\log_{10} N_0 \gtrsim 4$) and smaller N_0's ($\log_{10} N_0 \lesssim 4$), path-averaged Ze_X's are found to be about 30 dBZ and 37 dBZ, respectively. The theoretical value (ZeR_{calc}) is obtained as follows: By specifying Ze_X and N_0, an exponential DSD is uniquely determined. With this DSD, Ze_{Ka} and then ZeR_{calc} is calculated.

We can see that ZeR_{meas} is consistent with ZeR_{calc}, although the former is somewhat smaller at the small N_0 range. This discrepancy might be caused by the departure of natural DSD from the exponential shape. Note that the two large ZeR_{meas}'s ($\approx$ 3.8 dB) at $\log_{10} N_0$ = 5.0, shown in Figure 7-7, are obtained at the very sharp storm edge (Observation number $\approx$ 225 in Figure 7-5b), suggesting the existence of a non-uniform beam filling effect.

- *Comparisons of rain rates derived by different methods :*

The other way to check the validity of the N_0 estimate is to examine the consistency between rain rates calculated from X- and Ka-band *Ze*'s. We compare three different rain rate estimates; a rain rate derived from Ze_X with $\tilde{N}_0$ (R_{Zx}), that derived from Ze_{Ka} with $\tilde{N}_0$ ($R_{Zk,DSD}$), and that derived from Ze_{Ka} assuming the MP distribution ($R_{Zk,MP}$). R_{Zx} is defined by Eq.7.12, while the latter two are given by

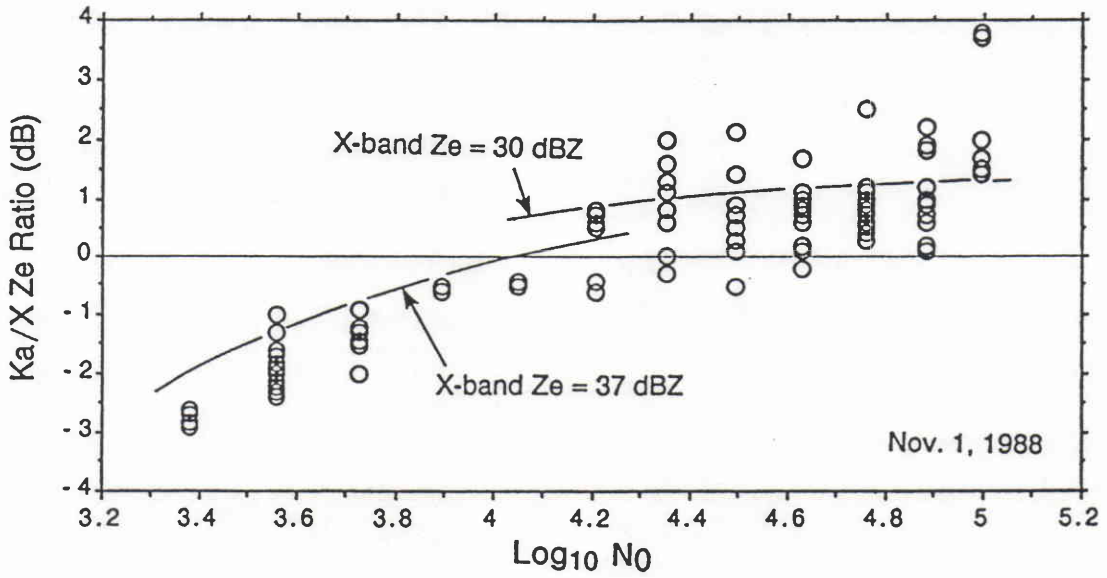

Figure 7-7. Scattergram of the ratio of retrieved Ka-band *Ze* to X-band *Ze* (Ka/X *Ze* ratio) versus estimated N_0 value ($\tilde{N}_0$).

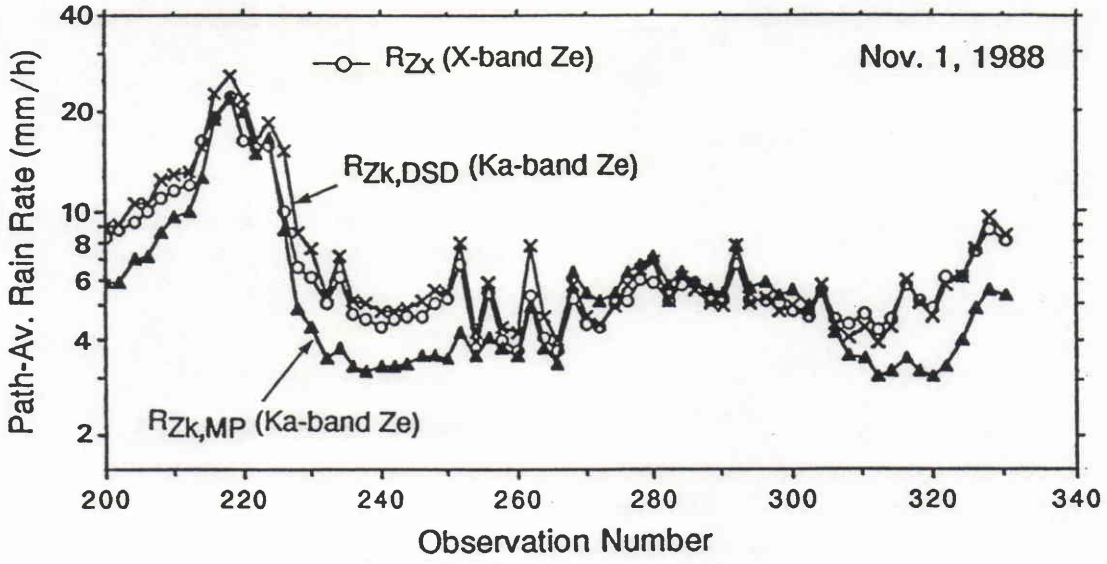

Figure 7-8. Comparison of path-averaged rain rates calculated from X-band and Ka-band *Ze* profiles: $R_{Zk,DSD}$ and $R_{Zk,MP}$ represent the Ka-band results using the estimated DSD, and the MP distribution, respectively. See the text for the details.

$$R_{Zk,DSD}(r_i) = a_{Ka}(\tilde{N}_0)\, Ze_{Ka}(r_i; \tilde{N}_0)^{b_{Ka}(\tilde{N}_0)} \tag{7.17}$$

$$R_{Zk,MP}(r_i) = a_{Ka}(N_{0MP})\, Ze_{Ka}(r_i; \tilde{N}_0)^{b_{Ka}(N_{0MP})} \tag{7.18}$$

where N_{0MP} (= 8000 $mm^{-1}m^{-3}$) is the N_0 value for the MP distribution. We use R_{Zx} as a "reference" since it is obtained under the constraint of the surface echo attenuation and should be the most reasonable rain rate profile. The total amount of attenuation correction for Ka-band *Zm*'s is constrained by the surface echo attenuation; however, the magnitude of the retrieved *Ze*'s should depend on the DSD and thus *Ze-R* relation has to be tuned depending on the DSD. The rain rate obtained through such tuning based on the N_0 estimate ($R_{Zk,DSD}$) should be consistent with R_{Zx}. The $R_{Zk,MP}$ is recognized as a rain rate to be obtained in such condition that Ze_{Ka} is known but DSD (i.e., Ze_{Ka}-*R* relation) is unknown.

Figure 7-8 shows a comparison of path-averaged values of R_{Zx} with $R_{Zk,DSD}$ and $R_{Zk,MP}$ for the same period as that used to obtain Figure 7-7. Excellent agreement is obtained between R_{Zx} and $R_{Zk,DSD}$. On the other hand, $R_{Zk,MP}$ is sometimes significantly smaller than R_{Zx}, which is caused by the assumption of a fixed DSD (in this case MP distribution). Similar comparisons have been made for other time periods on November 1 and October 28. The results generally indicate the validity of the estimated N_0 value; however, as suggested earlier, inconsistency has been observed between $R_{Zk,DSD}$ and R_{Zx} at the edges of intense storms.

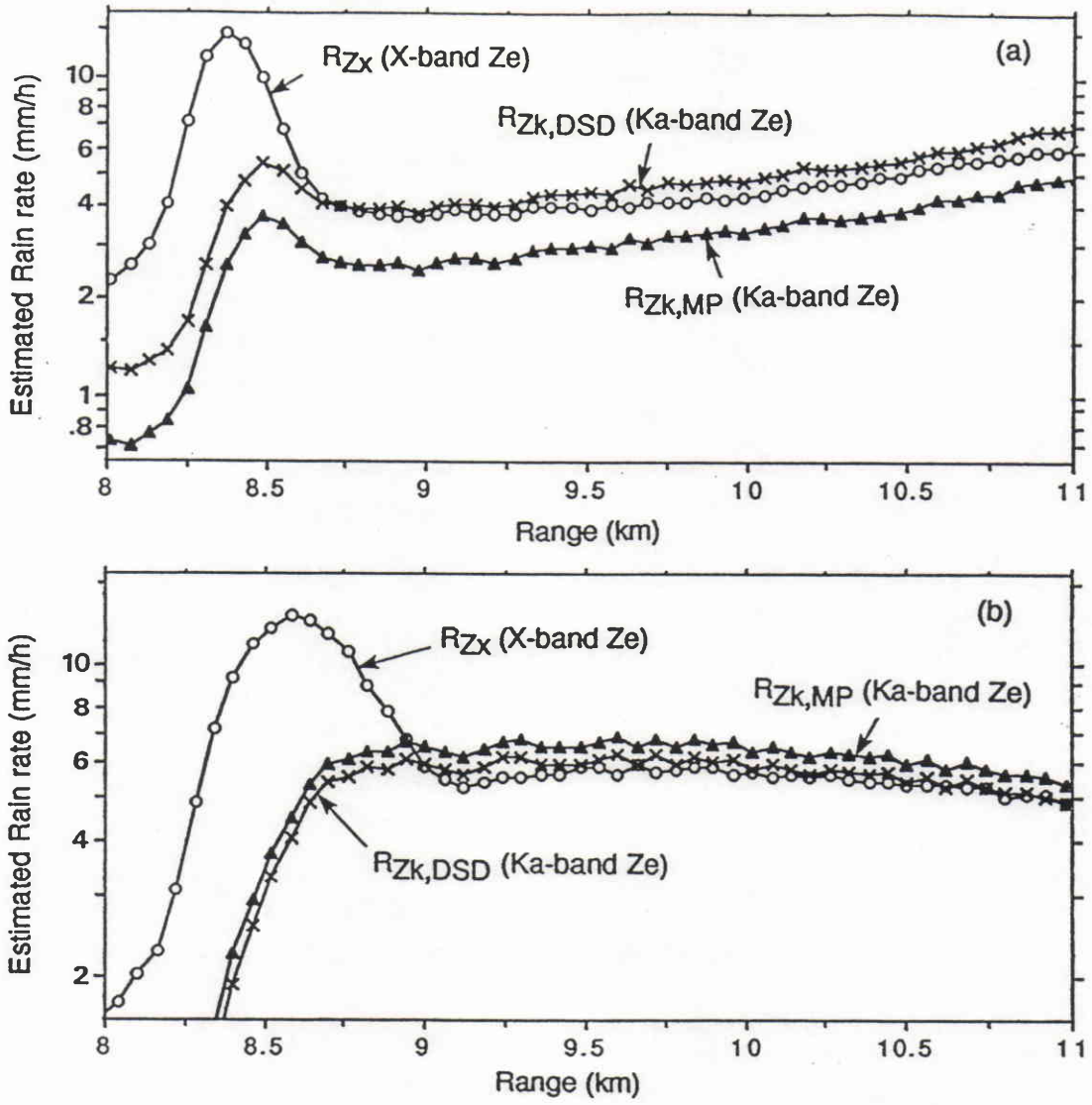

Figure 7-9. Comparison of rain rate profiles calculated from X-band and Ka-band *Ze* profiles. Profiles in (a) and (b) represent the results obtained from the periods during which the estimated N_0 is large ($3\times10^4 \sim 5\times10^4$) and small ($2\times10^3 \sim 4\times10^3$), respectively.

Moreover, $R_{Zk,DSD}$ tends to be slightly larger than R_{Zx}, suggesting either the existence of a small offset in the Ka-band Ze or limitations in the form of the DSD that we have used.

To check the rain rate consistency from the other aspect, we compare rain rate profiles. Figure 7-9 shows comparisons of R_{Zx} with $R_{Zk,DSD}$ and $R_{Zk,MP}$ as a function of range in the vertical direction measured from the aircraft. The plots (a) and (b) represent, respectively, the averages for the periods on November 1 during which estimated N_0's are large (Observation number 230 - 260 in Figure 7-5b) and small (Observation number 265 - 300). The rain rates at the bright band are not accurate since they are derived by using the Ze-R relation for rain region; they are shown in the figures only to see the location and the shape of the bright band. It is interesting to note that there is a clear difference in the bright-band thickness and shape between (a) and (b), which may be related to the difference in DSD. In this chapter, however, we concentrate our attention in the region from 9 to 11 km. As we have seen in the comparisons of path-averaged rain rates, $R_{Zk,DSD}$ agrees well with R_{Zx} with a slight overestimation, while $R_{Zk,MP}$ gives a significant underestimation in case (a) and some overestimation in case (b).

In Figures 7-8 and 7-9, we have compared path-averaged and lateral-averaged rain rates. The other question is the variability in rain rate estimates at each range bin for a single observation. A statistical analysis is made of the differences between the logarithms of R_{Zx} and $R_{Zk,DSD}$ (ΔLR_{DSD}) and between the logarithms of R_{Zx} and $R_{Zk,MP}$ (ΔLR_{MP}) for a given range bin in the rain region (approximately from 9 to 11 km) for the same periods shown in Figure 7-9. The result (mean $\pm$ standard deviation of ΔLR) is shown in Figure 7-10 as a function of range. The standard deviation of ΔLR_{DSD} is 0.5 ~ 0.8 dB for both periods (a) and (b), while ΔLR_{MP} has somewhat larger standard deviations (0.8 ~ 1.1 dB) in the period (a). The latter is probably due to the fact that the DSDs (and associated Ze-R relations) in the period (a) are more variable and different from the MP distribution than those in the period (b). If statistical fluctuations in X and Ka-band received powers are the only cause of the variation in ΔLR, the resultant standard deviation would be 0.4 ~ 0.5 dB. The observed standard deviations are somewhat larger than this limiting value, which is attributable to various error sources such as fluctuations in radar constants, errors in estimating path attenuation, and deviation of DSD from the assumed exponential model.

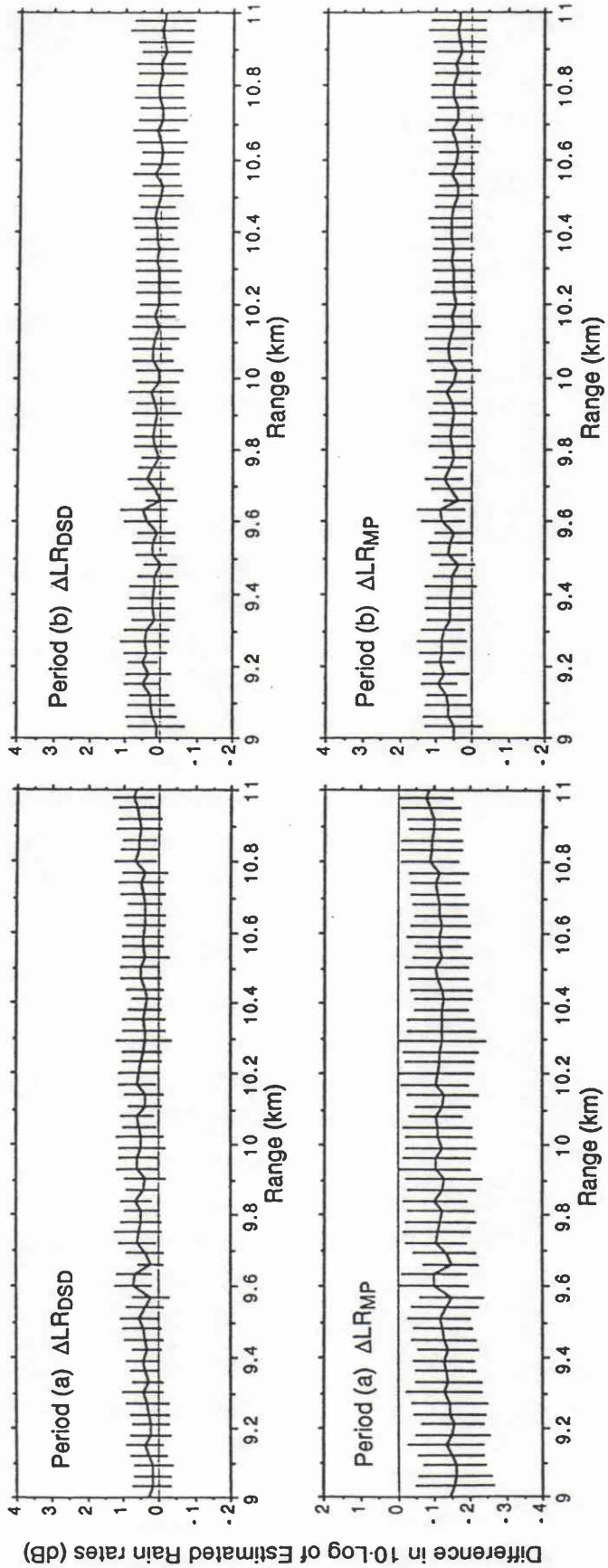

Figure 7-10. Differences between the logarithms of R_{Zx} and $R_{Zk,DSD}$ (ΔLR_{DSD}) and between the logarithms of R_{Zx} and $R_{Zk,MP}$ (ΔLR_{MP}) as a function of range for the same periods (a) and (b) shown in Fig.7-9. In the figure, solid curves represent the mean of the difference and vertical bars indicate the mean ± standard deviation.

7.2.3 Error sources

There are a number of uncertainties relating to the dual-parameter radar measurement. Some factors important for this method are summarized below.

- *Surface scattering cross section (σ^0):* Temporal and spatial variation in σ^0 is a major error source in estimating path-attenuation from surface return. It is known that over ocean, σ^0 depends strongly on surface wind condition (speed and direction) for intermediate to large incidence angles ($\gtrsim 15°$). For near-nadir incidence, the wind dependence of σ^0 is relatively small and becomes minimum around incidence angles of 8 ~ 10° [12]. Another source of error is the potential effect of raindrop striking on the sea surface scattering properties. This effect has been observed at large incidence angles [13,14]. Although no measurement on this effect has been reported for near-nadir incidence cases, it may be relatively small because of the dominant contribution of specular scattering component to σ^0. In the experiment conducted in the fall 1988, measurement was made at incidence angles around 7 degrees, at which σ^0 is expected to depend on the wind condition only slightly. This might be a reason for the relatively small standard deviation (1 ~ 1.5 dB) of surface returns we have observed in no-rain condition. Nevertheless, variability in σ^0 caused by environmental conditions such as wind, long gravity waves and the raindrop striking should be studied more to assess the accuracy in path-attenuation estimation from surface return. Over land, the use of surface return is more problematic than over ocean because of the larger spatial variability in σ^0. One way to reduce the errors is to use the difference of path-attenuation estimates at two frequencies instead of the estimate from a single frequency [15].

- *Bright band and convective storm modeling:* As mentioned in Section 7.2.1, errors in estimating the attenuation caused by hydrometeors at and above the bright band or 0°C isotherm height can cause non-negligible errors in estimating the DSD and other rain parameters. For stratiform rain, refinement of the bright band model would be required. For example, Figure 7-9 indicates that the bright band thickness depends on DSD and probably other precipitation properties as well, while the present model assumes a constant thickness of 900 m. The modeling of convective storm may be more difficult than the modeling of stratiform rain; unlike the stratiform rain, it is difficult to distinguish the hydrometeor phase state from the radar reflectivity profile especially when only a single-frequency, non-polarimetric radar is available. However, further analyses of the aircraft data may provide statistical models which depend upon storm intensity, vertical reflectivity profile, etc.

- *Non-uniform beam filling:* It has been observed in the present study, that the N_0 estimates sometimes show a positive or negative peak at the edge of an intense storm. This suggests the existence of errors due to the horizontal non-uniformity in rainfall within a radar resolution volume. Since the error caused by the non-uniformity is larger in the path-attenuation (or rain rate) estimate from the surface return than the rain rate estimate from the radar reflectivity [9,10], the dual-parameter methods employing the surface return may not be applicable to the storm edge or to rain cells having smaller horizontal sizes than the radar foot print size[11]. Conversely, it may be possible to detect the existence of partial beam filling by examining the spatial trend of estimated DSD parameters.

7.2.4 Effects of errors in Zm and A_{SR} on N_0 estimation

Errors in Zm measurement and A_{SR} estimation cause the error in the path-averaged N_0 estimation. In this section, we make a simple error analysis for the case where the DSD is uniform over the path. We also assume that X-band path attenuation is negligible ($Zm_X \approx Ze_X$) and that Ze_X and k_{Ka} are proportional to 6th and 4th moments of DSD. These assumptions approximately hold for the stratiform rains that we have analyzed in section 7.2.2. In this case, the N_0 estimate is given by

$$\tilde{N}_0^{1-\beta} = C\, A_{SR,Ka} \,/\, Ze_X^{\beta}, \quad \beta = 5/7 \tag{7.19}$$

where $A_{SR,Ka} = (n \cdot \Delta r)\, k_{Ka}$. For convenience, we consider the errors in the logarithms of measured and estimated quantities. Letting $U = 10 \cdot \log_{10}\tilde{N}_0$, $X = 10 \cdot \log_{10} A_{SR,Ka}$, and $Y = 10 \cdot \log_{10} Ze_X$, Eq.7.19 is expressed as

$$U = 10/(1-\beta)\, \log C + 1/(1-\beta)\, X - \beta/(1-\beta)\, Y. \tag{7.20}$$

By expressing X and Y as $X = X_0 + x$ and $Y = Y_0 + y$ where X_0 and Y_0 are true values, and x and y are corresponding errors, the error in U, u, becomes

$$u = 1/(1-\beta)\, x - \beta/(1-\beta)\, y \tag{7.21}$$

where C is assumed to have no error. Assuming that x and y are independent random variables with mean values of $\bar{x}$ and $\bar{y}$ and standard deviations of σ_x and σ_y, respectively, the mean and variance of u ($\bar{u}$ and σ_u^2, respectively) are

$$\bar{u} = 1/(1-\beta)\,\bar{x} - \beta/(1-\beta)\,\bar{y} \tag{7.22}$$

$$\sigma_u^2 = 1/(1-\beta)^2\,\sigma_x^2 + \beta^2/(1-\beta)^2\,\sigma_y^2. \tag{7.23}$$

Statistical fluctuation in radar received power is the major cause of the variation in Y. This contributes also to the variation in X; however, the major part of the variation is caused by the fluctuation in surface σ^0. Since the number of independent samples averaged (logarithmically in this system) is 128, $\sigma_y \approx 5.57/\sqrt{128} = 0.49$. In order to estimate σ_x, attenuated surface returns have been simulated by using Ka-band surface returns measured in no-rain condition subtracted by the sum of a constant attenuation and a received power fluctuation term approximated by a Gaussian noise having the standard deviation equal to σ_y. It has been found from a statistical analysis of this simulated data set that σ_x is 0.2 ~ 0.6 for $A_{SR,Ka}$ = 15 ~ 5 dB (2-way path attenuation 30 ~ 10 dB). Using these estimates of σ_x and σ_y, σ_u becomes 1.4 ~ 2.4. If we assume that $\bar{x} = 0$ and $\bar{y}$ = 1 dB (the latter represents the X-band radar calibration error), $\bar{u}$ = 2.5 dB. These errors are not negligible; however, they are still much smaller than the total variability in $10 \cdot \log N_0$ that ranges approximately from 30 to 50 ($N_0 \approx 10^3 \sim 10^5$).

The calibration error in the Ka-band radar does not affect the N_0 estimate but does the result of the consistency check. For example, the Ka/X Ze ratio shown in Figure 7-7 is offset by the same factor as a bias error in Zm_{Ka} (in dB unit); however, the $\log_{10}N_0$ dependence of the Ze ratio is still consistent with the theory in a relative sense. Similarly, a bias error in Zm_{Ka} simply causes an offset in the logarithm of $R_{Zk,DSD}$ and $R_{Zk,MP}$ shown in Figures 7-8 through 7-10. That is, $R_{Zk,MP}$ is still inconsistent with the reference rain rate R_{Zx}, because the difference between $R_{Zk,MP}$ and R_{Zx}, which has both positive and negative values depending on the period, cannot be explained by an offset in Zm_{Ka}.

7.3 Conclusions

We have shown test results of a dual-parameter rainfall measurement for a down-looking airborne or spaceborne radar, which combines a reflectivity profile and a path-integrated attenuation. It has been found that the values and the spatial trend of the path-averaged DSD parameter, N_0, estimated from the experimental data are reasonable and that they are consistent with the measured Ka-band reflectivity which is independent of the N_0 estimation. These results indicate the feasibility of estimating DSD parameters from space. The

DSD information provided from this method would lead to more accurate rainfall measurements and a deeper understanding of precipitation processes. It also has a potential to improve a wide range of radar rain measurements. For example, DSD properties and associated *Ze-R* relations (and other IRP relations) obtained at a part of a storm could also be applied to other part of the storm where path-attenuation data is difficult to obtain. Applying this method to spaceborne radar measurements with global coverage would extend our knowledge of the dependences of *Ze-R* relation on rain type, geographical location and synoptic conditions.

More studies are required to clarify uncertainties such as the raindrop striking effect on σ^0 and non-uniform beam filling. Although the storm models used in this study should be adequate as a first-order approximation, refinements in the bright band and convective storm models are required to improve the accuracy in estimating the attenuation due to non-liquid hydrometeors aloft. Using a gamma DSD model instead of the exponential model and incorporating storm-type and height dependences of the DSD model should also improve rainfall retrieval accuracy. In the aircraft experiment, multi-frequency radiometer data as well as the radar data were obtained. The DSD estimation is also possible by combining the radar and radiometer data instead of using the surface return. Combining such multiple sensor data would also be useful to develop the improved storm model and to achieve better rainfall retrievals.

References

(1) Kozu, T., R. Meneghini, W. C. Boncyk, K. Nakamura, and T. T. Wilheit, 1989: Airborne radar and radiometer experiment for quantitative remote measurements of rain. *Proc. GARSS'89*, Vancouver, Canada, 1499-1502.

(2) _____, K. Nakamura, and R. Meneghini, 1991: Estimation of raindrop size distribution parameters from a dual-parameter spaceborne radar measurement. Preprints, *25th Conf. Radar Meteor.*, Paris, Amer. Meteor. Soc., 384-387.

(3) _____, _____, _____, and W.C. Boncyk, 1991: Dual-parameter radar rainfall measurement from space: A test result from an aircraft experiment. *IEEE Trans.Geosci. and Remote Sens.*, **GE-29**, 690-703.

(4) Fujita, M., 1983: An algorithm for estimating rain rate by a dual-frequency radar. *Radio Sci.*, **18**, 697-708.

(5) Hitschfeld, W. and J. Bordan, 1954: Errors inherent in the radar measurement of rainfall at attenuating wavelengths. *J. Meteorol.*, **11**, 58-67.

(6) Meneghini, R. and K. Nakamura, 1990: Range profiling of the rain rate by an airborne weather radar. *Remote Sens. Environ.*, **31**, 193-209.

(7) Meneghini, R. and T. Kozu, 1990: *Spaceborne weather radar*. Artech House, Boston.

(8) Awaka, J., Y. Furuhama, M. Hoshiyama, and A. Nishitsuji, 1985: Model calculations of scattering properties of spherical bright-band particles made of composite dielectrics. *J. Radio Res. Lab.*, **32**, 73-87.

(9) Nakamura, K., 1989: A comparison of the rain retrievals by backscattering measurement and attenuation measurement. Preprints, *24th Conf. Radar Meteorol.*, Tallahassee, FL, Amer. Meteor. Soc., 689-692.

(10) Amayenc, P., M. Marzoug and J. Testud, 1989: Non uniform beam filling effects in measurements of rainfall rate from a spaceborne radar. *ibid*, 569-572.

(11) _____, _____ and _____, 1990: Analysis of cross-beam resolution effects in rainfall rate profile retrieval from a spaceborne radar. *Proc. GARSS'90*, College Park, MD, 433-436.

(12) Masuko, H., K. Okamoto, M. Shimada and S. Niwa, 1986: Measurement of microwave backscattering signatures of the ocean surface using X band and Ka band airborne scatterometers", *J. Geophys. Res.*, **91**, (C11), 13065-13083.

(13) Moore, R.K., Y.S. Yu, A.K. Fung, D. Kaneko, G.J. Dome, and R.E. Werp, 1979: Preliminary study of rain effects on radar scattering from water surfaces. *IEEE J. Oceanic Eng.*, **OE-4**, 31-32.

(14) Bliven, L.F. and G. Norcross, 1988: Effects of rainfall on scatterometer derived wind speeds. *Proc. IGARSS'88*, Edinburgh, UK, 565-566.

(15) Meneghini, R., J.A. Jones and L. H. Gesell, 1987: Analysis of a dual-wavelength surface reference radar technique. *IEEE Trans.Geosci. and Remote Sens.*, **GE-25**, 456-471.

CHAPTER 8. CONSIDERATION OF RADAR RAINFALL RETRIEVAL ALGORITHMS FROM SPACE

In this chapter, we consider algorithms to estimate rainfall parameters from a TRMM type spaceborne single-frequency radar, operated with a multi-frequency microwave radiometer and a visible/infrared radiometer. This is followed by a consideration of usefulness of the DSD estimation method we have studied in this thesis for the spaceborne radar rainfall measurement.

As described in Chapter 1, the strategy to estimate rainfall parameters depends on the resolution (both temporal and spatial) and accuracy requirements. Utilizing statistical properties of rainfall such as lognormal or gamma rainfall distribution function and a statistical correlation between area-integrated rain rate versus raining area for convective storms has been found to be useful to estimate low resolution rainfall parameters under limited measurement capabilities.

While the low resolution rainfall estimates are sufficient for many climatological studies, high resolution rainfall parameter estimation is essential for various local to mesoscale meteorological and hydrological studies. The high resolution rainfall information is also important for applications such as short-term weather forecast and flood warning. It is also necessary to develop and to refine various statistical and climatological methods for estimating low resolution rain parameters. The consideration in this chapter is, therefore, concentrated on the rainfall retrieval with the high resolution (every observation ~ one raining area).

8.1 Estimating Apparent Effective Radar Reflectivity Factor (Zm)

As discussed in Chapter 2, the radar rainfall retrieval begins with obtaining the apparent effective reflectivity factor (Zm), which can be derived from the radar equation neglecting rain attenuation. For the surface return, "apparent" normalized surface scattering cross section, σ^0_m, will be calculated similarly. It is important to generate σ^0_m as well as Zm, because: (1) For the algorithms using the surface return level, the data outside the rain region is essential to extract the path-attenuation; (2) from the σ^0_m measurement over the ocean, surface wind speed can be estimated; (3) a world wide surface scattering cross section map will be useful for future remote sensing of Earth surface from space.

Since Zm and σ^0_m are the quantities obtainable from only the instrument dependent

parameters, they can be derived in a straightforward manner. Therefore, they are suitable as "Level 1" products generated from "Level 0" product (original count value sent from the satellite with some ancillary data added). It should be noted that the radar calibration (both internal and external) is the most important task to assure the accuracy of those quantities. In this stage, several additional processing should be done: (1) geometrical information, e.g. the positions of the satellite and the center of a surface FOV, will be added to the product for each observation; (2) "bad" data, e.g. observations during a satellite maneuver or radar transmitter turn-off should be rejected; (3) in order to extract the signal power from the measured (signal + noise) power, an independent noise level monitoring and a noise level subtraction are required.

- Radar calibration

To assure the accuracy of *Zm* and σ^0_m, both internal and external calibration schemes are to be employed. The internal calibration includes: the periodical monitoring of the transmit power, and the total noise power of the receiver output when the receiver sees a stable internal terminator or a stable land background temperature, which provides a measure of the short-term variation in the receiver gain; and the measurement of receiver input-output transfer function using an internal signal generator which may be done on a weekly basis.

In addition to the internal calibration, external calibration is required to calibrate the radar as a whole. One useful method is to use a radar receiver and a beacon transmitter to calibrate "forward" and "backward" paths of the radar signal including antenna characteristics. The beacon transmitter, if it is arrayed with appropriate separation in space, could provide the transfer function of the backward path of the radar. The overall system gain can be calibrated by using an artificial reference target on the ground such as corner reflectors. In the case of down-looking spaceborne radar, however, the return signal from such a reference point target may be masked by strong surface clutter. Active radar transponders with some delay circuit would be necessary to provide sufficient scattering cross section and to separate the return signal from the ground clutter. It may also be a good scheme to use wide homogeneous surface targets such as sea surface and tropical rain forests to calibrate the radar, although it would be necessary to check the σ^0 value of such areas and its uniformity periodically by other means.

The most direct rain radar calibration would be to use rain itself as a reference, as we have tried in the T-39 experiment. The rain measurement on the ground may be made with raingages, disdrometers, ground-based radars, and micro- or millimeter wave links. The

success of the "rainfall" method depends on how "good" rain can be observed simultaneously by the ground-based and spaceborne sensors; the chance to conduct it may not be frequent. Nevertheless, once we have several such data sets, they should be very useful to calibrate the radar externally. The advantage of this method is that the radar equation same as that for the actual rain observation is used. An extension of this method is an adjustment of a radar constant based on the radar reflectivity and rain rate statistics[1,2]. Since this scheme does not necessarily require simultaneous measurements, it can be conducted widely by using existing rainfall measurement facilities over the world. This scheme, as necessity, requires a long integration time and therefore the temporal resolution of the calibration is poor.

One uncertainty in comparing the rain rates as measured by ground-based and by spaceborne radar is *Ze-R* relationship to be employed. If *Ze-R* relation is biased, the resultant system calibration constant is also biased. Accordingly, the use of such system constant would cause bias errors in rain rate estimation at other locations. During the calibration period, therefore, DSD measurement should be performed at the calibration site to relax such bias errors. Non-uniform beam filling within a radar resolution volume, which is another cause of the bias error, should be taken into consideration as well.

8.2 Estimating Rain Rate and Liquid Water Content

The general concept of rainfall retrieval is to estimate various rainfall parameters of interest from the radar measurables. From the single frequency spacebonre radar, we can expect the following measurables; *Zm* profile, surface return, and mirror image *Zm* profile. Although the mirror image may be used to estimate path-attenuation combined with the "direct" image, we concentrate the discussion on the former two. The use of the mirror image is a subject of future study. We consider here the processing of Level 1 products (*Zm* and σ^0_m) to rain rate and LWC profiles for each observation (Level 2 products). In addition, estimation of several DSD related quantities useful to improve the rainfall retrieval is discussed.

8.2.1 Z-R and Z-W methods

The conventional way to estimate rain rate, *R*, has been to use an empirical power-law *Z-R* or *Ze-R* relationship (for convenience, we call this type of method "Z-R" method even if the quantity *Ze* is employed instead of *Z*);

$$Ze = \alpha R^{\beta}. \tag{8.1}$$

An extension of this scheme is to adjust the coefficients (α,β) based on the past experience of rain-type or climatological dependences of the coefficients. The other extension is to use more general relationships between *Ze* and *R*, e.g., piece-wise regression lines for different rain rate ranges, since a single power law may not fit well over the total rain rate range. To establish such a *Ze-R* relation data base requires a comprehensive survey of past measurements over the world. Disdrometer data that have been collected at many locations in mid-latitudes and at several tropical sites[3,4] should be useful to study the properties of DSD; dependences on rain type, season, and climatological regimes. DSD properties and associated *Ze-R* relations of oceanic rainfall are poorly known, and have to be studied with airborne or shipborne sensors.

When rain attenuation up to a radar scattering volume is not negligible (2 or 3 dB or more), rain attenuation correction is required. The attenuation can be estimated in a similar manner to the Z-R method; using an empirical *k-Ze* relationship, *k* being a rain attenuation coefficient (usually in dB/km). If the attenuation becomes large (~5 dB or more), such an attenuation correction is known to be very unstable.

To estimate liquid water content (LWC; *W*), the same scheme, Z-W method, may be employed; however, the correlation between *Ze* and *W* is worse than that between *Ze* and *R*. Therefore, the Z-W method would be very erroneous unless a large amount of averaging is employed, and some dual-parameter methods would be necessary.

8.2.2 Surface Reference Target (SRT) method

A total path attenuation can be deduced from the surface return measurement. Since the microwave attenuation coefficient generally has a kernel closer to rain rate than that of radar reflectivity (see Section 2.1.6), one can expect higher accuracy than the Z-R and Z-W methods. It should be noted, however, that the estimation of *W* from microwave attenuation is not as accurate as the rain rate estimation because of the departure of the kernel of attenuation coefficient from that of liquid water content.

The success of this scheme depends on how well the path-integrated attenuation can be estimated; i.e., for light to moderate rain, the path attenuation is masked by a fluctuation in the surface σ^0, while for extremely heavy rain the surface return is below noise level. The σ^0 in a raining area, which is needed to extract the two-way path attenuation, can be estimated from measurements of σ^0 at an adjacent no-rain area or the measurements at the same location at times when rain is absent. The latter scheme is preferable for the application of the method over land because of the high variability of the type of terrain. Generally speaking, however,

the SRT method over land would be more erroneous than over ocean. Over ocean, the SRT method would be difficult to be applied to the measurement at incidence angle larger than about 15 degrees (depending on wind speed) because of the large wind speed and direction dependences of σ^0. The other uncertainty in ocean σ^0 is the effect of raindrop striking[5,6]. Although it is anticipated that the effect is small for near-nadir incidence angle region where specular scattering component is dominant, it is desirable to conduct both theoretical and experimental studies on this problem.

8.2.3 Range-profiling of *R* and *W*

To overcome the above mentioned problem of the instability of rain attenuation correction and to improve rainfall retrieval accuracy, several profiling algorithms have been proposed as discussed in Section 2.3.7. All of them utilize the path-integrated attenuation or rain rate derived from the surface return or passive microwave radiometric measurements.

It has been demonstrated that excellent stabilities can be obtained using the path-integrated quantity as a constraint. Although the approach is different from one method to another, it is expected that those methods provide similar rain rate profiles as far as the same path-integrated quantity is used. Since this type of methods use the path attenuation as a reference, the accuracy of the path-attenuation estimate is a dominating factor to determine the accuracy. Therefore, the limitation of the SRT method on the σ^0 uniformity and stability applies also to this type of methods.

8.2.4 Non-uniform beam filling (NUBF) effects

A problem, which may be serious in the case of local convective storms, is a non-uniform beam filling within a FOV. Considering the size and mass limitation of the antenna and the accuracy in manufacturing large reflectors, horizontal resolution of spaceborne radar would be at most 2 to 4 km. Since cell sizes of local convection may be comparable to these FOVs, evaluation is required of the effect of NUBF within the FOV on the accuracy of rainfall retrievals. It has been shown that the error caused by the non-uniformity is more serious in the SRT method than in the Z-R method[7-9]. Thus, the applicability of the SRT method and the related range profiling methods may be more limited than the Z-R method depending upon storm structure. It is necessary to develop methods to estimate the existence of non-uniformity of rain to avoid an unexpected error in the SRT related rainfall estimates.

8.2.5 Limitations of Z-R and SRT methods

The Z-R method and SRT method are complement to each other to some extent. For light to moderate rain, the Z-R method works fine except for the uncertainty in *Ze-R* relation. On the other hand, the SRT method works well for moderate to heavy rain; i.e., cases where path attenuation is detectable. In such heavy rain cases, the range profiling methods also work well. However, there are various limitations if only the Z-R and SRT methods are used to retrieve rainfall from the spaceborne radar; some of them are already addressed above.

- *Light to moderate rain rate cases*

The Z-R method is the only way to estimate rain rate; the accuracy of this method may not satisfy most scientific and application requirements. The estimation accuracy of LWC with the Z-W method is even worse than the rain rate estimation with the Z-R method.

- *Moderate to heavy rain rate cases*

Attenuation correction is required to retrieve *Ze* profile from the attenuated *Zm* profile. If SRT method can be used, stable attenuation correction and further better estimation of rain rate profile would be achieved with the range profiling methods. However, the SRT method is not applicable to areas where surface σ^0 is highly variable in space or time, and to some portion of the raining area where non-uniform beam filling may cause bias errors. Such limitations can significantly degrade the usefulness of the SRT and the range profiling methods.

8.3 Usefulness of SDP Measurement Estimating DSD

In the previous chapters, we have studied a method to estimate DSD parameters from the same combination of measurables as those for other range profiling methods. One difference is that *Zm* value should be calibrated to perform the DSD estimation. However, various benefits to relax the above mentioned limitations would be obtained from the DSD estimation method.

(1) *Wider applicability:* We have shown that the two-scale DSD model is valid within a limited time or space; the validity extends fairly well to a rain event (or to an entire rain area). This suggests that the two-scale DSD model parameter estimated at a part of the rain event or of the rain area can be a good representative of the two-scale model applicable to the entire rain event or area, although some caution is required to sub-structure of a storm system[10,11] and associated DSD change[3].

Therefore, even though the path-attenuation can be estimated by the SRT method only at limited areas, result of the DSD estimation would be useful to improve the rainfall retrieval with the Z-R method at remaining rain area where the SRT method can not be applyed. The same applies to the rain rate region; *Ze-R* relations estimated at high rain rate region may also be applied to lighter rain rate region within the same storm or sub-storm area.

As mentioned above, the success of this scheme depends upon how well the radar is calibrated and that how well the path-integrated attenuation is estimated. The accuracy is also related to the uniformity of rain within the radar FOV; if there is a significant non-uniformity, the estimated DSD parameter would be biased. Although the similar NUBF limitation applies to all methods using the surface-return derived path attenuation, there is a difference between the DSD estimation and other methods. That is, the former can provide an estimate of the storm properties in terms of DSD and IRP relationships, which could be applied to other parts of the storm or other storms having similar characteristics.

(2) *LWC estimation:* As we have studied in Chapter 4, DSD information is necessary to obtain acceptable accuracy in the LWC estimation from *Ze*; it is also desirable even when path attenuation is measured because of the larger scatter of the relation between attenuation and LWC than that between attenuation and rain rate. In short, the DSD estimation method is important to improve the accuracy in LWC estimation.

(3) *Non-uniform beam filling detection:* If there is a significant NUBF in a FOV, the resulting rain rate and other products can have large errors. It may be difficult to detect the existence of the NUBF only from the radar profiles. The aircraft experiment (Chapter 7) has shown that at the storm edge, the estimated DSD parameter has a clear spiky signature. The NUBF would cause negative peak in the N_0 trend. Since the result shows both positive and negative peaks, more study is required of the cause of such peaks. However, this result suggests that NUBF could be detected from a spatial trend analysis of DSD parameter correlated with *Ze* or rain rate trend. If more amount of DSD parameter data were accumulated, it may also be possible to generate a "warning" about the reliability of the satellite observation data from unrealistic DSD parameter estimates.

(4) IRP relation database:

It is anticipated that the IRP relationships change systematically with storm type, season and other long-term rainfall properties. It is possible to estimate storm (or sub-storm) averaged IRP relation data sets from the DSD estimation method. This is particularly important for the

rainfall over ocean where surface DSD measurements are difficult. An IRP relation data base, which is used for the standard Z-R and Z-W methods, can therefore be refined from on-going spaceborne radar measurements. This database should also benefit other wide range of radar rainfall measurements (both ground and space-based radars).

8.4 Radar Data Processing Flow

A conceptual flowchart to generate Level-2 products from the Level-0 product is shown in Figure 8-1. The processing of the Level-0 to the Level-1 products was discussed above. The processing of the Level-1 to the Level-2 products has several options depending on the combination of algorithms to be employed. Before processing the data, status of the Level-1 product is checked on a rain area basis in terms of various items such as *Zm* calibration, σ^0_m data reliability, the amount of path attenuation , rainfall type, and the existence of non-uniform beam filling (NUBF) error. The rainfall type classification can be made using a 3-D *Zm* map over the rain area. The last check item (NUBF) may be difficult to perform; however, it should be possible to generate some "warning" flag using an intensity gradient analysis of 2-D *Zm* factor map over a storm. As mentioned above, the 2-D signature of DSD parameter estimates may be useful to improve the NUBF detection capability. Other sensor data such as VIS/IR sensor would also be useful to classify rainfall type and possibly for NUBF detection.

Based upon the result of the status analysis, algorithms to be used for making primary products are determined. For example, if *Zm* calibration is good and rain attenuation is small, the Z-R method would be the primary algorithm. In using the Z-R method, the rainfall type information from the status analysis may be used to select a proper *Ze-R* relation. Such *Ze-R* (and *Ze-W*) relation data base should be established from a comprehensive survey of past ground-based or aircraft measurements. It should be noted that the results from the DSD estimation method can improve the estimates by the Z-R and Z-W methods by providing the *Ze-R* and *Ze-W* relations for the raining area involved, and that they can be used to expand or refine the database.

One problem of the SDP measurements combining *Zm* profile and path attenuation by the SRT method is that they are limited to moderate to intense rain rates. The combined radar and microwave radiometer methods are expected to work at lighter rain rates over the ocean. For example, the 19-GHz channel of the TMI (TRMM Microwave Imager) onboard the TRMM work well to estimate path-integrated attenuation or rain rate between about 1 mm/h

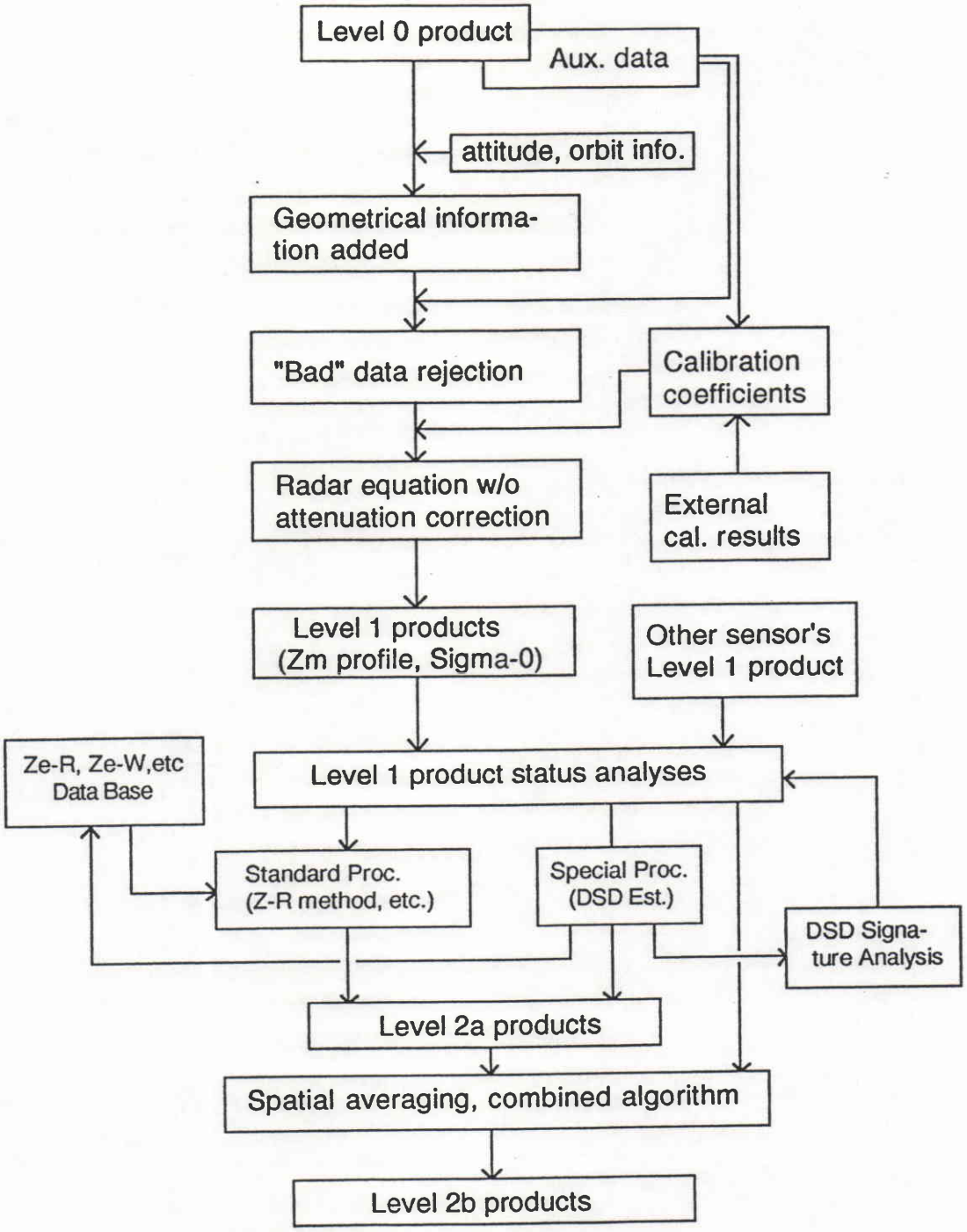

Figure 8-1. A flowchart of spaceborne radar data processing.

and 10 ~ 15 mm/h. The use of such radiometers as well as the SRT-derived path attenuation can expand the rain rate dynamic range to apply the SDP measurements[12].

As mentioned above and shown in Figure 8-1, it is a unique feature of the DSD estimation method to make a feed-back loop to improve the knowledge to improve the rainfall retrieval (*Ze-R* and *Ze-W* relations, NUBF detection, etc.). This is the consequence coming from the fact that the DSD is a fundamental rain parameter to make a primary link between the radar measurable quantities and meteorological quantities, and that storm-scale DSD properties are reasonably well described by a two-scale model the parameters of which can be estimated through the SDP radar measurement.

8.5 Issues to Develop Spaceborne Radar Algorithms

8.5.1. Modeling Studies

- Raindrop size distribution model

As we have studied in this thesis, the 3-parameter gamma or lognormal distribution can describe the natural DSD sufficiently well; the simple 2-parameter models also work well for limited domain such as relating higher order moments. It was concluded that the gamma model with the parameter m fixed to 3 ~ 6, for example, provides approximately unbiased estimates over a wide range of moments. The remaining issue is to reveal the systematic rain type and height dependences of DSD more in detail.

The modeling of multiple DSDs extending over a space or time, which is required to allow the estimation of DSD parameters from the SDP measurement, becomes more complicated. For this purpose we have proposed the "two-scale" DSD model, and found that several simple models such as the *constant* N_T model and the *constant* N_0 *exponential model* are adequate ones. The next step would be to reveal the rain type dependence of the optimum two-scale model, and to refine the model incorporating such rain type dependence or the systematic DSD evolution processes with altitude. Doppler radar measurement is important to estimate the height dependence of DSD. The uncertainty of vertical air velocity is a major cause of error in the Doppler radar DSD estimation; however, high power VHF Doppler radars, which can measure both precipitation and air motions, could diminish this problem[13].

It is also required to reveal the climatological dependences of the two-scale model, which would be essential to perform the global rainfall mapping. One interesting result is that

the DSDs of intense convective storms in summer at Kashima are very similar to those at Darwin, Australia[3]. More study is recommended to clarify if the similarity holds for other locations and for the rainfall over ocean. Such detailed DSD models should also be related to the modeling of bright band.

- *Bright band model*

For the radar measurement of precipitation, the modeling of bright band is important, because the bright band attenuation, which should be subtracted from the total path attenuation derived from the surface return, is not always negligible, and because a precise bright band model may improve the passive microwave retrievals. For example, results from the T-39 aircraft experiment have shown a clear difference in the thickness of bright band between two different values of a DSD parameter, N_0 (Chapter 7). This result suggests the necessity to incorporate a DSD dependence in the bright band model. We have used a simple Non-coalescence/Non-breakup model to evaluate the bright-band attenuation[14]. It appears that the model gives fairly good agreement with the measurement of *Ze* factor profile for the lower half of the bright band. However, it is required to refine the model by incorporating various physical processes such as coalescence, breakup, evaporation, etc.

8.5.2 Test and Validation of the Algorithms

The basic advantages and disadvantages of the algorithms have already been tested and recognized. We have considered a strategy based on such understanding. In order to compare those algorithms for actual spaceborne measurements and to evaluate the overall spaceborne radar performance, it is necessary to perform theoretical and simulation studies assuming the same and realistic DSD and storm models, and the same instrument performances. The DSD and bright band modeling mentioned above is also important to make these studies.

Aircraft experiments are important in the sense that the performances of algorithms can be tested in measurements similar to the space-based measurement. The experiment should be conducted together with measurements of ground or sea truth data, if possible. A series of NASA/CRL joint aircraft experiments has provided such data for various storm conditions. We have tested the DSD estimation method in this thesis using the T-39 experimental data. In September 1990, an experiment was conducted using the NASA DC-8 for obtaining the data of rainfall associated with typhoon activities over the west North Pacific[15]. Those data are invaluable to develop spaceborne radar algorithms.

Although the comparison with the ground-based measurements are preferable to verify the algorithm performance, it is usually difficult to conduct the simultaneous ground and aircraft measurements. An alternative method to verify the algorithm performance is to make a consistency check among various sensor data onboard the same aircraft, as we have used to test the DSD estimation method. In this sense, multi-parameter aircraft measurements are desirable. Such multi-parameter measurements would also be useful to develop detailed storm models.

References

(1) Atlas, D., D. Rosenfeld, and D.B. Wolff, 1990: Climatologically tuned reflectivity-rain rate relations and links to area-time integrals, *J. Appl. Meteorol.*, **29**, 1120-1135.

(2) Rosenfeld, D., D. B. Wolff, and D. Atlas, 1991: Derivation of non-power law effective Z-R relations by PDF matching method, *J. Appl. Meteorol.*, accepted.

(3) Short, D. A., T. Kozu, and K. Nakamura, 1990: Rainrate and raindrop size distribution observations in Darwin Australia, *URSI-F Open Symp. on regional factors in predicting radiowave attenuation due to rain,* Rio de Janeiro, 35-40.

(4) Ajayi, G.O., and R.L. Olsen, 1985: Modeling of a tropical raindrop size distribution for microwave and millimeter wave applications. *Radio Sci.*, **20**, 193-202.

(5) Moore, R.K., Y.S. Yu, A.K. Fung, D. Kaneko, G.J. Dome, and R.E. Werp, 1979: Preliminary study of rain effects on radar scattering from water surfaces. *IEEE J. Oceanic Eng.*, **OE-4**, 31-32.

(6) Bliven, L.F. and G. Norcross, 1988: Effects of rainfall on scatterometer derived wind speeds. *Proc. IGARSS'88*, Edinburgh, UK, 565-566.

(7) Nakamura, K., 1989: A comparison of the rain retrievals by backscattering measurement and attenuation measurement. Preprints, *24th Conf. Radar Meteorol.*, Tallahassee, FL, Amer. Meteor. Soc., 689-692.

(8) Amayenc, P., M. Marzoug and J. Testud, 1989: Non uniform beam filling effects in measurements of rainfall rate from a spaceborne radar. *ibid*, 569-572.

(9) _____, _____ and _____, 1990: Analysis of cross-beam resolution effects in rainfall rate profile retrieval from a spaceborne radar. *Proc. IGARSS'90*, College Park, MD, 433-436.

(10) Houze, R.A., Jr., 1977: Structure and dynamics of a tropical squall-line system. *Mon. Wea. Rev.*, **105**, 1540-1567.

(11) Houze, R.A., Jr., and A. K. Betts, 1981: Convection in GATE. *Rev. Geophys. and Space Phys.*, **41**, 541-576.

(12) Wilheit, T.T., 1986: Some comments on passive microwave measurement of rain. *Bull. Amer. Meteor. Soc.*, **67**, 1226-1232.

(13) Wakasugi, K., A. Mizutani, M. Matsuo, S. Fukao, and S. Kato, 1987: Further discussion on deriving drop-size distribution and vertical air velocities directly from VHF doppler radar spectra. *J. Atmos. Oceanic Technol.*, **4**, 170-179.

(14) Awaka, J., Y. Furuhama, M. Hoshiyama, and A. Nishitsuji: Model calculations of scattering properties of spherical bright-band particles made of composite dielectrics, J. Radio Res. Lab., **32**, (136), *73-87*, 1985.

(15) Kumagai, H., R. Meneghini, and T. Kozu, 1991: Multi-parameter airborne rain radar experiment in the Western Pacific. Preprints, *25th Conf. on Radar Meteorol.*, Paris, Amer. Meteor. Soc., 400-403.

CHAPTER 9. CONCLUSIONS

A major purpose of this study is to develop a method to estimate DSD parameters from spaceborne radar measurements. Since the complete dual-parameter (DP) measurement is difficult to perform for each scattering volume with the down-looking spaceborne radar, we tried to use "semi" DP (SDP) measurements in which the first measurement, *Z*-factor, has a fine range resolution but the second measurement is obtained only with a much coarser resolution. In order to investigate the DSD properties and to test estimation methods, we tried to use DSDs on the ground measured by a disdrometer. The validity to use such ground-measured DSD for radar rainfall remote sensing was confirmed through the analysis of slant-path propagation data and a calibration of 14-GHz FM-CW radar. Various statistical properties of DSD parameters modeled by the gamma and lognormal distribution models were investigated using the disdrometer data. To make the DSD estimation possible from SDP measurements, the concept of "two-scale" DSD model and a method to estimate parameters of the two-scale model were proposed. The performance of the method was tested by means of a simulation with the disdrometer data. Moreover, the method was tested using the data obtained from the CRL/NASA joint aircraft experiment. Finally, consideration was given to the strategy of overall algorithms for single frequency spaceborne radars like the TRMM radar. It was also discussed how the DSD estimation method developed here would contribute to improving the spaceborne radar rainfall measurement in the proposed overall algorithm strategy.

In the following, the major results obtained from Chapters 2 ~ 8 are summarized:

In Chapter 2, fundamental meteorological and radar quantities, their relationships, and basic theory of radar rainfall measurement were summarized. The existing radar rainfall retrieval methods and their problems were reviewed, and the necessity and usefulness to estimate DSD parameters from radar measurements were pointed out.

For the purpose of studying DSD estimation methods, the use of DSDs measured on the ground by a disdrometer was examined in Chapter 3. Considerations were also given to the raindrop sampling error by the disdrometer and to the effects of the possible degradation of the sensitivity at the small drop diameter channels. It is found that those errors are not negligible but the uncertainty in the measured DSD caused by those errors are much smaller than the natural DSD variabilities.

Followed by the above basic tests of the disdrometer, more practical evaluations were performed, in which the disdrometer data were employed for an analysis of slant-path rain attenuation properties and an external calibration of a Ku-band FM-CW radar.

From those tests and evaluations, it is concluded that the disdrometer data are useful to study the effects of DSD variation on radar rainfall measurements in detail. In particular, the Kashima disdrometer data used in our study, which were collected over more than two years, should provide reliable statistical properties.

Based on the experimental validation of the disdrometer data, in Chapter 4, statistical analyses of parameters of DSD modeled by gamma and lognormal models were performed, including rain rate and Z-factor dependences of the DSD parameters. In addition to the three-parameter gamma and lognormal DSD models, studies were made of two-parameter models in which the parameter m (gamma) or σ (lognormal) is fixed. It is found that many DSD parameters such as N_T, N_0 of the 2-parameter gamma model with m fixed to 0 ~ 3, and Λ are lognormally distributed. The parameter m of the 3-parameter gamma model is found to vary significantly (-1 ~ 30), which is partly caused by the estimation method used in this study, i.e., the method of moment with higher order moments. However, since the m values of 10 or larger are caused by a small change in the DSD shape, the m value may be limited to the value less than about 10 in practical applications. A similar discussion can be made for the parameter σ of the lognormal DSD model.

Relations between important integral rain parameters (IRPs) such as Ze-R, k-R and k-Ze relations were obtained from a regression analysis using the two-year disdrometer data set. The resultant Ze-R relations are somewhat different from the relations assuming typical exponential distributions such as Marshall-Palmer model. This is caused by the departure of measured DSDs from the exponential shape (measured DSDs are more "concave-down", i.e., the m value is higher than zero). Considering that this feature is widely observed including both tropical and midlatitude regions, the use of the classical exponential DSD model may not be adequate to model the actual DSD, especially for higher rain rates.

In order to test the performance of the DP and triple-parameter (TP) measurements combined with the assumption of the gamma and lognormal DSD models more precisely, a simulation of rain rate estimation has been made. From the simulation, it has been shown that if we can make a TP measurement using two kinds of attenuation in addition to Ze, the estimation is nearly perfect, and that even a DP measurement, in which only a kind of

attenuation can be measured, provides excellent estimation over a fairly wide range of m and σ values. In view of the results of the statistical analysis of m, of several moment estimates in the DP measurement simulation, and of the possible sensitivity degradation of the disdrometer at small drop diameters, the m values of 3 ~ 6 would be appropriate to model natural DSDs.

An error analysis was made to assess the effects of errors in DP measurements. The results indicate that the DP estimation of rain rate and LWC is generally superior to the single-parameter (SP) estimation under typical measurement error conditions. The superiority of the DP estimation is reduced to some extent if the attenuation coefficient is proportional to the moments higher than $M_{3.67}$ (rain rate), while the DP estimation becomes insensitive to the measurement error and the superiority is enhanced if the moment lower than 3.67 (i.e., millimeter wave attenuations) is measured together with Z-factor. This result is important because it indicates that accurate rain rate and LWC estimation would be achieved by combined radar and millimeter wave attenuation measurements at light rainfall where DSD variation is larger than at heavy rainfall. Combined radar and multifrequency attenuation measurements are also attractive to obtain the high accuracy over the wide range of rain rate.

In Chapter 5, a method was proposed to estimate DSD parameters from the SDP rainfall measurement combining a Z-factor profile and a path-integrated attenuation for estimating DSD parameters. To do this, the concept of "two-scale" DSD model was also proposed. From an event-scale statistical analysis of DSD moments, simple two-scale models adequate for describing short-term (or small spatial scale) DSD variations were proposed. These models assume that the N_0 parameter of the gamma DSD model with a small ($\lesssim 3$) m value or the N_T parameter is constant over a spatial or temporal region while the other parameter Λ variable.

Rain rate profiling accuracy of the SDP measurement was evaluated through a simulation employing the disdrometer dataset. The result indicates that the SDP measurement has an ability to estimate the rain rate profile reasonably well; 2 to 4 times better than the SP measurement using a Z-R relation, depending on the temporal or spatial resolution of the attenuation measurement and depending on the two-scale model assumed. Although the m value of 3 ~ 6 was suggested to be reasonable in Chapter 4, the result of the SDP measurement simulation shows little difference in the rain rate estimation accuracy between the results using $m = 0$ and $m = 6$. This is due to the fact that the accuracy is mainly determined by the decorrelation of DSD in space or time, not the goodness-of-fit of the single DSD. An important finding from the simulation is that the accuracy of the rain rate estimation is not degraded

rapidly within a rain event, which justifies the usefulness of estimating a DSD parameter averaged over a rain event; i.e., event-scale adjustment of IRP relations such as *Z-R* relation.

It should be noted that although the two-scale models used in this thesis are adequate ones as a first approximation, refinements of the model, incorporating rain type or height dependences of DSD, should further improve the rainfall retrieval accuracies.

The T-39 aircraft experiment conducted jointly by CRL and NASA was outlined in Chapter 6. The CRL radar/radiometer system (MARS) was upgraded for the T-39 experiment to improve radar performance. A versatile real-time monitor for MARS was also developed. An external calibration of the X-band radar was successfully performed employing data from a raingage network. The Ka-band radar calibration was performed by comparing Ka-band *Ze* value with the calibrated X-band ones far above the bright band during stratiform rains. With this system, various types of rainfall were observed mainly over the Atlantic Ocean.

Experimental tests of the DSD estimation method were performed using the data from the T-39 experiment, and described in Chapter 7. The method proposed in Chapter 5 was modified to some extent so as to allow to use more general IRP relationships and to accommodate the attenuated *Ze* (*Zm*) profile. The validity of estimated DSD parameters was confirmed by means of a consistency check with the Ka-band *Zm* profile that is independent of the DSD estimation process. The test result is found to be very encouraging in the sense that the estimated path-averaged N_0 generally shows excellent consistency with the results of comparative analysis between X- and Ka-band *Ze*'s and between rain rates derived from them.

It is suggested that the non-uniform beam filling and the attenuation due to hydrometeors aloft such as bright band particles can cause non-negligible errors in estimated DSDs and in final products such as rain rate and LWC. Further study is required on these problems. In the present analysis, no examination was made for the validity of the DSD estimates for heavy convection where neither Ka-band *Zm* profile nor surface return was available due to excessive rain attenuation. The 10-GHz and 19-GHz radiometer data, which were obtained simultaneously with the radar data in the T-39 experiment, should be useful to analyze such heavy intense rainfall cases.

Based on the results obtained in this study together with those obtained from previous studies, in Chapter 8, considerations were given to general strategies for processing spaceborne radar data to generate accurate and useful rainfall parameters. The usefulness of the DSD estimation method to improve the overall rainfall retrieval was also discussed.

Rainfall measurements employing path attenuation or microwave radiometer data together with the reflectivity profile may not always be applicable mainly because of the uncertainty in the surface σ^0, high background brightness temperature (for radiometer), and the effect of non-uniform beam filling. With such limited chance of observations the DSD estimation method providing DSD and associated IRP relations would still be useful, since this type of information would be applicable not only to the rain area involved in the DSD estimation but also to other areas of the same rain system or to other rainfall of similar type. Such information should therefore be useful to improve rainfall retrieval accuracies for a wide range of rainfall measurements. The wide applicability comes from the fact that storm-scale DSD properties are reasonably well described by a two-scale model the parameters of which can be estimated through spaceborne radar measurements, and that the such large-scale DSD properties or IRP relations are correlated with rainfall type.

ACKNOWLEDGMENTS

The author wishes to express his deepest gratitude to Profs. S. Fukao, I. Kimura and S. Ikebuchi of Kyoto University for their guidance and encouragement in writing this thesis.

A major part of this study was performed at Communications Research Laboratory (CRL) between 1985 and 1990. The author is grateful for the support received from Dr. N. Wakai, Mr. K. Tsukamoto and Dr. J. Suzuki. A special thanks is due to Dr. N. Fugono for his continuous efforts to direct the joint rainfall remote sensing studies with NASA and for his encouragement and support to preparing this thesis.

The author's rainfall remote sensing studies started at Kashima Space Research Center of CRL. The author would like to thank Mr. Y. Otsu, Mr. K. Kosaka, and Mr. M. Yamamoto for their support of the propagation and FM-CW radar experiments at Kashima. He also thanks his colleagues at Kashima; Dr. H. Fukuchi and Mr. M. Takeuchi for their help in conducting the experiment and stimulating discussions with them.

The author would like to thank Dr. S. Miyazaki, Mr. T. Ishimine, Dr. T. Oguchi, Mr. H. Inomata and Dr. T. Ojima for their support while conducting this study at CRL/HQ. A special thanks is due to Dr. K. Okamoto for his contribution to developing the CRL airborne radar/radiometer system and for his support during the preparation of this thesis. During the study at CRL, valuable suggestions and encouragements have been received from colleagues, Dr. M. Fujita, and Mr. T. Ihara among others. The author is most grateful to Dr. K. Nakamura for his numerous contribution during the course of this study, including providing the Kashima disdrometer data to the author. The author is also indebted to Dr. J. Awaka for his guidance in theoretical calculations. A part of disdrometer data analysis was made in collaboration with Dr. D. A. Short during his stay at CRL as a STA (Science and Technology Agency) fellow. His valuable comments and discussions with him are most appreciated.

The aircraft experiment and data analysis have been performed at NASA/Goddard Space Flight Center (GSFC). The author is most grateful to Mr. R. Meneghini for his guidance and many discussions during the study at GSFC. A special thanks is given to Dr. T. T. Wilheit for his guidance and support during the course of the aircraft experiment. Acknowledgment is also due to Dr. D. Atlas for his valuable comments and discussions. Many engineers at GSFC and WFF made the aircraft experiment possible; Mr. W. C. Boncyk, Mr. T. Dod, Mr. D. Clem, Mr. P. Bradfield, Mr. S. Sandlin, and Mr. J. Fuchs among others. The raingage data around WFF were provided from Dr. J. Goldhirsh and Mr. N. Gebo.

LIST OF PUBLICATIONS RELEVANT TO THIS STUDY†

On radar rainfall remote sensing

(1) Kozu, T., K. Nakamura, J. Awaka, and M. Takeuchi, 1983: 14-GHz FM-CW/pulse-compression radar for observation of precipitation on a satellite-Earth path. Preprints, *21st Conf. Radar Meteorol.*, Edmonton, Canada, Amer. Meteor. Soc., 256-262.

(2) Nakamura, K., J. Awaka, T. Kozu, H. Inomata, K. Okamoto, S. Yoshikado, H. Masuko, and T. Shinozuka, 1983: Simultaneous rain observation by C-, X-, Ku, and Ka-band radars. Preprints, *21st Conf. Radar Meteorol.*, Edmonton, Canada, Amer. Meteor. Soc., 213-220.

(3) Kozu, T., J. Awaka, K. Nakamura, and H. Inomata, 1986: Improved estimation of rain attenuation and rainfall rate for slant-paths by simultaneous radar and radiometer measurements. Preprints, *23rd Conf. Radar Meteor.*, Snowmass, CO, Amer. Meteor. Soc., 104-107.

(4) Kozu, T., K. Nakamura, J. Awaka and M. Takeuchi, 1987: Development of Ku-band FM-CW/Pulse-compression radar for rain observation on a slant-path. *J. Radio Res. Lab.*, **34**, (143), 95-113.

(5) Meneghini, R., T. Kozu, K. Nakamura and T. T. Wilheit, 1989: Airborne radar and radiometer measurements for TRMM algorithm development. Preprints, *4th Conf. Satellite Meteor. and Oceanog.*, San Diego, CA, Amer. Meteor. Soc.

(6) Kozu, T., R. Meneghini, W. C. Boncyk, K. Nakamura, and T. T. Wilheit, 1989: Airborne radar and radiometer experiment for quantitative remote measurements of rain, *Proc. IGARSS '89*, Vancouver, Canada, 1499-1502.

(7) Meneghini, R. and T. Kozu, 1990: *Spaceborne weather radar*. Artech House, Norwood, MA, 199pp.

(8) Kozu, T., K. Nakamura, R. Meneghini, and W.C. Boncyk, 1990: Dual-parameter rainfall measurements from space: Experimental test with an airborne radar system. *Proc. 17th International Symp. Space Technology and Science*, Tokyo, 1965-1970.

(9) Nakamura, K., H. Inomata, T. Kozu, J. Awaka, and K. Okamoto, 1990: Rain observation by an X- and Ka-band dual-wavelength radar. *J. Meteor. Soc. Japan*, **68**, 509-521.

(10) Meneghini, R., T. Kozu, H. Kumagai, and W. C. Boncyk, 1990: Analysis of airborne radar and radiometer rain measurements and their relationship to spaceborne observations. *Proc. IGARSS'90*, College Park, MD, 429-432.

† Publications written in English only.

(11) Short, D. A., T. Kozu, and K. Nakamura, 1990: Rainrate and raindrop size distribution observations in Darwin Australia, URSI-F Open Symp. on regional factors in predicting radiowave attenuation due to rain,, Rio de Janeiro., 35-40.

(12) Meneghini, R. and T. Kozu, 1991: A potential method for the estimation of drop size distribution from a dual-wavelength airborne radar. Preprints, *25th Conf. Radar Meteor.*, Paris, Amer. Meteor. Soc., 380-383.

(13) Kozu, T., K. Nakamura, and R. Meneghini, 1991: Estimation of raindrop size distribution parameters from a dual-parameter spaceborne radar measurement. Preprints, *25th Conf. Radar Meteor.*, Paris, Amer. Meteor. Soc., 384-387.

(14) Kumagai, H., R. Meneghini, and T. Kozu, 1991: Multi-parameter airborne rain radar experiment in the North Pacific. Preprints, *25th Conf. Radar Meteorol.*, Paris, Amer. Meteor. Soc., 400-403.

(15) Kozu, T. and K. Nakamura, 1991: Rainfall parameter estimation from dual radar measurements combining reflectivity profile and path-integrated attenuation. *J. Atmos. Ocean. Tech.*, **8**, 259-270.

(16) Kozu, T., K. Nakamura, R. Meneghini and W.C. Boncyk, 1991: Dual-parameter radar rainfall measurement from space: A test result from an aircraft experiment. *IEEE Trans. Geosci. and Remote Sens.*, **GE-29**, 690-703.

On spaceborne radar technology

(17) Okamoto, K., J. Awaka, T. Ihara, T. Manabe, K. Nakamura and T. Kozu, 1988: Conceptual design of rain radar in the Tropical Rainfall Measuring Mission. *Proc. 16th International Symp. Space Technology and Science,* Sapporo, 2277-2282.

(18) Awaka, J., T. Kozu, and K. Okamoto, 1988: A feasibility study of rain radar for the Tropical Rainfall Measuring Mission, 2. Determination of basic system parameters. *J. Comm. Res. Lab.*, **35**, (145), 111-133.

(19) Okamoto, K., J. Awaka, and T. Kozu, 1988: A feasibility study of rain radar for the Tropical Rainfall Measuring Mission, 6. A case study of rain radar system. *J. Comm. Res. Lab.*, **35**, (145), 183-208.

(20) Kozu, T., 1989: On the vertical resolution for near-nadir looking spaceborne radar. Preprints, *24th Conf. Radar Meteorol.*, Tallahassee, FL, Amer. Meteor. Soc., 593-596.

(21) Okamoto, K., J. Awaka, T. Ihara, K. Nakamura, T. Kozu and T. Manabe, 1989: Conceptual design of rain radar in the Tropical Rainfall Measuring Mission. Preprints, *24th Conf. Radar Meteorol.*, Tallahassee, FL, Amer. Meteor. Soc., 623-625.

(22) Okamoto, K., J. Awaka, T. Ihara, K. Nakamura, and T. Kozu, 1989: Conceptual designs of rain radars in the Tropical Rainfall Measuring Mission and on the Japanese Experiment Module at the manned Space Station program. Preprints,*4th Conf. Satellite Meteor. and Oceanog.*, San Diego, CA, Amer. Meteor. Soc., 18-21.

(23) Kozu, T., 1989: Consideration of vertical resolution for near-nadir looking spaceborne radar. *IEEE Trans. Geosci. Remote Sens.*, **GE-27**, 354-357.

(24) Kozu, T., 1990: Effects of return-signal decorrelation on pulse-compression properties for nadir-looking spaceborne radar. *Proc. IGARSS'90*, College Park, MD, 2073-2076.

(25) Nakamura, K., K. Okamoto, T. Ihara, J. Awaka, T. Kozu and T. Manabe, 1990: Conceptual design of rain radar for the Tropical Rainfall Measuring Mission. *International J. Satellite Communications*, **8**, 257-268.

(26) Okamoto, K., T. Ihara, J. Awaka, T. Kozu, K. Nakamura, and M. Fujita, 1990: Rain radar in the Tropical Rainfall Measuring Mission. *URSI-F Open Symp. on regional factors in predicting radiowave attenuation due to rain,*, Rio de Janeiro, 171-174.

(27) Ihara, T., K. Okamoto, T. Kozu, J. Awaka, K. Nakamura, and M. Fujita, 1991: Development of key devices for TRMM rain radar. *Proc. IGARSS'91*, Espoo Finland, 513-516.

(28) Okamoto, K., T. Ihara, J. Awaka, T. Kozu, K. Nakamura, and M. Fujita, 1991: Development status of rain radar in the tropical rainfall measuring mission. Preprints, *25th Conf. Radar Meteorol.*, Paris, Amer. Meteor. Soc., 388-391.

(29) Kozu, T., 1991: Effects of signal decorrelation on pulse-compressed waveform for nadir-looking spaceborne radar. *IEEE Trans. Geosci. and Remote Sens.*, **GE-29**, 786-790.

On propagation and rain scattering for satellite-Earth paths

(30) Fukuchi, H., T. Kozu, K. Nakamura, J. Awaka, H. Inomata, and Y. Otsu, 1983: Centimeter wave propagation experiments using the beacon signals of CS and BSE satellites. *IEEE Trans. Antennas Propag.*, **AP-31**, 603-613.

(31) Awaka, J., K. Nakamura, T. Kozu, and H. Inomata, 1983: Influence of bright band on the precipitation-scatter at 14.3 GHz. Preprints, *21st Conf. Radar Meteorol.*, Snowmass, CO, Amer. Meteor. Soc., 232-237.

(32) Awaka, J., T. Kozu, K. Nakamura, and H. Inomata, 1984: Experimental results on bistatic rain scattering at 14.3 GHz. *IEEE Trans. Antennas Propag.*, **AP-32**, 1345-1350.

(33) Awaka, J., H. Fukuchi, K. Nakamura, and T. Kozu, 1985: A property of D/U examined by using the data obtained in a rain scatter experiment at 14.3 GHz. *Proc. International Symp. on Antennas Propag. (ISAP)*, Kyoto, 281-284.

(34) Fukuchi, H., T. Kozu, and S. Tsuchiya, 1985: Worst month statistics of attenuation and XPD on Earth-space path. *IEEE Trans. Antennas Propag.*, **AP-33**, pp.390-396.

(35) Otsu, Y., T. Kozu, and Y. Takahashi, 1986: Simultaneous occurrence probabilities of rainfall among nine locations in Japan. *Elect. Lett.*, **22**, (18), 937-938.

(36) Kozu, T., H. Fukuchi, and Y. Otsu, 1986: Comparison of antenna noise temperature with rain attenuation of a satellite beacon signal at 12 GHz. *Electron. Lett.*, **22**, (24), 1274-1275.

(37) Kozu, T., J. Awaka, H. Fukuchi, and K. Nakamura, 1988: Rain attenuation ratios on 30/20- and 14/12-GHz satellite-to-Earth paths. *Radio Sci.*, **23**, 409-418.